CUKUROVA UNIVERSITY
INSTITUTE OF NATURAL AND APPLIED SCIENCES

PhD. THESIS

Zühal Şeyma DEMİROĞLU

DETERMINATION OF THE JET ENERGY SCALE CORRECTIONS FOR THE LOW P_T JETS IN PROTON-PROTON COLLISIONS AT $\sqrt{s} = 13$ TeV WITH THE CMS EXPERIMENT

DEPARTMENT OF PHYSICS

ADANA-2020

To my loving family

ABSTRACT

PhD. THESIS

DETERMINATION OF THE JET ENERGY SCALE CORRECTIONS FOR THE LOW P_T JETS IN PROTON-PROTON COLLISIONS AT $\sqrt{s} = 13$ TeV WITH THE CMS EXPERIMENT

Zühal Şeyma DEMİROĞLU

CUKUROVA UNIVERSITY
INSTITUTE OF NATURAL AND APPLIED SCIENCES
DEPARTMENT OF PHYSICS

Supervisor : Prof. Dr. Eda EŞKUT
II. Supervisor : Assoc. Prof. Dr. Salim ÇERÇİ
Year: 2020, Page: 205
Jury : Prof. Dr. Eda EŞKUT
: Prof. Dr. İsa DUMANOĞLU
: Prof. Dr. Ayşe POLATÖZ
: Prof. Dr. Deniz SUNAR ÇERÇİ
: Assoc. Prof. Dr. Hüseyin TOPAKLI

In this thesis, two analyses related to jet energy scale corrections focus on the low p_T region are performed. The first part of the thesis is dedicated to the Monte Carlo (MC) truth jet energy corrections for 2015 no pileup QCD PYTHIA8 sample. Particle-Flow Charged Hadron Subtraction (PFCHS) jets are reconstructed by using the anti-k_T clustering algorithm with the cone size parameters of 0.4. The study is performed in the pseudorapidity region of $|\eta| < 5.191$ and jet p_T region of $10 < p_T < 905$ GeV. The second part presents the calibration of the jet energy scale with respect to residual differences between data and simulation after simulation-based pre-calibrations is applied. This correction is called as L2 relative residual jet energy correction. In this analysis, $\sqrt{s}$ = 13 TeV low pileup data of 2015 and PYTHIA8 MC samples are used. The correction factors depending on jet p_T and η are derived by using two different methods based on the dijet final states in the region of $|\eta| < 5.191$ pseudorapidity and $20 < p_T < 114$ GeV. This will make an important contribution to the analysis to be performed using the low p_T jets in the physics analysis.

Key Words: CMS, Jet, Jet Energy Corrections, QCD, Low p_T

ÖZ

DOKTORA TEZİ

CMS DENEYİ İLE $\sqrt{s} = 13$ TeV'LİK PROTON-PROTON ÇARPIŞMALARINDA DÜŞÜK P_T'Lİ JETLER İÇİN JET ENERJİ ÖLÇEK DÜZELTMELERİNİN BELİRLENMESİ

Zühal Şeyma DEMİROĞLU

ÇUKUROVA ÜNİVERSİTESİ
FEN BİLİMLERİ ENSTİTÜSÜ
FİZİK ANABİLİM DALI

Danışman : Prof. Dr. Eda EŞKUT
II. Danışman : Doç. Dr. Salim ÇERÇİ
Yıl: 2020, Sayfa: 205
Jüri : Prof. Dr. Eda EŞKUT
: Prof. Dr. İsa DUMANOĞLU
: Prof. Dr. Ayşe POLATÖZ
: Prof. Dr. Deniz SUNAR ÇERÇİ
: Doç. Dr. Hüseyin TOPAKLI

Bu tezde, düşük p_T bölgesine odaklanan jet enerji ölçeği düzeltmeleri ile ilgili iki analiz sunulmuştur. Tezin ilk bölümü, yığınlık bilgisi olmayan 2015 QCD PYTHIA8 örneği için Monte Carlo (MC) gerçek jet enerji düzeltmelerine ayrılmıştır. Parçacık Akışı Yüklü Hadron Çıkarımı (PFCHS) jetleri, 0.4 koni parametresine sahip anti-k_T kümeleme algoritması kullanılarak yeniden yapılandırılmıştır. Çalışma, $|\eta| < 5.191$ psüdorapidite bölgesinde ve jetlerin dik momentum $10 < p_T < 905$ GeV bölgesinde gerçekleştirilmiştir. İkinci kısım, simülasyon tabanlı ön kalibrasyonlar uygulandıktan sonra jet enerji ölçeğinin veri ve simülasyon arasındaki artık farklılıklara göre kalibrasyonunu sunmaktadır. Bu düzeltmeye L2 göreceli artık jet enerji düzeltmesi denmektedir. Bu analizde, 2015'de $\sqrt{s} = 13$ TeV'lik düşük yığınlıklı proton-proton çarpışma verisi ve PYTHIA8 MC örnekleri kullanılmıştır. Jet p_T ve η'ya bağlı olarak düzeltme faktörleri, dijet olaylarını kullanan iki farklı yöntem ile $|\eta| < 5.191$ psüdorapidite ve $20 < p_T < 114$ GeV bölgesi için türetilmiştir. Bu düzeltmelerin elde edilmesi, düşük p_T jet bilgisi kullanılarak yapılacak fizik analizlerine önemli bir katkı sağlayacaktır.

Anahtar Kelimeler: CMS, Jet, Jet Enerji Düzeltmeleri, KRD, Düşük p_T

GENİŞLETİLMİŞ ÖZET

20. yüzyılın başlangıcında, gözlenebilir fiziksel olgular hakkındaki yorumumuzu kökten değiştiren iki fizik alanı ortaya çıkmıştır: özel görelilik ve kuantum mekaniği. Bu iki kuramı temel alan Parçacık Fiziğinin Standart Model (SM)'i, maddeyi oluşturan temel parçacıkları, bu parçacıklar ile taşıyıcı parçacıklar arasındaki etkileşimleri (elektromanyetik, zayıf ve güçlü etkileşim) tanımlayan kuramsal çerçeveyi oluşturmaktadır. Bu modelde fermiyonlar ve bozonlar olmak üzere iki grupta bulunan toplam 17 adet parçacık vardır. Bunlardan 12 tanesi maddenin temel bileşenlerini (6 kuark, 6 lepton), 5 tanesi ($W^{\pm}$, Z^0, γ, g, H bozonları) ise bu parçacıklar arasındaki taşıyıcı parçacıkları temsil etmektedir. Son 45 yılda, kuramın birçok öngörüsü, binlerce bilim insanının iş birliğiyle farklı deneylerde keşfedilmiştir. Örneğin, $W^{\pm}$ ve Z^0 bozonları 1983'te Super Proton Synchrotron (SPS)'de keşfedildi, 1995 yılında Tevatron'un CDF ve D0 iş birlikleri tarafından üst (*t*) kuark keşfedildi, 4 Temmuz 2012'de CERN'in Büyük Hadron Çarpıştırıcısı (BHÇ)'nda yer alan ATLAS ve CMS deneyleri tarafından uzun süre aranan Higgs bozonu ile tutarlı yeni bir parçacığın keşfi duyurulmuştur. 14 Mart 2013'te ATLAS ve CMS iş birlikleri bu yeni parçacığın gerçekten de temel parçacıklara kütle veren Brout-Englert-Higgs mekanizmasında merkezi rol oynayan bir Higgs bozonu olduğunu doğrulamıştır. SM'nin, büyük başarılarına rağmen, hâlâ çeşitli kuramsal eksiklikleri vardır. Örneğin; SM, elektrozayıf kuram ile elektromanyetik ve zayıf etkileşimlerin yüksek enerji ölçeklerinde birleşmesini açıklamaktadır ancak kuarklar ve gluonlar arasında bir etkileşim olan güçlü etkileşmenin elektrozayıf etkileşim ile birleştirilmesini öngörememektedir. Bu nedenle, SM'in ötesindeki fiziği keşfetmek için alternatif yeni modeller ve kuramlar geliştirilmiştir.

BHÇ, bu yeni fizik ve yeni parçacıkların keşfi için tasarlanmıştır. Şimdiye kadar yapılmış en güçlü proton-proton (p-p) çarpıştırıcısı olan BHÇ, 27 km çevre uzunluğuna sahiptir ve yerin 100 m altında bulunmaktadır. Bu hızlandırıcı, parçacık çarpışmalarında hiç beklenmeyen enerjilere ulaşmayı (Tera-elektronVolt ölçeğinde) ve böylece maddeyi yeni ölçeklerde araştırmayı ve SM'i derinlemesine test etmeyi mümkün kılmaktadır. BHÇ üzerinde bulunan dört büyük deney, üretilen çarpışmalardaki sinyalleri toplamaktadır ve çarpışma olayını mümkün olabildiğince en iyi şekilde yeniden yapılandırmaya çalışmaktadır. Bu deneylerden, ATLAS ve CMS, tüm fizik alanlarını kapsayan genel amaçlı deneylerdir. LHCb deneyi, yük-parite ihlali ölçümlerine ve çeşni fiziğinde nadir oluşan bozunumlara odaklanmaktadır. BHÇ'de p-p çarpışmalarının yanı sıra birkaç hafta boyunca ağır iyon çarpışmaları da gerçekleştirilmektedir. ALICE deneyi, bu çarpışma verilerini analiz ederek kuark-gluon plazmasını tanımlama ve keşfetme çalışmalarını gerçekleştirmektedir.

Bu tezde analiz edilen veri, CMS (Sıkı Müon Solenoid) dedektörü tarafından kayıt edilmiştir. CMS dedektörü, p-p ve ağır iyon çarpışmalarında ortaya çıkan parçacıkların özelliklerini ölçmek için tasarlanmıştır. Adı, dedektörün üç önemli özelliğini belirtmektedir: sıkı tasarımını, iç dedektörde homojen bir manyetik alan bulunmasını, müon ölçümü için özel tasarımını. CMS dedektörü, etkileşim noktası çevresinde katmanlar halinde bir yapıya sahiptir. Dedektörün alt sistemleri içten dışarıya doğru şu şekilde tanımlanmaktadır; iç izleyici, dış izleyici, elektromanyetik kalorimetre, hadronik kalorimetre, solenoid ve müon sistemi.

Bugünkü mevcut bilgimiz bölünmez madde parçacıklarının, kütlesiz gluonlar ile birbirine bağlı olan kuarklar olduğudur. Kuantum Renk Dinamiği (KRD), kuarklar ve gluonlar arasındaki güçlü etkileşmeyi tanımlayan bir kuramdır. KRD'nin kendine özgü bir yönü, renk hapsi adı verilen bir özellik nedeniyle kuarkların ve gluonların hiçbir zaman doğrudan makroskopik düzeyde gözlenememesidir. Bunun yerine, hadron olarak bilinen bileşik parçacıklar oluştururlar. Protonlar üç kuarktan oluşmaktadır; iki yukarı (u) kuark ve bir aşağı (d) kuark. KRD, proton çarpışmalarının etrafına jetler şeklinde imzasını bırakmaktadır. Jetler, çarpışmalarda fazladan yüksek momentum kazanan kuarklar ve gluonlar tarafından başlatılan toplanmış parçacık spreyleridir. Hızlandırılmış kuarklar ve gluonlar tekrar tekrar kuarklara ve gluonlara ayrılır ve sonunda deneyde tespit edilebilen bir parton (kuark/gluon) duşu oluşturmaktadır. BHÇ deneylerinde yeni fizik araştırmaları için kullanılan en güçlü analiz nesnelerinden biri jetlerdir ve birçok ilginç fizik çalışması için deneysel arka plan gürültüsünü oluşturmaktadır. Bu nedenle, jetlerin üretimini ve özelliklerini incelemek oldukça önemlidir.

Bir jetin dört-vektörü, neredeyse tek bir nesneye yakın olan parçacıkları kümeleyen bir jet algoritması ile tanımlanmaktadır. Temel olarak, koni ve kümeleme tipi olmak üzere iki farklı algoritma bulunmaktadır. Kümeleme tipi algoritması kendi içinde üçe ayrılmaktadır; k_T, Cambridge-Aachen ve anti-k_T jet algoritmaları. Bu tezde kullanılan jetler anti-k_T algoritmasına göre yeniden yapılandırılmıştır. CMS analizlerinde üç farklı jet tipi kullanılmaktadır: kalorimetre kulelerinden gelen enerji bilgisini kullanarak yeniden yapılandırılan kalorimetre jetleri, izleyicide ölçülen yüklü parçacıkların momentumu ile kalorimetre jetleri kullanılarak yeniden yapılandırılan Jet-Artı-İz (JPT) jetleri, tüm alt dedektörlerden gelen bilgileri kullanarak bir olaydaki tüm parçacıkları tanımlayan ve yeniden yapılandıran Parçacık Akışı (PF) jetleri.

Yeniden yapılandırılmış jetlerin enerjisinin birkaç nedenden dolayı kalibre edilmesi gerekmektedir. Birincisi, kullanılan yeniden yapılandırma jet algoritmaları hadronizasyon sırasında oluşan parçacıkları jet konisi içinde düzgün bir şekilde toplayamayabilir. Böylece, jetin özellikleri doğru bir şekilde belirlenemeyecektir. İkincisi, alt-dedektörlerin kalibrasyon problemleri jetlerin enerjisinin ölçümünü bozmaktadır. Bu yüzden, CMS'de bu etkileri uygun şekilde düzeltmeyi amaçlayan faktörlü bir jet enerji düzeltme yaklaşımı benimsenmiştir. Böylece, her biri belirli bir etkiyi düzelten birkaç düzeltme seviyesi tanımlanmıştır. Her seviye bir önceki seviyeye uygulanan düzeltmelere bağlıdır, bu nedenle bu düzeltmelerin uygulanma sırası önemlidir. Üç farklı düzeltme düzeyi vardır: Seviye-1, Seviye-2 ve Seviye-3. Seviye-1 düzeltmesi, yığınlık ve dedektör gürültüsünün etkilerini düzeltmektedir.

Seviye-2 ve 3 düzeltmeleri, jetlerin dik momentum ve psüdorapiditelerine bağlı olarak jetlerin yeniden yapılandırma verimliliğindeki değişiklikleri düzeltmeyi mümkün kılmaktadır. Bu düzeltmeler hem verilere hem de simülasyona uygulanmaktadır. Veri ve simülasyon arasındaki kalan farkları düzeltmek için artık düzeltmeler adı verilen düzeltmeler elde edilmektedir. Bu düzeltmeler yalnızca verilere uygulanmaktadır. Böylece, jet enerji düzeltmeleri ile yeniden yapılandırılmış jet enerjisi, gerçek jet enerjisiyle ilişkilendirilebilmektedir.

Tezin ilk çalışmasında düşük p_T bölgesi ($10 < p_T < 905$ GeV) için mutlak ve bağıl jet enerji düzeltme faktörleri (L2L3 MC truth) yığınlık bilgisi olmayan Monte Carlo (MC) örneği kullanılarak belirlenmiştir. MC olarak QCD PYTHIA8 örneği kullanılmıştır. Simüle edilmiş olaylarda jet yanıtı (p_T^{reco}/p_T^{gen}) farklı p_T ve η aralıkları için hesaplanmıştır. Belirlenen jet yanıtının tersi düzeltme faktörü olarak uygulanmaktadır. Bu seviye, simüle edilmiş olaylardaki düzeltmeleri tamamlamaktadır.

Tezin ikinci kısmında düşük p_T bölgesi ($20 < p_T < 114$ GeV) için L2 artık jet enerji düzeltmeleri elde edilmiştir. Bu çalışma, 2015 yılında CMS dedektöründe toplanan düşük yığınlığa sahip p-p çarpışma verileri ve QCD/MinimumBias PYTHIA8 MC örnekleri ile gerçekleştirilmiştir. Bu düzeltme, MC ile veri arasındaki karşılaştırmadan kaynaklanan jet enerji ölçeği farklılıklarını düzeltmektedir. Analiz sırasında dijet olay seçimi kullanılmıştır ve bu jetler 0.4 koni yarıçapına sahip olup anti-k_T jet algoritması ile yeniden yapılandırılmıştır. L2 artık düzeltmeleri, iki farklı yöntem kullanılarak elde edilmiştir: p_T denge metodu ve kayıp dik enerji projeksiyon fraksiyonu (MPF) metodu. Düzeltme faktörleri η ve p_T'nin bir fonksiyonu olarak türetilmiştir. MPF metodu kullanılarak elde edilen düzeltmeler L2 artık düzeltme faktörleri seçilmiştir.

ACKNOWLEDGMENTS

First and foremost, I would like to sincerely express my appreciation to my supervisor Prof. Dr. Eda Eşkut for her kind support, her guidance, help in every situation, and the trust she placed in me during the period I spent as her student at Cukurova University. Further, I would like to thank my co-supervisor Assoc. Prof. Dr. Salim Çerçi and Prof. Dr. Deniz Sunar Çerçi for getting me involved in CMS jet studies, providing me very beneficial advice, and steady support throughout my PhD studies. I am sincerely grateful for everything I have learned from them.

I would like to express my special thanks to the referee of my thesis committee, Prof. Dr. Eda Eşkut, Prof. Dr. Ayşe Polatöz, Prof. Dr. İsa Dumanoğlu, Prof. Dr. Deniz Sunar Çerçi, and Assoc. Prof. Dr. Hüseyin Topaklı for reading this thesis and their valuable comments. I also want to thank our High Energy Physics Group Members Prof. Dr. Gülsen Önengüt and Prof. Dr. Aysel Kayış Topaksu for their encouragement.

Moreover, I'm eternally grateful for Asst. Prof. Dr. İlknur Hoş and Dr. Çağlar Zorbilmez's close friendship, continuous support, ever-enduring patience. I have always felt that I was lucky to have started my PhD studies with you two in the same group. Thank both of you for reading of the first draft of the thesis and taking the time from your personal time to help me with all kinds of my problems in both physics and life.

In particular, I would like to thank all the people whom I worked directly in the CMS FSQ (later in SMP-HAD), JERC, and HCAL groups. My sincere thanks must also go to the US HCAL Management who provide me financial support to work on the assembly and quality control tests of HB calibration units during the HCAL Phase 1 upgrade. I am grateful to the CMS HCAL Project Management Team, especially Pawel De Barbaro, who give me the chance to partake in this project.

Special thanks to my friends and colleagues who have always listening, helping, and encouraging me throughout my PhD, in alphabetical order, Assoc. Prof. Dr. Aytül Adıgüzel, Dr. Semiray Girgis Chyla, Dr. Yalçın Güler, Asst. Prof. Dr. Emine Gürpınar Güler, Nebahat Kalkan, Doyeong Kim, Merve İnce Lezki, Dr. Samet Lezki, Assoc. Prof. Dr. Kadri Özdemir, and Semra Türkçapar.

I would like to thank Melek and Orhan Dönertaş for helping me to find a place during the period of my stay at CERN and for their moral support. I also want to thank my cousin, Mehmet Dartıcı, for signing the surety bond which was required to start my TÜBİTAK scholarship.

I am thankful to the Turkish Atomic Energy Authority (TAEK) who sponsored me during the time I have spent at CERN under the project codes of 2014 TAEKCERN-A5.H6.F2.12 and 2018TAEK(CERN)A5.H6.F2-19.

I extend my special thanks to the Scientific and Technical Research Council of Turkey (TÜBİTAK) for their financial support under the program of TÜBİTAK BİDEB 2211-A General Domestic PhD Scholarship.

Last but not least, I would like to wholeheartedly thank my loving parents, sisters, brothers-in-law, nieces, nephews, and extended family for their never-ending love, constant encouragement, and moral support you have all shown me throughout my life. This thesis is dedicated to them.

CONTENTS **PAGE**

LIST OF TABLES **PAGE**

LIST OF FIGURES **PAGE**

XXIX

ABBREVIATIONS

ALICE	: A Large Ion Collider Experiment
APD	: Avalanche Photodiodes
ASIC	: Application Specific Integrated Circuit
ATLAS	: A Toroidal LHC Apparatus
BCDMS	: Bologna-CERN-Dubna-Munich-Saclay
BFKL	: Balitski-Fadin-Kuraev-Lipatov
BPIX	: Barrel Pixel Detector
C-A	: Cambridge-Aachen
CCFM	: Catani-Ciafaloni-Fiorani-Marchesini
CDF	: Collider Detector at Fermilab
CERN	: Conseil Européen pour la Recherche Nucléaire
CMS	: Compact Muon Solenoid
CHS	: Charged Hadron Subtraction
CM	: Center of Mass
CSC	: Cathode Strip Chambers
CTEQ	: Coordinated Theoretical-Experimental Project on QCD
DGLAP	: Dokshitzer-Gribov-Lipatov-Altarelli-Parisi
DIS	: Deep Inelastic Scattering
DT	: Drift Tubes
E665	: Fermilab Experiment-665
EB	: Electromagnetic Barrel Calorimeter
ECAL	: Electromagnetic Calorimeter
EE	: Electromagnetic Endcap Calorimeter
EMF	: Electromagnetic Energy Fraction
EYETS	: Extended Year-End Technical Stop
FPGA	: Field-Programmable Gate Array
FSR	: Final-State Radiation

FPIX	: Forward Pixel Detector
GCT	: Global Calorimeter Trigger
GT	: Global Trigger
HB	: Barrel Hadronic Calorimeter
HCAL	: Hadronic Calorimeter
HERA	: Hadron-Elektron-Ring-Anlage
HERWIG	: Hadron Emission Reactions With Interfering Gluons
HF	: Hadronic Forward
HL-LHC	: High-Luminosity Large Hadron Collider
HLT	: High Level Trigger
HO	: Outer Barrel Hadronic Calorimeter
HPD	: Hybrid Photodiode
IRC	: Infrared and Collinear
ISR	: Initial-State Radiation
IT PU	: In-Time Pileup
JEC	: Jet Energy Correction
JERC	: Jet Energy Resolution and Corrections
JES	: Jet Energy Scale
L1	: Level-1 Trigger
LEIR	: Low Energy Ring Ion
LHA	: Les Houches Accord
LHC	: Large Hadron Collider
LHCb	: Large Hadron Collider Beauty Experiment
LHEF	: Les Houches Event Files
LINAC	: Linear Accelerator
LLA	: Leading Logarithmic Approximation
LO	: Leading Order
LS	: Long Shutdown
MB	: Muon Barrel

MC	: Monte Carlo
MET	: Missing Transverse Energy
MIB	: Machine Induced Background
MPF	: Missing Transverse Momentum Projection Fraction
MSTW	: Martin-Stirling-Thorne-Watt
NLO	: Next-to-Leading Order
NMC	: New Muon Collaboration
NNPDF	: Neural Network Parton Distribution Functions
OOT PU	: Out-of-Time Pileup
QIE	: Charge Integrating and Encoding
PDF	: Parton Density Function
PF	: Particle-Flow
PMT	: Photomultiplier Tubes
pQCD	: Perturbative Quantum Chromodynamics
PS	: Proton Synchrotron
PU	: Pileup
RBX	: Readout Box
RCT	: Regional Calorimeter Trigger
RGE	: Renormalization Group Equation
RPCs	: Resistive Plate Chambers
QCD	: Quantum Chromodynamics
QED	: Quantum Electrodynamics
SiPM	: Silicon Photomultiplier
SISCone	: Seedless Infrared Safe Cone
SLAC	: Standard Linear Accelerator Center
SM	: Standard Model
SPS	: Super Proton Synchrotron
ThePEG	: Toolkit for High Energy Physics Event Generation
TIB	: Inner Barrel

TOB	: Outer Barrel
TP	: Trigger Primitive
TPG	: Trigger Primitive Generators
TriDAS	: Trigger and Data Acquisition System
YETS	: Year-End Technical Stop
WLS	: Wavelength Shifting

1. INTRODUCTION

Particle physics or high energy physics is a branch of physics dedicated to the study of the elementary constituents of matter and their interactions. The Standard Model (SM) of particle physics has allowed a very precise description of elementary constituents and their interactions since early 1970s. In total, it describes the intermediate bosons of the electromagnetic, weak, and strong interactions and their interactions with the 12 fermions of the model. SM represents the studies of many thousands of scientists based on theoretical ideas and experimental results. Over the past 45 years, many predictions of this theory have been discovered at different experiments by the collaboration of many thousands of scientists, e.g. $W^{\pm}$ and Z^0 bosons were discovered at the Super Proton Synchrotron (SPS) in 1983, the top quark was discovered by the CDF (Collider Detector at Fermilab) and D0 collaborations of Tevatron in 1995, the discovery of a new particle consistent with long-sought Higgs boson is announced by ATLAS (A Toroidal LHC ApparatuS) and CMS (Compact Muon Solenoid) experiments at CERN's Large Hadron Collider (LHC) on July 4, 2012. On 14 March 2013, ATLAS and CMS collaborations have confirmed that the new particle is indeed a Higgs boson which plays a central role in the Brout-Englert-Higgs mechanism giving mass to elementary particles. Despite its great success, this theory still suffers from various theoretical deficiencies. For example, the SM foresees the unification of electromagnetic and weak interactions at high energy scales but not of the strong interaction which is an interaction between quarks and mediated by the exchange of gluons. Therefore, alternative new models and theories have been introduced to understand what is beyond the SM and the experiments at the LHC will help us to find more of new physics.

One of the powerful analysis objects used in LHC experiments for new physics searches is jets which are collimated streams of particles. The reason for this is that new hypothetical particles originate from protons collisions in the LHC and these particles have to be linked with quarks and gluons which then fragment into jets. Therefore, it is quite important to study the production and properties of jets that constitute the experimental background noise for most of the physics processes studied at the LHC. On the other hand, jets represent the main tool for accessing information concerning the dynamics of parton interactions during proton-proton (p-p) collisions at high energy. So, the jet production plays a critical role to test predictions of perturbative QCD (pQCD) over a wide kinematic region and constrains the parton distribution function of the proton.

Chapter 2 briefly summarizes the concepts of the SM in particle physics. As we mentioned above, unifying the electroweak interaction and strong interaction at a high energy scale is not possible in the SM. The strong interaction is described by Quantum Chromodynamics (QCD) and is more difficult to study. The second part of Chapter 2 is devoted to the QCD which improves the detailed description of the SM physics. The different evolution equations which are used to calculate the parton density functions in different kinematic regions of phase space are discussed at the end of this chapter.

The work presented in this thesis is interested in the identification of the low p_T jets produced in the p-p collisions of the LHC and was carried out in the CMS experiment collaboration. The third chapter is devoted to the instrumentation of the LHC and then specifically to the features of the CMS detector which is one of the two large general-purpose detectors at the LHC.

Chapter 4 is devoted to the tools used to simulate and reconstruct data. A physics analysis should be tested on simulated data before comparing the results with real data. These simulated data come from Monte Carlo (MC) event generators that describe the physics corresponding to quantify expected detector performance. In the second part of this chapter, methods for the reconstruction of high-level objects such as jets will be presented. This chapter will conclude with the description of the missing transverse energy which has an important role in physics analysis.

The analyses presented in this thesis include the extraction of two different jet energy scale (JES) corrections based on both data and MC samples. Chapter 5 presents the factorized approach to jet energy corrections used in CMS in detail. The aim of these corrections is that the reconstructed jets is calibrated to have the correct energy scale.

Chapter 6 will present the analysis related to MC truth jet energy correction which was explained in the previous chapter. This chapter presents the different stages of this analysis with the definition of the selection of events, the results obtained by the study of the determination of MC truth correction and the closure test.

Finally, Chapter 7 presents the results obtained by the study of the determination of L2 relative residual jet energy correction by using low pileup (PU) data at 13 TeV. Two different methods, p_T-balance and the Missing Transverse Momentum Projection Fraction (MPF), are used to determine the response in data and simulated events.

The last chapter presents the summary and conclusions of both analyses.

2. THEORETICAL FRAMEWORK

In this chapter, the main limits of the SM are briefly discussed. QCD which represents one of the most accredited theories for the description of the SM physics is also introduced.

2.1. The Standard Model

2.1.1. Phenomenology

The SM is a commonly accepted theory, used to describe interactions among elementary particles in processes occurring in a range of energies up to 1 TeV. The fundamental interactions between elementary particles are treated in this model by a local gauge invariance by the symmetry groups $SU(3)_C \otimes SU(2)_L \otimes U(1)_Y$. The SM can provide a quantitative description of three of the four interactions in nature: electromagnetism, weak, and strong interaction. The group $SU(3)_C$ describes strong interactions through QCD, which will be discussed in this chapter from Section 2.2 on, while the group $SU(2)_L \otimes U(1)_Y$ describes the unification of weak and electromagnetic interactions through the Glashow-Weinberg-Salam model (Glashow, 1961; Weinberg, 1967).

The constituent particles of matter in this model are fermions that are divided into leptons and quarks. They are the simplest components in the sense that they do not have substructures at the smallest distances probed by the high-energy accelerators. There are 12 fermions in the SM: 6 quarks and 6 leptons. Leptons and 2-by-2 quarks are grouped into three generations with identical quantum numbers but different masses. A doublet of quarks with three different color charges, a neutrino, and an electrically charged lepton is included in each generation in the SM (Altarelli, 2005):

$$1^{\text{st}}\ \text{generation:} \begin{bmatrix} u & u & u & \nu_e \\ d & d & d & e \end{bmatrix},$$

$$2^{\text{nd}}\ \text{generation:} \begin{bmatrix} c & c & c & \nu_\mu \\ s & s & s & \mu \end{bmatrix},$$

$$3^{\text{rd}}\ \text{generation:} \begin{bmatrix} t & t & t & \nu_\tau \\ b & b & b & \tau \end{bmatrix}.$$

Each of the 12 elementary particles is associated with an antiparticle that has the same mass, but with opposite quantum numbers and charge: there are therefore 24 elementary constituents of the matter. The general properties of the fundamental particles of the SM are summarized in Figure 2.1.

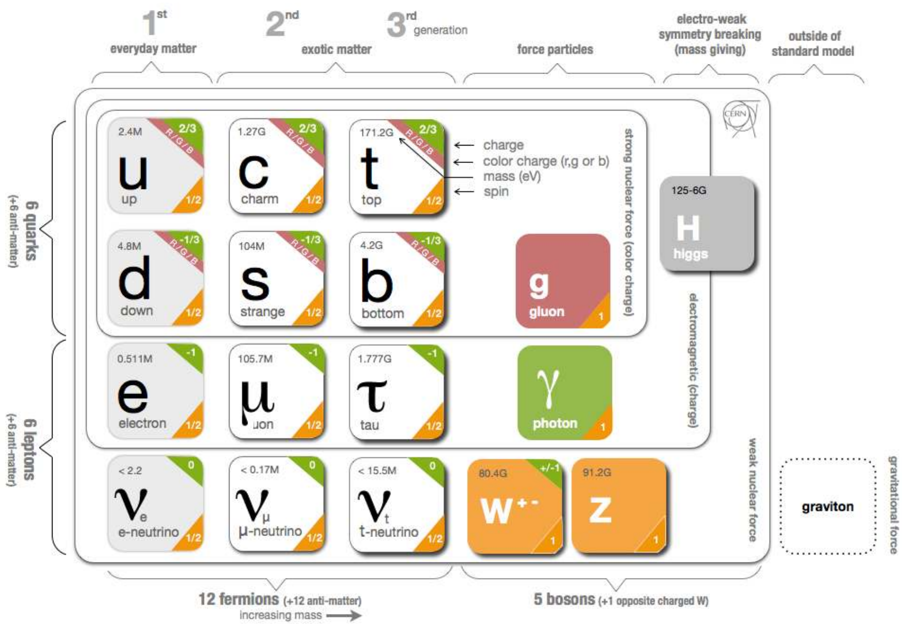

Figure 2.1. The figure shows the fundamental particles and the interactions which described in the SM (Galbraith, 2012).

Leptons are composed of electrons, muons, tau with the negative electrical charge and each lepton linked with a non-massive, electrically neutral particle: neutrinos. All these leptons have the same spin of ½.

The constituents of hadrons are quarks which consist of six different flavors: up (u), down (d), strange (s), charm (c), bottom (b), and top (t). Quarks can interact via electromagnetic and weak interactions as well as leptons, but also through the strong interaction which responsible for their confinement within hadrons. Hadrons are divided into two subgroups as baryons and mesons: (anti) baryons contain three valence quarks (or three antiquarks), while mesons are valence quark-antiquark systems, these quarks are linked together by gluons.

The interaction between elementary particles occurs through the exchange of particles, known as bosons, and identifies four fundamental interactions. All four of them have a specific relative strength, a specific range, and mediators. The $W^{\pm}$ and Z^0 bosons are the mediators of the weak interaction and are massive. The photon, γ, is the mediator of the electromagnetic interaction has no mass. The charge of the strong interaction is called color and it can take three values (red, green, blue) and their anti-values (anti-red, anti-green, anti-blue). The sum of the three color charges is neutral. The strong interaction is mediated by massless gluon, which also carries color and anti-color charge. As illustrated in Figure 2.2, if an elementary particle has several charges, it can be affected by more than one interaction (Woithe et al., 2017). The SM does not include gravitational interaction, which is negligible compared to other interactions in subatomic physics processes. The graviton is responsible for the gravitational interaction but has not yet been discovered.

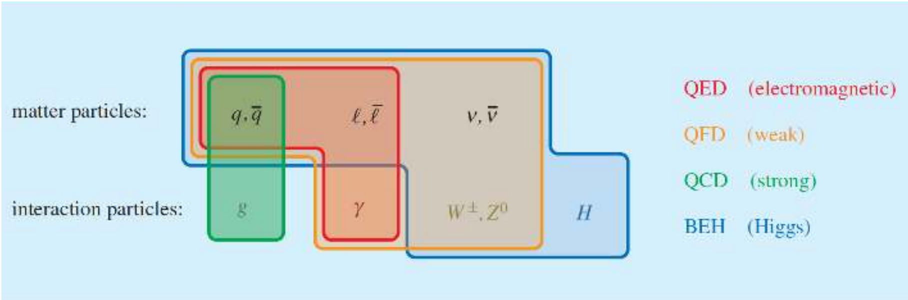

Figure 2.2. The matter can be classified into three groups: (quarks (q), antiquarks ($\bar{q}$)), (leptons (l), antileptons ($\bar{l}$)), and (neutrinos (ν), antineutrinos ($\bar{\nu}$)). Gluons (g) couple to quarks, antiquarks, and gluons. Photons (γ) couple to electrically charged particles. The $W^{\pm}$, Z^0 bosons couple to all the fermions and also interact with the γ through the weak interaction. The Brout–Englert–Higgs field interacts with all the particles which have mass (Woithe et al., 2017).

2.1.2. Lagrangian Formalism

The mathematical expression of the SM is formulated in a compact description, so-called 'Lagrangian'. Joseph–Louis Lagrange introduced Lagrangian mechanics as an alternative formulation of classical mechanics in 1788. The Lagrange function or Lagrangian is shown in Equation 2.1 in the case of particles or rigid bodies that can be treated as particles in classical mechanics:

$$L(\boldsymbol{q},\dot{\boldsymbol{q}},t) = T(\boldsymbol{q},\dot{\boldsymbol{q}},t) - V(\boldsymbol{q},t) \tag{2.1.}$$

where q is the generalized coordinates (say, $\boldsymbol{q}(t)=x$), $\dot{\boldsymbol{q}}$ is their time derivatives ($\dot{\boldsymbol{q}}(t)=v_x$), t is the time, T and V are respectively the kinetic and scalar potential energy of the system.

We define an action potential function $S[\boldsymbol{q}(t)]$ from time t_1 to t_2 is given by the integral,

$$S[\boldsymbol{q}(t)] = \int_{t_1}^{t_2} L(\boldsymbol{q},\dot{\boldsymbol{q}},t)dt \tag{2.2.}$$

Hamilton's principle says that for the actual motion of the system between the fixed times t_1 and t_2 is such that the integral is a minimum for the path $\boldsymbol{q}(t)$ of motion, therefore δS must be zero for this path. In this case, we can write as $\delta S[\boldsymbol{q}(t)] = 0$.

$$\delta S[\boldsymbol{q}(t)] = \int_{t_1}^{t_2} \delta L(\boldsymbol{q}, \dot{\boldsymbol{q}}, t) dt = 0 \tag{2.3.}$$

Using the variation of the Lagrangian into Hamilton's principle,

$$\int_{t_1}^{t_2} \left\{ \sum_i \left[\frac{\partial T}{\partial \dot{q}_i} \delta \dot{q}_i + \frac{\partial T}{\partial q_i} \delta q_i - \frac{\partial V}{\partial q_i} \delta q_i \right] \right\} dt = 0 \tag{2.4.}$$

where $\delta \dot{q}_i = \frac{d}{dt} \delta q_i$ and we integrate the first term in the integral by parts;

$$\int_{t_1}^{t_2} \frac{\partial T}{\partial \dot{q}_i} \delta \dot{q}_i = \frac{\partial T}{\partial \dot{q}_i} \delta q_i \Big|_{t_1}^{t_2} - \int_{t_1}^{t_2} \frac{d}{dt} \left(\frac{\partial T}{\partial \dot{q}_i} \right) \delta q_i dt = 0 \tag{2.5.}$$

Since $\delta \boldsymbol{q}(t_1) = 0$ and $\delta \boldsymbol{q}(t_2) = 0$;

$$\int_{t_1}^{t_2} \left\{ \sum_i \left[-\frac{d}{dt} \left(\frac{\partial T}{\partial \dot{q}_i} \right) \delta q_i dt + \frac{\partial T}{\partial q_i} \delta q_i - \frac{\partial V}{\partial q_i} \delta q_i \right] \right\} dt = 0 \tag{2.6.}$$

Since δq_i is arbitrary, the term in [] must be zero for all i, so we have finally (Gavin, 2016);

$$\frac{d}{dt} \left(\frac{\partial T}{\partial \dot{q}_i} \right) - \frac{\partial T}{\partial q_i} + \frac{\partial V}{\partial q_i} = 0 \tag{2.7.}$$

$$\frac{d}{dt}\frac{\partial L}{\partial \dot{q}} - \frac{\partial L}{\partial q} = 0 \text{ where } L(\boldsymbol{q}, \dot{\boldsymbol{q}}, t) = T(\boldsymbol{q}, \dot{\boldsymbol{q}}, t) - V(\boldsymbol{q}, t) \quad (2.8.)$$

The formalism presented in Equation 2.8 can be extended to the case of continuous space-time systems. A Lagrangian density is a function of generalized fields *ϕ(x, y, z, t)* with four-vectors of Lorentz *(x, y, z, t)* = x_μ.

$$L(\boldsymbol{q}, \dot{\boldsymbol{q}}, t) \rightarrow \mathcal{L}(\phi(x_\mu), \frac{\partial \phi}{\partial x_\mu}, x_\mu) \quad (2.9.)$$

where Lagrangian density $\mathcal{L}$ defined as $L = \int \mathcal{L} dx^3$.
The relativistic formulation of the Euler Lagrange Equation 2.8 becomes (University of Oulu, 2004);

$$\frac{\partial}{\partial x_\mu}\left(\frac{\partial \mathcal{L}}{\partial(\partial \phi / \partial x_\mu)}\right) - \frac{\partial \mathcal{L}}{\partial \phi} = 0 \quad (2.10.)$$

We will pick the Lagrangian density $\mathcal{L}$ as follows;

$$\mathcal{L} = \frac{1}{2}\partial_\mu \phi \partial^\mu \phi - \frac{1}{2}m^2\phi^2 \quad (2.11.)$$

Substituting this into the Euler-Lagrange equation we get;

$$\frac{\partial}{\partial x_\mu}\left(\frac{\partial \phi}{\partial x_\mu}\right) - m^2\phi = 0 \quad (2.12.)$$

By using the covariant notation (Webber, 2006);

$$\partial_\mu \partial^\mu = \frac{1}{c^2}\frac{\partial^2}{\partial t^2} - \nabla^2 \quad (2.13.)$$

$$(\partial_\mu \partial^\mu + m^2)\phi = 0 \tag{2.14.}$$

We end up with the Klein-Gordon equation. Hence, this tells us that the evolution of a free and relativistic particle by governed by the Klein-Gordon equation.

In the relativistic quantum field theory, the Klein-Gordon equation successfully describes spin-0 particles but it admits positive-ϕ and negative-ϕ energy free field solutions when $m^2 > 0$. Since the negative energy solutions have negative probability densities of the particle, this result led Dirac to develop a new relativistic quantum equation. He succeeded by requiring an equation that can be thought of in terms of a "square root" of the Klein-Gordon equation.

$$(i\gamma^\mu \partial_\mu - m)\psi = 0 \tag{2.15.}$$

where the coefficients $\gamma^\mu = (\gamma^0, \gamma) = (\gamma^0, \gamma^1, \gamma^2, \gamma^3)$ have defined as 4×4 unitary matrices and ψ is a four-element column matrix (Johannesson, 2014).

$$\gamma^0 = \begin{pmatrix} I & 0 \\ 0 & -I \end{pmatrix}, \ \gamma^i = \begin{pmatrix} 0 & \sigma_i \\ -\sigma_i & 0 \end{pmatrix} \tag{2.16.}$$

where 0 denotes a 2×2 null matrix, $\boldsymbol{I}$ denotes a 2×2 identity matrix, and the $\sigma_{i=1,2,3}$ are the matrices of Pauli (Johannesson, 2014):

$$\sigma^0 = \begin{pmatrix} 1 & 0 \\ 0 & 1 \end{pmatrix},$$

$$\sigma_1 = \begin{pmatrix} 0 & 1 \\ 1 & 0 \end{pmatrix}, \quad \sigma_2 = \begin{pmatrix} 0 & -i \\ i & 0 \end{pmatrix}, \quad \sigma_3 = \begin{pmatrix} 1 & 0 \\ 0 & -1 \end{pmatrix} \tag{2.17.}$$

2.1.3. Quantum Electrodynamics

Quantum Electrodynamics (QED) is perhaps the simplest formulation of quantum field theory in the SM. One can start by defining the Lagrangian density for a field theory in which electrically charged Dirac particles and antiparticles, i.e. electrons and positrons;

$$\mathcal{L}_0 = \overline{\psi}(i\gamma^\mu \partial_\mu - m)\psi \tag{2.18.}$$

where $\overline{\psi} = \psi^\dagger \gamma^0$ (Hollik, 2010). We apply a so-called global *U(1)* gauge transformation to the Lagrangian ψ field (Pich, 2007):

$$\psi(x) \xrightarrow{U(1)} \psi'(x) \equiv \exp\{iQ\theta\}\, \psi(x) \tag{2.19.}$$

in which $Q\theta$ are an arbitrary constants. We should note that the case where θ depends on the space-time coordinate (say, under local phase redefinitions $\theta = \theta(x)$), the Lagrangian density, $\mathcal{L}_0$, is no longer invariant under the phase transformation. This invariance can be restored by inducing an extra term;

$$\partial_\mu \psi(x) \xrightarrow{U(1)} \exp\{iQ\theta\}\,(\partial_\mu + iQ\partial_\mu \theta)\, \psi(x) \tag{2.20.}$$

It means that the same phase convention should be taken at all-space time points in order to be consistent with the theory however, this looks unnatural.

The gauge symmetry requires that the local *U(1)* phase invariance be held locally. This can only be done if an additional term is applied to the Lagrangian in order to cancel the previous $\partial_\mu \theta$ term in Equation 2.20. To do this we introduced a vector field $A_\mu(x)$, called gauge field, transforming as;

$$A_\mu(x) \xrightarrow{U(1)} A'_\mu(x) \equiv A_\mu(x) - \frac{1}{e}\partial_\mu\theta(x) \qquad (2.21.)$$

and we introduced a new covariant derivative (Pich, 2007):

$$D_\mu\psi(x) \equiv \left(\partial_\mu + ieQ\mathrm{A}_\mu(x)\right)\psi(x) \qquad (2.22.)$$

These replacements lead to a new Lagrangian which is invariant under local *U(1)* transformation and describes the interactions between the fermions ($\psi(x)$) and the gauge field ($A_\mu(x)$) for the photons.

$$\begin{aligned}\mathcal{L} &= i\overline{\psi}(x)\gamma^\mu D_\mu\psi(x) - m\overline{\psi}(x)\psi(x)\\ &= \mathcal{L}_0 + e\overline{\psi}(x)\gamma^\mu D_\mu\psi(x)\mathrm{A}_\mu\\ &= \mathcal{L}_0 + \mathcal{L}_{int} \qquad (2.23.)\end{aligned}$$

in which $\mathcal{L}_0$ is the free field part and $\mathcal{L}_{int}$ describes the interaction part. Now, we need a kinetic term for this gauge field $A_\mu(x)$ as in a physical field. The gauge field $A_\mu(x)$ corresponds to four-potential and the Lagrangian is the free electromagnetic field for the photon;

$$\mathcal{L} = -\frac{1}{4}F_{\mu\nu}F^{\mu\nu} \qquad (2.24.)$$

where $F_{\mu\nu} = \partial_\mu A_\nu - \partial_\nu A_\mu$ is the electromagnetic field tensor (Pich, 2007).

Since a possible mass term $\left(\mathcal{L}_m = \frac{1}{2}m^2A^\mu A_\mu\right)$ is not invariant under gauge transformations, adding this term for the gauge field is forbidden; therefore, it is expected to be massless for the photon field. Experimentally, it is known that $m_\gamma < 6.10^{-17}$ eV (Yao et al., 2010).

The final QED Lagrangian is thus given by:

$$\mathcal{L}_{QED} = \left(i\overline{\psi}\gamma^{\mu}\partial_{\mu}\psi - m\overline{\psi}\psi\right) - \left(\tfrac{1}{4}F_{\mu\nu}F^{\mu\nu}\right) + \left(e\overline{\psi}\gamma^{\mu}\psi A_{\mu}\right) \quad (2.25.)$$

2.2. Quantum Chromodynamics

2.2.1 The Lagrangian of QCD

QCD is the theory that describes and explains the interaction between quarks and non-Abelian massless gauge bosons called gluons. The formalism of the QCD Lagrangian is the same structure as the QED Lagrangian but the local gauge theory is based on symmetry group SU(3)$_C$ which is a non-abelian group, where the subscript C stands for the color charge.

The free-particle Lagrangian density for the quarks take the form (Pich, 1995);

$$\mathcal{L}_0 = \sum_f \bar{q}_f\,(i\gamma^{\mu}\partial_{\mu} - m)q_f \quad (2.26.)$$

where $q_f \equiv$ column(q_f^1, q_f^2, q_f^3) is a three-component wave function that represents the quark field in color space. *"f"* describes the six different flavors (u, d, s, c, b, t) of quarks and γ^{μ} are Dirac gamma matrices and *m* stands for the mass of quark (Pich, 1995).

We assume the free Lagrangian is invariant under the local SU(3)$_C$ transformations to derive the interaction (Halzen and Martin, 1984):

$$q(x) \to Uq(x) = e^{i\alpha^a(x)T^a}q(x) \quad (2.27.)$$

where U is an arbitrary 3×3 unitary matrix and the $\alpha^a(x)$ are real-valued functions of the space-time coordinates x^{μ} = (*t, x, y, z*). The $T^a, a = 1 \dots 8$ are generators of SU(3) transformation and obey the commutation relation (Halzen and Martin, 1984);

$$[T^a, T^b] = if^{abc}T^c \tag{2.28.}$$

where $f^{abc} = \epsilon^{abc}$, $(a, b, c = 1,2, \ldots ,8)$ is so-called structure constant of the symmetry group SU(3) which are real and antisymmetric in [abc] with values of (Paganini, 2014);

$$\begin{aligned}
&f^{123} = 1, \\
&f^{147} = -f^{156} = f^{246} = f^{257} = f^{345} = -f^{367} = \tfrac{1}{2}, \\
&f^{458} = f^{678} = \tfrac{\sqrt{3}}{2}, \\
&f^{abc} = f^{bca} = f^{cab} = -f^{bac} = -f^{acb}, \\
&f^{aab} = f^{abb} = 0, \\
&f^{abc} = 0 . \quad \text{for other index permutations}
\end{aligned}$$

One can take the Gell-Mann matrices for a representation of the generators $T^a = \lambda_a/2, 1 \leq a \leq 8$ where λ_a is the Gell-Mann SU(3) matrices (Paganini, 2014);

$$\lambda_1 = \begin{pmatrix} 0 & 1 & 0 \\ 1 & 0 & 0 \\ 0 & 0 & 0 \end{pmatrix}, \quad \lambda_2 = \begin{pmatrix} 0 & -i & 0 \\ i & 0 & 0 \\ 0 & 0 & 0 \end{pmatrix}, \quad \lambda_3 = \begin{pmatrix} 1 & 0 & 0 \\ 0 & -1 & 0 \\ 0 & 0 & 0 \end{pmatrix},$$
$$\lambda_4 = \begin{pmatrix} 0 & 0 & 1 \\ 0 & 0 & 0 \\ 1 & 0 & 0 \end{pmatrix}, \quad \lambda_5 = \begin{pmatrix} 0 & 0 & -i \\ 0 & 0 & 0 \\ i & 0 & 0 \end{pmatrix}, \quad \lambda_6 = \begin{pmatrix} 0 & 0 & 0 \\ 0 & 0 & 1 \\ 0 & 1 & 0 \end{pmatrix},$$
$$\lambda_7 = \begin{pmatrix} 0 & 0 & 0 \\ 0 & 0 & -i \\ 0 & i & 0 \end{pmatrix}, \quad \lambda_8 = \frac{1}{\sqrt{3}}\begin{pmatrix} 1 & 0 & 0 \\ 0 & 1 & 0 \\ 0 & 0 & -2 \end{pmatrix}. \tag{2.29.}$$

In order to ensure the local gauge invariance on the Lagrangian (Equation 2.26.), one has to replace the partial derivative ∂_μ with the covariant derivative D_μ (Halzen and Martin, 1984);

$$\partial_\mu \rightarrow D_\mu = \partial_\mu + ig\frac{\lambda_a}{2}G_\mu^a \tag{2.30.}$$

where g is the strong coupling constant which determines the strength of the interaction. Here, we introduce eight-gauge fields G_μ^a which describes the massless gluons and the kinetic term of the gluons is given by the gluon field strength tensor (Li, 2009);

$$G_\mu^a \rightarrow G_\mu^a - \frac{1}{g}\partial_\mu \alpha^a - f^{abc}\alpha^b G_\mu^c \tag{2.31.}$$

Finally, the Lagrangian of QCD can be written down as follows (Pich, 1995);

$$\mathcal{L}_{QCD} = -\frac{1}{4}G_{\mu\nu}^a G_a^{\mu\nu} + \sum_f \overline{q}_f(i\gamma^\mu D_\mu - m_f)q_f \tag{2.32.}$$

The Lagrangian density includes the interaction of the quark currents with the gluon fields as well as the gluon self-interactions (three-gluon and four-gluon vertices as in Figure 2.3.) which are responsible for asymptotic freedom, color confinement, and chiral symmetry breaking.

Figure 2.3. Self-interactions of gluons (Ji, 2007).

2.2.2. The Running Coupling Constant

Considering a dimensionless physical observable R which depends on a single energy scale, Q, which is much bigger than mass can be an example in order to introduce the concept of a running coupling. Because of the assumption $Q \gg m$, we can set the $m \to 0$ (assuming that R has this limit) and naive scaling would suggest that R should have a constant value that is independent of Q. Nonetheless, this simple scale invariance is not true in the renormalizable quantum field theory. Calculating R as a perturbation series in the coupling (which in QCD is $\alpha_s = g^2/4\pi$) requires renormalization in order to remove ultraviolet divergences. This renormalization procedure introduces a second mass scale μ and in general, R depends on the ratio Q/μ which is not constant. The renormalized coupling α_s also depends on the second mass scale μ.

The choice of the renormalization scale, μ, is arbitrary. Since the Lagrangian density of QCD does not mention the scale μ, R cannot depend on the choice made for it. It can only depend on the ratio Q^2/μ^2 and the renormalized coupling α_s since R is dimensionless.

We can write down the μ dependence of R as follows (Ellis and Stirling, 1990):

$$\mu^2 \frac{d}{d\mu^2} R\left(\frac{Q^2}{\mu^2}, \alpha_s\right) \equiv \left[\mu^2 \frac{\partial}{\partial\mu^2} + \mu^2 \frac{\partial\alpha_s}{\partial\mu^2}\frac{\partial}{\partial\alpha_s}\right] R = 0 \tag{2.33.}$$

And Equation 2.33 is called the "renormalization group equation (RGE)". The resulting sum depends on the renormalization scale because only a few first terms of variables can be calculated. This shows the running coupling constant is well approximated by

$$\alpha_s\left(\mu^2, \Lambda_{QCD}\right) = \frac{12\pi}{(33-2n_f)\ln\left(\mu^2/\Lambda_{QCD}^2\right)}, \qquad \mu^2 \gg \Lambda_{QCD} \tag{2.34.}$$

where n_f denotes the number of quark flavors contributing in the $q\bar{q}$ loops with $m_q^2 < \mu^2$. Λ_{QCD}^2 is a scale parameter of QCD determined experimentally from the measurement of α_s and can be defined as (Barr et al., 2016);

$$\Lambda_{QCD}^2 = \mu^2 e^{-\frac{12\pi}{(33-2n_f)\alpha_S(\mu^2)}} \tag{2.35.}$$

The evolution of the coupling constant as a function of energy scale Q by using the results from different experiments is presented in Figure 2.4. Here, the range of energy scale is from 5 GeV up to 2 TeV and experimental points from different experiments are compared to theoretical predictions. There are two consequences according to the lowest and highest threshold of energy scale;

Asymptotic freedom: At large $\mu^2(\mu^2 \gg \Lambda_{QCD}^2)$, the coupling α_s tends to zero logarithmically, which means that quarks do not interact much and can be treated as free particles for short-distance interactions. In this regime, the cross sections can be calculated within the pQCD (Pich, 2000).

IR slavery: At small values of $\mu^2(\mu^2 \approx \Lambda_{QCD}^2)$, the coupling constant becomes too large, so-called Landau pole, quarks and gluons will arrange themselves into strongly bound clusters, namely, hadrons and perturbation theory are no longer valid. So, a non–pQCD has to be applied when $\mu^2 \approx \Lambda_{QCD}^2$ (Brodsky et al., 2016).

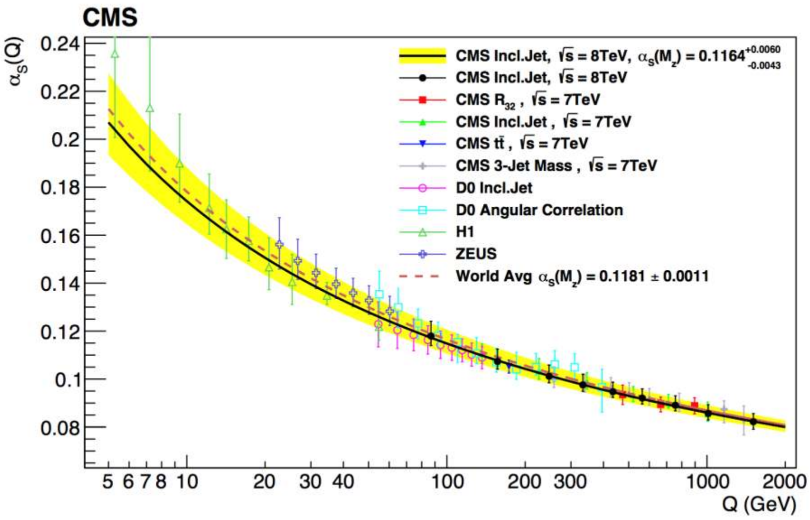

Figure 2.4. The coupling constant, α_s, as a function of energy scale Q is shown for different measurements obtained from the CMS (CMS Collaboration, 2013, 2014, 2015), D0 (D0 Collaboration, 2009, 2012), H1 (H1 Collaboration, 2017), and ZEUS (ZEUS Collaboration, 2012) experiments. The black dots represent the inclusive jet cross section measurement at $\sqrt{s}$ = 8 TeV. There is a good agreement between data points and the theoretical prediction which is the CT10 NLO PDF set as can be seen as a solid line in the figure (CMS Collaboration, 2017).

2.2.3. The Quark Parton Model

The model of the partons formalized by Bjorken and Paschos (1969) and formulated by Feynman (1972), considers the nucleon as a set of point-like centers of charge with spin ½, called "partons". These centers were later identified with the quarks invented by Gell-Mann (Gell-Mann, 1964) and Zweig (Zweig, 1964). The "parton" is a collective name for quarks and gluons (and antiquarks) in QCD.

The quark-parton model has been developed to allow the calculation of the cross section of the lepton-hadron scattering process in which the partons are considered as free and independent of each other. To describe the process, it is necessary in this case to distribute the total momentum of the nucleon between its constituents. If we represent the associated four vectors as $k^\mu = (k^\pm, \boldsymbol{k}_T)$ and k'^μ for the incoming and outgoing leptons, respectively, and then the momentum of the target hadron can be represented by $p^{\mu} = (p^{+}, m^2/(2p^{+}), \mathbf{0}_T)$ where $k^{\pm} = (k^0 \pm k^z)/\sqrt{2}$. The four-momentum transfer is given by $q^{\mu} = k^{\mu} - k'^{\mu}$, then the kinematic of the process are defined by various Lorentz invariants:

$$Q^2 = -q^2\,, \qquad p^2 = M^2, s = (p+k)^2$$
$$x = \frac{Q^2}{2p\cdot q} = \frac{Q^2}{2M(E-E\prime)}, \quad y = \frac{q\cdot p}{k\cdot p} = 1 - E'/E \tag{2.36.}$$

where s represents the center-of-mass (CM) energy squared, Q^2 is the negative of the invariant mass squared of the virtual exchanged boson, x is the Bjorken variable which is the fraction of the momentum of the incoming nucleon taken by the struck quark, and y gives a measure of the amount of energy transferred between the lepton and the hadron systems and also it is related to the scattering angle in the lepton-quark CM frame (Devenish and Cooper-Sarkar, 2003). When the electron or muon participate in the process as a lepton, then a virtual photon exchange occurs in the scattering as shown in Figure 2.5 (Ellis and Stirling, 1990).

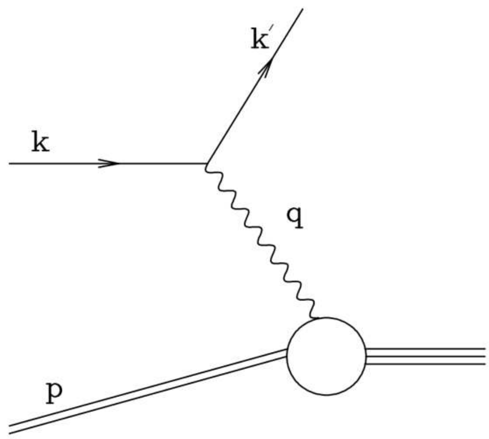

Figure 2.5. Deep inelastic charged lepton-proton scattering (Webber, 2008).

The application of this model to hadronic processes, such as deep inelastic scattering and Drell-Yan scattering, reveals a dimensionless quantity F called the "structure function" that parametrizes the hadron structure in the collision and can be measured in experiments. The structure function $F_i(x, Q^2)$ parametrizes the structure of the target as "seen" by the virtual exchanged boson. Experimentally it is observed that the structure functions depend only on the dimensionless variable *x* over a wide range:

$$F_i(x, Q^2) \rightarrow F_i(x) \tag{2.37.}$$

This was predicted by James Bjorken in 1968 (Bjorken, 1969) and is known as Bjorken scaling which defined as Q^2, $p \cdot q \rightarrow \infty$ with fixed scaling variable x. This approach was confirmed at Stanford Linear Accelerator Center (SLAC) (Breidenbach et al., 1969). The structure function $F_1(x) = 1/2 \sum_i q_i^2 \, f_i(x)$ measures the parton density as a function of the energy fraction *x* carried by the parton, whereas the structure function $F_2(x) = \sum_i q_i^2 \, x f_i(x) = 2xF_1(x)$ describes the momentum density, and each being weighted by the parton charge q_i. The function $xf_i(x)$ are called parton distribution functions (PDFs) and describes the probability of finding a parton of type *i* carrying a fraction *x* of the momentum of a proton. The equation $F_2(x) = 2xF_1(x)$ is known as the Callan-Gross relation (Callan et al., 1969), which is a direct consequence of assuming that the partons are made of point-like constituents and it was experimentally observed in the SLAC experiments, showing that the partons were, in principle, quarks. This relation was also observed at CERN by the Gargamelle detector (Eichten et al., 1973) and they provided evidence that quarks constituents carry about 50% of the proton's momentum. Then something else must be in the proton to carry the rest of the proton's momentum, it is attributed to gluon constituents.

2.2.3.1. Hadronization

The partons that produced during a QCD process are only "free" at very short distances and only colorless combinations are detected. In a collision experiment, the transition from a parton to a final state consisting of observed hadrons is called hadronization. The process of hadronization is shown in Figure 2.6, a hadron is generated in several stages: PDFs, the hard process, the development of the partonic shower, hadronization, and underlying event. These stages will be discussed in more detail in Section 4.1.1.

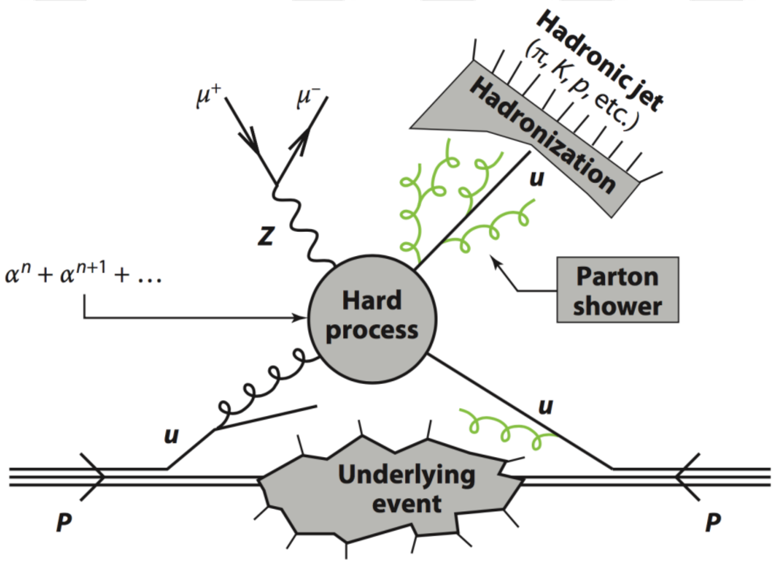

Figure 2.6. A p-p collision schematically showing the underlying event, hard process, parton shower, and hadronization (Butterworth et al., 2012).

The hadronization processes take place in a region where α_s is too strong and cannot be calculated in pQCD. A strong interaction on a typical Q scale occurs on the distance scale with the order of $1/Q$ with the uncertainty principle. Meanwhile, the subsequent hadronization process occurs on a much later time scale, characterized by $1/\Lambda$ (Λ is the typical hadronic scale where strong coupling strengthens).

It is then necessary either to resort to non-perturbative models or to rely on data measured in many experiments and, according to the factorization theorem, to assume the universality of the fragmentation functions. The detailed descriptions of the hadronization processes are provided by models. One general approach to hadronization is the local parton-hadron duality which supposes that the flows of energy-momentum and flavor quantum numbers at the hadronic level should follow the flow at the partonic level. This approach does not try to describe the mechanism of hadronization and we must resort to models. Two of the main models, *cluster* and *string* hadronization (Figure 2.7) (Webber, 1994, 1999), are described in the following:

1. Cluster model (Marchesini and Webber, 1984, 1988; Webber, 1984; Marchesini et al., 1992, 1996): This model developed by Webber, is based on the idea to force "by hand" all virtual gluons to split into $q\bar{q}$ pairs, $g \rightarrow q\bar{q}$, at the end of the parton shower and also based on preconfinement. A new set of low-mass color-singlet clusters is obtained after the splittings, formed only by quark-antiquark pairs. These color-singlet $q\bar{q}$ combinations have a smaller mass than that of the virtual gluon due to preconfinement property of parton shower. This model has few parameters and a natural mechanism to produce transverse moments and to suppress heavy particle production in hadronization. Nevertheless, it has problems dealing with the decay of very massive clusters and also suppressing the production of baryon and heavy quarks.

2. String model: The Lund group of Andersson, Gustafson, and Sjöstrand (Andersson et al., 1980, 1982) had developed this model and it is known also as the "Lund" model. This model is based on the idea of combining fragmentation with the concept of the color string, which is stretched from the quark via the gluon to antiquark. The aim of this color string is to break first to produce a hadron which carries a significant fraction of the gluon energy. The rest of the gluon energy is then distributed between the two parts of the broken string, which are fragmented independently in their respective center-of-mass systems. The Lund model today is the most commonly used model for simulating the properties of fragmentation processes.

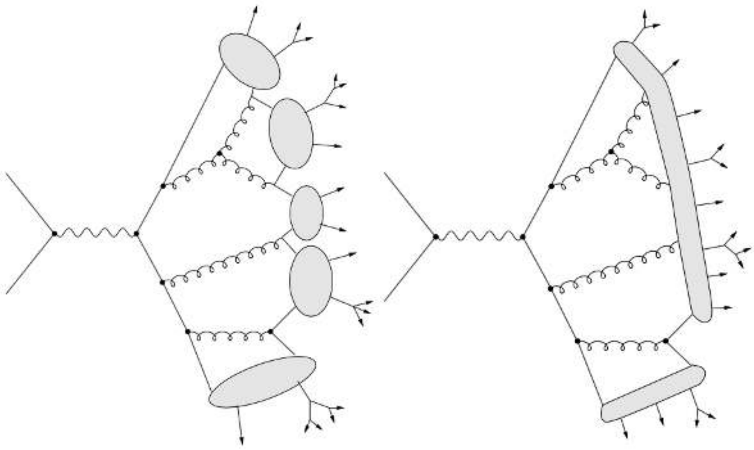

Figure 2.7. Sketch of cluster (left) and string (right) process hadronization (Webber, 1999).

2.2.4. Cross Sections and Parton Distribution Functions

In collision experiments, the most basic measurement consists of counting and categorizing the produced entities of interest, e.g. specific types of particles or jets according to their kinematic quantities. The counts, of course, depend on the efficiency of the respective particle collider, expressed in terms of its luminosity. Measured reaction rates $\dot{N}$ are then related through the underlying physical reaction, which is defined by its cross section, σ, that is independent of experimental conditions such as the collider performance.

$$\dot{N} = \mathcal{L} \cdot \sigma \tag{2.38.}$$

Equation 2.38 can be written in term of the integrated luminosity $\mathcal{L}_{int}$ over a period of data taking:

$$N = \sigma \int \mathcal{L}\, dt = \sigma \mathcal{L}_{int} \tag{2.39.}$$

It is now possible to compare the measured cross section with predictions of any adopted theory, such as the SM of particle physics, and a nice summary of the cross section SM particles produced in association with jets by the CMS collaboration is shown in Figure 2.8, where each marker presents a different analysis. There is a good agreement between the measurements and the respective theoretical expectations.

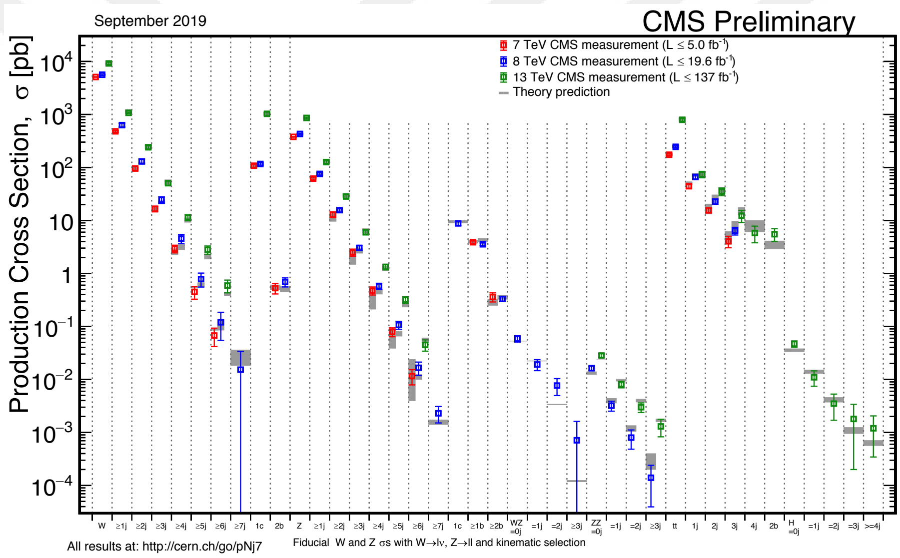

Figure 2.8. Summary of SM production cross sections for a variety of W, Z, and Higgs bosons production process with and without jets at $\sqrt{s}$ = 7 (red markers), 8 (blue markers), and 13 (green markers) TeV. The SM production cross sections are compared to their theoretical expectations (gray lines). The range of production cross sections varies from 10^{-5} mb to 0.1 fb, thus there is an excellent agreement over 8 orders of magnitude (CMS Public Combined Physics Results, 2019).

The differential form can be used to make a clear kinematic dependency, e.g. on a p_T;

$$\frac{d\sigma}{dp_T} = \frac{1}{\varepsilon \cdot \mathcal{L}_{int}} \cdot \frac{N}{\Delta p_T} \tag{2.40.}$$

where Δp_T is the measurement interval in p_T and the factor ε represents experimental efficiencies.

When selected entities are counted in the same event irregardless of everything else that is produced within the same event then the cross section is inclusive. On the other hand, exclusive cross sections set limits on the presence of further jets in an event, so-called jet vetoes, for example. As a result, the exclusive cross sections are precision to all energy depositions or particles in an event and are more difficult to handle experimentally and theoretically.

We can write down the double-differential inclusive cross section as a function of the jet p_T and, if feasible, of the jet rapidity y.

$$\frac{d^2\sigma}{dp_T dy} = \frac{1}{\varepsilon \cdot \mathcal{L}_{int}} \cdot \frac{N_{jets}}{\Delta p_T \Delta y} \tag{2.41.}$$

where N_{jets} is the number of jets counted within a bin and corrected for detector defects, ε is the experimental efficiency, Δp_T and Δy are the bin widths in jet transverse momentum and rapidity (Rabbertz, 2017).

The measurement of the production cross section at hadron colliders is based on an understanding of the distribution of the momentum fraction x of the partons within the proton in the corresponding kinematic range for both signal and background processes. (Campbell et al., 2006). The PDFs encode this knowledge in the collinear QCD factorization system. PDFs cannot be calculated perturbatively and have to be determined using data from various hard scattering cross sections obtained experimentally in various hadron collisions. (Gao et al., 2018).

PDFs are often presented as functions of x and μ_F and are generally defined as the probability densities to find a parton within a hadron, with its momentum fraction between x and $x+dx$. The evolution of PDFs according to the factorization scale (μ_F) can be calculated by the set of coupled integrodifferential evolution equations (Gribov and Lipatov, 1972; Altarelli and Parisi, 1977).

The evolution of PDF along with x is however not analytically calculable. Their determination is based on global fits to data from deep inelastic scattering (DIS), Drell-Yan (DY), and jet production at precision measurements in hadron colliders. Many PDF sets are available, which differ by the adjustment method used, the number of parameters involved, and the data sets considered. The most common are CTEQ (Lai et al., 2010), MSTW (Martin et al., 2009), HERA (Aaron et al., 2010), or even NNPDF (Ball et al., 2012). The LHC's energy range provides access to new areas in PDFs: at high energy and small x, as shown in Figure 2.9.

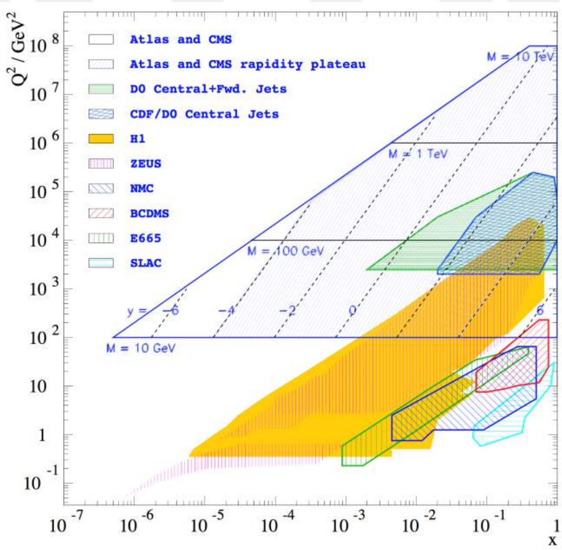

Figure 2.9. Representation of the parton kinematics of different experiments in (x, Q^2) phase space. The LHC covers the high energy and small-x region which is unexplored by previous experiments (Glazov and H1 Collaboration, 2007).

2.2.5. Perturbative QCD and Factorization Theorem

From the QCD point of view, the asymptotic freedom regime makes it possible to apply a perturbative method, since the coupling constant is low, which is no longer the case in the confinement regime. The goal of pQCD is to quantitatively describe the structure of multi-partonic systems formed by QCD cascades in order to gain some actual knowledge about confinement by comparing the computable characteristics of quark-gluon ensembles with measurable characteristics in hard processes of the final hadronic state (Dokshitzer et al., 1991). The confinement of quarks implies non-perturbative effects of the strong interaction which must be considered for the calculation of a cross section.

The cross section of the interaction process between hadrons h_1 and h_2 can be written as an incoherent sum of partonic processes (Dissertori et al., 2003):

$$d\sigma(h_1 h_2 \to CD) = \int dx_1 dx_2 \sum_{a,b} f_{a/h_1}(x_1) f_{b/h_2}(x_2) d\sigma^{ab\to cd}(x_1, x_2)\, D_{c\to C}(z_1) D_{d\to D}(z_2) \quad (2.42.)$$

where $f(x_i)$ represents PDF and $\sigma(x_1, x_2)$ is the cross section of the partonic process that contains the effects at short-distance. The summation is made on the set of possible partonic processes where the indices a and $b \in \{q, \bar{q}, g\}$. A combination of the partonic process at short- and long- distance allows us to calculate the overall cross section. (Collins et al., 2004). The short-distance process can be calculated in perturbation theory, but the long-distance process is not calculable within this model. The factorization theorem (Drell and Yan, 1971) is one solution to this problem and allows us to express predictions for these cross sections, by factorizing the calculable short-distance scattering of quarks and gluons from the long-distance with hadronic binding. For example, the factorization theorem makes it possible to decompose the calculation of the cross section $\sigma_{h_1 h_2 \to CD}$ into a convolution product. In order to use the factorization theorem, it is necessary to introduce a factorization scale μ_F for the cross section of the hadronic process,

$$\sigma_{h_1 h_2 \to CD} = PDFs \otimes \sigma_{partonic} \otimes FFs \tag{2.43.}$$
$$\sigma_{h_1 h_2 \to CD} = \left[f_{h_1}(x_1, Q^2) \otimes f_{h_2}(x_2, Q^2)\right] \otimes \sigma(x_1, x_2, Q^2) \otimes D(z, Q^2)$$
$$\sigma(h_1 h_2 \to CD) =$$
$$\int \sum_{a,b} dx_1 dx_2 f_{a/h_1}(x_1, \mu_F^2) f_{b/h_2}(x_2, \mu_F^2) d\sigma^{(ab \to cd)}(Q^2, \mu_F^2) D_{c \to C}(z_1) D_{d \to D}(z_2)$$

The first term, $f_{i/h_j}(x_j, \mu_F^2)$, corresponds to PDFs, which depend on the structure functions $F_i(x)$, represent long-distance effects and cannot be completely determined by perturbative processing. The second term represents the partonic section and includes only perturbative physics. Finally, the last term, $D_{i \to I}(z)$, corresponds to the fragmentation functions, they give the probability that hadron results from the fragmentation of partons by taking away the momentum fraction z. The ingredients of this process are illustrated in Figure 2.10. The decomposition allowed by the factorization theorem implies the choice of a factorization scale μ_F, which separates the perturbative regime (partonic section) from the non-perturbative regime (PDFs), but also the choice of a fragmentation scale μ_F which fixes the separation between hard and fragmentation processes.

The final hadronic cross section should not depend on this scale but the fact that the perturbative calculations are only carried out to a certain order in perturbation introduces a dependence of this cross section on the scale of factorization. The terms of calculation which involve terms $\ln(Q^2/\mu_F^2)$ do not become too large so that the perturbative approach remains valid, the factorization scale must remain the order of the scale Q. For this reason, the choice of scales is often: $\mu_{F=}\mu_{=}Q$ (Dissertori et al., 2003).

In pQCD, the PDFs, $f_{i/h_j}(x_j, Q^2)$, cannot be calculated and must be determined experimentally. Nevertheless, knowing the PDF at a certain value Q_0^2

within the region of applicability pQCD allows us to determine the $f_{i/h_j}(x_j, Q^2)$ (Donnelly et al., 2017). It can be done by using so-called evolution equations as will be discussed in the next Section 2.3.

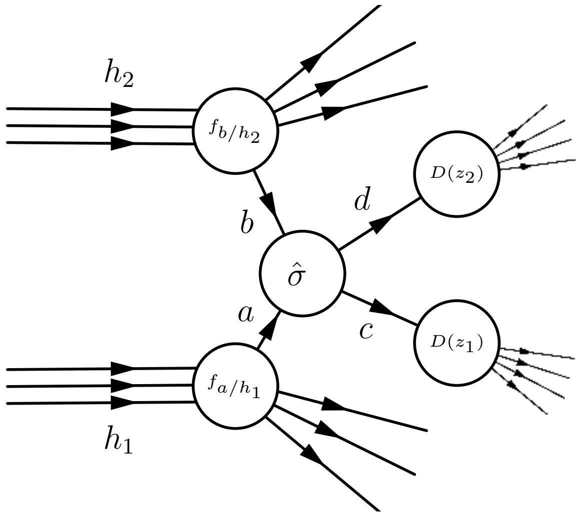

Figure 2.10. A schematic illustration for the hard collision of two hadrons h_1 and h_2 with the production of final state partons c and d. Here, f_{i/h_j} is the parton distribution functions, $\hat{\sigma}^{(ab\to cd)}$ is the cross section of the hard partonic process, and $D(z_j)$ presents the fragmentation functions. Reproduced from Reference (Dissertori et al., 2003).

2.3. QCD Evolution Equations

As a result of the theorem of factorization, once perturbative parton distributions are determined at a scale μ, they can be predicted at any scale μ' by using QCD evolution equations for a given order. The scale dependence of the PDFs is a consequence of effects of gluon emission and gluon splitting that are incorporated into three different evolutions schemes, called DGLAP (Dokshitzer-Gribov-Lipatov-Altarelli-Parisi) (Kuraev et al., 1976, 1977; Balitsky and Lipatov, 1978; H1 Collaboration, 2000), BFKL (Balitski-Fadin-Kuraev-Lipatov) (H1 Collaboration, 1997, 2000a; ZEUS Collaboration, 2002) and CCFM (Catani-

Ciafaloni-Fiorani-Marchesini) (H1 Collaboration, 1995, 1996, 2000b, 2002; ZEUS Collaboration, 2000).

Figure 2.11 shows the proton and its evolution with the scale of the process. The left part of the illustration shows a proton as seen by an exchanged boson with virtuality Q_0. By considering the virtual boson as a probe of the proton, the exchanged boson's virtuality has a spatial resolution scale $\sim 1/Q_0$. On the right, the proton is probed by an exchanged boson with higher virtuality $Q > Q_0$. This illustration is a physical picture of the DGLAP evolution equation that will be discussed in the next section.

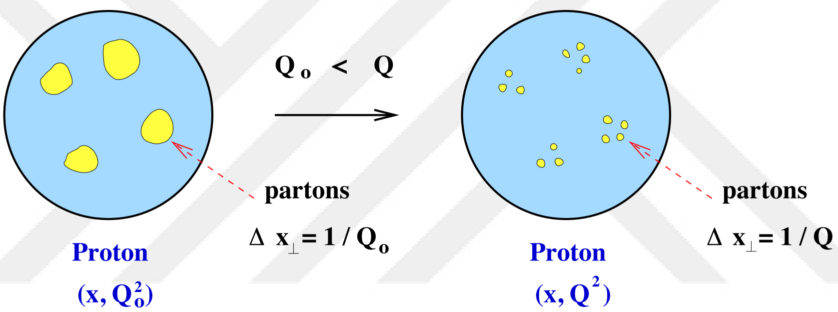

Figure 2.11. Illustration of the DGLAP evolution equations. Virtual boson with virtuality Q^2 is large than Q_0^2, it can resolve more partons inside the proton (Kovchegov and Levin, 2012).

2.3.1. The DGLAP Equations

The DGLAP evolution scheme uses the leading $log(Q^2)$ approximation (LLA) to resum terms (x, Q^2) in the perturbative expansion in $\alpha_s^m \ln Q^2$. The pQCD does not predict the complete dependence in x and Q^2 of structure function F_2, but, the DGLAP kinematics predicts the densities of partons as a function of Q^2 when Q^2 is large enough, usually larger than 1 GeV^2. These predictions can be formulated as integrodifferential equations (Lipatov, 1974; Dokshitzer, 1977);

$$\frac{df_i(x,Q^2)}{d\ln Q^2} = \frac{\alpha_s(Q^2)}{2\pi} \sum_j \int_x^1 \frac{dz}{z} P_{ij}(z,\alpha_s) f_j\left(\frac{x}{z}, Q^2\right) \qquad (2.44.)$$

where P_{ij} is the splitting function which depends on two terms; the splitting variable z and the running coupling $\alpha_s(\mu^2)$. They can be calculated as a power series in α_s (say $z = x'/x$) (Botje, 2013):

$$P_{ij}(z, \alpha_s) = P_{ij}^{LO}(z) + \frac{\alpha_s}{2\pi} P_{ij}^{NLO}(z) + \left(\frac{\alpha_s}{2\pi}\right)^2 P_{ij}^{NNLO}(z) + \cdots \tag{2.45.}$$

The splitting functions can be interpreted as the emission probability densities of a parton i by a parton j carrying an energy fraction z from a parent parton. They are quark flavor-independent since the strong interaction is flavor independent and are the same for quarks and antiquarks at any order in α_s (Botje, 2013):

$$P_{q_i q_j} = P_{\bar{q}_i \bar{q}_j}, \tag{2.46.}$$

$$P_{q_i \bar{q}_j} = P_{\bar{q}_i q_j}, \tag{2.47.}$$

$$P_{q_i g} = P_{\bar{q}_i g} \equiv P_{qg}, \tag{2.48.}$$

$$P_{g q_i} = P_{g \bar{q}_i} \equiv P_{gq}. \tag{2.49.}$$

Graphically the splitting functions are summarized in Figure 2.12. The leading-order splitting functions are (Botje, 2013)

$$P_{qq} = \frac{4}{3}\left[\frac{1+z^2}{(1-z)}\right]_+ = \frac{4}{3}\left[\frac{1+z^2}{(1-z)_+}\right] + 2\delta(1-z), \tag{2.50.}$$

$$P_{qg} = \frac{1}{2}\left[z^2 + (1-z)^2\right], \tag{2.51.}$$

$$P_{gq} = \frac{4}{3}\left[\frac{1+(1-z)^2}{z}\right], \tag{2.52.}$$

$$P_{gg} = 6\left[\frac{1-z}{z} + z(1-z) + \frac{z}{(1-z)_+}\right] + \left[\frac{11}{2} - \frac{n_f}{3}\right]\delta(1-z). \tag{2.53.}$$

where n_f is the number of (active) quark flavors and the "+ prescription" was used for regularization which defined by the property (Devenish and Cooper-Sarkar, 2003)

$$\int_0^1 dz \frac{f(z)}{(1-z)_+} = \int_0^1 dz \frac{f(z)-f(1)}{1-z} \tag{2.54.}$$

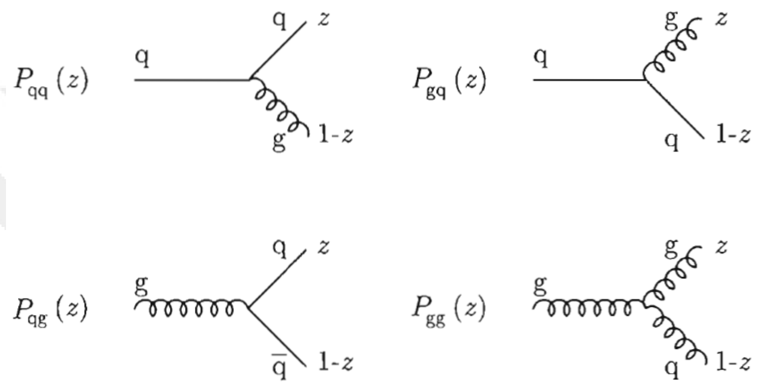

Figure 2.12. q-q, g-q, q-g, and g-g splitting functions (Devenish and Cooper-Sarkar, 2003).

2.3.2. The BFKL Equations

We have seen that the DGLAP equations are deduced from the formal summation of all the terms in $\alpha_s^m \ln Q^2$; consequently, these equations neglect terms of the $\alpha_s^m \ln^m(1/x)$ type, yet, these terms become dominant at low x. Therefore, another approach is necessary for the region of low x; in this new approach, we summarize all the dominant terms in $\alpha_s^m \ln^m(1/x)$ with $\alpha_s \ln(1/x) \simeq 1, \alpha_s << 1$ and this leads to the BFKL framework. It predicts the evolution of the gluon density as a function of x once the latter has been specified at $x = x_0$. The domain of validity of this equation is $\alpha_s \ln(1/x) \simeq 1, \alpha_s \ll 1$.

The evolution equation for gluon can be written in the form (Gay Ducati, 2014):

$$\frac{\partial\phi(x,k_\perp^2)}{\partial\ln(1/x)} = \frac{3\alpha_s}{\pi}k_\perp^2\int_0^\infty\frac{dk_\perp'^2}{k_\perp'^2}\left\{\frac{\phi(x,k_\perp'^2)-\phi(x,k_\perp^2)}{|k_\perp'^2-k_\perp^2|}+\frac{\phi(x,k_\perp^2)}{\sqrt{4k_\perp'^4+k_\perp^4}}\right\} \tag{2.55.}$$

where $\phi(x,k_\perp^2)$ is the distribution of a non-integrated function of gluons carrying the fraction of longitudinal momentum x and transverse momentum $k_\perp^2$; moreover, ϕ is linked to the usual function of gluons $xg(x,Q^2)$ by the formula (Kwieciński, 1994):

$$xg(x,Q^2) = \int_0^{Q^2}\frac{dk_\perp^2}{k_\perp^2}\phi(x,k_\perp^2) \tag{2.56.}$$

This provides that the number of partons in a hadron at a given value of $k_\perp$ and x can be counted by the non-integrated gluon function, $\phi(x,k_\perp^2)$ (Kovchegov and Levin, 2012). An illustration of the BFKL evolution equation in the transverse plane is shown in Figure 2.13.

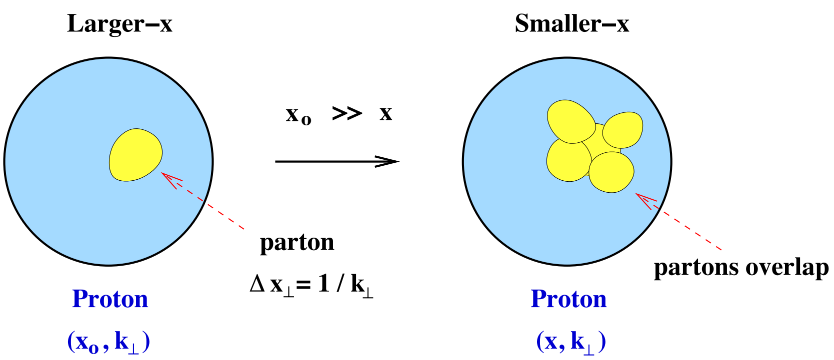

Figure 2.13. Illustration of the BFKL evolution equations. The gluons are represented with the blobs. More gluons (partons) are generated in the hadron wave function when $x \ll x_0$ and it may start to overlap with each other (Kovchegov and Levin, 2012).

2.3.3. The CCFM Equations

The CCFM equation combines the DGLAP ($\alpha_s \ln Q^2$) and BFKL ($\alpha_s \ln(1/x)$) approaches and therefore it is valid in large values of x and Q^2 (Ryan, 2005). The coherence effects of gluon emission in the CCFM evolution equation are taken into account by angular order (Jung, 1999);

$$\theta_j > \theta_{j-1} > \cdots > \theta_0 \tag{2.57.}$$

gives the condition that $q_i > z_{i-1}q_{i-1}$ with $z_i = x_i/x_{i-1}$. Here, θ_j is the angle of emitted gluons with respect to incoming gluons, q_i is the emitted gluon, k_i is the transverse momentum of gluons between emissions, and x_i terms represent the usual fractions of the initial longitudinal momentum as in Figure 2.14. The CCFM equation for the unintegrated gluon density has the following form (Jung and Salam, 2001);

$$F(x,k_t,\bar{q}) = F_0(x,k_t,\bar{q}) + \int \frac{dz}{z} \int \frac{d^2q}{\pi q^2} \Theta(\bar{q} - zq)\Delta_s(\bar{q},zq)\tilde{P}(z,q,k_t)F(\frac{x}{z},k_t',q) \tag{2.58.}$$

where $k_t' = |\vec{k}_t + (1-z)\vec{q}|$, $\bar{q}$ is the maximum angle for the gluon emission and the $\Theta(\bar{q} - zq)$ functions donate the angular ordering constraint on the emitted gluon. $\tilde{P}(z,q,k_t)$ is the gluon splitting function which is given by

$$\tilde{P}_g^i = \frac{\bar{\alpha}_s(q_i^2(1-z_i)^2)}{1-z_i} + \frac{\bar{\alpha}_s(k_{ti}^2)}{z_i}\Delta_{ns}(z_i, q_i^2, k_{ti}^2) \tag{2.59.}$$

with $\bar{\alpha}_s = \frac{3\alpha_s}{\pi}$ Δ_{ns} respresents the non-Sudakov form factor is defined as (Jung and Salam, 2001):

$$\log \Delta_{ns} = -\bar{\alpha}_s(k_{ti}^2) \int_0^1 \frac{dz'}{z'} \int \frac{dq^2}{q^2} \Theta(k_{ti} - q)\Theta(q - z' q_{ti}) \quad (2.60.)$$

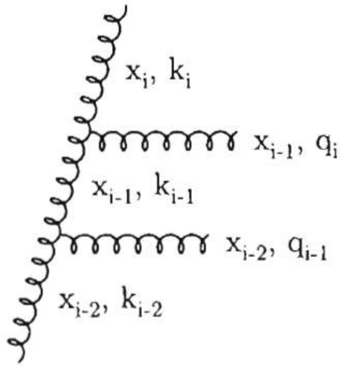

Figure 2.14. A section of the CCFM gluon ladder (Devenish and Cooper-Sarkar, 2003).

3. The LHC and The CMS EXPERIMENT

In this chapter, the CMS experimental apparatus is described in detail after a brief description of the Large Hadron Collider (LHC), by focusing on its different subdetectors and their performance.

3.1. The Large Hadron Collider

The LHC (LHC Study Group, 1995) is a particle accelerator built at CERN in Swiss-French border in order to obtain collisions between high-energy particle beams. LHC is formed by a sequence of superconducting magnets, dipoles, and quadrupoles, placed inside a tunnel of circumference equal to 27 km. It was designed to collide proton beams at the center-of-mass energy of $\sqrt{s}$ = 14 TeV, with a luminosity of $\mathcal{L} = 10^{34}$ cm^{-2}s^{-1} and to collide heavy-ions with an energy of $\sqrt{s}$ = 5.5 TeV per pair of nucleons.

The set of CERN accelerators is shown in Figure 3.1. LINAC 2 is the first link in the CERN accelerator chain and protons created by ionization of dihydrogen are first accelerated by LINAC 2 up to 50 MeV. Then, they are injected into the booster in which their energy is mounted at 1.4 GeV, before being transferred to the Proton Synchrotron or PS, which takes them to 25 GeV and sculpts the packet trains. Finally, the Super Proton Synchrotron or SPS accelerates them up to 450 GeV. Their injection into the LHC takes place via two transfer lines, which make it possible to obtain two beams circulating in opposite directions. The beams circulate, one in the clockwise direction (Beam 1) and the other in the anti-clockwise direction (Beam 2), in two distinct rings and can collide in four interaction points. At the points of interaction, four detectors are positioned: ALICE (A Large Ion Collider Experiment) (ALICE Collaboration, 2008), ATLAS (ATLAS Collaboration, 2008), CMS (CMS Collaboration, 2008), and LHCb (Large Hadron Collider Beauty) (LHCb Collaboration, 2008). ALICE is mainly dedicated to the study of the deconfinement of nuclear matter, quark-gluon plasma in heavy-ion collisions (Pb-Pb or p-Pb). ATLAS and CMS are two general-purpose detectors dedicated to the search for the Higgs boson, new physics, and the precision measurements of SM. LHCb is mainly dedicated to the measurements of CP (charge and parity) violation by studying rare decays of hadrons containing bottom (b, also known as the beauty quark) and charm (c) quarks.

The LHC is also used for research programs using heavy-ion collisions. The beginning of the acceleration chain is then distinct from the protons: before being injected into the PS, the ions are accelerated by the LINAC3, accumulated in the LEIR (Low Energy Ring Ion), and prepared the bunch structure for PS.

From the beginning of the LHC activity to today, two phases, called Run 1 and Run 2, have followed. Run 1 started in 2009 and ended in 2012. In this phase, the energy at the center-of-mass of p-p collisions has been increased to reach the value of 8 TeV in 2012. After Run 1 period, there was a shut-down period in the years of 2013 and 2014 in which an upgrade is carried out to allow the achievement of the instantaneous luminosity expected by the original design of the LHC. Run 2 phase begun in 2015 and ended in 2018, and the energy of the p-p collisions was reached $\sqrt{s}$ = 13 TeV.

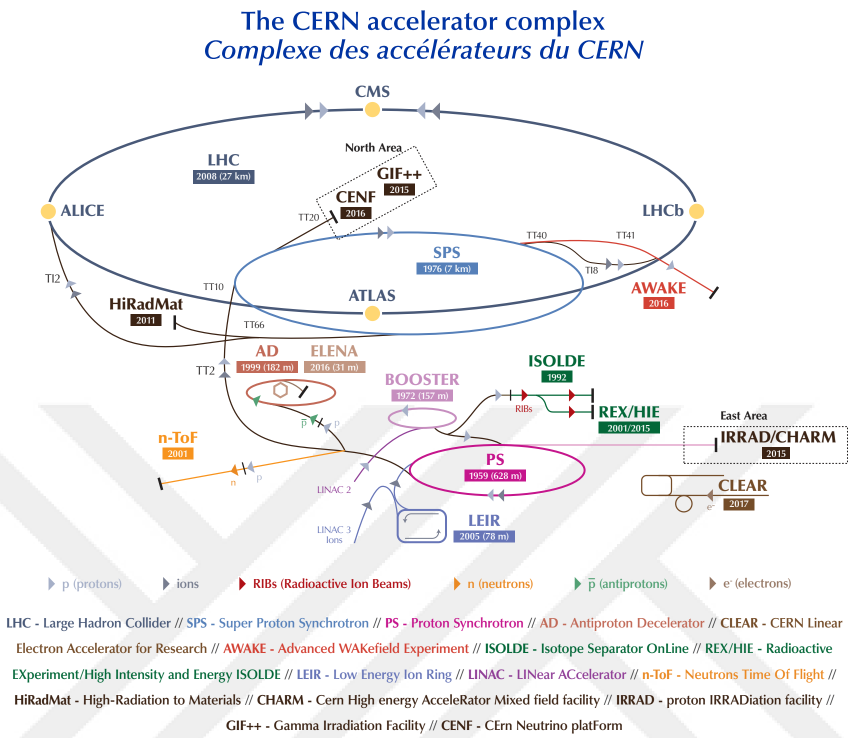

Figure 3.1. Diagram of the CERN Accelerator Complex. The proton and ion paths for the LHC are shown in light gray and dark, respectively (Mobs, 2018).

3.1.1. Instantaneous and Integrated Luminosity

From an experimental point of view, the performance of the collider is measured by the instantaneous luminosity, $\mathcal{L}$, that it is capable of delivering it. As discussed in Section 2.2.4, instantaneous luminosity is the coefficient of proportionality which makes it possible to link the event rate of a process to the cross section σ:

$$\frac{dN}{dt} = \mathcal{L} \cdot \sigma \tag{3.1.}$$

where N is the total number of events. In contrast, from the point of view of the machine, the luminosity is computable according to the parameters of the beams, by:

$$\mathcal{L} = \frac{N_p^2 N_b f \gamma}{4\pi\epsilon\beta^*} R \tag{3.2.}$$

where R is a geometrical factor accounting for the beam crossing angle and given by

$$\frac{1}{R} = \sqrt{1 + \left(\frac{\theta\sigma_z}{2\sigma^*}\right)^2} \tag{3.3.}$$

LHC design beam parameters in Equations 3.2–3.3 are defined and summarized in Table 3.1 (AC Team, 1999; Brüning et al., 2004; Baird, 2007). These parameters yield a peak instantaneous luminosity of $\mathcal{L} = 10^{34}$ cm^{-2}s^{-1}.

In order to characterize a quantity of data collected during a certain period, the integrated luminosity $\mathcal{L}_{int}$ is used. The integrated luminosity is defined as the luminosity accumulated for a given time interval ($\mathcal{L}_{int} = \int \mathcal{L}\, dt$). The total number of events expected for a phenomenon with cross section σ is then given by the integrated luminosity times the cross section, as can be seen from Equation 2.39.

A detector like CMS cannot record all the collisions taking place. There are indeed dead time periods of one or more subdetectors or their electronics. This is why the integrated luminosity recorded by a detector is lower than the integrated luminosity delivered by the accelerator (Figure 3.2 (a)). Figure 3.2 (b) shows the total integrated luminosity provided by the LHC in the CMS detector for the various data taken between 2010 and 2018, as well as the built-in luminosity recorded and operated by CMS throughout Run 2. This thesis presents an analysis using data taken by the CMS experiment in 2015.

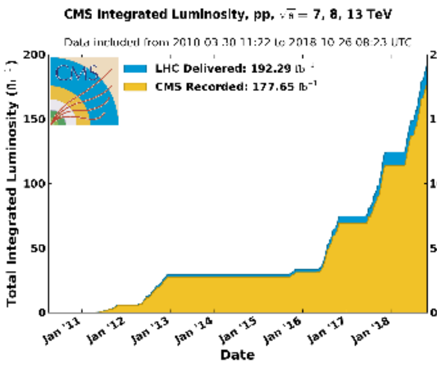

(a)

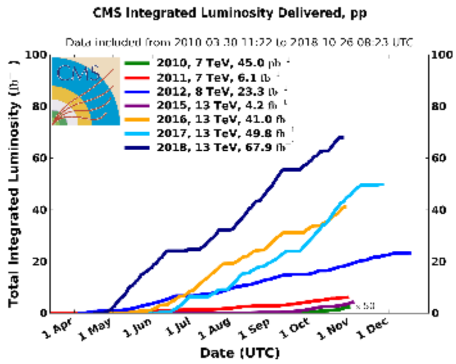

(b)

Figure 3.2. (a) Cumulative delivered and recorded luminosity overall years during stable beams for p-p collisions at nominal center-of-mass energy. (b) Total p-p integrated luminosity recorded by CMS during Run 1 and Run 2 by year and month (CMS Luminosity Public TWiki Page, 2019).

Table 3.1. LHC nominal design beam parameters (Brüning et al., 2004).

Symbol	Name	Value
N_p	protons per bunch	$1.15\text{x}10^{11}$
N_b	bunches per beam	2808
f	revolution frequency (1/24.95 ns/3564)	11.25 kHz
γ	relativistic Lorentz factor for protons (E_p /m_p)	7461
ϵ	normalized transverse beam emittance	3.75μm
β^*	optical β function (amplitude of betatron oscillations)	55 cm
θ	beam crossing angle	285 μrad
σ_z	longitudinal RMS bunch length	7.55 cm
σ^*	Transverse RMS beam size	16.7μm

3.1.2. The Challenge of Stacking (Pileup)

The LHC circulates protons within its beampipes in several very closely packed bunches, not in a continuous stream. The LHC tries to pack as many protons as it can into the beam and squeeze it as narrowly as possible to maximize the probability of the tiny protons colliding with the other. The luminosity becomes higher with the narrower beam contains more protons. At every crossing of these bunches with each other, several p-p collisions can occur during the same crossover of these bunches (Stenson and Rao, 2012). These multiple interactions (also called stacking or pileup (PU)) are actually inelastic collisions that are superimposed on the hard event. The PU level depends on the configuration of the LHC. It is a function of the frequency of the collisions, the number of protons per packet, the profile of the beams, and so on. The mean number of interactions per bunch crossing is given by $\mu = \sigma_{pp} \times \mathcal{L}/f_c$ where $\mathcal{L}$ is the instantaneous luminosity per bunch, σ_{pp} is the inelastic cross section, and f_c is the LHC revolution frequency. In 2018, p-p collisions at 13 TeV, the PU should have been in the order of $\mu \simeq 32$ and the mean number of interactions per bunch crossing is 69.2 mb as the recommended CMS value which is determined by finding the best agreement with data (CMS Luminosity Public TWiki Page, 2018).

Figure 3.3 shows the event display for a high-PU run (Run Number = 280327). It shows 86 reconstructed vertices in one beam crossing which are very closely spaced.

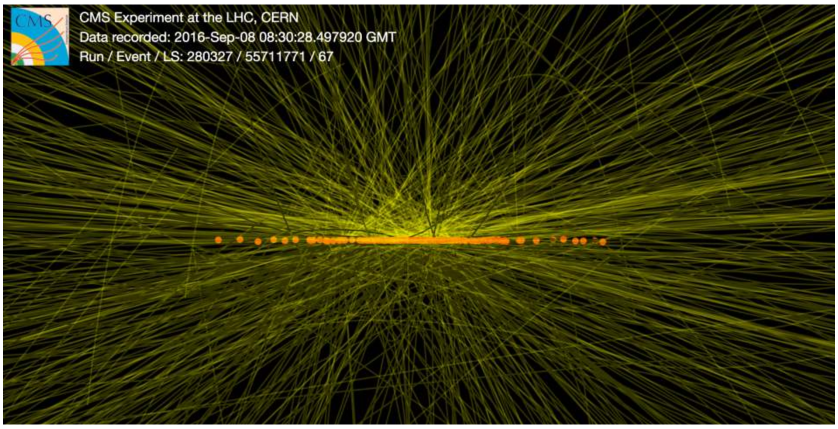

Figure 3.3. An example of a high multiplicity event in CMS, which shows how closely spaced the 86 collisions are (McCauley and CMS Collaboration, 2017).

3.1.3. HL-LHC: High-Luminosity LHC

The project called High-Luminosity LHC (HL-LHC) is expected to improve LHC performance from 2024 onwards. Replacing the superconducting magnets and other machine elements allow luminosity to reach $\mathcal{L}_{int} = 5{\times}10^{34}$ $cm^{-2}s^{-1}$ and therefore an integrated luminosity of 250 fb^{-1} per year, with the aim of reaching 3000 fb^{-1} within a dozen years of the upgrade. This integrated luminosity is ten times higher than expected for the first 12 years of LHC operation, as shown in Figure 3.4 (Apollinari et al., 2017).

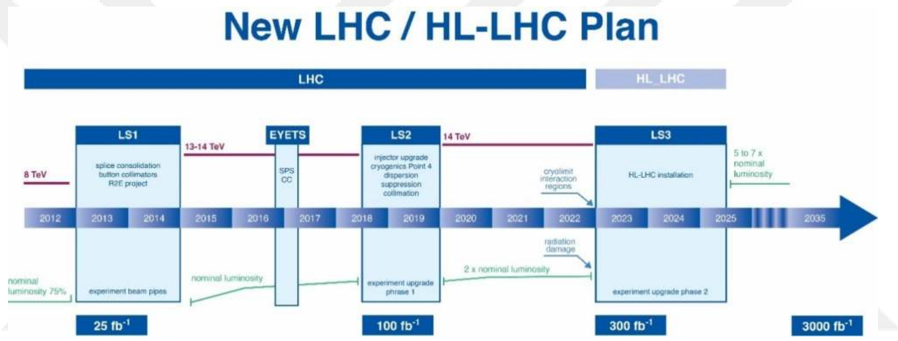

Figure 3.4. The program of the HL-LHC (Apollinari et al., 2017). The purple line indicates the energy of the collisions while the green line indicates the luminosity.

The expected average PU is 140, up to a maximum of 200, with the improvement in the instantaneous luminosity expected by the HL-LHC system (ATLAS Collaboration, 2013). To deal with these new operating conditions, the upgrade of the four major LHC experiments is scheduled to begin in 2024.

3.2. The CMS Experiment

The CMS detector (CMS Collaboration, 2008) (Figure 3.5) is equipped with a 13 m long superconducting solenoid magnet with an internal diameter of 5.9 m which generates a magnetic field of 3.8 T. A muon detector system is located outside the magnet with 21 m long with a diameter of 14.6 m. There is a device for tracking charged particles and a calorimeter, divided into two sections (the electromagnetic calorimeter ECAL and the hadron calorimeter HCAL) are located inside the magnet.

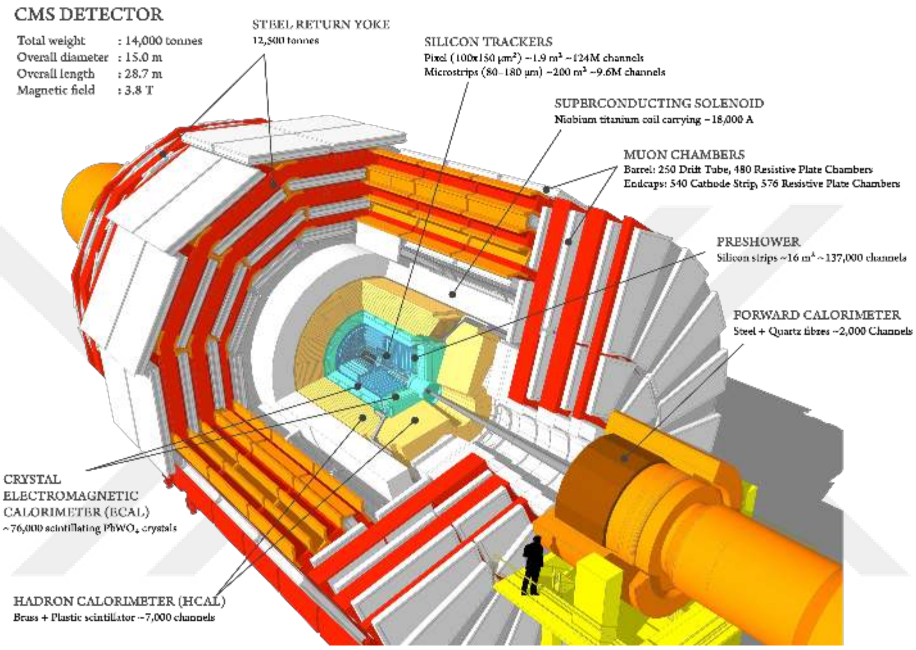

Figure 3.5. Schematic view of CMS (Sakuma and McCauley, 2014).

3.2.1. The Coordinate System and Kinematic Variables

The right-handed Cartesian system is used to define the geometry of the detector, which has its origin at the collision point of the beams and is defined so that the x-axis points towards the center of the LHC ring, the y-axis points vertically upwards (perpendicular to the LHC plane) and the z-axis is directed along the beam 2 (opposite beam) direction (Figure 3.6).

The cylindrical coordinate system (r, ϕ, z) can also be used as a coordinate system for the reconstruction algorithms since the geometry of the CMS detector is cylindrical: The radial coordinate r indicates the distance from the z-axis. The azimuth angle ϕ is measured from the positive x-axis in the x-y plane and the polar angle θ is defined in the *r*-*z* plane but is usually expressed through the pseudorapidity, η, which is defined as:

$$\eta = -ln \tan\frac{\theta}{2} \quad (3.4.)$$

The rapidity of a high energy particle, *y*, is defined as:

$$y = \frac{1}{2}\log\left(\frac{E+p_z}{E-p_z}\right) \quad (3.5.)$$

where p_z the longitudinal momentum and E is the energy of the particle. Measuring the rapidity can be hard for highly relativistic particles because it is difficult to obtain the total momentum vector of a particle, especially at high values of the rapidity. This leads to use of pseudorapidity for highly relativistic particles, $y \simeq \eta$.

Another useful variable is the distance, ΔR, in the η-ϕ plane, which is defined as

$$\Delta R = \sqrt{\Delta\eta^2 + \Delta\phi^2} \quad (3.6.)$$

The transverse momentum, p_T, is defined as the component of the momentum of the particles on the transverse plane *x*-*y*, while the transverse energy is defined as $E_T = E \sin\theta$.

$$p_T = \sqrt{p_x^2 + p_y^2} \quad (3.7.)$$

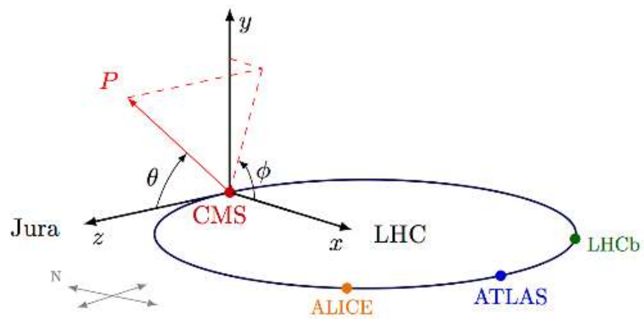

Figure 3.6. The CMS coordinate system (Neutelings, 2017).

3.2.2. Tracking System

The tracker is a detector that aims to reconstruct the trajectories of charged particles by covering ranges up to $|\eta| = 2.5$ (CMS Collaboration, 1997). The particle momentum, its projection and charge sign can be calculated on the transverse plane via the reconstruction of the trajectories. The main requirements of the CMS tracking system are as follows:

- High granularity and fast response due to the high track multiplicity produced at each bunch crossing, produced by an average of more than twenty p-p interactions.
- High radiation hardness to deal with the intense particle flux in the region close to the beamline.
- Extremely low material budget to be the least invasive as possible and to limit some processes that can mislead the trajectory reconstruction, such as multiple scattering, bremsstrahlung, photon transformation, and nuclear interactions.

The CMS tracking system can be divided into two silicon subdetectors: pixel and strip tracker.

Pixel Tracker: It is the innermost CMS detector subsystem and placed near the vertex of interaction. The pixel detector was designed for LHC design luminosity of 10^{34} $cm^{-2}s^{-1}$ and 25ns bunch crossing. The Phase0 pixel detector could not have been able to deal with the rates that are observed at LHC recently, which already exceeds the design luminosity. Thus, the phase0 pixel detector was replaced in the Extended Year-End Technical Stop (EYETS) 2016/2017. The innermost layer of the pixel detector is 29 mm away from the center of the beam pipe, see Figure 3.7. It is now formed by four-layer barrel (BPIX), three-disk endcap system (FPIX). The phase1 pixel detector consists of n^+-in-n sensors with 66560 pixels of the size $100 \times 150\mu m^2$. Each sensor includes a total active area of 16.2×64.8 mm^2 per 16 readout chips (one module), so that all 1856 modules of the new pixel detector cover 1.95 m^2 (Sonneveld and CMS Collaboration, 2017).

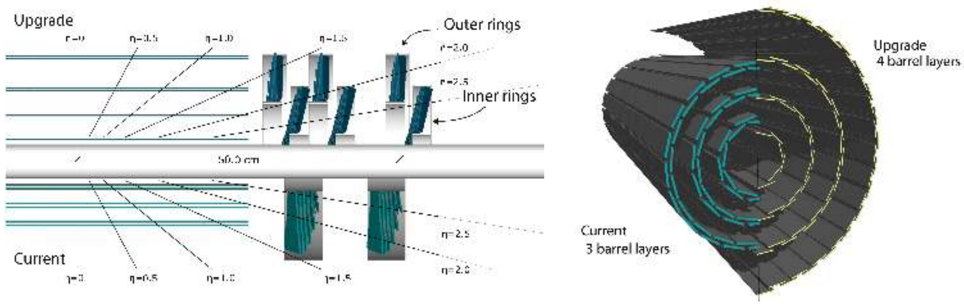

Figure 3.7. Geometry and modules of the phase1 pixel detector (CMS Collaboration, 2013a).

Strip Tracker: It is located in the outermost region of the tracker. In the barrel region, there are four cylindrical layers of the Inner Barrel (TIB) and six layers of the Outer Barrel (TOB), while the Endcaps are formed by nine layers each.

3.2.3. Electromagnetic Calorimeter

The aim of the electromagnetic calorimeter is to measure the energy of electrons and photons. In CMS, the electromagnetic calorimeter (ECAL) is a homogeneous calorimeter, which consists of $PbWO_4$ lead tungstate crystals.

ECAL is composed of three main parts:

- The Barrel (EB) (range of $|\eta| < 1.48$)
- Endcap (EE) (range of $1.48 < |\eta| < 3.0$)
- The Pre-shower (located in front of the endcaps, range with $1.653 < |\eta| < 2.6$)

In EB, the signal is read through avalanche photodiodes (APDs) while in the endcap vacuum phototriodes, more resistant to radiation than APDs, are used.

The energy resolution of the ECAL calorimeter is parameterized by three different contributions:

$$\frac{\sigma_E}{E} = \frac{a}{\sqrt{E}} \oplus \frac{b}{E} \oplus c \qquad (3.8.)$$

where the first term represents a stochastic term (a = 2.8%) which considers the statistical variations in the identification of shower, the second takes the electronic noise and the PU (b = 12%) into account and the third term is related to the calibration (c = 0.3%). These values were determined by measuring the resolution for electrons in beam tests (Adzic et al., 2007).

3.2.4. Hadronic Calorimeter

The primary aim of the Hadron Calorimeter (HCAL) in CMS is the measurement of hadronic energy from collisions. In addition to the energy measurement, the HCAL is used to identify and measure the missing transverse energy resulting from neutrinos or exotic particles in collision events. The HCAL is a sampling calorimeter consisting of alternating layers of absorbing brass plates and plastic scintillator tiles. HCAL is divided into four main parts:

- The Barrel calorimeter (HB), pseudorapidity range with $|\eta| < 1.3$.
- The Endcap calorimeter (HE), pseudorapidity range with $1.3 < |\eta| < 3$.
- The Forward calorimeter (HF), pseudorapidity range with $3 < |\eta| < 5$.

- The Outer calorimeter (HO) up to $|\eta| < 1.3$.

As seen from the interaction point, the hadron calorimeter barrel and endcaps are located behind the tracker and the ECAL. The HB is radially limited between the outer range of the ECAL (R=1.77 m) and the inner range of the magnet coil (R=2.95 m). This placement limits the total quantity of material that can be used to absorb the hadronic shower (CMS Collaboration, 2008). The absorber plates are 5 cm thick in HB and 8 cm thick in HE. The plastic scintillators are 4 mm thick in the entire central hadron calorimeter. In the HF, the active material consists of longitudinal 5 mm-thick quartz fibers.

The scintillation light is collected from the scintillator tiles by using a wavelength shifting (WLS) fibers which are embedded in a groove in the scintillator. Outside of the scintillator, the WLS fiber is connected to an optical fiber that carries the signal to the reading device. Hybrid Photodiodes (HPDs) were used in HB, HE and HO as the reading devices and then replaced by Silicon Photomultipliers (SiPMs) during the Phase 1 upgrade which will be discussed below.

The barrel part of the HCAL calorimeter does not provide enough containment for hadron showers because of the space constraint within the magnet cryostat. Scintillator layers are located outside the solenoid cryostat in order to catch the energy leakage from HB called as HO or tail-catcher. In η, HO composed of five rings and each ring has 12 identical ϕ-sectors.

There are two HF calorimeters that have located both sides of the interaction point at 11.1 meters in order to extend the hermeticity of the central hadron calorimeter system to pseudorapidity of 5. Thus, the HF covers the pseudorapidity of $3.0 < |\eta| < 5.0$. It uses quartz fibers as the active material, embedded in a matrix of copper absorber. Quartz fibers are used as the active element in the HF since they are predominantly sensitive to Cherenkov light from neutral pions. Photomultiplier Tubes (PMTs) are used to collect light from these quartz fibers.

The energy resolution of the HCAL calorimeter is

$$\frac{\sigma_E}{E} = \frac{a}{\sqrt{E(GeV)}} \oplus b \qquad (3.9.)$$

where a = 84.7 ± 1.6% and b = 7.4 ± 0.8% in the barrel region (CMS HCAL/ECAL Collaborations, 2009).

During the CMS detector's initial operation, Run1, anomalous signals associated with particle showers passing through the PMT used in the HF calorimeter were detected. Besides this problem, electrical discharges and gain drifts were observed in the HPD when high voltage is applied in HB, HE and HO calorimeters. The Phase 1 upgrade in HCAL is designed to improve the performance of the subcalorimeters at high luminosity. It is achieved by increasing the depth segmentation of the calorimeter and by offering new features for anomalous background signals rejection (Mans et al., 2012). As part of the Phase 1 upgrade program, the following improvements have been implemented at HCAL, a more detailed description can be found in References (Mans et al., 2012; Lobanov and CMS Collaboration, 2015; CMS Collaboration, 2011).

- During the first long shutdown of the LHC (LS1, 2013-2014), the HPDs in HO were upgraded with the SiPMs.
- QIE (Charge Integrating and Encoding) is an electronic chip that measures the photodetector signals in HCAL. During the YETS 2015-16, QIE8 was replaced with QIE10 with an integrated TDC in the front-end electronics of HF.
- During the EYETS 2016-17, the single-channel PMTs were replaced by multi-anode PMTs operated in a dual-anode configuration in the HF. Also,

four of the HPDs in the HE sector (HEP17) were replaced with SiPMs and QIE8 based readout electronics were replaced with QIE11. During the 2017-18 YETS, the rest of the HPDs of the HE calorimeters were replaced with SiPMs.

- During the Long Shutdown 2 (LS2, 2019), the HPDs in the HB calorimeter were upgraded with SiPMs and QIE8 chips were replaced with QIE11.

After the above-mentioned actions of upgrading, the current depth segmentation of the HCAL calorimeter is shown in Figure 3.8.

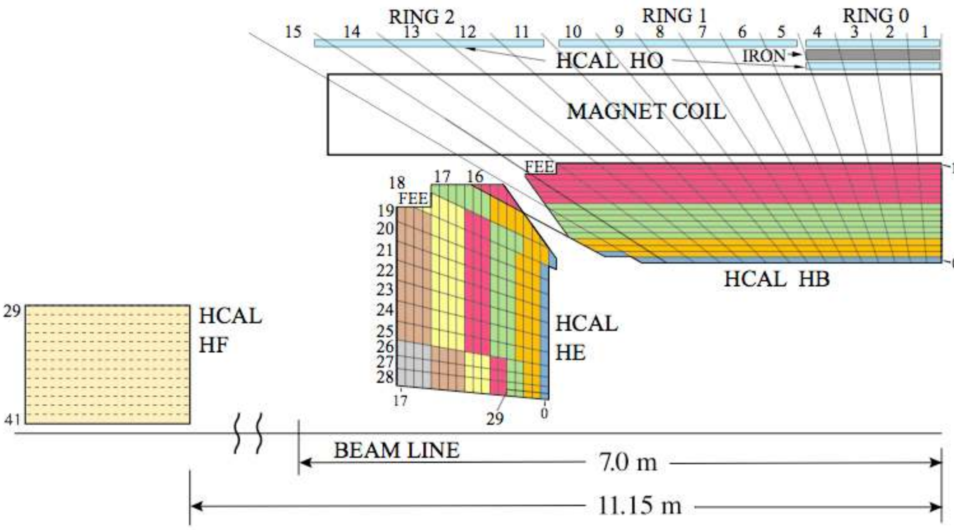

Figure 3.8. Longitudinal section of the HB, HE, HF, and HO detectors. The depth segmentation in the upgraded HE and HB are increased. FEE represents the locations of the front-end electronics in HB and HE calorimeters. Each small box indicates a scintillator tile. The color/shading of tile structure corresponds to depth segmentation (https://home.fnal.gov/~chlebana/CMS/Phase1/figs/HCAL-Depth-Segmentation-Phase1-HE-HBOption1.pdf).

3.2.5. Magnet

The momentum of the charged particles is measured by reconstructing the curvature of their trajectory in the presence of a magnetic field. In CMS, the magnetic field is produced by a superconducting solenoid electromagnet (CMS Collaboration, 1997a) with a massive return yoke (12 500 tonnes) that is part of the external muon spectrometer. The level of the magnetic field is required to achieve a high resolution compatible with the high luminosity of the LHC.

The solenoid winding is made of niobium-titanium superconducting cables coated with aluminum. In order to obtain the superconductivity phase, the entire solenoid is maintained at a temperature of 4 K by means of a liquid helium cooling system. It is necessary to operate the magnet of 19.5 kA current inside the winding and at steady in order to produce a magnetic field of 4 T, at which the magnet will store the energy of 2.69 GJ. The CMS solenoid has more stored energy per unit mass of coil (12 $kJ \cdot kg^{-1}$) than any large superconducting magnet ever constructed (Védrine, 2015).

3.2.6. Muon System

The muon detector system was designed to perform three main functions: muon identification, momentum measurement, and muon triggering. The system is positioned outside of the magnet coil and interleaved with iron return yoke plates. The high resolution of the detector, the high magnetic field of the solenoid magnet and its flux-return yoke provide a good momentum resolution of the muon. The muon detector is composed of three different types of gas-ionization particle detectors for muon identification: drift tubes (DT) in the barrel region, cathode strip chambers (CSC) in the endcap region, and resistive plate chambers (RPC) in both barrel and endcap (Figure 3.9). The basic physical modules are called "chambers" and they are self-operating devices that are mounted into the overall muon detector system of CMS (CMS Collaboration, 2013b).

Drift Tubes (DT): They are used in the barrel region ($|\eta| < 1.2$) where the residual magnetic field is mostly uniform with intensity below 0.4 T and the low muon rate (except in the outermost station of DT Chambers). Four layers of DT chambers named MB1, MB2, MB3 and MB4 (from inside to outside) are arranged on five wheels along the z-dimension and each divided into 12 ϕ-sections, where ϕ is the azimuth angle and MB stands for Muon Barrel. According to the studies, made by using 2016 data, the spatial resolution in the ϕ superlayers is better than 250 μm in MB1, MB2 and MB3, and better than 300 μm in MB4. In the θ superlayers, the resolution varies from about 250 to 600 μm except in the outer wheels of MB1 (CMS Collaboration, 2018).

Cathode Strip Chambers (CSC): CSCs are used in endcap regions and cover pseudorapidity ranges of $0.9 < |\eta| < 2.4$. In this region, the rate of muon particles is high and the magnetic field is strong and non-uniform (Figure 3.10). A CSC composed of six layers, each of them measures the muon position in the bending plane ($R\phi$). The chambers are arranged on four disks for each endcap, divided into concentric rings. The spatial resolution of the CSC varies from about 45 μm to 134 μm (CMS Collaboration, 2018).

Resistive Plate Chambers (RPC): 1056 RPCs are positioned both in the barrel and in the endcap and cover the pseudorapidity range of $|\eta| < 1.9$. The RPCs are used as trigger detectors; additionally, RPC hits are useful for reconstruction and muon identification.

The RPCs have a spatial resolution worse than that of DT and CSC but provide a fast response with a good temporal resolution (1 ns), which is why they are useful for triggering.

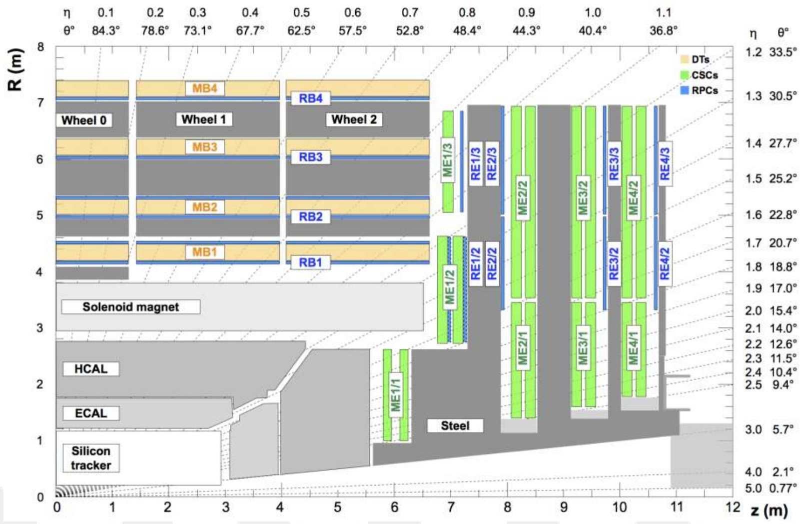

Figure 3.9. A schematic representation of a quadrant of the CMS detector. The steel flux-return disks are indicated by dark gray areas. The four DTs (in light orange) are indicated by MB (Muon Barrel) label and the CSCs (in green) are indicated by ME (Muon Endcap) label. RPCs (in blue) are positioned in both barrel (RB) and endcaps (RE) of CMS. (CMS Collaboration, 2018).

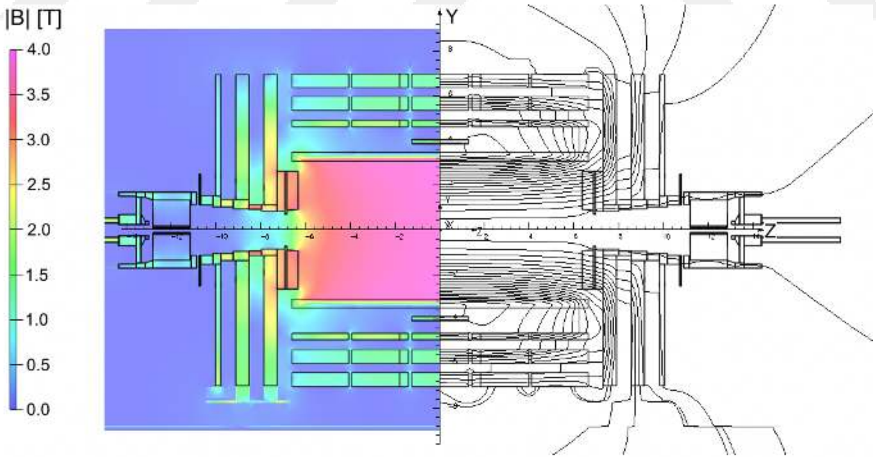

Figure 3.10. Left: Map of the intensity of the magnetic field. Right: A longitudinal view of the CMS detector with magnetic field lines. (CMS Collaboration, 2009).

3.2.7. CMS Trigger System

At the nominal LHC design luminosity of 10^{34} $cm^{-2}s^{-1}$, the rate of p-p interactions is greater than 1 GHz with the bunch crossing frequency of 25 ns. Only a small fraction of these collisions contains events of interest for the CMS experiment and only a small fraction of these can be stored for subsequent analysis. It is the task of the trigger system to select interesting events to archive offline. In CMS, the trigger system is constructed in two levels: L1 and HLT. When the L1 trigger provides a positive decision about the event, the acquisition system aggregates the data related to that event and provides the information to the next trigger system (HLT) which makes the final decision. The reliability of the trigger system is very important since each discarded event is not saved so the information will be lost. Figure 3.11 shows the Trigger and Data Acquisition System (TriDAS) which the trigger system is part of it.

- **L1:** The L1 system is based on a hardware trigger in the sense of being developed almost entirely programmable electronics such as the FPGA or the ASIC, in order to have a high computational speed. The first level of the CMS trigger takes the decision to accept or reject the event based on measurement roughness of the energy deposited in the calorimetric towers and on the information coming from the muon detectors within a latency time of up to 4 μs per crossing (CMS Collaboration, 2017a). The L1 triggers reduce the event rate from the LHC collision rate (~40 MHz) to 100 kHz (CMS Collaboration, 2010). Figure 3.12 shows the schematic view of the trigger decision algorithm, divided into three main components of the L1 trigger: the muon trigger, the calorimeter trigger, and the global trigger. Both calorimeter and muon trigger have local, regional, and global components. The local components, called Trigger Primitive Generators (TPG) are based on tower energy sums in ECAL and HCAL for the calorimeter trigger, track segments and hit patterns in the muon detectors.

The Regional Calorimeter Trigger (RCT) combines the information of the calorimeter TPG, determines isolated and non-isolated candidate electromagnetic (*e*-*γ*) objects, transverse energy sums per calorimeter region and tau-veto bits, and sends them to the Global Calorimeter Trigger (GCT). Then, jets and *e*-*γ* objects are sorted based on their transverse energies and the highest-rank four objects from each category are then sent to the Global Trigger (GT). If the event passes the L1 trigger, is then examined by the HLT trigger (CMS Collaboration, 2010).

- **HLT:** The High-Level Trigger (HLT) system is based on commercial processors. The HLT has all the available information coming from the detectors and therefore the processing a large amount of data has the need for much more computing power. The HLT is a huge software running on a PC farm which set of computers connected in a network to exchange the information to process data quickly and efficiently. The task of HLT is to reduce the event rate from 100 kHz to a frequency of ~1 kHz (CMS Collaboration, 2010; Donatoa, 2018).

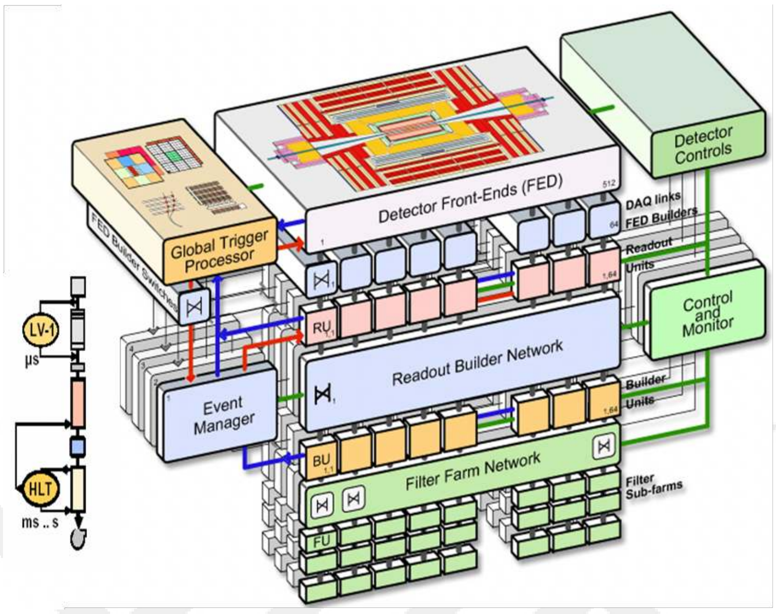

Figure 3.11. Architecture of CMS Trigger and Data Acquisition System (CMS Collaboration, 2010).

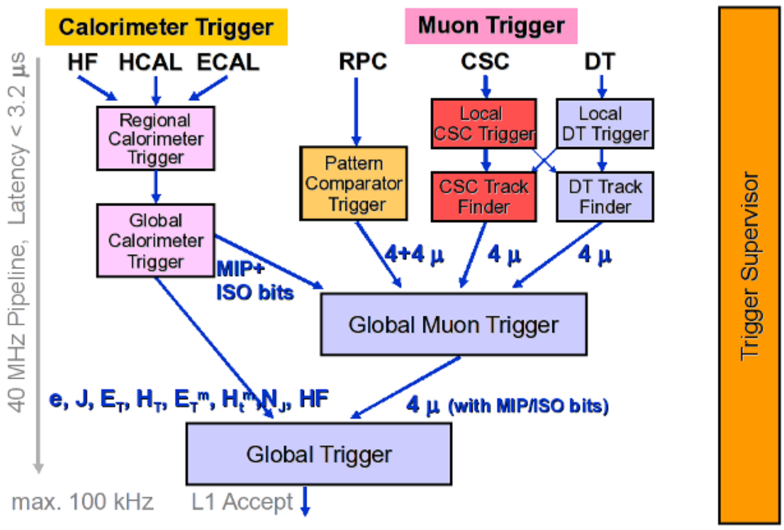

Figure 3.12. CMS Level-1 Trigger System (CMS Collaboration, 2010).

4. PHYSICS OBJECTS

In this chapter, firstly, the computer programs used to calculate or simulate p-p collisions are presented. Two types of programs that are based on MC methods are described; PYTHIA and HERWIG++. This chapter will conclude with the sections corresponding to the algorithms dedicated to the reconstruction of higher-level objects such as jets and missing transverse energy. These are the basic elements of all physics analyses.

4.1. Monte Carlo Generation

MC generators are used in particle physics to make theoretical predictions of the result of high-energy collisions and thus it can be compared directly with the data coming from the detectors. The MC event generators are computer programs that have been specially created for this task. How different programs can be combined in the event-generation chain can be seen in Figure 4.1. There are two production chains for parallel events; one for the data coming out of the detectors (left lane) and the other for simulated events (right). The starting point of the simulated events is the generators of MC events like PYTHIA (Sjöstrand et al., 2001; Sjöstrand, 2008) or HERWIG++ (Bähr et al., 2008).

They output the four-momentum of all the partons in the final state of a simulated collision and then one can reproduce very precisely the effect that these events would have had in the detector. At the end, the two chains meet and we turn exactly the same reconstruction algorithms on the data and the simulation. This is a cornerstone of the data analysis system which will allow us to make consistent data/MC comparisons.

Now, the different stages of the production of a complete MC event can be examined as in the following subsections.

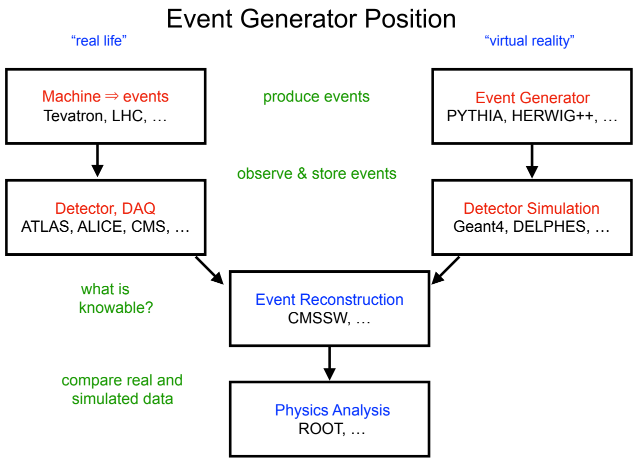

Figure 4.1. Comparison of the event generation chain for data (left) and simulation (right) (Ahmad et al., 2019).

4.1.1. Monte Carlo Event Generation Chain

An MC generator (Sjöstrand et al., 2006) is used for a process $ab \rightarrow XY$ given the different matrix-elements $2 \rightarrow 2$, $2 \rightarrow 1$, and $1 \rightarrow 2$ to calculate the production cross section σ of the process and describe the composition and kinematic characteristics from the process. The latter is obtained by the random variable of the MC type so as to find the probabilistic distributions described by the quantum mechanics underlying the theory. The partons as described by an MC generator had no interaction with the detector.

The MC generation can be separated into several stages, the main ones of which are as follows (Sjöstrand et al., 2005):

- The energy of the two-beam particles in the colliders requires a description of the internal structure of the protons. Normally each particle is characterized by the PDFs.
- The process, which we are interested in, consists of the collision of the two incoming partons and the particles which result from them. The description

at the level of the matrix elements of this process corresponds to what is called “hard event” and leads to the production of partons directly resulting from the hard process. However, statistically, the collision between the protons mainly leads to simple particle-particle interactions such as inelastic, diffractive, and non-diffractive interactions. All of these interactions are called “minimum bias events” (Minimum Bias) because they correspond to all the events that would be selected if there were no trigger condition. These events must also be added to the description of the hard event (Moraes, 2007; Sjöstrand, 2014).

- The hard process requires large transfers of momentum and thus the partons involved are dramatically accelerated. An accelerated electric charge emits QED radiation (photons), the accelerated colored partons will emit QCD radiation in the form of gluons that carry color charges and can thus emit further radiation. The description of these emissions is generally modeled by what is called “Parton Shower (PS)” or partonic shower generator (Sjöstrand et al., 2006). These radiations are composed of gluons and photons and can be cataloged according to their type of production before or after the hard event:
    - Initial-State Radiation (ISR): An initial-state radiation is one that occurs on an incoming parton of the hard process. These irradiations can cause the production of jets in a direction close to that of the incident hadrons.
    - Final-State Radiation (FSR): A final-state radiation is one that occurs from an outgoing parton of the hard process. These are the main sources of radiation emitted co-linearly with partons from the hard event.
- The partons emitted during the process move away from each other and the interactions between them can no longer be described by the perturbative calculation since α_s increases at low values of the shower evolution scales.

We, therefore, use hadronization models, i.e. string model and cluster model, (Andersson et al., 1983; Christova and Leader, 2009) to describe the formation of detectable particles of neutral color charge.

- There is an extra hadron production in hadron collider events that arise from collisions between those partons in the incoming hadrons that do not directly participate in the hard process. Thus, it is an additional source of energy that can reach the detector, known as the "underlying event" is greater than minimum-bias events. It is important to model this additional activity to properly reproduce the data. Indeed, for the partons carrying color charges, the radiation of quarks and gluons will add after the hadronization of many particles in the final state. Different types of models (Sjöstrand and van Zijl, 1987; Gustafson, 2007) were developed and implemented in generators and then validated by comparison with the data. Each time, these are phenomenological models that must be parameterized according to the data.
- In the last stage of the event generation, the sequential decay of the unstable hadrons produced depending on their lifetimes occurs in the hadronization process. (Webber, 2011). The next step corresponds to considering the disintegration of unstable particles (mesons, baryon, ...). The decay products are obtained in accordance with the known phase space of the parent particle from the decay modes and their branching ratio.

Figure 4.2 summarizes this entire sequence. There are many generators of various capacities which fall into practice in two categories: there are those which stop at the generation of the hard event which will be called generators with elements of matrices (Matrix Element) and those which manage the entire generation chain, which we will call parton shower generators. PYTHIA and HERWIG are versatile and general partonic shower generators in terms of the physical processes described. While others are more specialized at the level of matrix elements and/or do not deal with the complete generation chain and must, in this case, be combined with a partonic spray generator to describe the PS and hadronization. The final product of MC generators consists of a collection of "events" made up of particles in an observable final state (photons, leptons, and hadrons) with their complete kinematic characteristics and information on the vertex of the event.

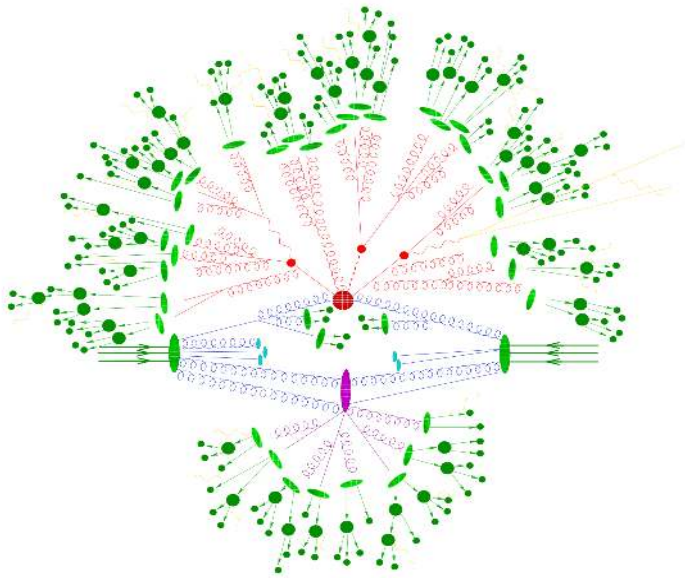

Figure 4.2. Pictorial representation of a p-p collision as simulated by an MC event generator, where the different colors indicate the different stages involved in event generation. The large green ellipses indicate two partons from the incoming protons. The red blob in the center represents the hard interaction, surrounded by a tree-like structure representing Bremsstrahlung as simulated by parton showers (red), the blue lines which represent ISR become red lines which represent FSR after the hard interaction. The resulting partons hadronize into colorless states (light green blobs) that subsequently decay into stable particles (dark green circles). The purple blob indicates a secondary hard scattering between proton remnants which is again creating a PS (purple). This is part of the underlying event, together with the beam remnants is shown as the light blue blobs. Yellow lines represent electromagnetic radiation which occurs at any stage (Höche, 2014).

4.1.2. PYTHIA

One of the most frequently used pieces of software in particle physics is the PYTHIA event generator which was developed mainly by Torbjörn Sjöstrand. PYTHIA is designed to simulate a wide variety of physics processes with more than 300 different subprocesses including hard QCD, soft QCD, electroweak, onia, top, Higgs, Supersymmetry, new-gauge boson, left-right symmetry, compositeness, technicolor, leptoquark, extra-dimensional, dark matter processes. PYTHIA is specially optimized for the $2 \rightarrow 1$ and $2 \rightarrow 2$ processes which sometimes limits its use only to the PS and hadronization part (Sjöstrand et al., 2006). Once the center of mass-energy, the PDF, and the process are specified, the generation of events begins with the simulation of the hard process followed by the disintegration of the unstable particles. Then the generated partonic system is evolved with PS, in PYTHIA using the interleaved evolution of both ISR and FSR. The simulation of the underlying event is then considered for the parts that have not participated in the hard interaction. Finally, it simulates the hadronization of disintegration products according to the Lund string model which is discussed in Section 2.2.3.1. PYTHIA also is interlinked with Les Houches Accord (LHA) and its associated Les Houches Event Files (LHEF). In this way, it offers the possibility of reading the hard process produced by such programs as MadGraph, Sherpa, CompHEP, CalcHEP, etc. in LHE format and taking charge of the rest of the generation (PS then hadronization). At the end of the chain, one obtains the list of the stable particles generated as well as their four-momentum. We, therefore, classify PYTHIA in the category of generators at the hadronic level, and the list of particles can be directly read by a simulation program of the detector.

For our analysis, the most recent version PYTHIA8, with tune CUETP8M1, is used and an event number equivalent to 9,960,448 is generated for the QCD sample at average energy in the center of mass of 13 TeV.

4.1.3. HERWIG++

HERWIG (Hadron Emission Reactions With Interfering Gluons) (Corcella et al., 2005) is another prominent example of event generator for the simulation of hadron-hadron and lepton-lepton collisions at high-energy colliders. HERWIG is using angular ordering in the generation of the parton shower and it simulates the full hadronic interaction by the cluster model as discussed in Section 2.2.3.1

HERWIG++ (Bähr et al., 2008), as in HERWIG, describes the main stages of the simulation of high energy collisions (i.e. hard subprocess, initial- and final-state parton showers, the decay of heavy objects, multiple scattering, hadronization, hadron decays) but it has a new parton shower and an improved cluster hadronization model features. HERWIG++ is built on the Toolkit for High Energy Physics Event Generation (ThePEG) (Lonnblad, 2006) framework and it provides a much more flexible structure.

4.2. Jet Production in Hadron Collisions

The high-energy partons produced by the p-p scattering manifest themselves in the final state as a collimated spray of particles that we call a jet, as illustrated in Figure 4.3. In hadron-collider experiments, jets are ubiquitous and indispensable to study the underlying dynamics and interactions. Jets have played the main role in the discovery and property measurements of many fundamental particles such as the gluon (*g*) (JADE Collaboration, 1980; PLUTO Collaboration, 1979; MARK-J Collaboration, 1979; TASSO Collaboration, 1979) and the top quark (*t*) (D0 Collaboration, 1995; CDF Collaboration, 1995). Jets are a highly powerful object in search of new physics and precision measurements of SM properties due to their large production rate at the LHC (Kogler, 2019).

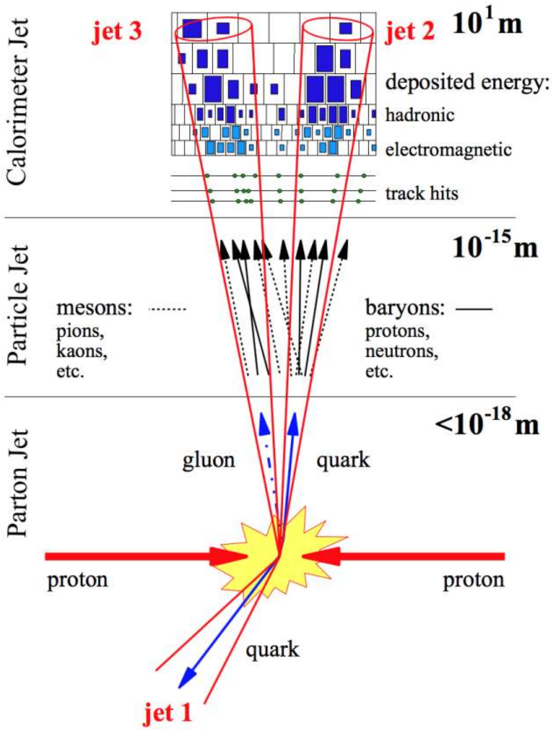

Figure 4.3. Schematic overview of a jet to which bundles of partons, hadrons, or detector measurements are clustered together (Carli et al., 2015).

There is no single and objective way to define the concept of a jet with theoretically or experimentally. The precise definition of a jet requires a full specification about the output of a jet reconstruction algorithm. The aim of the jet algorithms is to reverse the hadronization, so, one may wish to reduce the complexity of the final state to understand the initial state or to measure certain parameters.

A jet reconstruction algorithm is divided into two parts (Catani et al., 2000). The first step is to select all the relevant final-state particles that will define a jet and the selection process is often called, by synecdoche, the jet algorithm. The second step is to combine the four-momenta of the jet constituents to obtain the four-momenta jet and this known as “recombination scheme”.

Jets are reconstructed from topologically associated energy depositions in calorimeter cells, charged-particle tracks, or simulated particles. Ideally, they are corrected due to the intrinsic limitations of the system (such as the non-linear response of the calorimeters, zero-suppression effects, PU, noise due to electronics) so that the resultant four-momentum vector corresponds to that of the sum of the original hadrons comprising the jet (Ellis et al., 2007).

CMS defines three types of jets according to the different ways of combining the information of the different subdetectors (CMS Collaboration, 2011a):

- **Calorimeter (CALO) jets** are reconstructed with the information coming from towers in calorimeters. Such a calorimeter tower consists of one or more HCAL cells and the geometrically corresponding ECAL crystals (Rabbertz, 2017).
- **Jet-Plus-Track (JPT) jets** are reconstructed calorimeter jets by replacing calorimeter energy response and resolution with the charged particles measured in the tracker system, according to the Jet-Plus-Track algorithm (CMS Collaboration, 2009a).
- **Particle-Flow (PF) jets** obtained by clustering the four-momentum vectors of the PF candidates. The PF algorithm aims at reconstructing and identifying all visible particles in the event by combining the information from CMS subdetectors (CMS Collaboration, 2011a). The PF algorithm will be discussed in detail in Section 4.2.3.

In this thesis, we focused on the PF typology, because compared to the CALO typology it provides more information about the jet, also using the information coming from the tracker.

4.2.1. Jet Algorithms

In order to construct an ideal jet algorithm, it should satisfy the following general criteria.

- **Fully Specified:** The method of jet selection, the jet kinematic variables, and the various corrections should be explicitly and completely described.
- **Theoretically Well Behaved:** The algorithm should be infrared and collinear safe without parameters of ad hoc clustering.
- **Detector Independence:** Algorithm should be independent of segmentation, the energy response, or the resolution of the calorimeter
- **Order Independence:** The algorithms should behave evenly at the parton, particle, and detector levels. This point is very important since it guarantees the possibility of comparing the data from the experiments with MC simulations and theoretical calculations (Blazey et al., 2000).

The jet finding algorithm was first published by Sterman and Weinberg in 1977 (Sterman and Weinberg, 1977) and since then several jet algorithms have been developed for hadron colliders (Ali and Kramer, 2011; Salam, 2009; Ellis et al., 2007; Moretti et al., 1998). The jet algorithms are capable of working on different types of objects, such as calorimeter towers (CaloJets), but they can also use the generated particles (GenJets) to distinguish the effects due to the detectors and the algorithms. It is possible to categorize the jet algorithms into two main classes: sequential recombination algorithms and cone algorithms.

4.2.1.1. Cone Algorithms

Cone jet algorithms try to associate the set of energy corresponding to a jet in a cone of radius R ($\Delta R_{ij}^2 = \left(y_i - y_j\right)^2 + \left(\phi_i - \phi_j\right)^2 < R^2$) fixed in the plane (y, ϕ). This algorithm has the advantage of having a simple geometric interpretation and being easy to implement, while the disadvantages of being slow and consuming a lot of computing time. Despite the development of "seed" reconstruction methods that reduce the computation time, this method has the disadvantage of bringing sensitivity to infrared and uniform singularities.

In the past, experimentalists used cone algorithms because it was easier to implement, but theorists do not prefer to use them because they contain non-physical constants and generally, it is not infrared and collinear (IRC) safe as well.

The only IRC safe cone algorithm is the seedless infrared safe cone algorithm (SISCone) (Atkin, 2015). Although it provides good stability for infrared and collinear singularities and is fast enough to be used in the experimental analysis, it is still neglected in favor of generally more efficient sequential recombination algorithms (Coco et al., 2009).

4.2.1.2. Sequential Recombination Algorithms

The family of sequential recombination algorithms (Ellis and Soper, 1993; Catani et al., 1998; Wobisch and Wengler, 1998; Cacciari et al., 2008; CMS Collaboration, 2009b) corresponds to the second class of algorithms, the principle of which is based directly on the concepts of singularities. Indeed, the purpose of these algorithms is to collect the particles having the greatest probability of belonging to a collinear or infrared safety. They try to do this by grouping pairs of close particles sorted in transverse momentum. The sequential recombination algorithm is used as a standard method class for jet reconstruction in hadron collider experiments. There are several variations of this algorithm are typically embedded in physical or geometrical criteria, such as the k_T algorithm, Cambridge-Aachen and anti-k_T. Cambridge-Aachen, and anti-k_T algorithms will be discussed in Section 4.2.2.

4.2.2. Reconstructed Jet Types at CMS

The reconstruction of a jet occurs through a clustering algorithm and CMS mainly uses two types of algorithms: the anti-k_T algorithm (Cacciari et al., 2008) and the Cambridge-Aachen (C-A) algorithm (Dokshitzer et al., 1997). The C-A algorithm is mainly used when looking for a possible substructure within a jet. The anti-k_T algorithm consists in coupling particles reconstructed by the PF algorithm, starting from those closest to each other. The distance (d_{ij}) between two particles i and j and the distance (d_{iB}) between a particle i and the beam B are defined by the following quantities (Cacciari et al., 2008):

$$d_{ij} = \min\,(k_{Ti}^{2p}, k_{Tj}^{2p})\,\frac{\Delta_{ij}^2}{R^2} \qquad (4.1.)$$

$$d_{iB} = k_{Ti}^{2p} \qquad (4.2.)$$

where k_{Ti} and k_{Tj} are the transverse momentum of the two particles, p is a value that depends on the chosen reconstruction algorithm, $\Delta_{ij}(\sqrt{\Delta y^2 + \Delta\phi^2})$ is the geometric distance between the two particles in the (y, ϕ) plane and R is the parameter that defines the width of the spray (it is 0.4 in standard jets). For the anti-k_T algorithm, we have $p = -1$, while for Cambridge-Aachen we have $p = 0$.

For each pair of particles i and j it is checked which of the two distances just defined is the smaller. If the minimum is obtained for a value of d_{ij}, then, the particles i and j are merged together (their four-vectors are summed) and the algorithm starts again. On the contrary, if the minimum is obtained for d_{iB}, the particle i (often resulting from the fusion of several other particles during previous iterations of the algorithm) is considered as a jet and removed from the list of particles. The algorithm stops when no particles remain.

The only difference between these two algorithms comes from the way the choice of particles to the group is made. For the anti-k_T algorithm, the weight of each pair is proportional to min $(1/k_{Ti}^2, 1/k_{Tj}^2)$, which comes down to merging the closest large momentum particles first. In the case of the C-A algorithm, the weight is only proportional to the distance between the pairs: the closest particles are merged first. Figure 4.4 shows an example of a reconstruction of the jets on the same event by the two algorithms.

An alternative to the reconstruction of PF jets exists, using the calorimetric clusters at the input of the algorithms for reconstructing the jets. This method was used by CMS before the implementation of the PF, much more efficient.

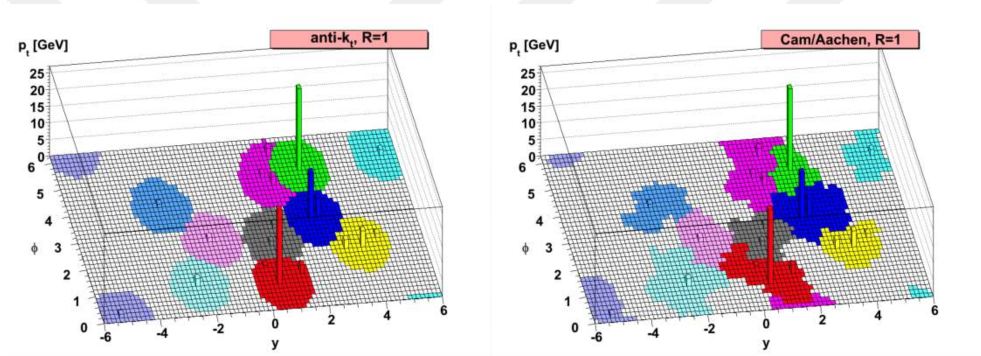

Figure 4.4. Reconstruction of the jets in the (y, ϕ) plane for a distance R = 1 performed in the same event by the anti-k_T algorithm (left) and by the C-A algorithm (right) (Cacciari et al., 2008).

4.2.3. Particle-Flow Algorithm

In this section, we will provide a very brief description of the Particle-Flow (PF) algorithm (CMS Collaboration, 2009c) for particle reconstruction. The aim of the PF algorithm is to identify all the stable particles present in the event, i.e., electrons, muons, photons, charged hadrons, and neutral hadrons, through an appropriate combination of all the information coming from CMS subdetectors, in order to obtain an optimal determination of their energy, direction, and type. Physical objects are reconstructed as traces associated with ECAL and HCAL deposits, pre-shower detectors, and muon detectors. This association occurs by means of a link algorithm that connects the PF elements from different subdetectors (CMS Collaboration, 2009c). Any pair of elements can be tested via this algorithm. When the algorithm finds that two elements are linked, it defines a distance between these two elements. This distance aims to measure the quality of the connection (link). It then generates PF blocks of the elements associated with either an indirect link or a direct link through common elements. (CMS Collaboration, 2018a).

The operation of the PF algorithm can be described as follows: each block consisting of a track hit in the tracker and a track of a muon in muon detectors is classified as a muon and the corresponding track is removed from the set of blocks to be analyzed. Subsequently, the electrons are reconstructed: each track of the block is submitted to a pre-identification stage, in which the tracker is used as a pre-shower detector for the electrons, exploiting the fact that the electrons tend to give rise to short tracks and to lose energy by Bremsstrahlung. The tracks of the pre-identified electrons are obtained with a fit and followed in an attempt to establish their trajectories in the ECAL. The final identification of the electron is made on the basis of a combination of variables related to the tracking and the calorimetric deposit, giving rise to a “PF electron”. The detection of the neutral particles (photons and neutral hadrons) in the block occurs through the comparison between their momentum and the energy detected in the calorimeters. If a few tracks can be linked to the same HCAL cluster, the sum of their momenta is compared to the calibrated calorimetric energy. If only one track is linked to several HCAL clusters, the link to the nearest cluster is held for the comparison (CMS Collaboration, 2009c).

A track can also be linked to more than one ECAL clusters that those clusters first sorted by their distance to the closest track. Then, the ordered list is scanned and the link where the total calibrated calorimetric energy remains smaller than the sum of the momentum of the charged-particles is kept (CMS Collaboration, 2009c).

The “PF charged hadron”, which takes its momentum and energy directly from the momentum of the track, is formed from the remaining tracks in the block. The momentum of charged hadron can be defined again by the fit of the measurements in the tracker and the calorimeters if the calibrated calorimetric energy is consistent with the track momentum within the uncertainties of the measurement (CMS Collaboration, 2009c).

As mentioned above, the calibrated energy of the nearest ECAL and HCAL clusters connected to the tracks needs to be larger than the total associated charged particle momentum. In particular, if the relative energy excess is greater than the total ECAL energy, it gives rise to a “PF photon”, and possibly to a “PF neutral hadron”. The ECAL and HCAL clusters that are not originally linked to any track or for which the link was disabled, lead to PF photons and PF neutral hadrons, respectively. The neutral-hadron energies are calculated only by applying the calibration method to the HCAL clusters (CMS Collaboration, 2009c). A simulation of a jet reconstructed with the anti-k_T PF algorithm is shown in Figure 4.5.

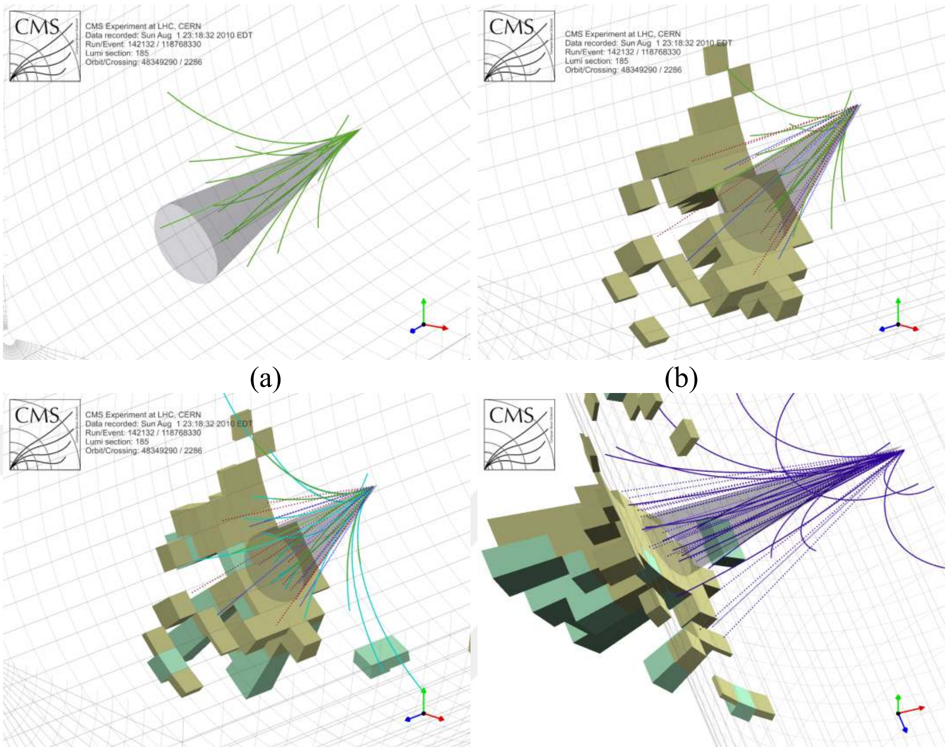

(a) (b) (c) (d)

Figure 4.5. A simulation of a PF jet reconstructed with the anti-k_T algorithm in the CMS detector. The data was recorded by CMS detector in 2010 and the jet p_T is chosen as 115 GeV. (a) presents a jet cone with its tracks (green lines) reconstructed in the silicon tracker. (b) presents a jet and its tracks, photon candidates (dotted red lines), neutral hadrons (dotted blue lines), energy deposits in ECAL (yellowish rectangles). (c) presents a jet and its tracks, photon candidates, neutral hadrons, charged hadrons (cyan lines), energy deposits in ECAL and HCAL (teal rectangles). (d) presents the final view of the calorimeter deposits of a jet with all of its constituents in CMS detector (Dorney, 2011).

In a high PU environment, the CMS PF algorithm is the first technique to be optimized. Not only is the performance of PF energy reconstruction maintained at high luminosity by using track information on the vertex position, but the CMS PF algorithm has also been effective in reducing the PU effect by removing PF candidates originating from well-reconstructed PU vertices. This new aspect of PF is called Charged Hadron Subtraction (CHS) and reduces the in-time pileup contribution from charged particles (CMS Collaboration, 2009c; Schwartzman, 2015).

4.3. The Reconstruction of the Missing Transverse Energy

The missing transverse energy (MET, $\vec{\not{E}}_T$) is the observable one uses to obtain information on neutral weakly interacting particles that do not interact with detectors such as neutrinos, muons. Particles that cross the detector's improperly instrumented regions can be a cause of apparent $\vec{\not{E}}_T$ (CMS Collaboration, 2011b). The CMS detector architecture was designed to maximize the hermeticity of the calorimeters by experimentally covering the largest pseudorapidity coverage ranges from −5 to 5 (CMS Collaboration, 2007). Although CMS is usually hermetic, there are uninstrumented areas at the border between the barrel and endcap parts and between the endcap and forward calorimeters in the CMS calorimeter (CMS Collaboration, 2011b).

In the hypothesis of a perfect hermetic detector, we can estimate that if a particle does not interact with the detectors all its transverse energy is missing. Similarly, particles that are poorly reconstructed or escape without being detected due to the blind area of the detector will only deposit some of their energy in the detector. It is, therefore, necessary to distinguish between the actual MET carried away by particles that do not interact with any detector and poorly instrumented regions of the detector and measurements.

The MET is determined as the negative vector sum of p_T of all reconstructed particles;

$$\vec{\not{E}}_T = -\sum_{i \in X} \vec{p}_{T_i} \qquad (4.3.)$$

where $\vec{p}_{T_i} = (\vec{p}_{x_i}, \vec{p}_{y_i})$ represents the measured transverse momentum of the i^{th} reconstructed object and X is the set of reconstructed objects.

At CMS, several types of input objects are used to calculate $\not{E}_T$ which is the magnitude of $\vec{\not{E}}_T$ (CMS Collaboration, 2011b):

- Calo $\not{E}_T$, which is calculated using only the information of the calorimeter towers (CMS Collaboration, 2007a).
- TC $\not{E}_T$ (Track-corrected MET), which is based on Calo $\not{E}_T$, but also adds the tracker information to reconstruct the particles (CMS Collaboration, 2009d).
- PF $\not{E}_T$ is calculated from the reconstructed PF particles which is the most precise because it uses data from all subdetectors (CMS Collaboration, 2009c).

The $\not{E}_T$ can be underestimated or overestimated due to a variety of effects, such as the nonlinearity of the calorimeter response, non-instrumented areas of the detector, inefficiencies in the tracker, minimum energy thresholds in the subdetectors, electronic noise, PU, and underlying event. To remove the bias in the $\not{E}_T$ scale, a two-stage correction was developed; Type-I and Type-II MET corrections. The Type-II MET correction is not recommended for PF MET which is used in this thesis, so missing transverse energy is corrected by using the Type-I correction.

4.3.1. Type-I MET Correction

In each event, the Type-I correction is based on the energy response of reconstructed jets and hence this correction propagates the jet energy corrections (JECs) to MET. The Type-I MET correction, $\vec{C}_T^{Type-I}$, replaces the raw of the p_T of particles which can be clustered as jets with the vector sum of the p_T of the jets to which JECs are applied. Usually, PF MET clustered from PF candidates is used however in this thesis, MET clustered from PF CHS candidates, so-called CHS

MET, is used. Thus, the Type-I correction for the CHS MET can be written as follows (Reimers and Karavdina, 2016; CMS Web JetMET TWiki Page, 2013);

$$\vec{C}_T^{Type-I} = -\sum_{\vec{p}_{T_{jet}}^{L123} > 15GeV} \left(\vec{p}_{T_{jet}}^{L123} - \vec{p}_{T_{jet}}^{L1RC} \right) \quad (4.4.)$$

$$\vec{E}_T^{Type-I} = \vec{E}_T^{raw} + \vec{C}_T^{Type-I} \quad (4.5.)$$

where L1, L2, and L3 are levels of JECs which will be discussed in Section 5, and RC represents for Random Cone. A detailed description of the RC method can be found in Reference (CMS Collaboration, 2017b).

4.3.2. MET Filters

As discussed in Section 4.3, various instrumental, reconstruction effects and electronic noise can cause fake MET. The CMS-MET collaboration recommended the following filters to remove the events which are produced by spurious signals;

- **HBHE Noise Filter:** HPDs are used as a photodetector in the HB and HE subcalorimeters of the HCAL. During the collision runs, anomalous noise based on the feature of HPDs was recorded in the HB and HE. The noise can be recorded only in one or a few HPD pixels (Ion Noise Feedback Noise), in most or all pixels in a given HPD (HPD Noise), or in all 72 channels in a given readout box (RBX Noise). The HBHE noise filter is used to remove these noisy pixels (Saka, 2016). Figure 4.6 shows an example display of noisy event which rejected by this filter.
- **HBHE Noise Iso Filter:** In addition to HBHE noise filter, there is an isolation-based noise filter which is a topological algorithm that combines candidate noise clusters in the HCAL and ECAL, and compared with

measurements from the tracker in the event-rejection decision (CMS Collaboration, 2019).

- **CSC Tight Halo 2015 Filter:** When beam protons suffer collisions with the nuclei of the gas' atom and the LHC beam collimators in the upstream of the detector producing the Machine Induced Background (MIB, "beam halo") events where parallel to the beampipe. MIB events can cause an abnormally large MET (Pivarski, 2008; CMS Collaboration, 2015a). The CMS Muon Cathode Strip Chamber (CSC) subsystem can detect beam halo events since the system has broad geometric coverage in the transverse plane to the beamline and has a good reconstruction performance for both collision and non-collision muons. Hence, the CMS-CSC beam-halo event filter can be used to remove these MIB events by using trigger and reconstruction level information from this subsystem (CMS Collaboration, 2011b; CMS Collaboration, 2012).
- **Ecal Dead Cell Trigger Primitive Filter:** Some of the ECAL towers have not the crystal-by-crystal precision readout. However, the trigger primitive (TP) information is still available and can be used to estimate the energy deposited in those towers. This filter removes events with a TP close to the saturation value (127.5 GeV) (CMS Collaboration, 2019; CMS MET Group, 2017).
- **Primary Vertex Filter,** which removes events that do not include a good primary vertex.
- **EE Bad Supercrystals Filter:** In 2015, the ECAL had four noisy 5×5 endcap supercrystals which leading to anomalously high energy deposits (TeV regime) in supercrystals. This filter rejects events with such high amplitude anomalous pulses (CMS HyperNews ECAL Performance Forum, 2015).

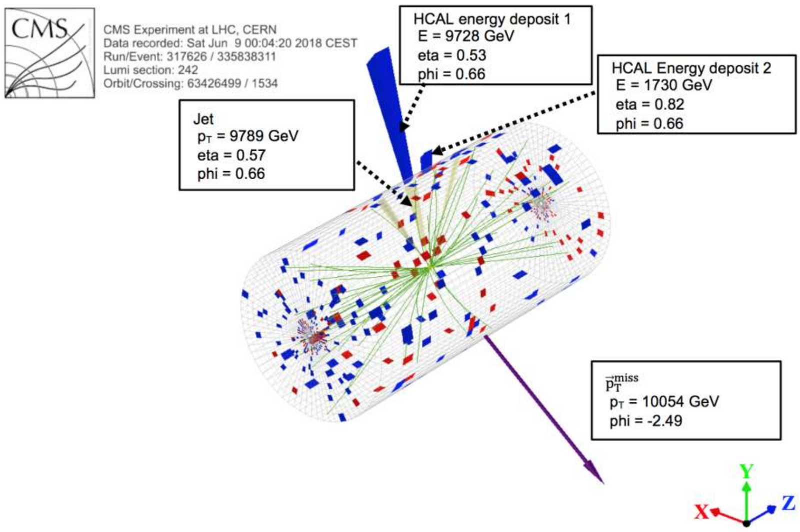

Figure 4.6. A display of a noisy event rejected by the HCAL noise filter in Run 317626. Green lines indicate the high-quality PF tracks, yellow lines indicate the reconstructed jets, red/blue bars represent the energy deposited by the PF candidates in ECAL/HCAL respectively. The violet arrow represents the missing transverse energy's direction and magnitude (CMS Collaboration, 2020).

5. JET ENERGY CORRECTIONS at CMS

In an event, the jets reconstructed by clustering from four-momentum vectors of PF candidates. The measured energy of the reconstructed jet can be different from the final-state particle level jet which is clustered from all stable and visible particles except neutrinos. This difference can be caused by several reasons, e.g. non-linearities in the detector response, the particles created during the hadronization do not correctly form into jets. Therefore, the energy of the reconstructed jets needs to be calibrated. This chapter is dedicated to the jet energy corrections which are performed in different stages.

5.1. CMS Factorized Jet Energy Correction Scheme

In general, the energy of the jets measured by the calorimeters will be different from the exact energy of the particles constituting the jet because of the reconstruction algorithms and the detector's imperfections as listed below:

- The energy lost in the inactive areas of the detector. Although the detectors have been designed to maximize hermeticity, we cannot avoid the presence of non-instrumented areas upstream of calorimeter which leads to a degradation of the measurement.
- Unequal calorimeter responses to the electromagnetic and hadronic showers.
- The particles other than reconstructed jets: Some of the particles in the initial spray may eventually not be contained in the restructured jet. Typically, the low energy charged particles can be deflected by the magnetic field and interact in another region of the calorimeters, far away from the area where the jet is reconstructed.

- In the process of jet reconstruction, there is a set of cuts on the tower energies to eliminate the electronic noise effect and this is based on the balance between jet reconstruction efficiency and instrumental fake rates. It is necessary to take into account the possible losses introduced into this method during the reconstruction of the jets and their constituents (Heister et al., 2005).

Each of these effects is a source of uncertainty in the measurement of the quantities linked to the jets and a calibration method must be applied in order to restore equality between reconstructed and particle-level jets so that the simulation reproduces the data well. Thus, the purpose of the jet energy calibration, so-called JES correction, is to evaluate the energy that they actually have from the energy that the jets deposit in the detector (CMS Collaboration, 2011a). JES calibration can be performed by calculating the average of the jet response distribution in bins of p_T and η. An illustration of jet energy response distribution is shown in Figure 5.1. Here, in general, the width of the jet response distribution is known as the Jet Energy Resolution (JER). The stochastic nature of shower processes, the electronic noise, and the PU factors can cause the deviations in the jet response. As can be seen from Equation 3.8, the stochastic term is proportional to $1/\sqrt{E}$ and the electronic noise term is proportional to $1/E$. Thus, when the jet energy increased the JER becomes less significant.

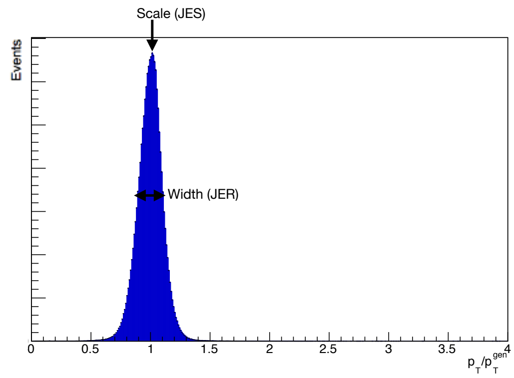

Figure 5.1. An illustration of the jet energy response distribution. JES is the average response and the width of the distribution indicates the JER. Reproduced from Reference (Kirschenmann, 2014).

In order to understand all the factors involved in the jet-energy calibration, it has been proposed to use a factorized approach on several steps. The detailed description of this approach is presented in (CMS Collaboration, 2011a; Esen et al., 2007). In this approach, we apply sequentially a correction factor, C, to each component of the raw jet four-momentum vector p_μ^{raw}. We then obtain the corrected jet four-momentum vector p_μ^{cor} (CMS Collaboration, 2011a):

$$p_\mu^{cor} = C \cdot p_\mu^{raw} \tag{5.1.}$$

The correction factor consists of the offset correction C_{offset}, the MC calibration factor C_{MC}, the relative residual energy scale correction C_{rel} and absolute energy scale correction C_{abs}. The different steps of the jet-energy calibration in CMS are depicted in Figure 5.2. The offset correction corrects jets for the extra energy due to noise and PU, the MC correction minimizes the effect of non-uniformity in η and the non-linearity in p_T, and the residual correction corrects for differences between data and simulation as shown in Equation 5.2:

$$C = C_{offset}(p_T^{raw}) \cdot C_{MC}(p_T', \eta) \cdot C_{rel}(\eta) \cdot C_{abs}(p_T'') \tag{5.2.}$$

where p'_T represents the jet p_T after applying the offset correction and p''_T is the jet p_T after the offset, MC, and relative corrections. In this thesis, we mostly are interested in the MC truth and L2 relative residual corrections. Each component of the jet energy calibration will be discussed separately in the following sections (CMS Collaboration, 2011a).

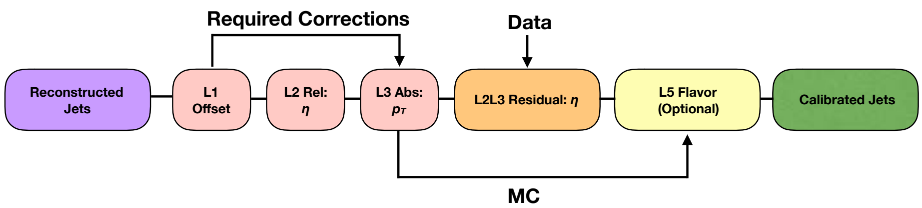

Figure 5.2. Illustration of factorized approach to jet-energy corrections where L represents for level and the numbers show the location in the scheme. Reproduced from Reference (Perloff, 2012).

5.2. L1 Offset Correction

There are different sources of noise that contaminate the signal of an event in CMS such as electronic noise, underlying events, and PU. The Level 1 offset correction is the first level in the correction chain and aims to estimate and to get rid of the contributions from the energy that is not associated with hard events, in other words, to reduce the additional offset in jet energy coming from electronic noise and PU. The first source of PU is that the PU interactions that coming from collisions occurring within the same bunch-crossing, it produces additional tracks in the tracker and deposits extra energy in the calorimeters. This source is called in-time pileup (IT PU). The second one is that the PU interactions coming from collisions in the previous or next bunch-crossing, this also produces additional deposit energy in the calorimeters. This source is called out-of-time pileup (OOT PU). The offset correction helps to eliminate both contributions from the jet momentum. The amount of IT PU from charged particles can be reduced by determining and removing the charged PF candidates originate from PU vertices, as illustrated in Figure 5.3 (CHS method, see Section 4.2.3.). The large amount of OOT PU can be reduced by using the hybrid jet area method. This method uses the average energy density multiplied by the jet active area in the event and then this is subtracted from the jet energy to calculate the offset energy (CMS Collaboration, 2017b).

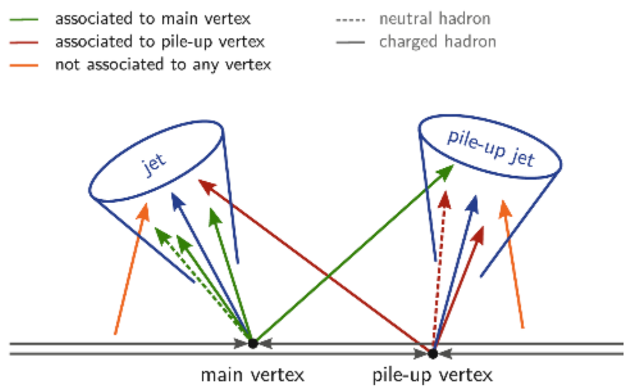

Figure 5.3. Illustration of a simulated event containing a PU jet and a hard-scatter jet (Berger, 2014).

5.3. L2L3: Monte Carlo Based Corrections

There are many benefits to derive a large part of the JEC from the simulation. Firstly, the available phase space is not limited to the availability of data and so initial corrections can be obtained without any collision data. Later, the data-driven approaches have many of the biases due to energy resolution, we can avoid those biases by using the simulation-driven approaches (Rabbertz, 2017). The simulation based response corrections are derived after applying the L1 offset step, and it corrects the energy of the reconstructed jet averagely equal to the energy of the generated particle jet. This correction is evaluated by using the simulated QCD jet events, generated with PYTHIA8 and we can define the jet response in these events as;

$$\mathcal{R}_{ptcl}(\langle p_T\rangle,\eta) = \frac{\langle p_T\rangle}{\langle p_T^{ptcl}\rangle}[p_T^{ptcl},\eta] \tag{5.3.}$$

where $\mathcal{R}_{ptcl}$ is the simulated particle response which is the ratio of arithmetic means of the p_T of matched reconstructed and the p_T of particle-level jets. The binning variables are represented as the square brackets [p_T^{ptcl}, η]; where p_T^{ptcl} is showing bin of the particle level jet p_T, η is for the reconstructed pseudorapidity. The angle brackets ⟨ ⟩ denote the average of the variables within the binning (CMS Collaboration, 2017b).

The MC based corrections include two types of corrections: Level 2 (L2) relative and Level 3 (L3) absolute. The goal of the L2 relative and L3 absolute corrections is to eliminate the dependency of the jet response on the jet η and jet p_T, respectively. The jet response corrected by the L2L3 factor is;

$$\mathcal{R}_{L2L3} = \frac{p_T^{L2L3}}{p_T^{ptcl}} \tag{5.4.}$$

where p_T^{L2L3} denotes the p_T of the jet after the L2L3 correction and the jet response should be close to one.

5.4. Residual Corrections

MC-driven response corrections should be complemented with data-driven corrections since the simulation does not have perfect modeling of real detectors. Therefore, we need to minimize the difference between the MC response and the data response. To do this, an analysis method is developed to reconstruct the response of jets and is applied to data/MC in the same way to evaluate differences.

The residual corrections for data are performed in two steps because of statistical and systematic precision (Rabbertz, 2017).

5.4.1. L2 Relative Residual Corrections in η

In the first step, most of the non-uniformity of the detector response in η is removed by the relative residual correction. Since the objects are better reconstructed, the variation of jets' response is small and the detector is uniform, the response in the barrel region ($|\eta|$ <1.3) is taken as a reference. To evaluate these corrections, events composed of the two leading jets, called dijet events, in the final state are used. An illustration of the dijet event topology in the transverse plane is shown in Figure 5.4. One of the jets should be in the barrel region and called a tag (barrel) jet. The other jet is at any η, called a probe jet. The bias caused in the dijet events by the reference object which has poor energy resolution is minimized by binning in average jet $p_T, p_T^{ave} = \bar{p}_T = 0.5 \cdot (p_T^{tag} + p_T^{probe})$, instead of p_T^{tag}. Choosing this p_T binning also helps to suppress events with first order hard radiation (ISR+FSR). This radiation can cause an imbalance in p_T between the reconstructed leading two jets.

Two methods were developed to evaluate p_T imbalances: the p_T-balance and the missing transverse momentum projection fraction (MPF) method (CMS Collaboration, 2011a; CMS Collaboration, 2009e).

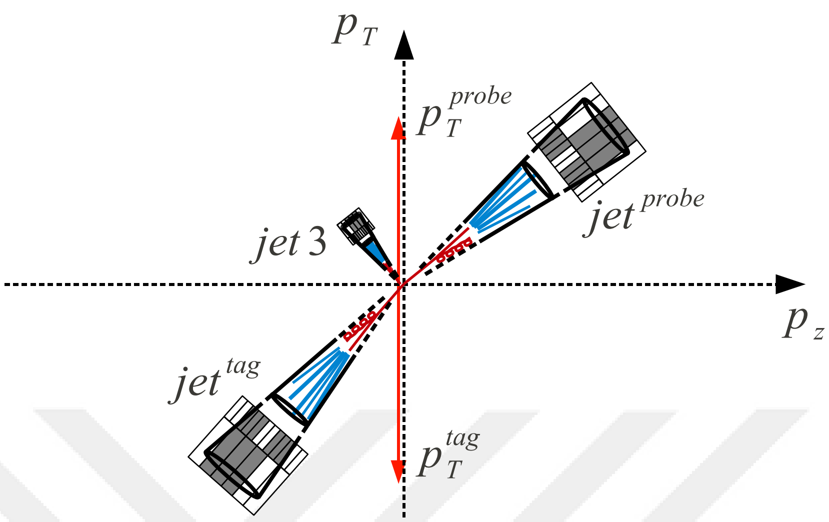

Figure 5.4. Illustration of a dijet event topology in the transverse plane. The two leading jets are back-to-back, while the ideal dijet topology is compromised by additional jets (Karavdina et al., 2016).

5.4.1.1. p_T-Balance Method

The p_T-balance method was developed at the $\mathrm{p\bar{p}}$ collider ($\mathrm{S\bar{P}\bar{P}S}$, CERN) (UA2 Collaboration, 1983), then improved through the D0-CDF experiments at Tevatron (D0 Collaboration, 1999; CDF Collaboration, 2006) and also used for the jet energy calibration in CMS (CMS Collaboration, 2011a). The p_T-balance method is based on the principle of p_T conservation: in an ideal dijet event case is composed of two jets back-to-back in the azimuthal angle ϕ with $\Delta\phi > 2.7$ and the p_T of two jets is equal. However, the p_T of jets is not balanced at the calorimeter level due to the non-uniformity of the detector response in η. As we explained in the previous section, one jet is required to be in the barrel region as a reference and the other jet is at arbitrary η for the calculation of the relative jet response (CMS Collaboration, 2011a).

The asymmetry variable, $\mathcal{A}$, is defined as follows for the events with at least two leading jets;

$$\mathcal{A} = \frac{p_T^{probe} - p_T^{barrel}}{p_T^{probe} + p_T^{barrel}} \tag{5.5.}$$

where p_T^{probe} and p_T^{barrel} denote the probe and barrel jet p_T, respectively. The variance of the asymmetry variable can be defined as;

$$\sigma_{\mathcal{A}}^2 = \left|\frac{\partial \mathcal{A}}{\partial p_T^{probe}}\right|^2 \cdot \sigma^2\left(p_T^{probe}\right) + \left|\frac{\partial \mathcal{A}}{\partial p_T^{barrel}}\right|^2 \cdot \sigma^2\left(p_T^{barrel}\right) \tag{5.6.}$$

If both jets are in the same η region, $p_T \equiv \langle p_T^{probe} \rangle = \langle p_T^{barrel} \rangle$ and respective uncertainties $\sigma(p_T) \equiv \sigma\left(p_T^{probe}\right) = \sigma\left(p_T^{barrel}\right)$ are equal. If we substitute these last expressions into Equation 5.6, we can calculate the fractional resolution of the jet p_T as follows:

$$\frac{(p_T)}{\langle p_T \rangle} = \sqrt{2}\sigma_{\mathcal{A}} \tag{5.7.}$$

The relative response, $\mathcal{R}_{rel}$, of the probe jet according to the barrel jet is determined by using the average value of the asymmetry, $\langle \mathcal{A} \rangle$, for all events;

$$\mathcal{R}_{rel}\left(\eta^{probe}, \bar{p}_T\right) = \frac{1 + \langle \mathcal{A} \rangle}{1 - \langle \mathcal{A} \rangle} \tag{5.8.}$$

If a proper fine binning is used in $\bar{p}_T$, Equation 5.8 reduces to

$$\mathcal{R}_{rel}\left(\eta^{probe}, \bar{p}_T\right) = \frac{p_T^{probe}}{p_T^{barrel}} \tag{5.9.}$$

and the resolution of jet p_T is minimized for a single event. Since the presence of ISR or FSR can violate the balance of the dijet topology, the relative response is also sensitive to these radiations. It is possible to correct this bias related to ISR and FSR by applying a correction factor as described in Section 7.2.1.

5.4.1.2. Missing Transverse Momentum Projection Fraction Method

The missing transverse momentum projection fraction method (MPF) was used by the experiments at the Tevatron (D0 Collaboration, 1999) and also used for the jet energy calibration in CMS during RunI (CMS Collaboration, 2011a) and RunII (Stöver and CMS Collaboration, 2017; CMS Collaboration, 2020a) period. The MPF method is based on the idea that dijet events as shown in Figure 5.5 have no real missing transverse energy at the particle level. Thus, the tag jet p_T should be perfectly balanced by the hadronic recoil in the transverse plane;

$$\vec{p}_{T,true}^{\,barrel} + \vec{p}_{T,true}^{\,recoil} = 0 \tag{5.10.}$$

where $\vec{p}_T^{\,recoil}$ is the vectorial sum of the momentum of the total hadronic activity which comprises the events that are not represented by reconstructed particles. The hadronic recoil includes probe jet but may not be the whole of it (Esen et al., 2007).

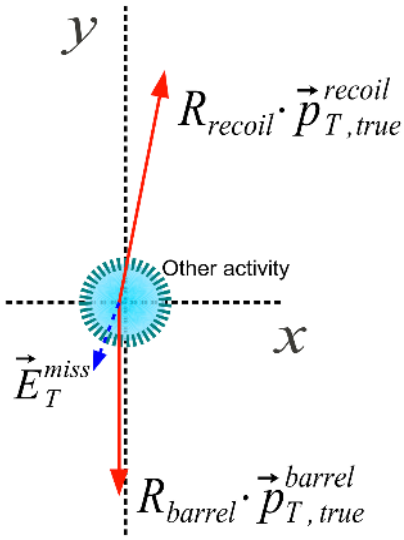

Figure 5.5. Sketch of the $\vec{E}_T$ Projection Fraction (MPF) method showing the barrel jet and recoiling hadronic activity (Kirschenmann et al., 2011).

The response of the barrel jet ($\mathcal{R}_{barrel}$) and the hadronic recoil ($\mathcal{R}_{recoil}$) might be different at the detector level and this can cause the p_T imbalance. We can now write down Equation 5.10 as;

$$\mathcal{R}_{barrel} \cdot \vec{p}_{T,true}^{\,barrel} + \mathcal{R}_{recoil} \cdot \vec{p}_{T,true}^{\,recoil} = -\vec{E}_T \tag{5.11.}$$

It is possible to write the $\mathcal{R}_{recoil}$ down from Equations 5.10-5.11 as follows (Kirschenmann et al., 2011);

$$\mathcal{R}_{recoil} = \mathcal{R}_{barrel} + \frac{\vec{E}_T \cdot \vec{p}_{T,true}^{\,barrel}}{(\vec{p}_{T,true}^{\,barrel})^2} \tag{5.12.}$$

Since the variation of the jet response in the barrel region is very small we can assume $\mathcal{R}_{barrel} = 1$, $\vec{p}_{T,true}^{\,barrel} = \vec{p}_T^{\,barrel}$ and write down the Equation 5.12 as;

$$\mathcal{R}_{recoil} = 1 + \frac{\vec{E}_T \cdot \vec{p}_T^{barrel}}{(\vec{p}_T^{barrel})^2} \equiv \mathcal{R}_{MPF} \quad (5.13.)$$

which shows the MPF response variable. The MPF response is an evolution of the p_T-balance and more reliable since it evaluates the total hadronic recoil activity and very low sensitivity to additional ISR or FSR. The MPF method is used to produce the official jet energy corrections. The p_T-balance method can be used to check the compatibility of the corrections obtained.

5.4.2. L3 Absolute Residual Corrections in p_T

In the Level 3 absolute residual correction, the response of the detectors is measured as a function of p_T and removes the variation of jet response that results from the non-linear calorimeter response. We have already discussed this correction derived from MC truth in Section 5.3. The data-driven techniques are used in $\gamma + \text{jet}$, $Z \rightarrow e^+e^- + \text{jet}$, and $Z \rightarrow \mu^+\mu^- + \text{jet}$ event topologies to evaluate the absolute residual correction. As the energy of γ, Z are measured with great precision in the ECAL, the p_T of the γ and Z are used as reference objects to calibrate the jet. The jet should be in the barrel region and back-to-back to the reference object. Both methods (p_T-balance and MPF) used during the determination of the L2 relative residual correction are also used for the L3 residual correction. Thus, we can rewrite Equations 5.9 and 5.12 for the responses of the p_T-balance and MPF methods, respectively, as follows;

$$\mathcal{R}_{balance} = \frac{p_T^{jet}}{p_T^{\gamma,Z}} \quad (5.14.)$$

$$\mathcal{R}_{recoil} = \mathcal{R}_{\gamma,Z} + \frac{\vec{E}_T \cdot \vec{p}_T^{\gamma,Z}}{\left(\vec{p}_T^{\gamma,Z}\right)^2} \equiv \mathcal{R}_{MPF} \quad (5.15.)$$

where $\mathcal{R}_{\gamma,Z}$ denote the detector response to the photon or Z-boson (CMS Collaboration, 2011a).

5.5. Optional Corrections

There are a few more planned steps that can be used optionally in the factorized approach of JEC:

- Level 4 EMF correction corrects the variation of jets' response with the electromagnetic energy fraction (EMF). The L4 EMF correction describes the response of the detector as a linear combination of the response for electromagnetic, hadronic, and invisible particle types (Esen and Landsberg, 2009).
- Level 5 Flavor correction corrects the jet to the particle level considering that the jet originates from a single parton flavor (light quark, c, b, gluon) (Cammin, 2009; Naumann-Emme et al., 2010).
- Level 6 Underlying Event correction is meant to remove the luminosity independent underlying events, which are not coming from the hard process, from the jet (Esen et al., 2007).
- Level 7 Parton correction corrects the particle level jet back to parton level after the previous corrections.

6. DETERMINATION of RELATIVE and ABSOLUTE MC TRUTH JET ENERGY CORRECTIONS

The jet energy recorded at the detector level and the energy calculated at the generator level are different. This variance mostly varies depending on the response of the detector and the technique used in clustering the jets. It is therefore important to make corrections to calculated jet energy in order to estimate the jet energies at the generator level. As discussed in Chapter 5, the jet energy correction scheme is factorized in CMS and each factor is corrected for a different source. The following chapter is denoted the event selection that is employed in the determination of relative and absolute L2L3 MC truth jet energy corrections.

6.1. Dataset and Event Selection

MC is the primary source of knowledge about the JES until data is collected and the behavior of the detector is well understood. The data-based techniques can then be the source when data is started to be collected. Through this period, the MC truth, that is, processing particle jets information before it reaches the detectors play a significant role in determining early corrections and the biases of data-based techniques (Harris and Kousouris, 2008).

In this study, an analysis package is developed to run the MINIAODSIM sample. L1FastJet jet energy correction was not considered because the MC sample used in this analysis has produced without PU which is listed in Table 6.1. The MC was reconstructed by using CMSSW_7_6_3 with the global tag 76X_mcRun2_asymptotic_RunIIFall15DR76_v1.

Table 6.1. MC set name with cross section information used in the analysis.

MC sample	Cross section σ (pb)	Raw Events
/QCD_Pt-15to7000_TuneCUETP8M1_Flat_13TeV_pythia8/RunIIFall15MiniAODv2-25nsNoPURaw_magnetOn_76X_mcRun2_asymptotic_v12-v1/MINIAODSIM	20221×10^{5}	9960448

The MC events are used to determine the jet response measurements based on the MC truth information. The events are requested to contain one well-reconstructed primary vertex with at least four tracks, and with the *z*-component of the primary vertex to be less than 24 cm ($|z(\mathrm{PV})| < 24$ cm) to ensure that selected events are not coming from PU interactions. The generated and reconstructed jets are required to match in (η, ϕ) space by a criterion of $\Delta R < 0.2$;

$$\sqrt{(\eta^{jet} - \eta^{ref})^2 + (\phi^{jet} - \phi^{ref})^2} < \Delta R_{max} = 0.2 \qquad (6.1.)$$

where the generated jets are used as the reference jets ($p_T^{gen} = p_T^{ref}$). The PF jets with CHS which reconstructed with the anti-k_T jet clustering algorithm with the cone size parameter of $R = 0.4$ are studied in this study. The jets are asked to have a p_T above 10 GeV.

6.2. Determination of the L2L3 MC Truth Correction

The distribution of the reconstructed jet p_T^{reco} and the response are analyzed in fine bins of jet η and p_T^{ref} for the matched jets. The fine η and p_T^{ref} bins which are used in this study are shown in Table 6.2. The correction factor can then be calculated as the inverse of the mean response as a function of p_T^{reco} in each fine η and p_T^{ref} bins as follows;

$$R(\langle p_T^{reco}\rangle, \eta) = \frac{\langle p_T^{reco}\rangle}{\langle p_T^{ref}\rangle}\left[p_T^{ref}, \eta\right] \quad (6.2.)$$

Table 6.2. Bins of the η and p_T used in the analysis.

$\lvert\eta\rvert$	0, 0.087, 0.174, 0.261, 0.348, 0.435, 0.522, 0.609, 0.696, 0.783, 0.879, 0.957, 1.044, 1.131, 1.218, 1.305, 1.392, 1.479, 1.566, 1.653, 1.74, 1.83, 1.93, 2.043, 2.172, 2.322, 2.5, 2.65, 2.853, 2.964, 3.139, 3.314, 3.489, 3.664, 3.839, 4.013, 4.191, 4.363, 4.4538, 4.716, 4.889, 5.191
p_T (GeV)	10, 15, 21, 28, 37, 49, 64, 84, 114, 153, 196, 245, 300, 362, 430, 507, 592, 686, 790, 905

The official framework (Perloff and Eusebi, 2013) provided by the JetMET group has been combined the factorized L2Relative and L3Absolute corrections and produced in a single step, so-called combined L2L3 correction. Nevertheless, in this analysis, the L3 absolute correction is produced separately to make cross-checks. While deriving the L3 jet energy correction, the central region of the calorimeter ($|\eta| < 1.3$) was used as the reference region. It aims to obtain a factor that corrects the mean calorimeter jet p_T back to the particle level p_T^{ref} in the control region, $|\eta| < 1.3$.

The L3 correction in p_T can be determined by the following strategy:

- Selection of a p_T in the barrel region,
- The response, $p_T^{reco} = R(p_T^{ref}) \cdot p_T^{ref}$, is measured for the matched jets.
- L3 correction is calculated as the inverse of the response in the same p_T^{ref} bin, $\frac{1}{R(p_T^{ref})}$. The response and L3 correction are fitted by smooth functions.

Figure 6.1 shows the distributions of jet response in $|\eta| < 1.3$ with four different p_T regions.

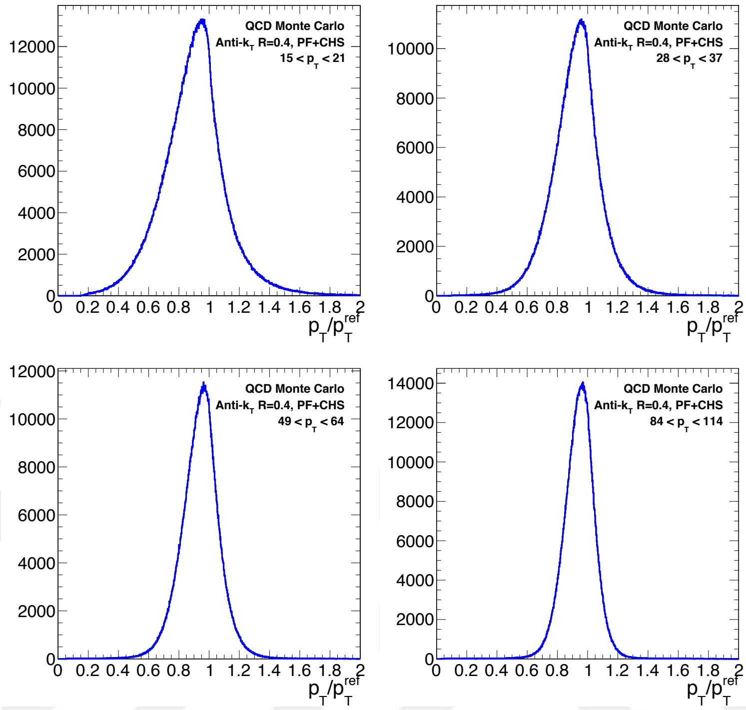

Figure 6.1. AK4 PFCHS jet energy response distributions in the control region $|\eta| < 1.3$ and $15 < p_T^{ref} < 21$ GeV (upper left), $28 < p_T^{ref} < 37$ GeV (upper right), $49 < p_T^{ref} < 64$ GeV (bottom left) and $84 < p_T^{ref} < 114$ GeV (bottom right).

Figure 6.2 left shows the L3Absolute correction as a function of jet p_T and Figure 6.2 right represents the jet response as a function of p_T^{ref}. The jet response and L3 correction distributions are fitted with the smooth functions shown in Equation 6.3 and 6.4, respectively;

$$R\left(\langle p_T^{ref} \rangle\right) = b_0 - \frac{b_1}{\left[\log\left(\langle p_T^{ref} \rangle\right)\right]^{b_2} + b_3} + \frac{b_4}{\langle p_T^{ref} \rangle} \tag{6.3.}$$

$$C(\langle p_T \rangle) = c_0 + \frac{c_1}{[\log(\langle p_T \rangle)]^{c_2} + c_3} - \frac{c_4}{\langle p_T \rangle} \tag{6.4.}$$

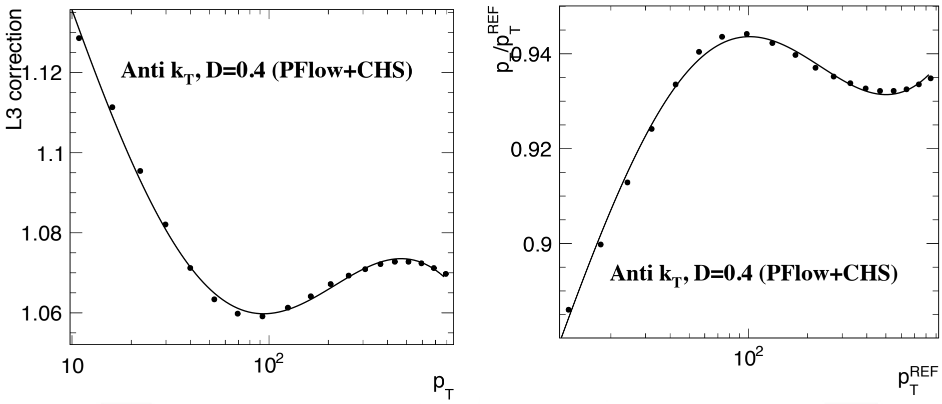

Figure 6.2. Left: The L3 absolute correction in the control region as a function of jet p_T for the AK4 PFCHS jets. Right: The jet response in the control region $|\eta| < 1.3$ as a function of p_T^{ref} for the AK4 PFCHS jets. The points come from the relevant response measurement by using the mean values and the curve is the smooth fit.

As mentioned before, the JERC group has started to use combined L2L3 MC truth correction instead of the factorized L2 Relative and L3 Absolute jet corrections. While deriving the combined L2L3 correction, at least 100 entries are required in jet energy response distributions. Figure 6.3 shows the distributions of jet response in three different detector regions for three different p_T bins. The jet responses obtained for the jets with very low p_T are shown in the left part of Figure 6.3 As the p_T^{ref} value grows, these distributions are becoming narrower and more comparable to Gaussian distributions. Then, these distributions can be fitted with a Gaussian function. The distributions for the very low p_T do not show a narrow Gaussian distribution as it is expected. Because of this reason, the mean of fit or arithmetic mean of the distributions didn't use in the analysis. Instead of this, the median is used as the histogram metric. The median of the distributions is calculated as follows;

$$Med = L_m + \left[\frac{\frac{N}{2} - F_{m-1}}{f_m}\right] \cdot c \qquad (6.5.)$$

where L_m represents the lower limit of the median bin, N represents the total number of entries, F_{m-1} represents the total number of entries in all bins below the median bin, f_m is the total number of entries of the median bin, c is the width of median bin. The standard error on the median is evaluated as follows;

$$\sigma_{median} = 1.253 \cdot \frac{\sigma}{\sqrt{N}} \quad (6.6.)$$

where σ is the standard deviation of the gaussian distribution and N represents the total number of entries.

The next step is that the absolute jet response and correction distributions created as a function of p_T^{ref} for each η bin. Then, the absolute correction distribution is fitted by spline5 function, [$p_0 + ((p_T - p_1).(p_2 + ((p_T - p_1).(p_3 + ((p_T - p_1).(p_4 + ((p_T - p_1).(p_5 + ((p_T - p_1).p_6)))))))))$], in each η bin. Figure 6.4 shows the distributions of absolute jet response and correction in $0.087 < \eta < 0.174$, $1.74 < \eta < 1.83$, and $4.013 < \eta < 4.191$.

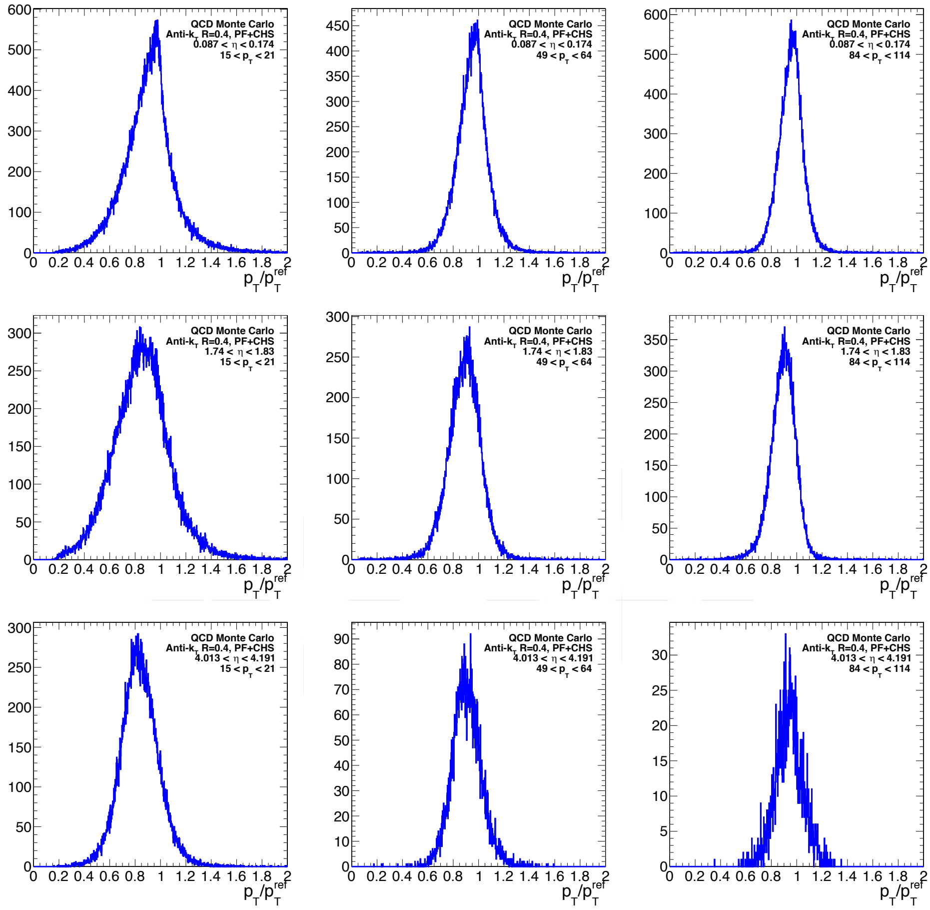

Figure 6.3. AK4 PFCHS jet energy response distributions in $0.087 < \eta < 0.174$ (top), $1.74 < \eta < 1.83$ (middle), and $4.013 < \eta < 4.191$ (bottom) for three p_T^{ref} bins ($15 < p_T^{ref} < 21$ GeV (left), $49 < p_T^{ref} < 64$ GeV (middle), and $84 < p_T^{ref} < 114$ GeV (right)).

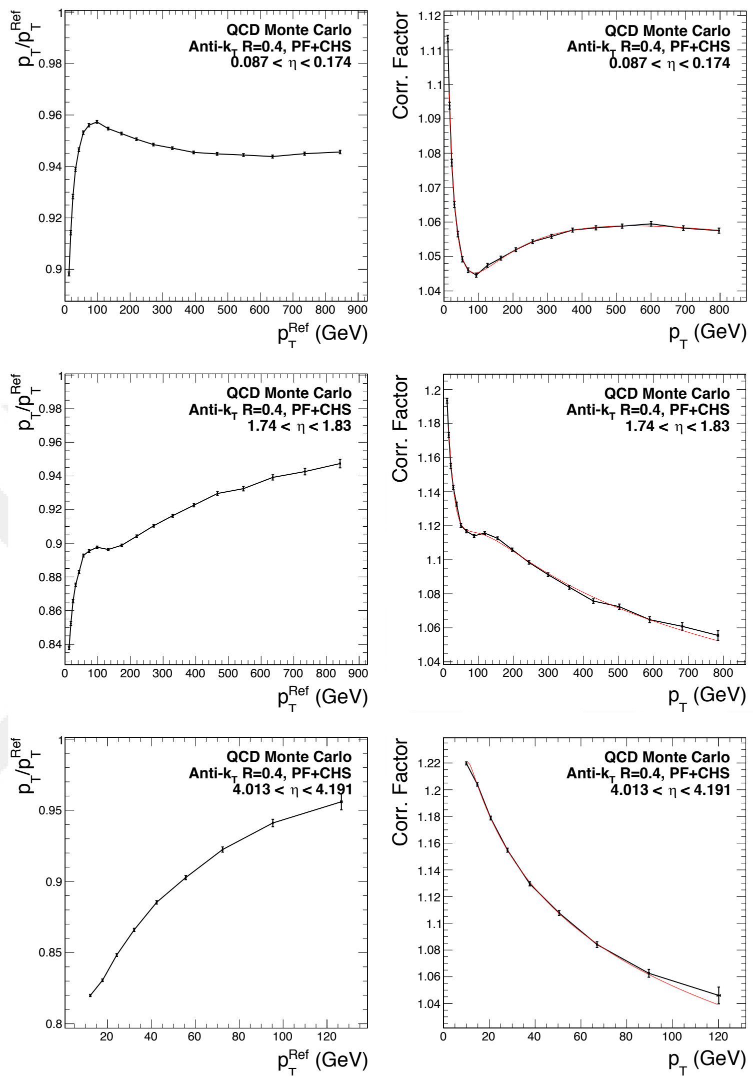

Figure 6.4. Left: Absolute response as a function of p_T^{ref} in $0.087 < \eta < 0.174$ (upper), $1.74 < \eta < 1.83$ (middle), and $4.013 < \eta < 4.191$ (bottom) for AK4 PFCHS jets. Right: Absolute correction as a function of jet p_T in $0.087 < \eta < 0.174$ (upper), $1.74 < \eta < 1.83$ (middle), and $4.013 < \eta < 4.191$ (bottom) for AK4 PFCHS jets.

In Figures 6.5 and 6.6 we examine the behavior of MC truth corrections as a function of p_T^{reco} for all η bins. It is observed that the corrections behave smooth, in a similar way for positive and negative η bins. In Figure 6.7, we examine the behavior of corrections as a function of η for various p_T^{reco} values. It can be seen that the corrections are symmetric between positive and negative η bins.

The produced L2L3 correction differs continuously per p_T bin in a given η bin but it differs discontinuously from one η bin to another. Therefore, a spline interpolation is performed between the correction factor provided by the particular bin a jet belongs to and the factors provided by the two neighboring bins during the implementation of the correction.

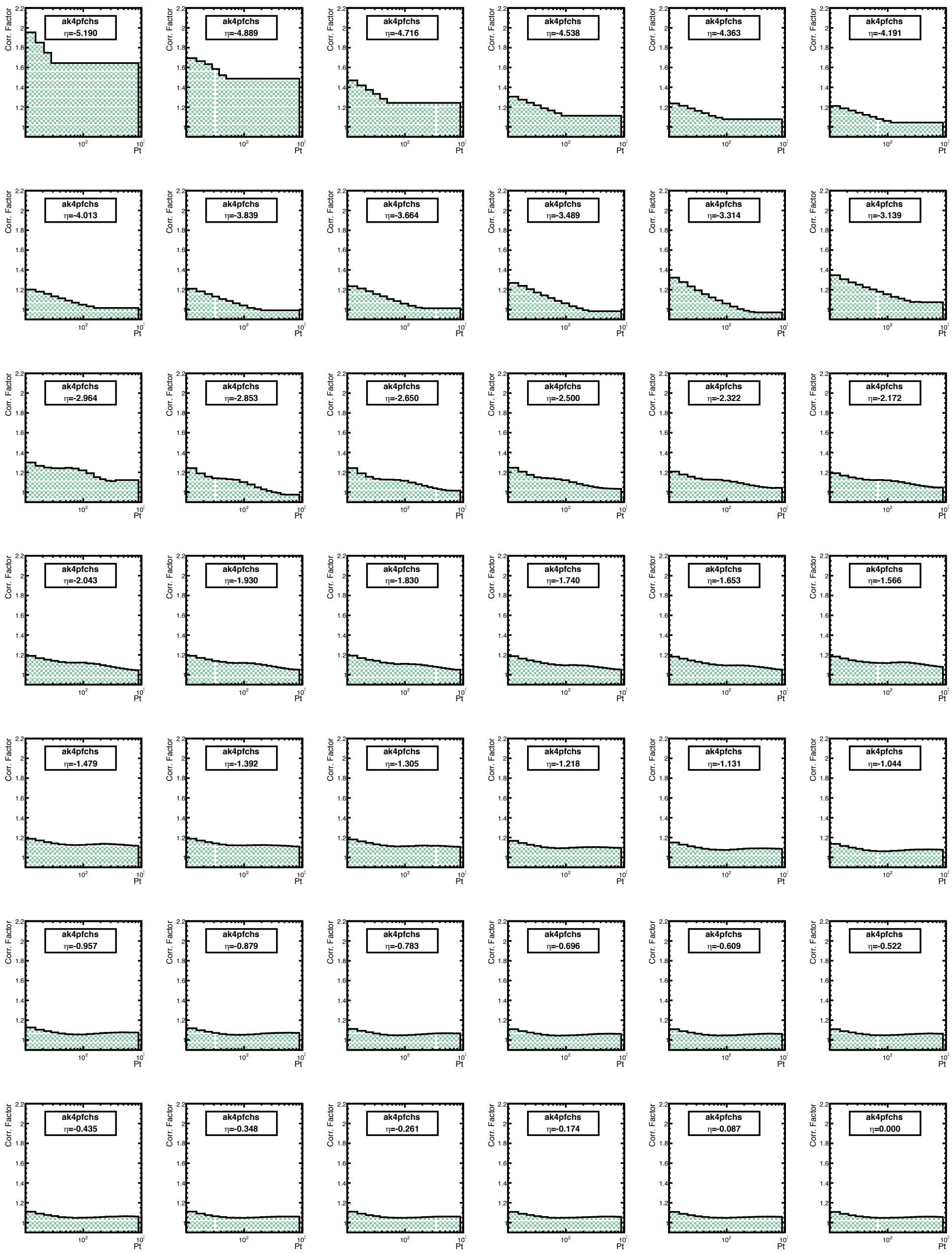

Figure 6.5. The behavior of L2L3 MC truth corrections as a function of p_T^{reco} for fine η bins, from –5.19 to 0.

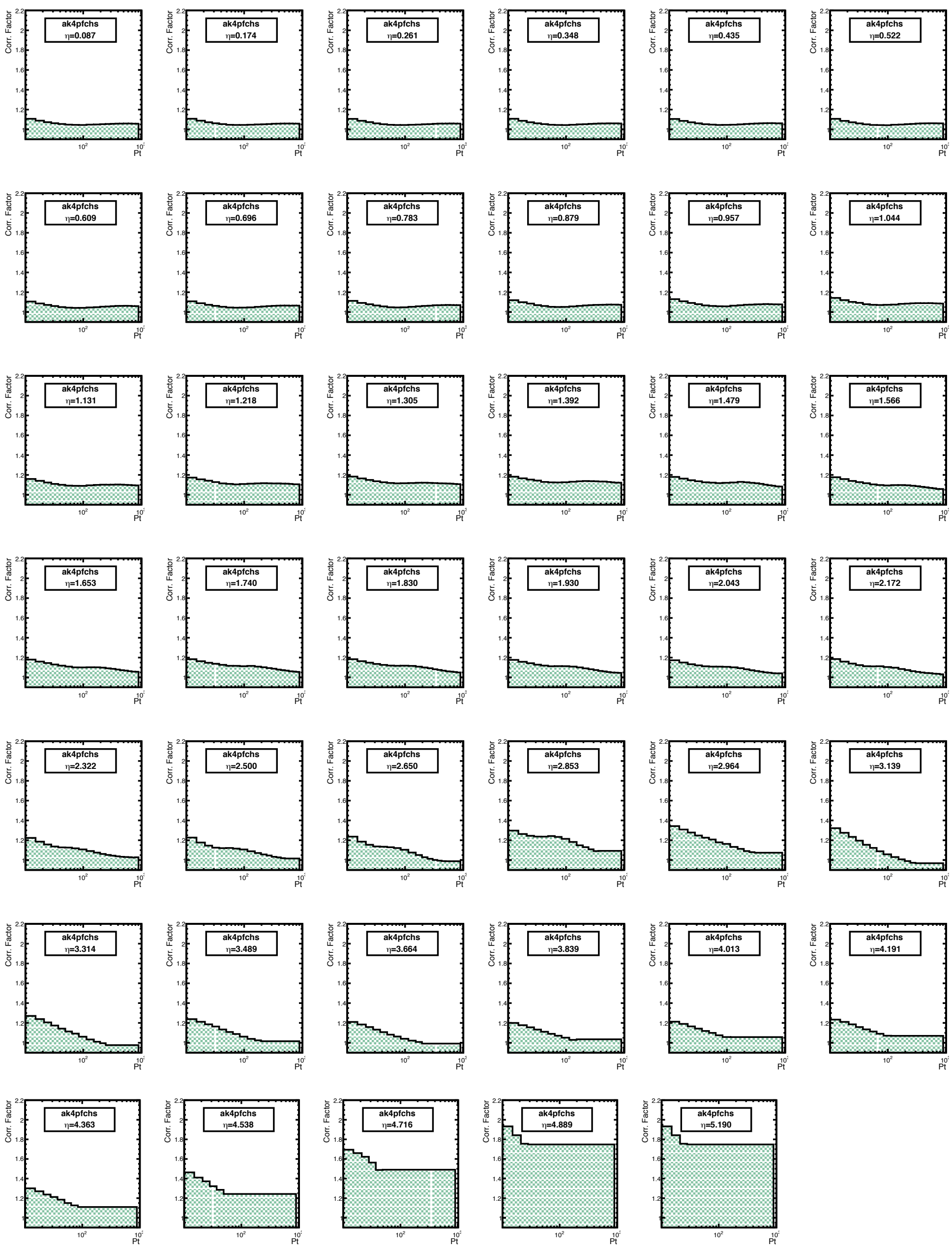

Figure 6.6. The behavior of L2L3 MC truth corrections as a function of p_T^{reco} for fine η bins, from 0.087 to 5.19.

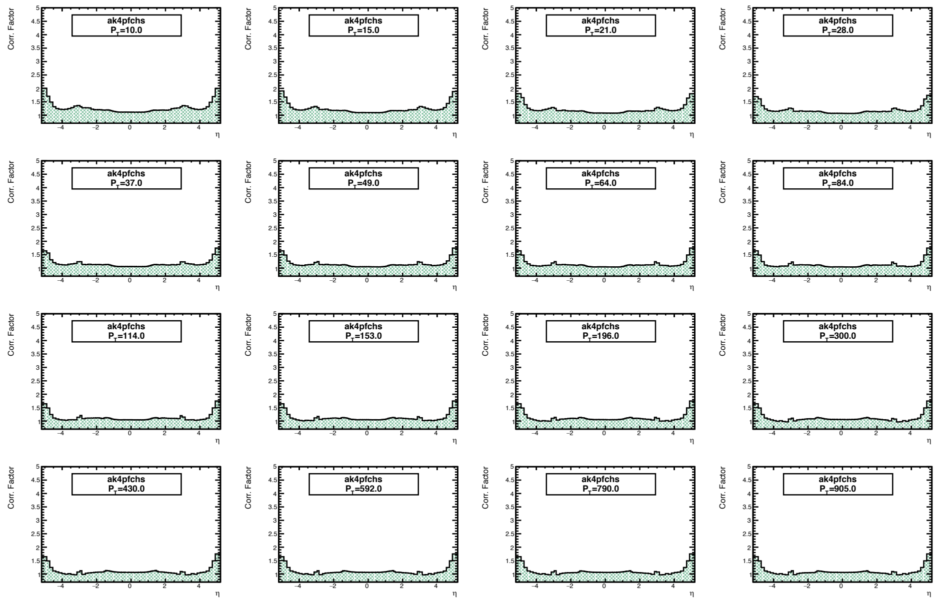

Figure 6.7. The behavior of L2L3 MC truth corrections as a function of η for various p_T^{reco} values.

Figure 6.8 presents the simulated jet response as a function of the reconstructed jet η for anti-k_T PFCHS jets with a distance parameter R = 0.4 for jet p_T's from 15 GeV up to 400 GeV. More than 80% of the original p_T are retained in $|\eta|$ < 3.0 region with jet p_T less than 400 GeV. A much larger portion of jet p_T is lost in $|\eta|$ > 3.0 region with p_T = 15 GeV, up to around 35 percent.

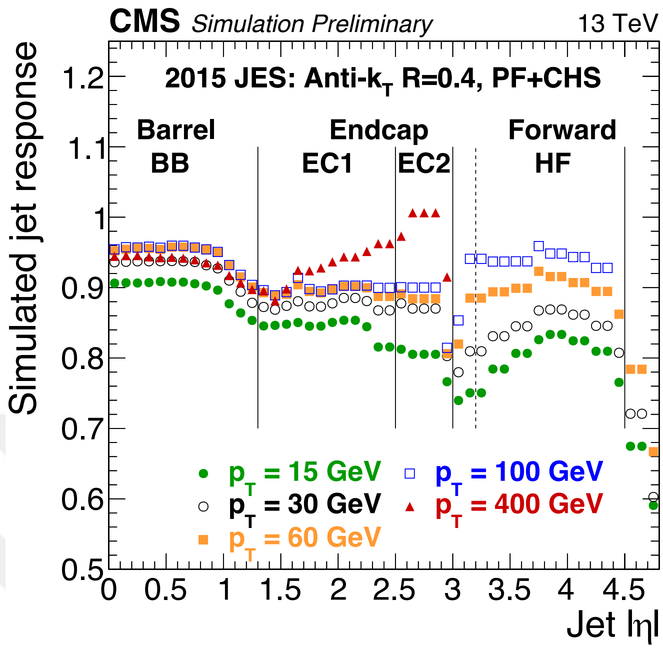

Figure 6.8. The simulated jet response as a function of jet $|\eta|$ for anti-k_T PFCHS jets with the distance parameter of R = 0.4 for jet p_T's from 15 GeV up to 400 GeV. The dotted line presents the transition region between HE and HF in which parts of the incident jets cannot be reconstructed.

The correction factor is a global multiplicative factor as shown in Equation 5.1. Figure 6.9 presents the multiplicative scale factors as a function of η for jets with three different p_T values; 30, 100, and 300 GeV. Correction factors behave very smoothly in the barrel region of the detector. While the correction factors are slightly larger in the transition regions between the subdetectors, they, particularly the jets with the lowest energy, are much larger in the forward region.

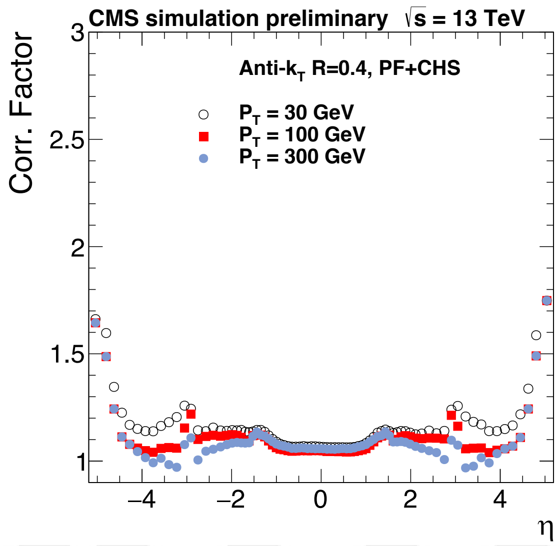

Figure 6.9. The multiplicative scale factors as a function of η for p_T = 30, 100, and 300 GeV.

Figure 6.10 presents the correction factors in the plane of jet η and p_T. In order to show the variability in a given plot as a function of the bin-to-bin distances, a semi-variogram analysis was performed. The variogram is a quantitative descriptive statistic that can be graphically represented in a manner that characterizes the spatial continuity (i.e. roughness) of a dataset. The semi-variogram plot obtained for this analysis is also shown inside Figure 6.10. A typical semi-variogram analysis consists of the experimental semi-variogram obtained from the data and the semi-variogram model fitted to data. An appropriate model, the spherical variogram model used in this analysis, is chosen by matching the shape of the curve of the experimental semi-variogram to the shape of the curve of the mathematical function. The black line with the dots is the experimental semi-variogram for data, while the red line is a fitted variogram function. This method is most helpful to compare different sets of JECs.

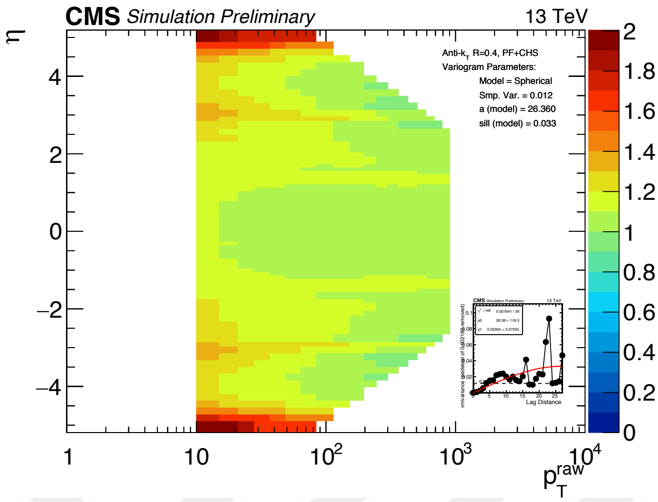

Figure 6.10. The correction factor as a function of η and p_T.

6.3. Closure Test

The term "closure test" refers to numerous tests that aim to verify the validity of the applied corrections. The derived L2L3 MC truth corrections are applied to the same sample and exactly the same jets from which we derived them.

We study the p_T^{reco} corrected with 2015 MC truth corrections over the p_T^{ref}. The simulated jet response after applying the MC truth corrections as a function of η^{reco} for various p_T^{ref} bins is shown in Figure 6.11, Figure 6.12, and Figure 6.13.

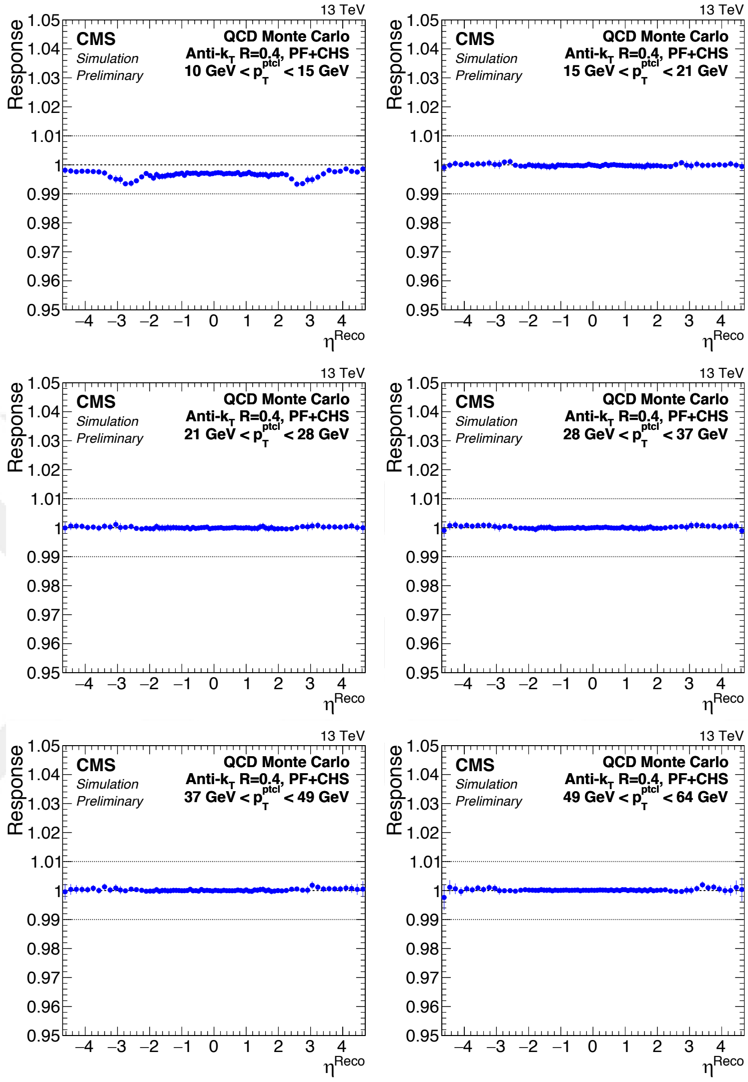

Figure 6.11. The simulated jet response of AK4 PFCHS jets, after L2L3 MC truth JECs have been applied, as a function of η^{reco} for various p_T^{ref} bins from 10 to 64 GeV, using a no PU sample.

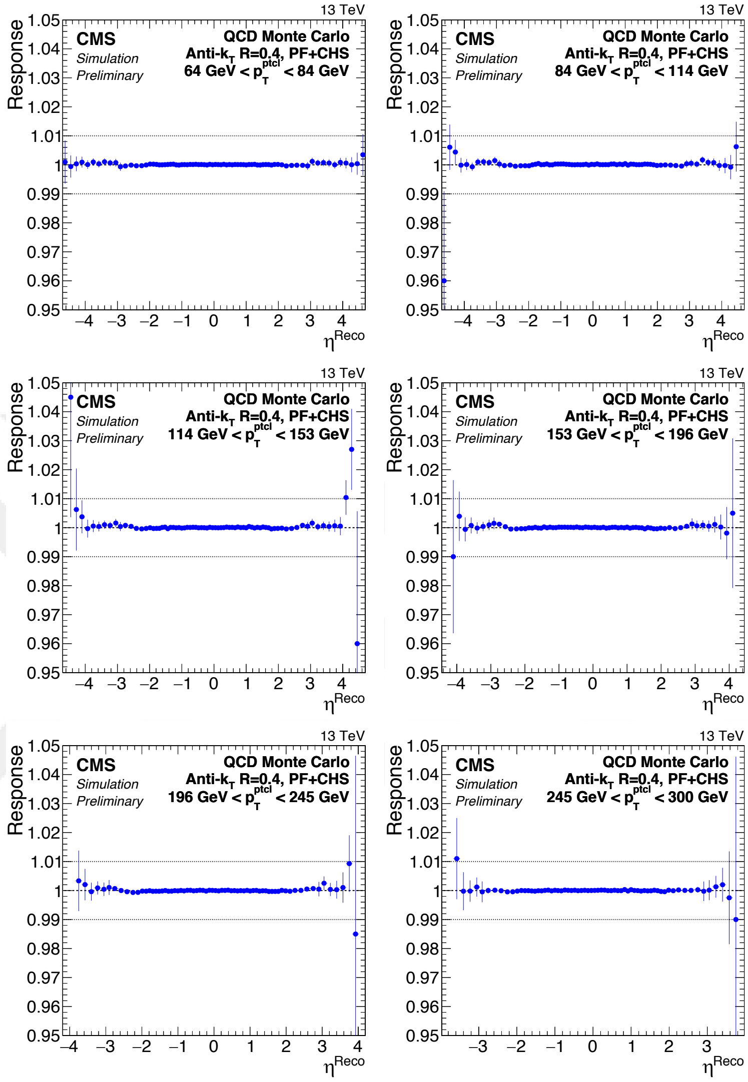

Figure 6.12. The simulated jet response of AK4 PFCHS jets, after L2L3 MC truth JECs have been applied, as a function of η^{reco} for various p_T^{ref} bins from 64 to 300 GeV, using a no PU sample.

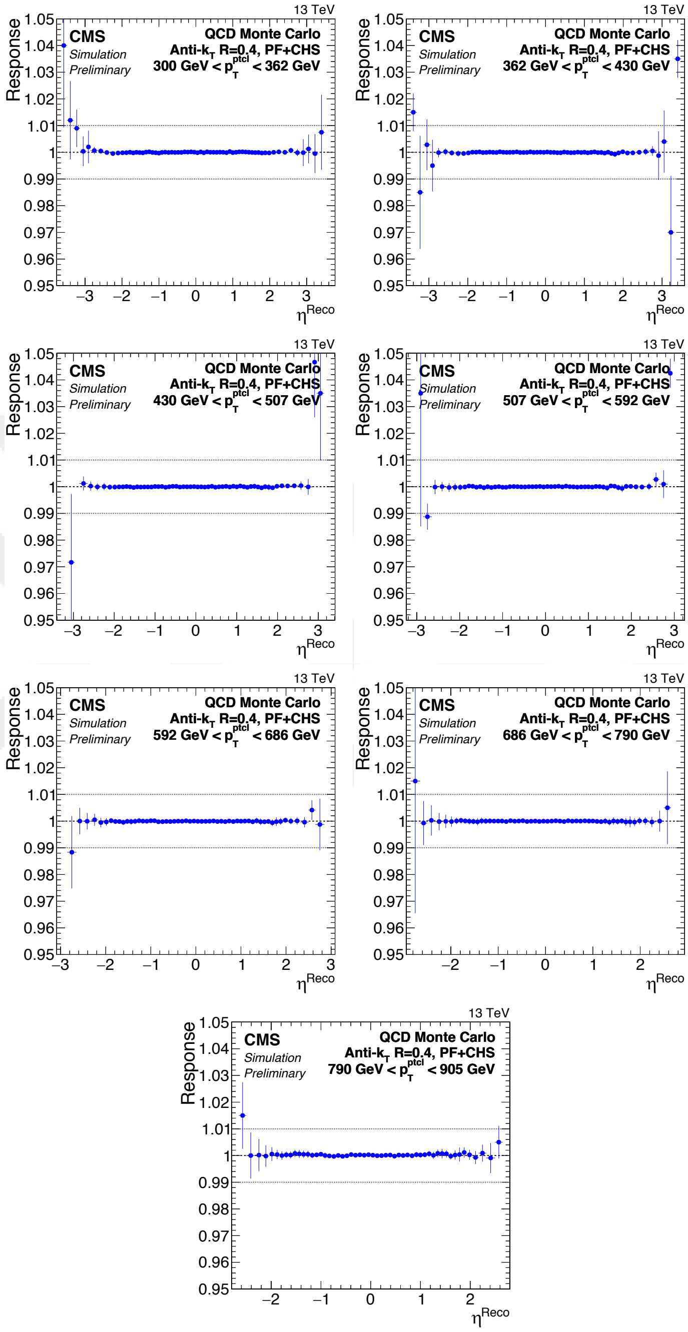

Figure 6.13. The simulated jet response of AK4 PFCHS jets, after L2L3 MC truth JECs have been applied, as a function of η^{reco} for various p_T^{ref} bins from 300 to 905 GeV, using a no PU sample.

Figure 6.14 shows the jet response as a function of the p_T^{ref} after the correction in the four different regions of the detector which defined in Figure 6.8. As can be seen from the distribution, it shows full closure within ±1% for p_T is from 15 GeV up to 400 GeV except some bins in the HE and HF regions because of a lack of statistics. There is non-closure for the jets with p_T < 20 GeV in all regions.

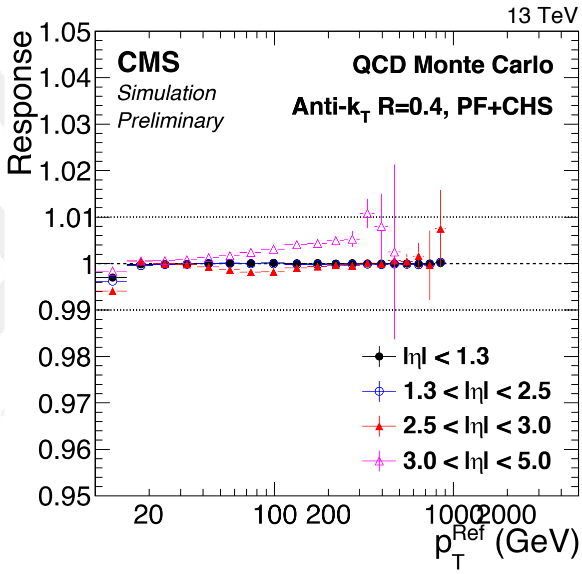

Figure 6.14. The closure test on anti-k_T PFCHS jets with the distance parameter of R = 0.4 as a function of p_T^{ref} in the four regions, using a no PU MC sample. Black dots are for the barrel region, the open blue circle represents the inner endcap region, red full triangle-up is for the outer endcap and the forward region is shown as magenta open triangle-up.

7. DETERMINATION of L2 RELATIVE RESIDUAL JET ENERGY CORRECTIONS with 2015 LOW PILEUP DATA at $\sqrt{s}$ = 13 TeV

The determination of the relative residual jet energy corrections for the 2015 low PU data at 13 TeV is presented in this chapter. The data and MC samples used in the analysis, the trigger efficiency is discussed in the following sections. It is then followed by the criteria of the dijet event selection and the distributions of jet response comparing the data with simulated events.

7.1. Data Samples and Event Selection

7.1.1. Data Samples

The low PU runs which are recorded during the 2015 running period of LHC at the center-of-mass energy of 13 TeV have been used. The dataset corresponds to an integrated luminosity of $\mathcal{L}_{int} = 0.41$ pb^{-1} which calculated using the official CMS brilcalc tool. The data and MC samples used in this analysis are listed in Table 7.1 and Table 7.2, respectively. The data and MC samples were reconstructed by using CMSSW_7_6_3. The certified low PU runs and the luminosity sections recommended by the CMS Physics Validation group are listed in Table 7.3. The JEC correction sets, Fall15_lowPU_V1_DATA.db and Fall15_lowPU_V1_MC.db which includes new 2015 L2L3 MC truth corrections are applied to sample of MC and data, respectively.

Table 7.1.The reprocessed dataset samples for the 2015 low PU runs.

Dataset	**Total Recorded Lumi (pb^{-1})**
/FSQJets1/Run2015D-16Dec2015-v1/MINIAOD	0.410368278
/FSQJets2/Run2015D-16Dec2015-v1/MINIAOD	0.410368278
/FSQJets3/Run2015D-16Dec2015-v1/MINIAOD	0.410368278
/L1MinimumBiasHF1/Run2015D-16Dec2015-v1/MINIAOD	0.40431008
/L1MinimumBiasHF2/Run2015D-16Dec2015-v1/MINIAOD	0.40431008
/L1MinimumBiasHF3/Run2015D-16Dec2015-v1/MINIAOD	0.40431008
/L1MinimumBiasHF4/Run2015D-16Dec2015-v1/MINIAOD	0.40431008
/L1MinimumBiasHF5/Run2015D-16Dec2015-v1/MINIAOD	0.40431008
/L1MinimumBiasHF6/Run2015D-16Dec2015-v1/MINIAOD	0.40431008
/L1MinimumBiasHF7/Run2015D-16Dec2015-v1/MINIAOD	0.40431008
/L1MinimumBiasHF8/Run2015D-16Dec2015-v1/MINIAOD	0.40431008

Table 7.2. The reprocessed MC samples for the 2015.

MC sample	**Cross section σ (pb)**	**Raw Events**
/QCD_Pt-15to7000_TuneCUETP8M1_Flat_13TeV_pythia8/RunIIFall15MiniAODv2-25nsNoPURaw_magnetOn_76X_mcRun2_asymptotic_v12-v1/MINIAODSIM	20221×10^{5}	9960448
/MinBias_TuneCUETP8M1_13TeV_PYTHIA8/RunIIFall15MiniAODv2-noPU_76X_mcRun2_asymptotic_v12-v1/MINIAODSIM	2355×10^{9}	9946888

Table 7.3. The official JSON file name which filters good runs and luminosity sections.

JSON File	**Low PU Runs with Luminosity Sections**
Cert_13TeV_16Dec2015ReReco_ Collisions15_25ns_Totem_JSON_v2.txt	259237: [[1, 270], [273, 309], [312, 576]] 259385: [[1, 514], [517, 539], [541, 545], [548, 549]] 259388: [[1, 185], [188, 339], [342, 447], [450, 455], [458, 726], [729, 747]] 259399: [[127, 279], [282, 511], [514, 526], [529, 589]]

7.1.2. Trigger Efficiency

To calculate the trigger efficiency, /FSQJets1/Run2015D-16Dec2015-v1/AOD dataset is used. The events preselected by DiPFJetAveX_Central, DiPFJetAveX_HFJEC, and L1MinimumBiasHF1OR_partY triggers were used in this analysis, where X stands for energy thresholds 15, 25, 35 GeV, and Y stands for the number of part 0, 1, 2, 3, 4, 5, 6, 7. Each high-level trigger is seeded by a different Level-1 jet trigger; i.e., HLT_DiPFJetAveX triggers are seeded by L1_SingleJet, HLT_L1MinimumBiasHF1OR triggers are seeded by L1_MinimumBiasHF1_OR, more details can be found in Table 7.4. DiPFJetAveX_Central and DiPFJetAveX_HFJEC are the jet calibration triggers which specifically designed to obtain low PU runs and they trigger in p_T^{ave} instead of p_T of a single jet. These triggers are built from hltAk4pfjetCorrected with $p_T >$ 10 GeV and three different p_T^{ave} thresholds (15, 25, 35) are used. For the Central triggers; the tag jet is required to be in $|\eta| < 1.4$ and probe jet is in the $|\eta| < 2.7$. For the HFJEC triggers; the tag jet is required to be in $|\eta| < 1.4$ and probe jet is in the $|\eta| > 2.7$.

Table 7.4. Trigger rates [kHz] of the triggers in different runs used for this analysis.

HLT Path	L1 Seed	Run 259237	Run 259385	Run 259388	Run 259399
DiPFJetAve15_HFJEC	SingleJet8_BptxAND	0.87	0.64	1.08	0.79
DiPFJetAve25_HFJEC	SingleJet12_BptxAND	3.90	1.50	4.82	3.46
DiPFJetAve35_HFJEC	SingleJet16_BptxAND	5.83	1.50	7.19	5.18
DiPFJetAve15_Central	SingleJet8_BptxAND	1.72	1.27	2.10	1.53
DiPFJetAve25_Central	SingleJet12_BptxAND	8.72	3.31	10.72	7.73
DiPFJetAve35_Central	SingleJet16_BptxAND	14.66	3.75	18.05	13.00
L1MinimumBiasHF1OR_partX; X = [0, …, 7]	L1_MinimumBiasHF1_OR	35.72	5.35	42.41	31.08

The determination of trigger efficiency has been performed by using a so-called tag-and-probe method on balanced back-to-back dijet events. In this method, the dijet events produced back-to-back in the transverse plane ($\Delta\phi > 2.7$) have been used and one of the jets is selected as the tag and the other one as the probe jet, such that the selection applied to the probe jet is not biased by the trigger under study. Events are selected from the FSQJets datasets with the DiPFJetAveX trigger paths. It is explicitly required that the tag jet should be in the barrel region ($|\eta| < 1.3$) passing the offline trigger threshold of the emulated trigger and has the jet matched to the HLT jet within a distance of $\Delta R < 0.2$. The probe jet is matched to the leading HLT-like calorimeter jet within a distance of $\Delta R < 0.2$. To calculate the trigger efficiency, the p_T distribution of matched probe jets having HLT-like p_T above the nominal energy threshold is divided by the p_T distribution of all probe jets.

The efficiency distributions for different triggers are shown in Figure 7.1. To define the trigger thresholds, each trigger efficiency is fitted separately with an error function which includes three free parameters as the following:

$$f(p_T^{ave}) = a + 0.5 \cdot (1 - a) \cdot (1 + \text{erf}((p_T^{ave} - \mu)/\sigma)) \quad (7.1.)$$

The trigger threshold, $p_{T,98}^{ave}$, can be correctly computed from $f(p_{T,98}^{ave})$, where the efficiency equals 98% of the plateau-value. The $p_{T,98}^{ave}$ thresholds for all trigger paths are listed in Table 7.5.

Table 7.5. Trigger thresholds of DiPFJetAve triggers.

Central Triggers	**Threshold (GeV)**	**HF Triggers**	**Threshold (GeV)**
HLT_DiPFJetAve15_Central_v2	33	HLT_DiPFJetAve15_HFJEC_v2	29
HLT_DiPFJetAve25_Central_v2	48	HLT_DiPFJetAve15_HFJEC_v2	43
HLT_DiPFJetAve35_Central_v3	61	HLT_DiPFJetAve15_HFJEC_v3	56

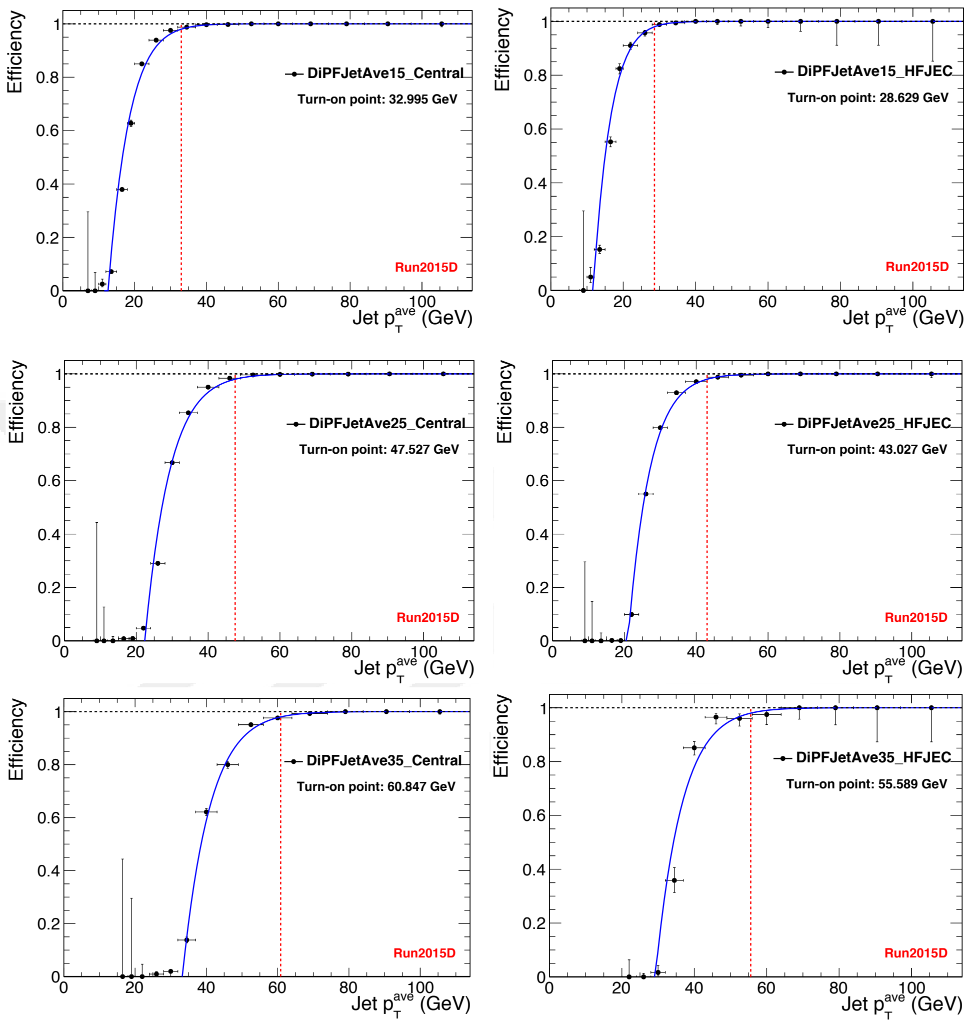

Figure 7.1. The measured trigger efficiency curves for DiPFJetAve_Central (left) and DiPFJetAve_HFJEC (right) triggers as a function of jet p_T^{ave}.

7.1.3. Event Selection

The determination of L2 relative residual corrections is studied by using the dijet events with anti-k_T PFCHS jets distance parameter of 0.4. Each event has to fulfill the following selection requirements in order to considered as a dijet event and reduce the beam background:

- At least one well-reconstructed primary vertex is required to be reconstructed from at least four tracks with $|z| < 24$ cm.
- An event, which includes at least two jets, has to pass one DiPFJetAve trigger and also pass its determined turn-on threshold value in p_T^{ave} as shown in Table 7.5. The events preselected L1MinimumBiasHF1OR triggers from the L1MinimumBias dataset that requires jets with $p_T^{ave} > 20$ GeV. We also applied $p_T^{ave,gen} > 20$ GeV cut for the MC samples.
- At least one of the two leading jets serves as a reference and is in the control region, $|\eta| < 1.3$.
- The two leading jets are required to be back-to-back, $\Delta\phi(j_1, j_2) > 2.7$.
- If the event contains more than two jets, a cut on the relative third jet fraction with $\alpha = p_{T,j_3}/p_T^{ave} < 0.3$ is applied, where $p_T^{ave} = \frac{p_{T,j_1}+p_{T,j_2}}{2}$.
- The $\not{E}_T$ is corrected according to the (L123(L2L3Res)−L1RC) scheme as discussed in Section 4.3.1.
- Finally, the jets are corrected with L1FastJet, L2Relative, and L3Absolute from Fall15_lowPU_V1 JEC version for the reconstructed data and simulated events.

The p_T^{ave} and α binning chosen for this analysis are listed in Table 7.6. The binning in absolute pseudorapidity which corresponds to the detector edges are specified in Table 7.7.

Table 7.6. Bins of the p_T^{ave} and α used in the analysis.

p_T^{ave}	20, 28, 37, 49, 64, 84, 114
α	0.050, 0.100, 0.150, 0.200, 0.250, 0.300, 0.350, 0.400, 0.450

Table 7.7. The η bin edges used in the analysis.

Region	$\|\eta\|$
Barrel	0, 0.783, 1.305
Endcaps	1.93, 2.322, 2.853
Hadronic Forward	3.139, 3.839, 5.191

The number of events accumulated with each trigger used in this analysis as a function of p_T^{ave} and η is shown in Figures 7.2 and 7.3, respectively. The previously determined trigger threshold values as shown in Table 7.5 are applied on p_T^{ave}.

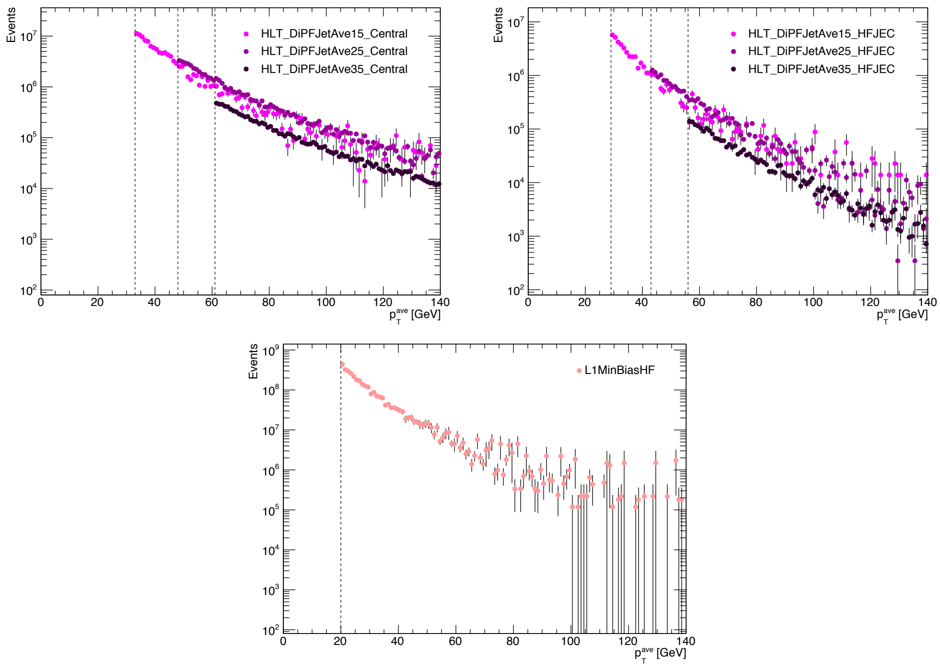

Figure 7.2. Number of events accumulated with DiPFJetAveX_Central (upper left), DiPFJetAveX_HFJEC (upper right), and L1MinimumBiasHF1OR_partY with Y= [0, …, 7] (bottom) triggers as a function of p_T^{ave} in Runs 259237, 259385, 259388, 259399.

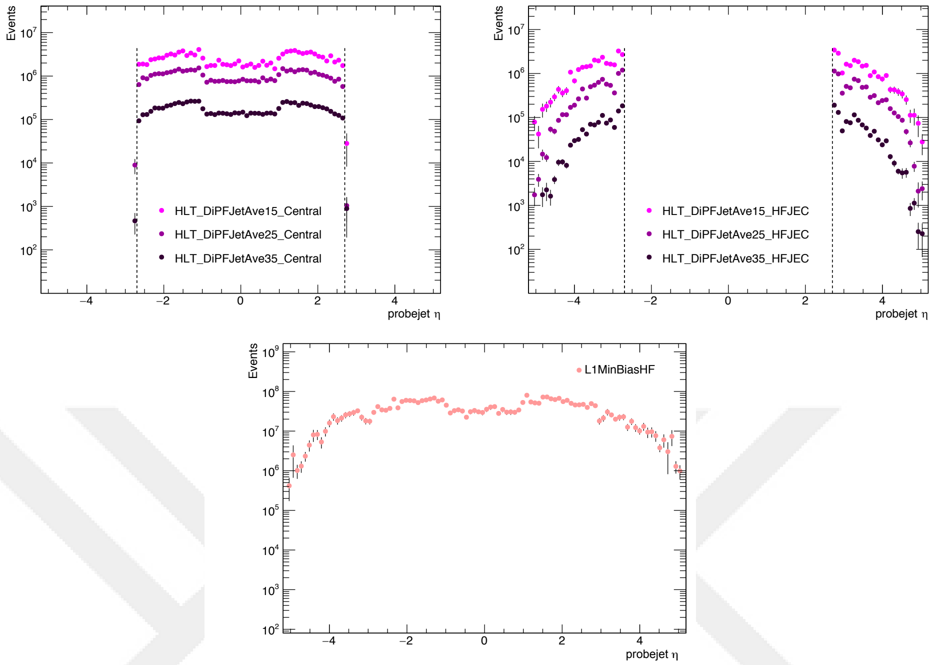

Figure 7.3. Number of events accumulated with DiPFJetAveX_Central (upper left), DiPFJetAveX_HFJEC (upper right), and L1MinimumBiasHF1OR_partY with Y= [0, …, 7] (bottom) triggers as a function of η in Runs 259237, 259385, 259388, 259399.

7.2. Determination of the L2 Relative Residual Correction

As we discussed in Section 5.4, two different methods were used in order to measure the L2 relative residual corrections; the p_T-balance and the MPF methods. Equations 5.8 and 5.13 are evaluated in data and simulation to estimate the responses (relative response via asymmetry distribution and MPF response).

The distribution of the asymmetry is shown in Figure 7.4 in two different η regions with all p_T bins for data and MC. Each colored line represents a different p_T bin. The full set of plots for data and MC can be found in Appendix A.1.

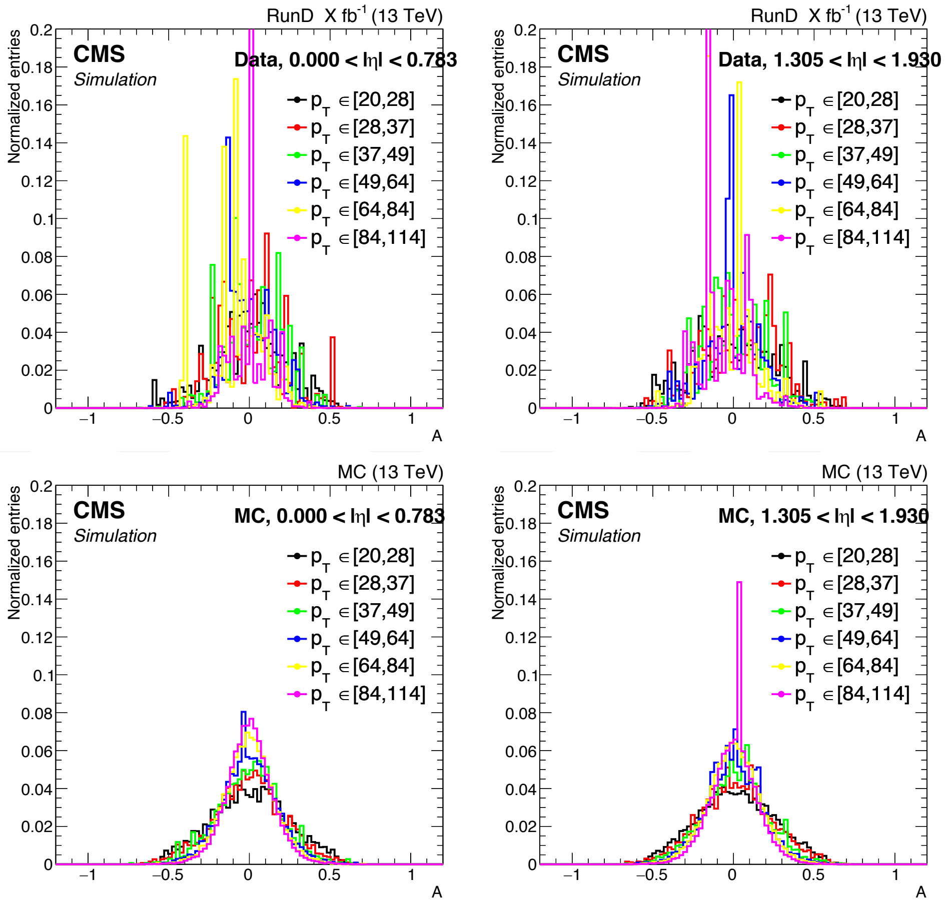

Figure 7.4. The asymmetry distributions in two different regions, $0 < |\eta| < 0.783$ (left) and $1.305 < |\eta| < 1.93$ (right) for the data (top) and MC (bottom). The distributions are normalized to integral of the histogram.

MPF response can also be formulated by using an alternative way as in Reference (CMS Collaboration, 2015b);

$$\mathcal{R}_{rel}^{MPF} = \frac{1+\langle\mathcal{B}\rangle}{1-\langle\mathcal{B}\rangle} \tag{7.2.}$$

where $\mathcal{B}$ is a quantity that can be defined as follows;

$$\mathcal{B} = \frac{\vec{E}_T \cdot \vec{p}_T^{\,tag}}{2p_T^{ave} \cdot \left|\vec{p}_T^{\,tag}\right|} \tag{7.3.}$$

Two different definitions of MPF response which are shown in Equations 5.13 and 7.2 are completely equivalent. Figure 7.5 shows the distribution of the balance quantity $\mathcal{B}$ in two different η regions with all p_T bins for data and MC, the full set of plots in Appendix A.2. Each colored line represents a different p_T bin.

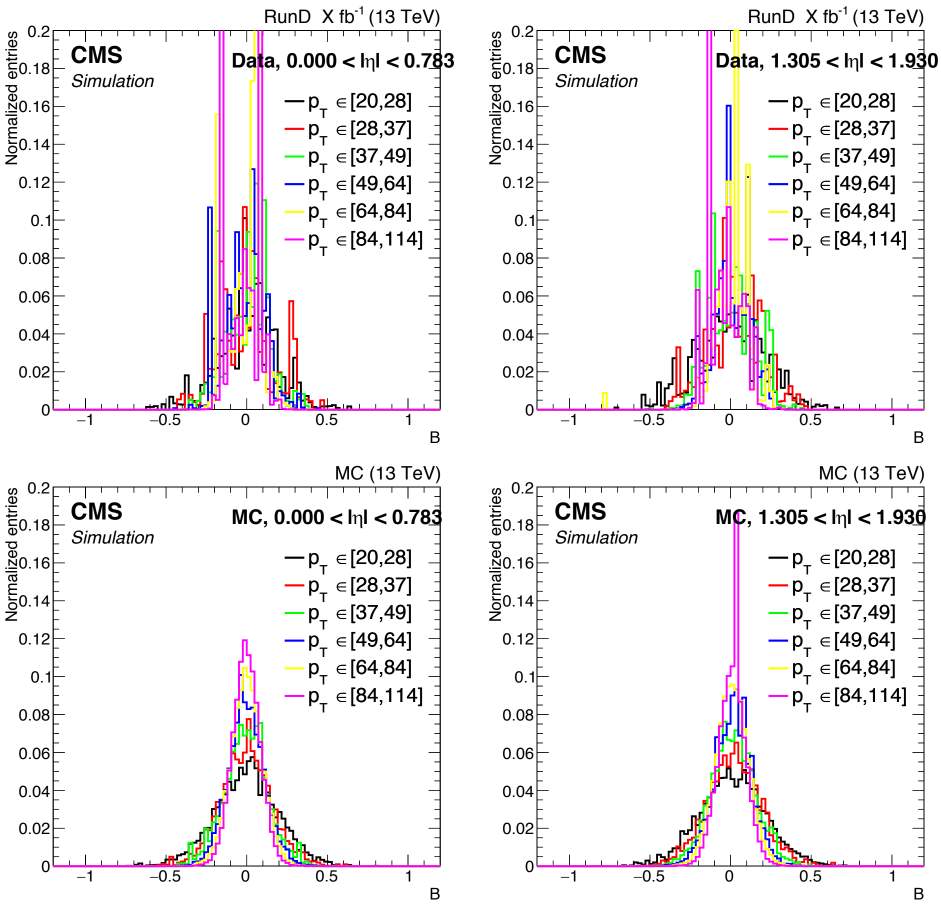

Figure 7.5. The MPF distributions in two different regions, $0 < |\eta| < 0.783$ (left) and $1.305 < |\eta| < 1.93$ (right) for the data (top) and MC (bottom). The distributions are normalized to integral of the histogram.

The distribution of asymmetry quantity as a function of p_T^{ave} in bins of two different η regions and $\alpha = 0.05$ is shown in Figure 7.6 for data and MC. Appendix A.3 and A.4 show the full set of plots for data and MC, respectively. For $\mathcal{B}$ quantity, a similar distribution is shown in Figure 7.7, the full set of these plots in Appendix A.5 and A.6.

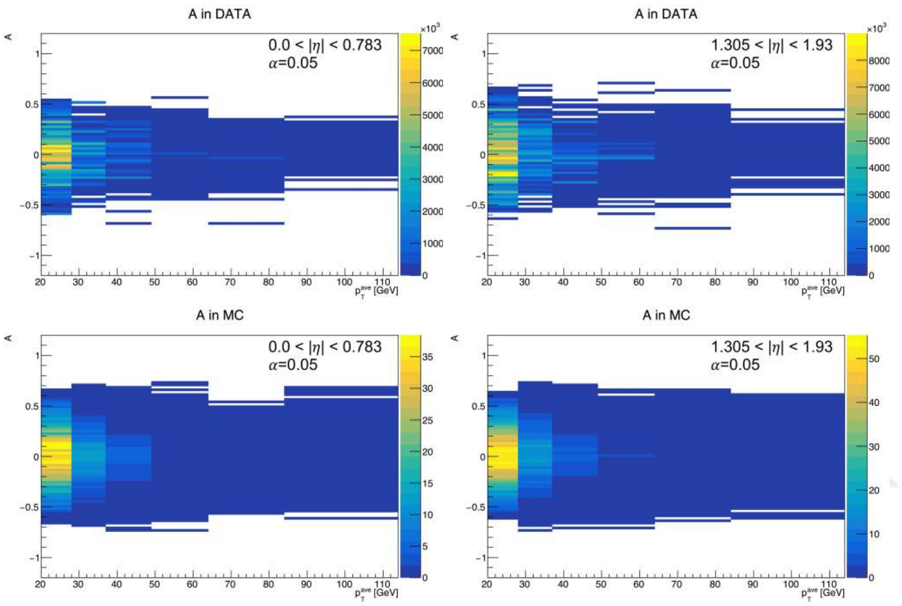

Figure 7.6. Top: The distribution of asymmetry quantity as a function of p_T^{ave} in bins of two different detector regions, $0 < |\eta| < 0.783$ (left) and $1.305 < |\eta| < 1.93$ (right), and $\alpha = 0.05$ for data. Bottom: The distribution of asymmetry quantity as a function of p_T^{ave} in bins of two different detector regions, $0 < |\eta| < 0.783$ (left) and $1.305 < |\eta| < 1.93$ (right), and $\alpha = 0.05$ for MC.

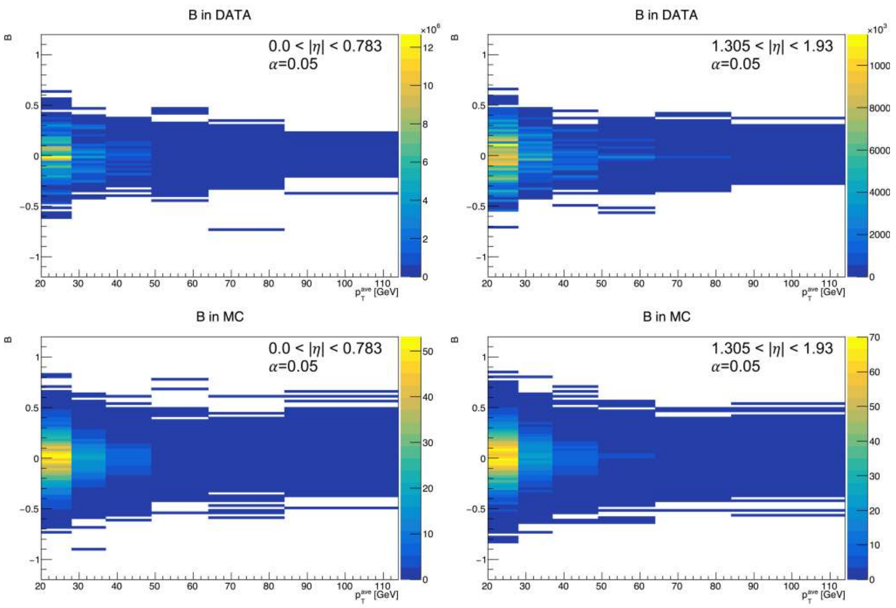

Figure 7.7. Top: The distribution of $\mathcal{B}$ quantity as a function of p_T^{ave} in bins of two different detector regions, $0 < |\eta| < 0.783$ (left) and $1.305 < |\eta| < 1.93$ (right), and $\alpha = 0.05$ for data. Bottom: The distribution of $\mathcal{B}$ quantity as a function of p_T^{ave} in bins of two different detector regions, $0 < |\eta| < 0.783$ (left) and $1.305 < |\eta| < 1.93$ (right), and $\alpha = 0.05$ for MC.

As can be seen from Equations 5.8 and 7.2, the average value of the balance quantity $\mathcal{A}$ and $\mathcal{B}$ are used to determine the relative responses for p_T-balance and MPF methods, respectively. The average value of the balance quantity $\mathcal{A}$ as a function of p_T^{ave} in the seven different η bins for data and MC is shown in Figure 7.8. Figure 7.9 shows the measured average value of the balance quantity $\mathcal{B}$.

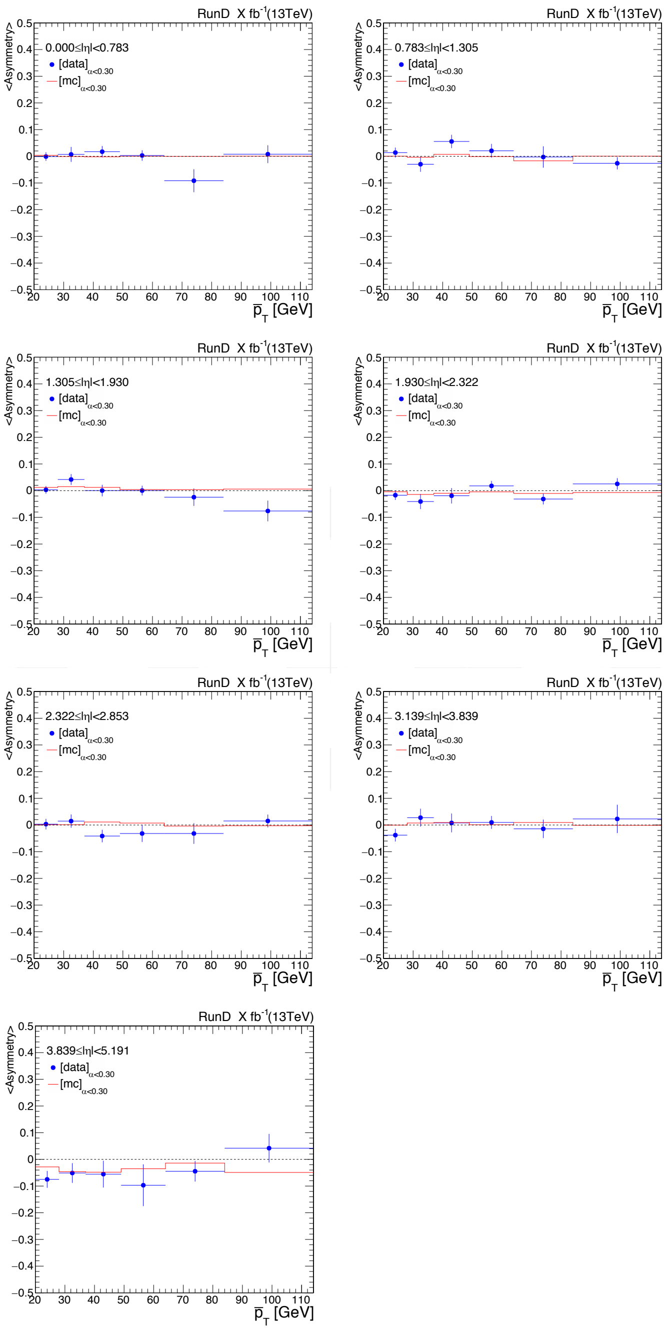

Figure 7.8. The average value of the balance quantity $\mathcal{A}$ as a function of p_T^{ave} in the seven different η regions with $\alpha < 0.3$ for data and MC. Here, data and MC are indicated as blue dot and red line, respectively.

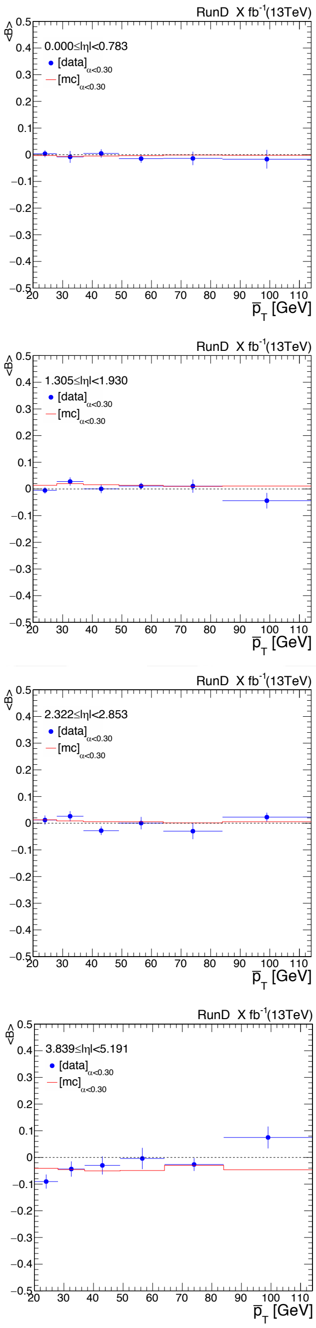

Figure 7.9. The average value of the balance quantity $\mathcal{B}$ as a function of p_T^{ave} in the seven different η regions with $\alpha < 0.3$ for data and MC. Here, data and MC are indicated as blue dot and red line, respectively.

Figure 7.10 shows the relative response by using the p_T-balance method as a function of p_T^{ave} in all η regions with the nominal working point $\alpha < 0.3$ for data and MC. The relative response for the MPF method is shown in Figure 7.11. The relative response of the corrected jets in the simulation should be equal to unity in an ideal world. However, there can be bias on the measured relative response in the data due to inherent biases associated with detector effects and to the physical properties which will be discussed in Section 7.2.1. The comparison of simulation with data also assumes that this bias in simulation exists in the same amount in data. This is why the relative response in the simulation deviates from unity.

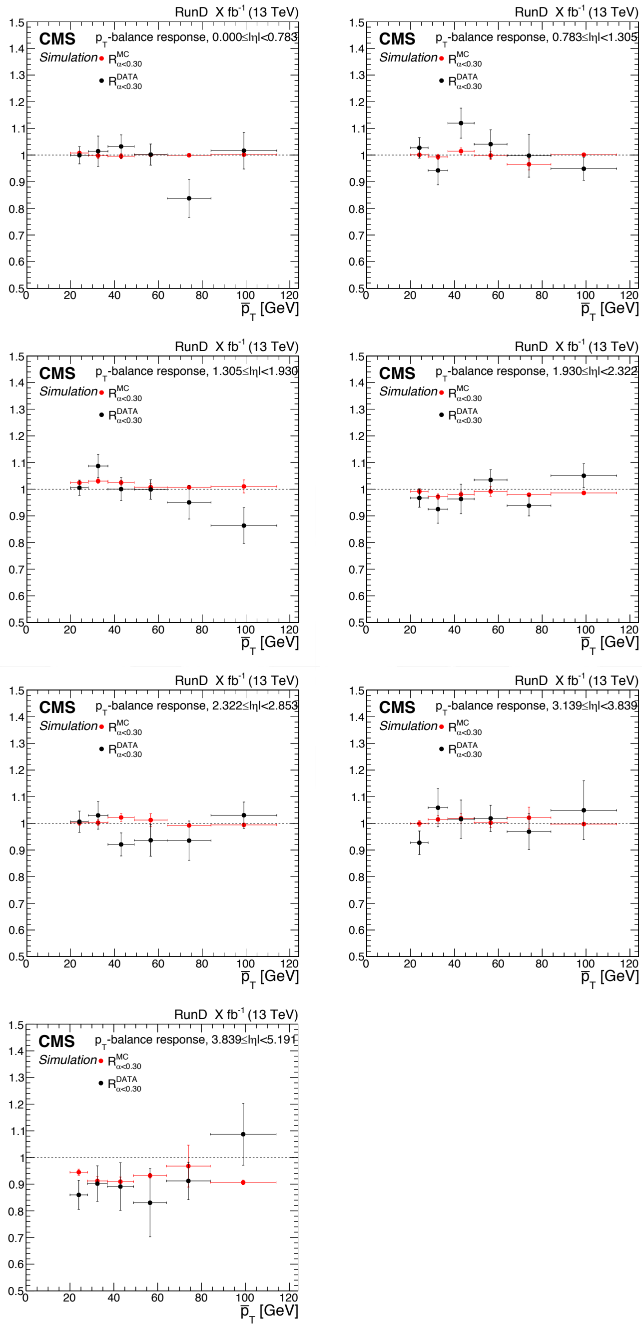

Figure 7.10. p_T^{ave}- dependence of the relative response estimator determined from the simulation (red dots) and compared with the data (black dots) for the seven different η bins at the nominal working point $\alpha < 0.3$.

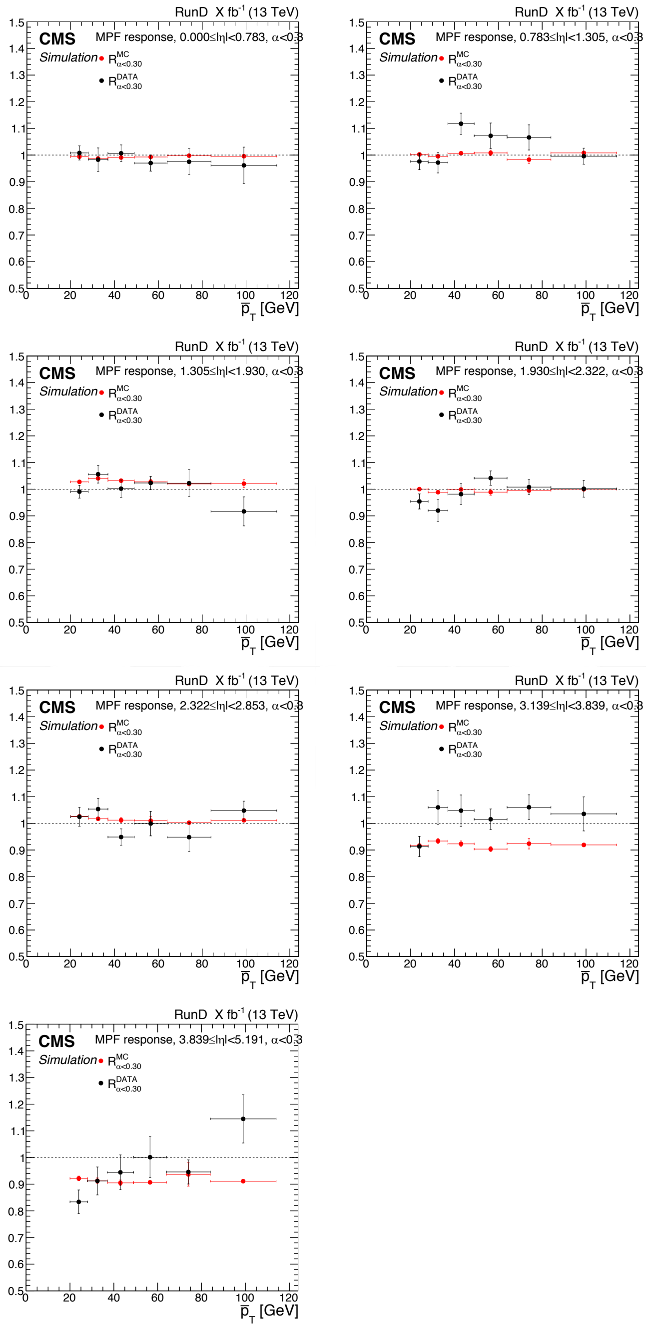

Figure 7.11. p_T^{ave}- dependence of the MPF response estimator determined from the simulation (red dots) and compared with the data (black dots) for the seven different η bins at the nominal working point $\alpha < 0.3$.

After calculating the relative responses for both methods, the ratio of the response estimators, $\mathcal{R}_{MC}/\mathcal{R}_{DATA}$, in each bin of η and p_T^{ave} are calculated. If the L1L2L3 corrections worked as expected and the detector effects were well understood, we would expect the ratio of response estimators to be flat as a function of p_T^{ave} and use a constant fit (zero-degree polynomial function) in the ratio of response estimators. However, all detector effects may not be well known, which causes p_T^{ave}-dependence of the responses and it can be fitted by the loglinear fit ($p_0 + p_1 \cdot \log x$). Figure 7.12 shows the ratio of the response estimators in data and simulation as a function of p_T^{ave} for the seven different η bins using the p_T-balance method. Here, the constant and loglinear fits are indicated with a blue dashed line and a red constant line, respectively. The p_T^{ave} extrapolation results are also obtained by using the MPF method, which is shown in Figure 7.13. In the MC/data ratio at the working point, log-linear behavior has been observed and the measured relative response corrections will be compatible with log-linear. The absence of a tracker prevents the proper reconstruction of the charged hadrons and the response becomes very poor for the forward region.

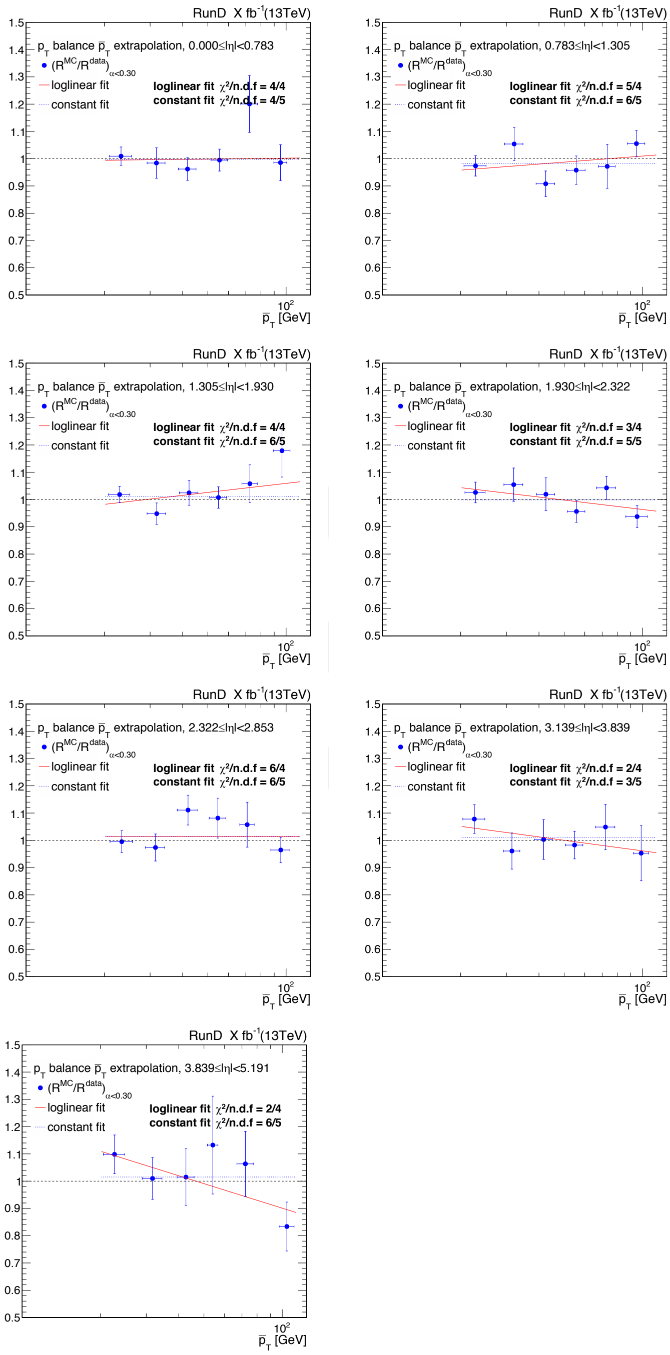

Figure 7.12. The ratio of the response estimators in data and simulation as a function of p_T^{ave} in $|\eta| \in [0; 5.191]$ bins for the p_T-balance method.

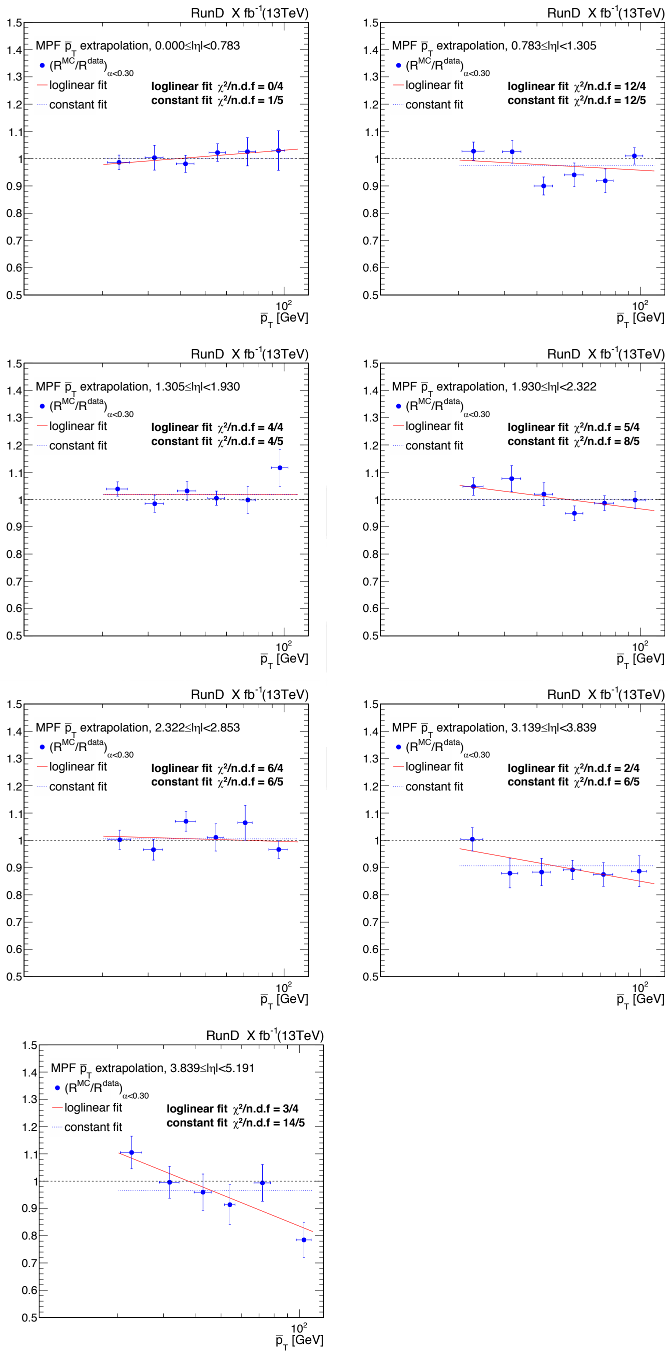

Figure 7.13. The ratio of the response estimators in data and simulation as a function of p_T^{ave} in $|\eta| \in [0; 5.191]$ bins for the MPF method.

7.2.1. Initial- and Final-State Radiation Correction

The measurement of the jet energy response is done by comparison to a reference object. In the dijet events, the reference object is selected as a jet in the barrel region since the resolution is much better in the barrel region of the detector. So, the two objects have comparable resolutions. The calculated relative responses are biased in favor of the jet with the worse resolution. This is because a reconstructed jet p_T bin can be filled not only by the p_T of true-particle jets which is in the same bin but also by the p_T of jets that are outside the bin. This contribution can cause fluctuation in the p_T of the jets. The relative response is measured in bins of p_T^{ave} in order to reduce the bias, therefore the bias can be canceled on average if the two jets have the same resolution, that is (to) say both jets are in the same η region. Since both jets can be in separate η regions the cancellation of the resolution bias effect is only partial (CMS Collaboration, 2011c).

Gluon radiation is another source that can cause a bias on jet energy response. As we mentioned in Section 5.4.1.1, two jets should be back-to-back in the transverse plane in an ideal dijet topology. But, the additional jet activity which arises from ISR or FSR can bias the momentum balance of two jets. In order to estimate this bias, the variable α can be defined as follows;

$$\alpha = \frac{p_T^{jet\ 3}}{p_T^{ave}} \tag{7.4.}$$

which shows the estimator related to additional jet activity in the events. Thus, a cut on the p_T of the third-leading jet fraction α is applied in order to improve the fraction of the ideal dijet events, $\alpha < 0.3$. L2 relative residual correction is determined as a function of η by a linear extrapolation $\alpha \to 0$ and $\alpha < 0.3$ respectively, and then we compute the data over simulation double ratio as;

$$k_{FSR}(\alpha = 0.3) = \left(\frac{\mathcal{R}_{rel}^{MC}(\alpha\to 0)}{\mathcal{R}_{rel}^{data}(\alpha\to 0)}\right) \Big/ \left(\frac{\mathcal{R}_{rel}^{MC}(\alpha<0.3)}{\mathcal{R}_{rel}^{data}(\alpha<0.3)}\right) \tag{7.5.}$$

where k_{FSR} is the final state correction factor and $\mathcal{R}$ denotes the response estimator coming from either the p_T-balance or MPF method (CMS Collaboration, 2017c). The extrapolation to zero additional event activity is performed by varying the cuts on α parameter. Figure 7.14 shows the extrapolation of the measured ratio of the response with additional jet activity in data and simulation as a function of parameter α in all η and p_T^{ave} bins for the p_T-balance method. The results by using the MPF method is depicted in Figure 7.15. Since the 0.3 value is selected as a cut on α, we are making normalization to the value of α = 0.3 and the ratio of the responses is equal at 1. These distributions are fitted by a first-degree polynomial function in the range of [0.14, 0.36] where doesn't have a lack of statistics. The constant parameter of the fit as a function of p_T and η for p_T-balance and MPF method is shown in Figure 7.16. It is very clear that the p_T-balance method is much more dependent on the presence of additional activity than the MPF method, as expected.

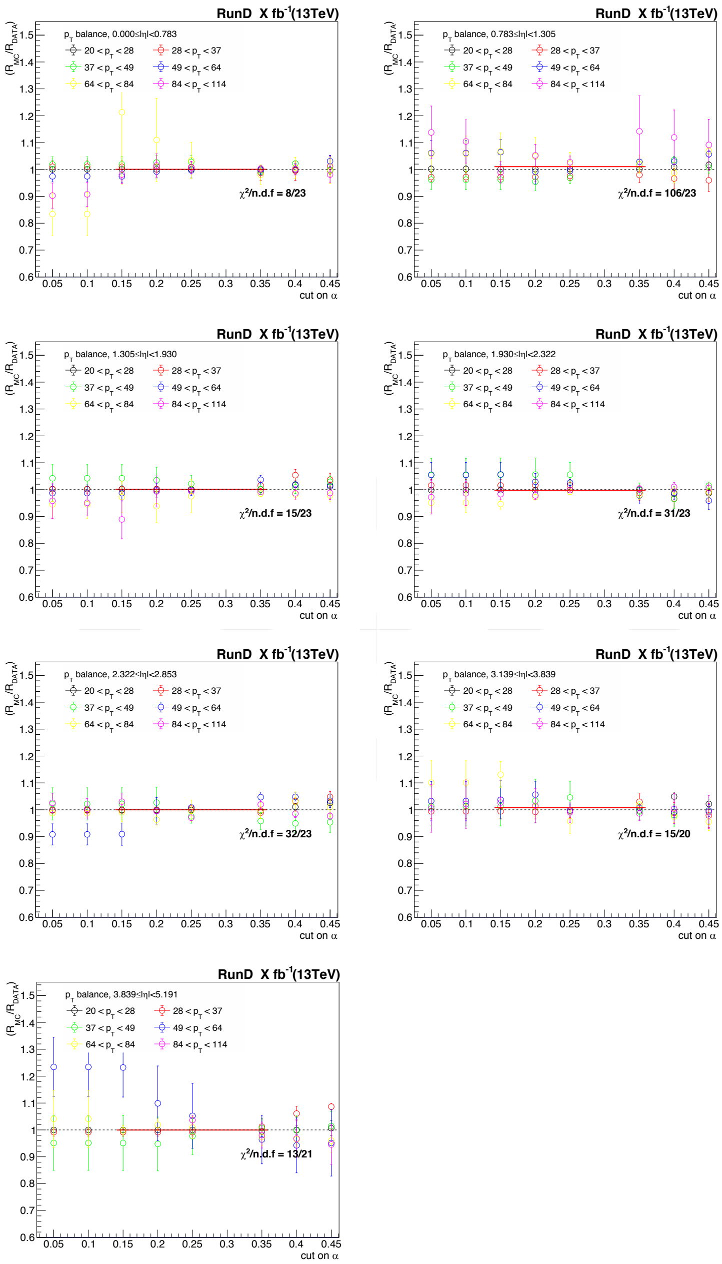

Figure 7.14. k_{FSR} correction to extrapolate the ratio of the response estimators for the p_T-balance methods. Here, each p_T bins are indicated as a different colored open circle and the fit is shown as a solid red line.

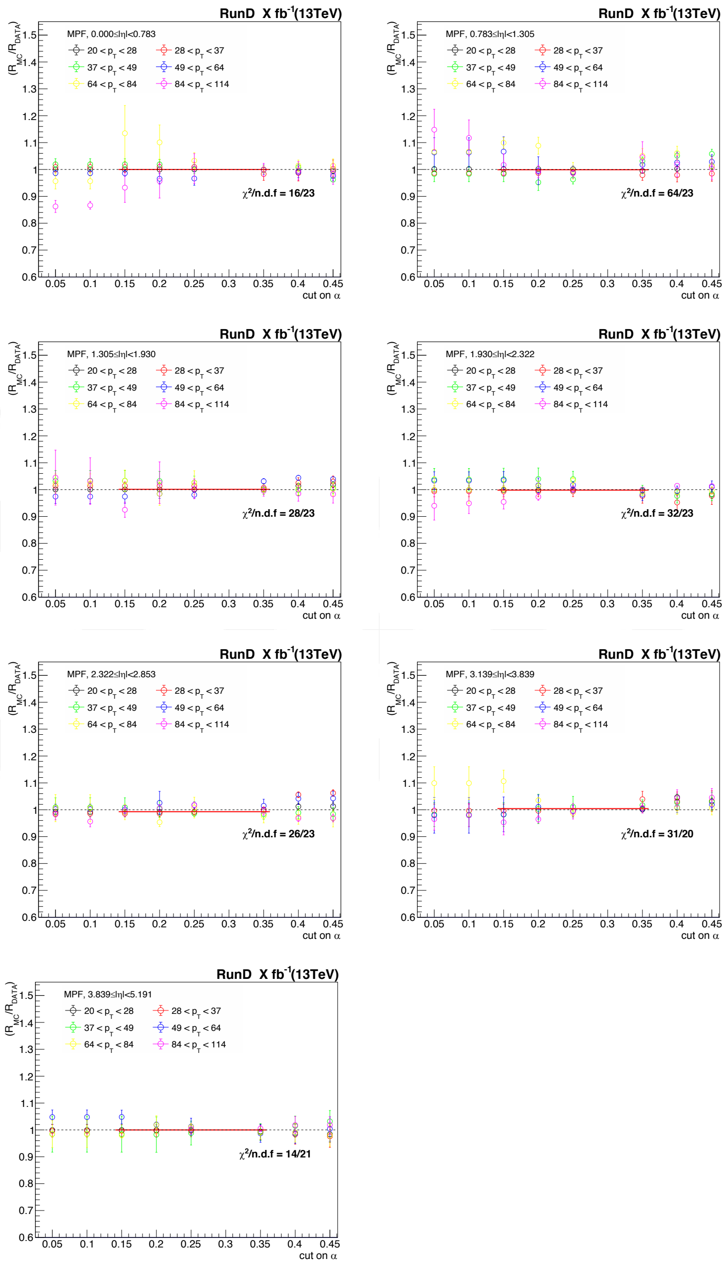

Figure 7.15. k_{FSR} correction to extrapolate the ratio of the response estimators for the MPF methods. Here, each p_T bins are indicated as a different colored open circle and the fit is shown as a solid red line.

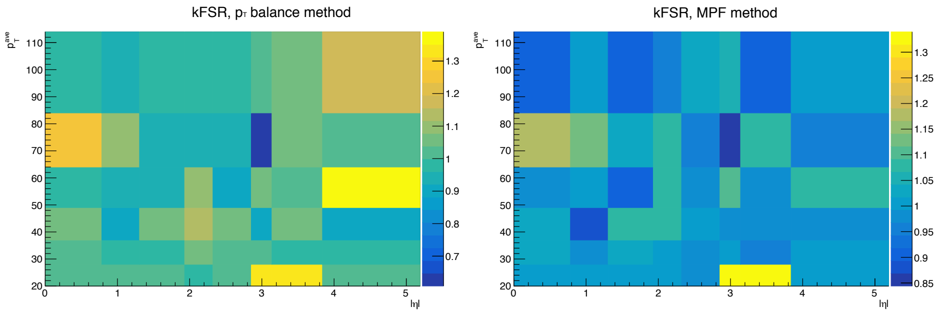

Figure 7.16. The ratio of the response estimators as a function α are fitted by a linear fit in [0.14, 0.36]. The constant parameter of this fit is shown as a function of p_T and η for p_T-balance (left) and MPF method (right).

7.2.2. The L2 Relative Residual Correction for 2015 Low Pileup Data

After the correction factor k_{FSR} as described and obtained as a function of the cut on the third jet in different p_T and η bins in Section 7.2.1, the ratio of response estimators and k_{FSR} are estimated as a function of η. The results are depicted in Figure 7.17. On the left, the ratio of responses is shown as a function of η for both p_T-balance and MPF methods. The results were obtained by using log-linear and constant fit values for both models. Here, the results related to constant fit is indicated as a dashed line, a solid line is for the log-linear fit. The k_{FSR} correction factor in each bin of η is indicated in the right of Figure 7.17. It is obtained by using both methods for AK4 PFCHS jets. k_{FSR} extrapolation is fitted by $p_0 + ((p_1 \cdot \cosh(\eta))/(1 + p_2 \cdot \cosh(\eta)))$ in previous JECs studies related to high PU runs since the additional jet activity is much stronger (i.e. Figure 16, Reference (CMS Collaboration, 2017c)). It was recommended by JERC experts that the k_{FSR}-histogram values instead of fit values should be used while deriving the final L2 relative residual correction. The k_{FSR} extrapolation factor is almost negligible for the MPF method but this correction factor goes up to 2% in some detector regions for the p_T-balance method. An improvement can be mentioned when the MPF method compared with the p_T-balance method: the ratio of responses is closer to unity in overall since the MPF method is much less sensitive to additional jet activity.

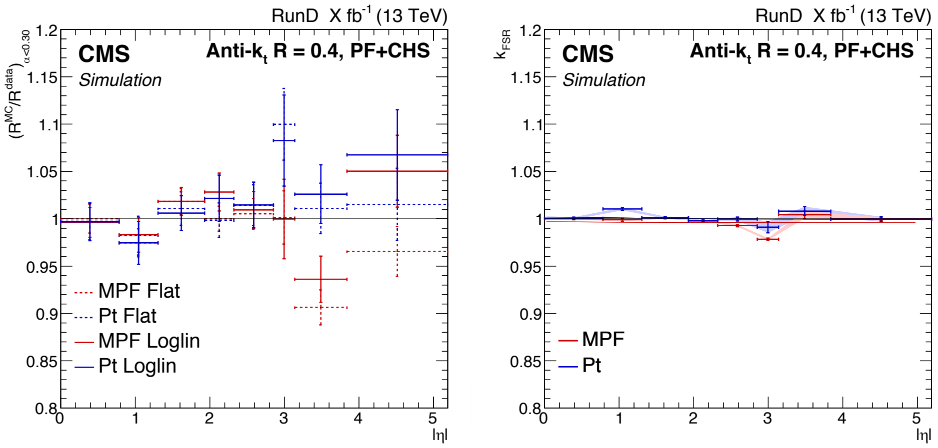

Figure 7.17. Left: The relative residuals as a function of absolute η for AK4 PFCHS jets. Right: k_{FSR} correction factors as a function of absolute η for AK4PFCHS jets.

The final L2 relative residual correction factors can be defined as follows;

$$\mathcal{C}(|\eta^{probe}|) = \left\langle \frac{\mathcal{R}_{MC}}{\mathcal{R}_{DATA}} \right\rangle_{\alpha<0.3} \cdot k_{FSR}(|\eta^{probe}|) \qquad (7.6.)$$

The final L2 relative residual correction factors are obtained by using both p_T-balance and MPF methods for AK4 PFCHS jets and the results are shown in Figure 7.18. In addition, the residual corrections have been obtained per bin in η with four different p_T values to show the impact of the p_T-dependency of the corrections. The p_T-dependence of the relative residual corrections for AK4 PFCHS is shown in Figure 7.19. The p_T-dependence is much larger for the transition region between the endcaps and HF region for both p_T-balance and MPF methods while a good agreement was observed in the $\eta < 2.853$ region.

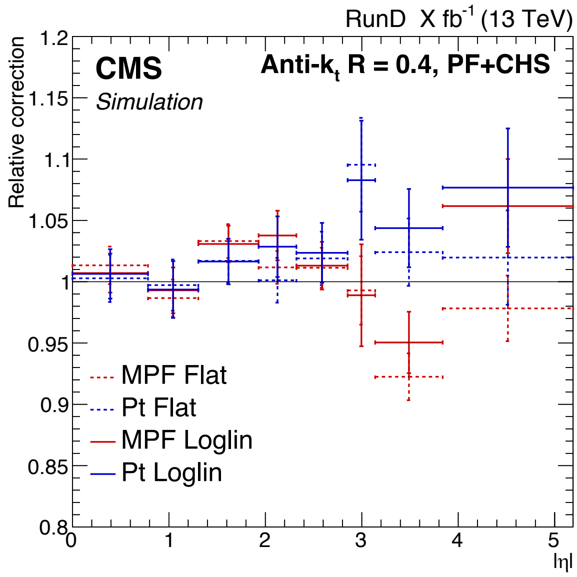

Figure 7.18. The final L2 relative residual correction factors as a function of $|\eta|$ for AK4 PFCHS jets.

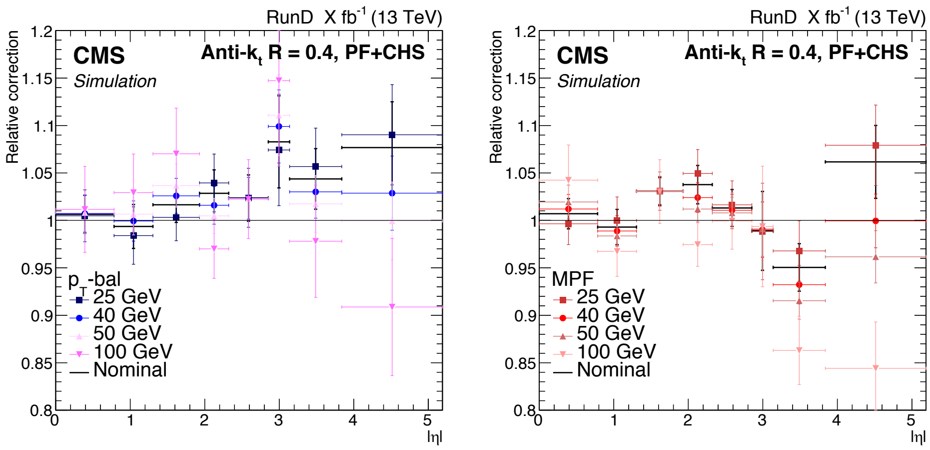

Figure 7.19. The relative residual correction as a function of $|\eta|$ for both p_T-balance (left) and MPF (right) methods is shown for p_T = 25, 40, 50, and 100 GeV. The nominal value of the p_T is indicated as a black solid line.

7.2.3. Closure Test

After obtaining the residual corrections, we now can check the effect produced. To perform this, the analysis is repeated by correcting the jets with all the levels of corrections and obtaining the new relative response ratios.

The values of the final L2 residual corrections per η bin shown in Figure 7.18 is recorded in a different text file for each method. The MPF_Loglin text file was applied to the data as the L2L3Residual correction. The jets in data are now corrected with L2L3Residuals in the closure test and then the correction factors are re-derived per η bins. In this step, the re-deriving correction factors should be near one. Figure 7.20 shows the distribution of MPF responses on data and simulation as a function of p_T^{ave} in $1.93 < \eta < 2.322$, without L2 residual corrections (left) and with (right). After applying the residual corrections, there is a clearly observed an improvement in the previously observed discrepancy between the distribution of responses data and the simulation. Figure 7.21 left shows the ratio of the responses per each η bins, and the distribution of k_{FSR} corrections is shown in the right part of Figure 7.21. The final L2 relative residual correction factors per each η bins after applying the newly derived JECs for Run2015D is shown in Figure 7.22. The closure test shows the non-closure is $\sim 5-10\%$ for the forward region and nominal values of p_T. The p_T-dependence of the relative residual corrections derived after JECs have been applied is depicted in Figure 7.23.

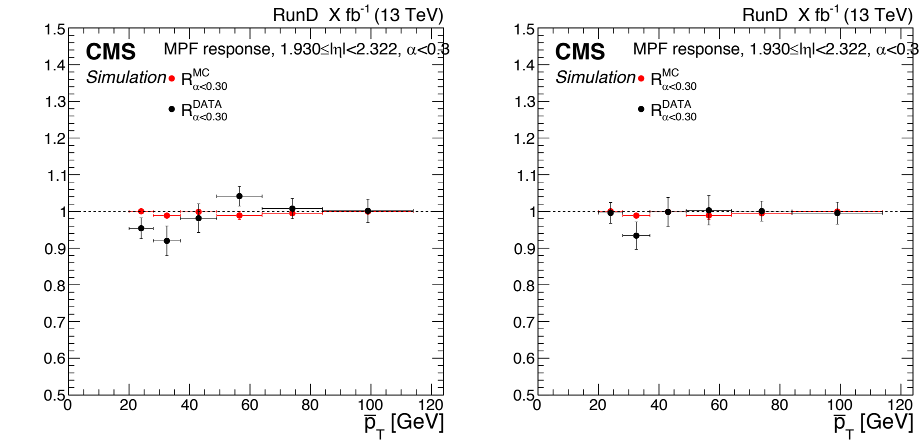

Figure 7.20. The MPF response estimator determined from the simulation (red dots) and compared with the data (black dots) in $1.93 < \eta < 2.322$ at the nominal working point $\alpha < 0.3$, without (left) and with (right) residual corrections.

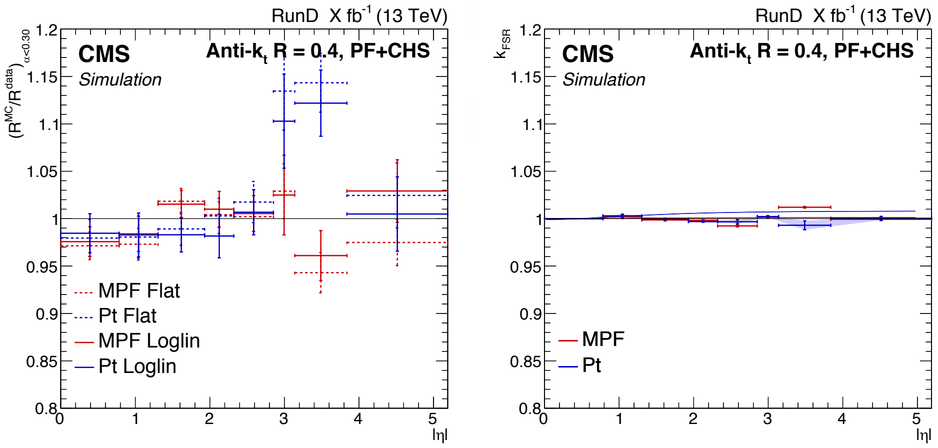

Figure 7.21. Left: The relative residuals as a function of absolute η for AK4 PFCHS jets. Right: k_{FSR} correction factors as a function of absolute η for AK4 PFCHS jets.

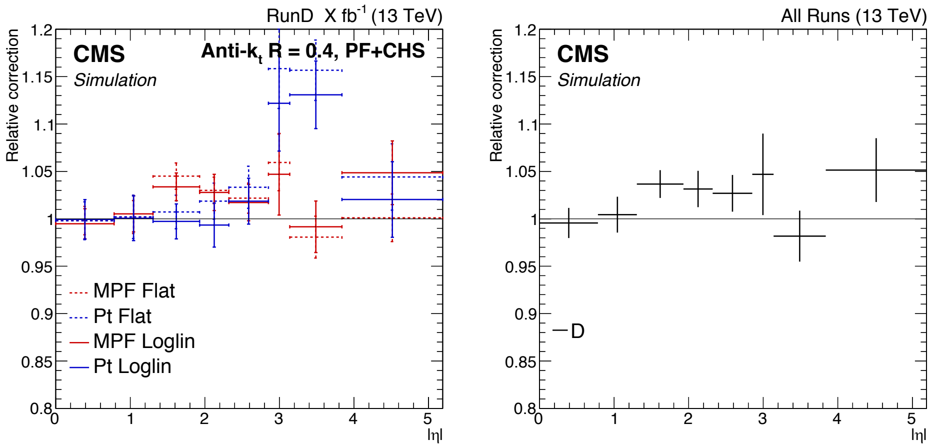

Figure 7.22. Left: The L2 relative residual correction factors as a function of $|\eta|$ for both p_T-balance and MPF methods with k_{FSR}-histogram values applied. Right: The L2 relative residual correction factors as a function of $|\eta|$ for Run2015D, in which the MPF Loglin results are selected as the final correction factor.

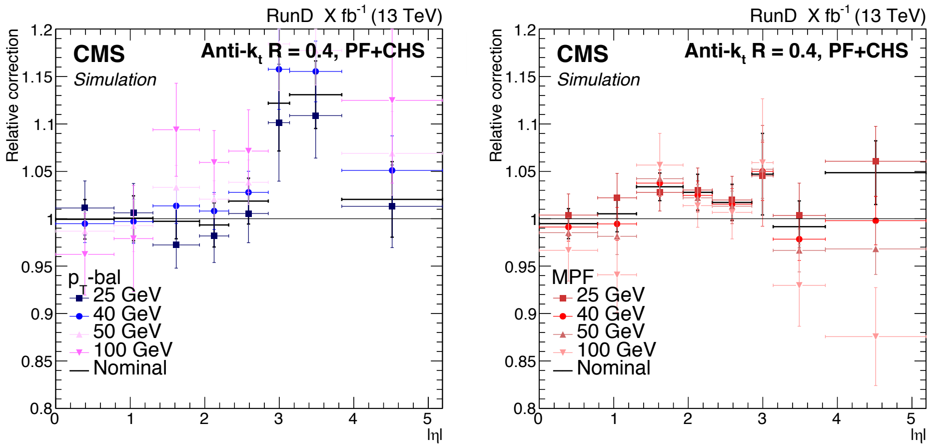

Figure 7.23. The p_T-dependence of the relative residual correction for p_T-balance (left) and for MPF (right) methods for AK4 PFCHS jets with k_{FSR}-histogram values applied.

8. SUMMARY AND CONCLUSIONS

The reconstructed jet energy differs from the true jet energy because of the failure in the jet reconstruction algorithm or the calibration problems of the subdetectors. Therefore, the energy of reconstructed jets needs to be calibrated to remove these deviations. The jets reconstructed in CMS are calibrated by using a factorized approach. In this approach, several levels of correction are available and each of these levels corrects a particular detector effect. Each level depends on the corrections applied in the previous level, so the order in which these corrections are applied is also important. The pileup offset (L1FastJet) correction factors remove the effects of PU and detector noise. The L2Relative and L3Absolute correction factors correct detector effects and the non-linearity in the jet response in bins of η and p_T. The first three correction factors are applied to both data and simulation. Furthermore, a residual correction (L2L3Residual) is extracted and applied only to data in order to correct the biases in jet response between the data and simulation. The optional corrections are also available depending on the jet flavor and it is derived from the simulation. After applying these correction factors, the reconstructed jet energy can be associated with true jet energy. The measurement of the true energy of the jets is the essential requirement to perform precision measurements which includes hadronic final states and also in all analyses where the jet objects are considered as background noise. Two different correction levels by focusing on the low p_T region are obtained in this thesis.

The first part of these analyses has been devoted/allocated to the L2Relative (η dependence) and L3Absolute (p_T dependence) jet energy corrections from simulated events. It has been done by using the events based on MC truth information from QCD PYTHIA8 MC set tuned with CUETP8M1 at 13 TeV which has no PU. We have derived MC truth jet energy correction for PFCHS jets reconstructed with the cone size parameters of 0.4 for jet p_T's from 10 GeV up to

905 GeV. The jet response, the reconstructed jet p_T^{reco} over the p_T^{ref}, has been obtained as a function of jet η and p_T^{ref} for the matched jets. The closure test has been performed on the corrected jets which are coming from the same events used for the derivation of the corrections. In the closure test, the calculated jet response is expected to close to one. The corrections are symmetric for positive and negative η bins. They are also smooth as a function of p_T^{reco}. We observed that more than 80% of the original p_T are retained in $|\eta| < 3.0$ region when considering the jet p_T less than 400 GeV. When considering the jet p_T = 15 GeV in $|\eta| > 3.0$ region, 35% of jet p_T is lost. The results are showed full closure within ±1% for p_T is from 15 GeV up to 400 GeV except some bins in the HE and HF regions because of a lack of statistics and non-closure for the jets with p_T < 20 GeV in all regions of the detector. These results have been approved by the CMS JetMET group and have been published in the CMS JEC database under title Fall15_lowPU_V1_ MC.

The work presented in the second part of this thesis has been carried out by using the low PU data collected at 13 TeV in the initial period of the LHC's second run (Run2). The collected low PU data correspond to an integrated luminosity of $\mathcal{L}_{int}$=0.41 pb^{-1}. After the MC truth jet energy correction chain, the reconstruction performance of jets is studied by measuring their energy scale using two different techniques on dijet events at low energy in data and simulation. p_T-balance and MPF methods show correction factors are less than 3% in $|\eta| < 2.5$. In the endcaps and the forward regions ($|\eta| \geq 2.5$) some differences show up as the correction factor grows up to $\sim$1.1 for the p_T-balance method, meanwhile, the MPF method shows the correction factors less than 5%. Therefore, the result obtained with the MPF method is chosen as L2 relative residual correction, provided for the usage in CMS physics analyses. The analysis results of the "Determination of L2L3 MCTruth and L2 Residual jet-energy corrections with Low PU data at 13 TeV" are presented in this thesis are documented in CMS Analysis Notes (Cerci, Sunar Cerci, and Demiroglu, 2020).

REFERENCES

Aaron, F.D., et al., 2010. Combined Measurement and QCD Analysis of the Inclusive $e^{\pm}p$ Scattering Cross Sections at HERA. JHEP 01 (2010) 109. DOI: 10.1007/JHEP01(2010)109.

AC Team, 1999. Diagram of an LHC dipole magnet. Schéma d'un aimant dipôle du LHC. CERN PhotoLab. CERN-DI-9906025. CERN, Geneva, Switzerland (1999). https://cds.cern.ch/record/40524.

Adzic, P., et al., 2007. Energy resolution of the barrel of the CMS Electromagnetic Calorimeter. JINST 2 P04004. DOI: 10.1088/1748-0221/2/04/P04004.

Ahmad, M. A., et al., 2019. Fluctuations in produced charged particle multiplicities in relativistic nuclear collisions for simulated events. J. Phys.: Conf. Ser. 1258 (2019) 012010. DOI : 10.1088/1742-6596/1258/1/012010.

Ali, A., and Kramer, G., 2011. Jets and QCD: A Historical Review of the Discovery of the Quark and Gluon Jets and its Impact on QCD. Eur. Phys. J. H 36 (2011) 245-326. DOI: 10.1140/epjh/e2011-10047-1.

ALICE Collaboration, 2008. The ALICE experiment at the CERN LHC. JINST, 3: S08002, 2008. DOI: 10.1088/1748-0221/3/08/S08002.

Altarelli, G., 2005. The Standard Model of Particle Physics. CERN-PH-TH/2005-206, arXiv: hep-ph/0510281v1.

Altarelli, G., and Parisi, G., 1977. Asymptotic Freedom in Parton Language. Nucl. Phys. B 126 (1977) 298-318. DOI: 10.1016/0550-3213(77)90384-4.

Andersson, B., Gustafson, G., and Sjöstrand, T., 1980. A three-dimensional model for quark and gluon jets. Z. Phys. C- Particles and Fields 6, 235–240 (1980). DOI: 10.1007/BF01557774.

______, 1982. A Model for Baryon Production in Quark and Gluon Jets. Nucl. Phys. B197 (1982) 45. LU TP 81-3. DOI: 10.1016/0550-3213(82)90153-5.

Andersson, B., et al., 1983. Parton Fragmentation and String Dynamics. Phys. Rept. 97 (1983) 31-145. LU-TP-83-10. DOI: 10.1016/0370-1573(83)90080-7.

Apollinari, G., et al., 2017. High Luminosity Large Hadron Collider HL-LHC. CERN Yellow Report. arXiv:1705.08830 [physics.acc-ph]. FERMILAB-PUB-15-699-TD. DOI: 10.5170/CERN-2015-005.1.

Atkin, R., 2015. Review of jet reconstruction algorithms. J. Phys. Conf. Ser. 645 (2015) 1, 012008. DOI: 10.1088/1742-6596/645/1/012008.

ATLAS Collaboration, 2008. The ATLAS Experiment at the CERN Large Hadron Collider. JINST, 3: S08003, 2008. DOI: 10.1088/1748-0221/3/08/S08003.

_______, 2013. Expected pileup values at the HL-LHC. ATL-UPGRADE-PUB-2013-014, https://cds.cern.ch/record/1604492/.

Bähr, M., et al., 2008. Herwig++ Physics and Manual. Eur. Phys. J. C 58 (2008) 639-707. DOI: 10.1140/epjc/s10052-008-0798-9.

Baird, S., 2007. Accelerators for pedestrians; rev. version. Internal Note. AB-Note-2007-014; CERN-AB-Note-2007-014; PS-OP-Note-95-17-Rev-2; CERN-PS-OP-Note-95-17-Rev-2. http://cds.cern.ch/record/1017689.

Balitsky, I. I., and Lipatov L. N., 1978. The Pomeranchuk Singularity in Quantum Chromodynamics. Sov. J. Nucl. Phys. 28 (1978) 822-829, Yad. Fiz. 28 (1978) 1597-1611.

Ball, R. D., et al., 2012. Unbiased global determination of parton distributions and their uncertainties at NNLO and at LO. Nucl. Phys. B 855 (2012) 153-221. DOI: 10.1016/j.nuclphysb.2011.09.024.

Barr, G., Devenish, R., Walczak, R., and Weidberg, T., 2016. Particle Physics in the LHC Era. Oxford University Press (2016) 403 p. ISBN-13: 9780198748557.

Berger, J., 2014. Search for the Higgs Boson Produced via Vector Boson Fusion in the Decay Channel $H \to \tau\tau$. PhD thesis, KIT (Karlsruher Institut für

Technologie), Jun, 2014, https://cds.cern.ch/record/1747055/files/CERN-THESIS-2014-092.pdf.

Bjorken, J. D., 1969. Asymptotic Sum Rules at Infinite Momentum. Phys. Rev. 179 (1969) 1547–1553. DOI: 10.1103/PhysRev.179.1547.

Blazey, G. C., et al., 2000. Run II Jet Physics. FERMILAB-CONF-00-092-E. arXiv: hep-ex/0005012v2.

Botje, M., 2013. The QCD improved Parton Model. Lecture notes for Particle Physics II. Nikhef, Science Park, Amsterdam. Available: https://www.nikhef.nl/~h24/qcdcourse/section-9.pdf. (Accessed: 14 January 2020).

Breidenbach, M., Friedman, J. I., Kendall, H. W., et al., 1969. Observed Behavior of Highly Inelastic Electron-Proton Scattering. Phys. Rev. Lett. 23 (1969) 935. DOI: 10.1103/PhysRevLett.23.935.

Brodsky, S. J., Deur, A., and de Teramond, G. F., 2016. The QCD Running Coupling. Prog. Part. Nuc. Phys. 90 1 (2016). arXiv: 1604.08082v3 [hep-ph].

Brüning, O. S. et al., 2004. LHC Design Report. CERN Yellow Reports: Monographs. CERN-2004-003-V-1. DOI: 10.5170/CERN-2004-003-V-1.

Butterworth, J. M., Dissertori, G., and Salam, G. P., 2012. Hard Processes in Proton-Proton Collisions at the Large Hadron Collider. Annual Review of Nuclear and Particle Science Vol. 62:387-405. DOI: 10.1146/annurev-nucl-102711-094913, arXiv:1202.0583 [hep-ex].

Cacciari, M., et al., 2008. The anti-k_t jet clustering algorithm. JHEP 04 (2008) 063. DOI: 10.1088/1126-6708/2008/04/063.

Callan, C. G., Jr., and Gross, D. J., 1969. High-Energy Electroproduction and the Constitution of the Electric Current. Phys. Rev. Lett. 22 (1969) 156. DOI: 10.1103/PhysRevLett.22.156.

Cammin, J., 2009. Flavor Specific Jet Energy Corrections and Closure Tests for Factorized Jet Energy Corrections. CMS Analysis Note. CMS AN-2009/010

http://cms.cern.ch/iCMS/user/noteinfo?cmsnoteid=CMS%20AN-2009/010

Campbell, J. M., Huston, J. W., and Stirling, W. J., 2006. Hard Interactions of Quarks and Gluons: a Primer for LHC Physics. Rept. Prog. Phys. 70 (2007) 89. arXiv: hep-ph/0611148v1. DOI: 10.1088/0034-4885/70/1/R02.

Carli, T., Rabbertz, K., and Schumann, S., 2015. Studies of Quantum Chromodynamics at the LHC. arXiv:1506.03239v2 [hep-ex]

Catani, S., Dokshitzer, Yu. L., Seymour, M. H., and Webber, B. R., 1993. Longitudinally invariant K_t clustering algorithms for hadron hadron collisions. Nucl. Phys. B 406 (1993) 187-224. DOI: 10.1016/0550-3213(93)90166-M.

Catani, S., et al., 2000. The QCD and Standard Model Working Group: Summary Report from Les Houches. arXiv: hep-ph/0005114.

CDF Collaboration, 1995. Observation of Top Quark Production in $\bar{p}p$ Collisions with the Collider Detector at Fermilab. Phys. Rev. Lett. 74 (1995) 2626-2631. DOI: 10.1103/PhysRevLett.74.2626.

______, 2006. Determination of the jet energy scale at the Collider Detector at Fermilab. Nucl. Instrum. Meth. A 566 (2006) 375-412. DOI: 10.1016/j.nima.2006.05.269.

Cerci, S., Sunar Cerci, D., and Demiroglu, Z. S., 2020. Determination of L2L3 MCTruth and L2 Residual jet-energy corrections with Low PU data at 13 TeV. CMS Analysis Note. CMS AN-2020/048.

Christova, E., and Leader, E., 2009. Towards a model independent approach to fragmentation functions. Phys. Rev. D 79 (2009) 014019. DOI: 10.1103/PhysRevD.79.014019.

CMS Collaboration, 1997. The CMS tracker system project: Technical Design Report. CERN-LHCC-98-006. CMS-TDR-5. https://cds.cern.ch/record/368412.

_______, 1997a. The CMS magnet project: Technical Design Report. CERN-LHCC-97-010. CMS-TDR-1. https://cds.cern.ch/record/331056.

_______, 2007. $\not{E}_T$ performance in CMS. CMS CR PAS based on AN–2007/041. http://cms-physics.web.cern.ch/cms-physics/public/JME-07-001-pas.pdf.

_______, 2007a. Performance of Jet Algorithms in CMS. CMS Physics Analysis Summaries. CMS-PAS-JME-07-003. http://cds.cern.ch/record/1198227.

_______, 2008. The CMS experiment at the CERN LHC. JINST, 3: S08004, 2008. DOI: 10.1088/1748-0221/3/08/S08004.

_______, 2009. Precise Mapping of the Magnetic Field in the CMS Barrel Yoke using Cosmic Rays. CMS-CFT-09-015 http://cds.cern.ch/record/1215500.

_______, 2009a. Jet Plus Tracks Algorithm for Calorimeter Jet Energy Corrections in CMS. CMS Physics Analysis Summary CMS-PAS-JME-09-002 (2009).

_______, 2009b. A Cambridge-Aachen (C-A) based Jet Algorithm for boosted top-jet tagging. CMS-PAS-JME-09-001. http://cds.cern.ch/record/1194489.

_______, 2009c. Particle-Flow Event Reconstruction in CMS and Performance for Jets, Taus, and MET. CMS-PAS-PFT-09-001.

_______, 2009d. Performance of Track-Corrected Missing Transverse Energy in CMS. CMS Physics Analysis Summary. CMS-PAS-JME-09-010.

_______, 2009e. Determination of the Relative Jet Energy Scale at CMS from Dijet Balance. CMS Physics Analysis Summary. CMS-PAS-JME-08-003. http://cds.cern.ch/record/1194488.

_______, 2010. The CMS L1 trigger emulation software. J. Phys. Conf. Ser. 219 (2010) 032009. DOI: 10.1088/1742-6596/219/3/032009.

_______, 2011. Technical proposal for the upgrade of the CMS detector through 2020. CERN-LHCC-2011-006, CMS-UG-TP-1, LHCC-P-004. https://cds.cern.ch/record/1355706/files/LHCC-P-004.pdf.

_______, 2011a. Determination of Jet Energy Calibration and Transverse Momentum Resolution in CMS. JINST 6 (2011) P11002. CERN-PH-EP-2011-102, CMS-JME-10-011. DOI: 10.1088/1748-0221/6/11/P11002.

_______, 2011b. Missing transverse energy performance of the CMS detector. JINST 6 (2011) 09001. DOI: 10.1088/1748-0221/6/09/P09001.

_______, 2011c. Determination of Jet Energy Calibration and Transverse Momentum Resolution in CMS. CMS-JME-10-011. arXiv:1107.4277v1 [physics.ins-det].

_______, 2012. Performance of CMS Muon Reconstruction in *pp* Collision Events at $\sqrt{s}$ = 7 TeV. JINST 7 (2012) P10002. CMS-MUO-10-004. CERN-PH-EP-2012-173. DOI: 10.1088/1748-0221/7/10/P10002.

_______, 2013. Measurement of the ratio of the inclusive 3-jet cross section to the inclusive 2-jet cross section in *pp* collisions at $\sqrt{s}$ = 7 TeV and first determination of the strong coupling constant in the TeV range. Eur. Phys. J. C 73 (2013) 2604, DOI:10.1140/epjc/s10052-013-2604-6, arXiv: 1304.7498 [hep-ex].

_______, 2013a. Projected Performance of an Upgraded CMS Detector at the LHC and HL-LHC: Contribution to the Snowmass Process. CERN-CMS-NOTE-2013-002. https://cds.cern.ch/record/1565454/.

_______, 2013b. The performance of the CMS muon detector in proton-proton collisions at $\sqrt{s}$ = 7 TeV at the LHC. JINST 8 (2013) P11002. DOI: 10.1088/1748-0221/8/11/P11002.

_______, 2014. Determination of the top-quark pole mass and strong coupling constant from the $t\bar{t}$ production cross section in *pp* collisions at $\sqrt{s}$ = 7 TeV. Phys. Lett. B 728 (2014) 496, DOI: 10.1016/j.physletb.2013.12.009, arXiv: 1307.1907 [hep-ex].

_______, 2015. Measurement of the inclusive 3-jet production differential cross section in proton-proton collisions at 7 TeV and determination of the strong coupling constant in the TeV range. Eur. Phys. J. C 75 (2015) 186, DOI: 10.1140/epjc/s10052-015-3376-y, arXiv: 1412.1633 [hep-ex].

_______, 2015a. The CMS Beam Halo Monitor Detector System. arXiv: 1511.00264v1 [physics.ins-det].

_______, 2015b. Jet Energy Scale and Resolution in the 8 TeV *pp* data. CMS PAS JME-13-004. http://cms.cern.ch/iCMS/analysisadmin/get?analysis=JME-13-004-pas-v7.pdf

_______, 2017. Measurement and QCD analysis of double-differential inclusive jet cross sections in *pp* collisions at $\sqrt{s}$ = 8 TeV and cross section ratios to 2.76 and 7 TeV. J. High Energ. Phys. 2017, 156 (2017). DOI: 10.1007/JHEP03(2017)156.

_______, 2017a. The CMS trigger system. JINST 12 (2017) P01020. DOI: 10.1088/1748-0221/12/01/P01020.

_______, 2017b. Jet energy scale and resolution in the CMS experiment in *pp* collisions at 8 TeV. JINST 12 (2017) P02014. DOI: 10.1088/1748-0221/12/02/P02014.

_______, 2017c. Jet energy scale and resolution in the CMS experiment in pp collisions at 8 TeV. CMS-JME-13-004. arXiv: 1607.03663v2 [hep-ex].

_______, 2018. Performance of the CMS muon detector and muon reconstruction with proton-proton collisions at $\sqrt{s}$ = 13 TeV. JINST 13 (2018) P06015. DOI: 10.1088/1748-0221/13/06/P06015.

_______, 2018a. The CMS Particle Flow Algorithm. EPJ Web Conf. 191 (2018) 02016. DOI: 10.1051/epjconf/201819102016.

_______, 2019. Performance of missing transverse momentum reconstruction in proton-proton collisions at $\sqrt{s}$ = 13 TeV using the CMS detector. JINST 14 (2019) 07, P07004. CMS-JME-17-001. CERN-EP-2018-335. DOI: 10.1088/1748-0221/14/07/P07004.

_______, 2020. Mitigation of anomalous missing transverse momentum measurements in data collected by CMS at sqrt(s) = 13 TeV during the LHC Run 2. CMS Performance Note. CMS DP-2020/018.

_______, 2020a. Jet energy scale and resolution performance with 13 TeV data collected by CMS in 2016-2018. CMS Detector Performance Summaries. CERN-CMS-DP-2020-019.

CMS HCAL/ECAL Collaborations, 2009. The CMS barrel calorimeter response to particle beams from 2 to 350 GeV/c. Eur. Phys. J. C (2009) 60: 359–373 DOI 10.1140/epjc/s10052-009-0959-5.

CMS HyperNews ECAL Performance Forum, 2015. https://hypernews.cern.ch/HyperNews/CMS/get/ecal-performance/839/2/1/1.html. (Accessed: 06 May 2020).

CMS Luminosity Public TWiki Page, 2018. CMS Twiki: Public CMS Luminosity Information. 2018 proton-proton collisions at 13 TeV. https://twiki.cern.ch/twiki/bin/view/CMSPublic/LumiPublicResults#2018_proton_proton_collisions. (Accessed: 03 May 2020).

_______, 2019. CMS Twiki: Public CMS Luminosity Information. Multi-year plots. Integrated and peak luminosity, 2010-2018 (run1+run2). Available:https://twiki.cern.ch/twiki/bin/view/CMSPublic/LumiPublicResults#Multi_year_plots. (Accessed: 03 May 2020).

CMS MET Group, 2017. Performance of missing transverse momentum in *pp* collision at 13 TeV using the full 2016 data. CMS Draft Analysis Note. CMS AN-18-003.

CMS Public Combined Physics Results, 2019. CMS Public TWiki Page. Available: https://twiki.cern.ch/twiki/bin/view/CMSPublic/PhysicsResultsCombined (Accessed: 08 June 2020).

CMS Web JetMET TWiki Page, 2013. Formulae for pfMET Type-I and Type-II Corrections.https://twiki.cern.ch/twiki/bin/viewauth/CMS/METType1Type2Formulae (Accessed: 06 May 2020).

Coco, V., Delsart, P.-A., Rojo-Chacon, J., Soyez, G., and Sander, C., 2009. Jets and jet algorithms. HERA and the LHC: 4th Workshop on the Implications of HERA for LHC Physics, 182-204. DOI: 10.3204/DESY-PROC-2009-02/54.

Collins, J. C., et al., 2004, Factorization of Hard Processes in QCD. arXiv: hep-ph/0409313.

Corcella, G., et al., 2005. HERWIG 6.5 Release Note. arXiv: hep-ph/0210213.

D0 Collaboration, 1995. Observation of the top quark. Phys. Rev. 74 (1995) 2632-2637. DOI: 10.1103/PhysRevLett.74.2632.

______, 1999. Determination of the absolute jet energy scale in the D0 calorimeters. Nucl. Instrum. Meth. A 424 (1999) 352-394. DOI: 10.1016/S0168-9002(98)01368-0.

______, 2009. Determination of the strong coupling constant from the inclusive jet cross section in $p\bar{p}$ collisions at $\sqrt{s}$ = 1.96 TeV. Phys. Rev. D 80 (2009) 111107. DOI: 10.1103/PhysRevD.80.111107, arXiv: 0911.2710 [hep-ex].

______, 2012. Measurement of angular correlations of jets at $\sqrt{s}$ = 1.96 TeV and determination of the strong coupling at high momentum transfers. Phys. Lett. B 718 (2012) 56, DOI: 10.1016/j.physletb.2012.10.003, arXiv: 1207.4957 [hep-ex].

Devenish, R., and Cooper-Sarkar, A., 2003. Deep Inelastic Scattering. Oxford University Press. 416 p. Print ISBN-13: 9780198506713. DOI: 10.1093/acprof:oso/9780198506713.001.0001.

Dissertori, G., et al., 2003. Quantum Chromodynamics: High Energy Experiments and Theory (International Series of Monographs on Physics). Clarendon Press. 560 p.

Dokshitzer, Yu. L., 1977. Calculation of the Structure Functions for Deep Inelastic Scattering and e^+e^- Annihilation by Perturbation Theory in Quantum Chromodynamics. Sov. Phys. JETP 46 (1977) 641-653. Zh. Eksp. Teor. Fiz. 73 (1977) 1216-1240.

Dokshitzer, Yu. L., Khoze, V. A., Mueller, A. H., and Troyan, S. I., 1991. Basics of Perturbative QCD (ed. J. Tran Thanh Van). Editions Frontières, Paris (1991) 367 p.

Dokshitzer, Yu. L., et al., 1997. Better jet clustering algorithms. JHEP 08 (1997) 001. DOI: 10.1088/1126-6708/1997/08/001.

Donatoa, S., 2018. CMS trigger performance. 6th International Conference on New Frontiers in Physics (ICNFP 2017). EPJ Web of Conferences 182, 02037 (2018). DOI: 10.1051/epjconf/201818202037.

Donnelly, T. W., Formaggio, J. A., Holstein, B. R., Milner, R. G., and Surrow, B., 2017. Foundations of Nuclear and Particle Physics. Cambridge University Press, 658 p.

Dorney, B., 2011. Anatomy of a Jet in CMS. Quantum Diaries. Available: https://www.quantumdiaries.org/2011/06/01/anatomy-of-a-jet-in-cms/. (Accessed: 10 June 2020).

Drell, S.D., and Yan, T. M., 1971. Partons and their applications at high energies. Annals of Physics 66 (1971) 578-623. DOI: 10.1016/0003-4916(71)90071-6.

Eichten, T., et al., 1973. Measurement of the Neutrino-Nucleon and Antineutrino-Nucleon Total Cross sections. Phys. Lett. B 46 (1973) 274. DOI: 10.1016/0370-2693(73)90702-8.

Ellis, R. K., and Stirling, W. J., 1990. QCD and Collider Physics. FERMILAB-CONF-90-164-T. DOI: 10.5170/CERN-1991-001.135.

Ellis, S. D., and Soper, D. E., 1993. Successive combination jet algorithm for hadron collisions. Phys. Rev. D 48 (1993) 3160-3166. DOI: 10.1103/PhysRevD.48.3160.

Ellis, S.D., et al., 2007. Jets in Hadron-Hadron Collisions. Prog. Part. Nucl. Phys. 60 (2008) 484-551. DOI: 10.1016/j.ppnp.2007.12.002.

Esen, S., Landsberg, G., Dissertori G., et al., 2007. Plans for Jet Energy Corrections. CMS Analysis Note. CMS AN 2007/055.

Esen, S., and Landsberg, G., 2009. MC Truth L4 EMF-Based Factorized Jet Corrections in CMS. CMS Analysis Note. CMS AN-2009/013.

Galbraith, D., et al., 2012, CERN Summer Student Webfest. Available: https://webfest.web.cern.ch/content/standard-model-standard-infographic. (Accessed: 03 November 2019).

Gao, J., Harland-Lang, L., and Rojo J., 2018. The Structure of the Proton in the LHC Precision Era. Phys. Rept. 742 (2018) 1-121. DOI: 10.1016/j.physrep.2018.03.002.

Gavin, H. P., 2016. Generalized Coordinates, Lagrange's Equations, and Constraints. Lecture Notes for CEE 541-Structural Dynamics. Duke University. http://people.duke.edu/~hpgavin/cee541/LagrangesEqns.pdf. (Accessed: 03 November 2019).

Gay Ducati, M. B., 2014. From DGLAP to Non-Linear Evolution. Summer School and Workshop on High Energy Physics at the LHC. https://indico.cern.ch/event/346738/contributions/813706/attachments/684139/939708/NatalClass_1_MBGD.pdf. (Accessed: 14 January 2020).

Gell-Mann, M., 1964. A Schematic Model of Baryons and Mesons. Phys. Lett., 8 (1964) 214-215. DOI: 10.1016/S0031-9163(64)92001-3.

Glashow, S. L., 1961. Partial Symmetries of Weak Interactions. Nucl. Phys. 22, 579 (1961). DOI: 10.1016/0029-5582(61)90469-2.

Glazov, S., and H1 Collaboration, 2007. Measurement of DIS cross section at HERA. Braz. J. Phys. [online]. 2007, vol.37, n.2c, pp.793-797. ISSN 0103-9733. DOI: 10.1590/S0103-97332007000500030.

Gleisberg, T., et al., 2009. Event generation with SHERPA 1.1. JHEP 02 (2009) 007. DOI: 10.1088/1126-6708/2009/02/007.

Gribov, V.N., and Lipatov, L.N., 1972. Deep inelastic e p scattering in perturbation theory. Sov. J. Nucl. Phys. 15 (1972) 438-450. Yad. Fiz. 15 (1972) 781-807.

Gustafson, G., 2007. Multiple scattering, underlying event, and minimum bias. LU-TP 07-39. arXiv: 0712.1941 [hep-ph].

H1 Collaboration, 1995. Transverse energy and forward jet production in the low *x* regime at HERA. Phys. Lett. B 356 (1995) 118-128. DOI: 10.1016/0370-2693(95)00804-T.

______, 1996. Measurement of charged particle transverse momentum spectra in deep inelastic scattering. Nucl. Phys. B 485 (1997) 3-24. DOI: 10.1016/S0550-3213(96)00675-X.

______, 1997. Low Q^2 jet production at HERA and virtual photon structure. Phys. Lett. B 415 (1997) 418-434. DOI: 10.1016/S0370-2693(97)01264-1.

______, 2000. Measurement of Dijet Cross-Sections at Low Q^2 and the Extraction of an Effective Parton Density for the Virtual Photon. Eur. Phys. J. C 13 (2000) 397-414. DOI: 10.1007/s100520050704.

______, 2000a. Dijet event rates in deep inelastic scattering at HERA. Eur. Phys. J. C 13 (2000) 415-426. DOI: 10.1007/s100520050705.

______, 2000b. Measurements of transverse energy flow in deep inelastic scattering at HERA. Eur. Phys. J. C 12 (2000) 595-607. DOI: 10.1007/s100520000287.

______, 2002. Measurement of inclusive jet cross-sections in deep inelastic *ep* scattering at HERA. Phys. Lett. B 542 (2002) 193-206. DOI: 10.1016/S0370-2693(02)02375-4.

______, 2017. Measurement of Jet Production Cross Sections in Deep-inelastic *ep* Scattering at HERA. DESY-16-200. arXiv: 1611.03421 [hep-ex]. DOI: 10.1140/epjc/s10052-017-4717-9.

Halzen, F., and Martin, A. D., 1984. Quarks and leptons: An introductory course in modern particle physics. John Wiley & Sons, New York, USA (1984) 396 p. ISBN: 9780471887416.

Harris, R., and Kousouris, K., 2008. MC Truth L2 & L3 Factorized Jet Corrections at CMS. CMS Analysis Note. CMS AN-2008/003.

Heister, A., et al., 2005. Jet Reconstruction and Performance in the CMS Detector. CMS NOTE AN2005/005. https://w3.iihe.ac.be/~bclerbau/jet.pdf.

Hollik, W., 2010. Quantum field theory and the Standard Model. Max Planck Institut für Physik, Munich, Germany. arXiv: 1012.3883v1 [hep-ph].

Höche, S., 2014. Introduction to parton-shower event generators. SLAC-PUB 16160. arXiv:1411.4085 [hep-ph].

JADE Collaboration, 1980. Observation of Planar Three Jet Events in $e^+ e^-$ Annihilation and Evidence for Gluon Bremsstrahlung. Phys. Lett. B 91 (1980) 142-147. DOI: 10.1016/0370-2693(80)90680-2.

Ji, X., 2007. Lecture Notes for Quarks, Nuclei and the Cosmos: An Introduction to Modern Nuclear Physics. University of Maryland. Available: https://www.physics.umd.edu/courses/Phys741/xji/chapter1.pdf. (Accessed: 30 October 2019).

Johannesson, H., 2014. Lecture Notes for Topological Quantum Matter. Department of Physics, University of Gothenburg. Available: http://physics.gu.se/~tfkhj/TOPO/DiracEquation.pdf. (Accessed: 05 November 2019).

Jung, H., 1999. CCFM prediction on forward jets and F_2: parton level predictions and a new hadron level Monte Carlo generator Cascade. arXiv: hep-ph/9908497.

Jung, H., and Salam, G. P., 2001. Hadronic final state predictions from CCFM: the hadron-level Monte Carlo generator Cascade. Eur. Phys. J. C 19 (2001) 351-360. DOI: 10.1007/s100520100604.

Karavdina, A., et al., 2016. Determination of the residual jet-energy corrections with dijet events at 13 TeV. CMS Draft Analysis Note. CMS AN-16-334.

Kirschenmann, H., et al., 2011. Determination of residual jet-energy corrections using the dijet-balance method. CMS Analysis Note. CMS AN-2011/352.

Kirschenmann, H., 2014. Jet Energy Scale Corrections and their Impact on Measurements of the Top-Quark Mass at CMS. University of Hamburg. PhD Thesis. DOI: 10.3204/DESY-THESIS-2014-031.

Kogler, R., et al., 2019. Jet Substructure at the Large Hadron Collider. Rev. Mod. Phys. 91 (2019) 4, 045003. DOI: 10.1103/RevModPhys.91.045003.

Kovchegov, Y. V., and Levin, E., 2012. Quantum Chromodynamics at High Energy. Cambridge University Press, Cambridge Monographs on Particle Physics, Nuclear Physics and Cosmology 33 (2012) 1-350. DOI: 10.1017/CBO9781139022187. (A color version of the figures are retrieved from www.cambridge.org/9780521112574).

Kuraev, E. A., Lipatov, L. N., and Fadin, V. S., 1976. Multi-Reggeon Processes in the Yang-Mills Theory. Sov. Phys. JETP 44 (1976) 443-450. Zh. Eksp. Teor. Fiz. 71 (1976) 840-855.

______, 1977. The Pomeranchuk Singularity in Nonabelian Gauge Theories. Sov. Phys. JETP 45 (1977) 199-204, Zh. Eksp. Teor. Fiz. 72 (1977) 377-389.

Kwieciński, J., 1994. Physics at Low x. arXiv: hep-ph/9409456.

Lai, H.-L., et al., 2010. New parton distributions for collider physics. Phys. Rev. D 82 (2010) 074024. DOI: 10.1103/PhysRevD.82.074024.

LHC Study Group (eds. Lefèvre, P., and Pettersson, T. S.), 1995. The Large Hadron Collider: Conceptual Design. CERN-AC-95-05- LHC 223 p. http://cds.cern.ch/record/291782.

LHCb Collaboration, 2008. The LHCb Detector at the LHC. JINST, 3: S08005, 2008. DOI: 10.1088/1748-0221/3/08/S08005.

Li, J., 2009. Light front Hamiltonian and its application in QCD, Graduate Theses and Dissertations. 11067, Iowa State University, https://lib.dr.iastate.edu/etd/11067. (Accessed: 11 November 2019).

Lipatov, L. N., 1974. The parton model and perturbation theory. Sov. J. Nucl. Phys. 20 (1975) 94–102. Yad. Fiz. 20 (1974) 181-198.

Lobanov, A., and CMS Collaboration, 2015. The CMS Outer HCAL SiPM Upgrade. J. Phys.: Conf. Ser. 587 012005. DOI:10.1088/1742-6596/587/1/012005.

Lonnblad, L., 2006. ThePEG, PYTHIA7, Herwig++ and ARIADNE. Nucl. Instrum. Meth. A 559 (2006) 246–248. DOI: 10.1016/j.nima.2005.11.143.

Mans, J., (ed.), Anderson, J. (ed.), Dahmes, B. (ed.), de Barbaro, P. (ed.), Freeman, J. (ed.), Grassi, T. (ed.), Hazen, E. (ed.), Ruchti, R. (ed.), Schimdt, I. (ed.), Shaw, T. (ed.), Tully, C. (ed.), Whitmore, J. (ed.), and Yetkin, T. (ed.), 2012. CMS Technical Design Report for the Phase 1 Upgrade of the Hadron Calorimeter. CERN-LHCC-2012-015. CMS-TDR-10. https://cds.cern.ch/record/1481837/files/CMS-TDR-010.pdf.

Marchesini, G., and Webber, B. R., 1984. Simulation of QCD Jets Including Soft Gluon Interference. Nucl. Phys. B 238 (1984) 1-29. DOI: 10.1016/0550-3213(84)90463-2.

______, 1988. Monte Carlo Simulation of General Hard Processes with Coherent QCD Radiation. Nucl. Phys. B 310 (1988) 461-526. DOI: 10.1016/0550-3213(88)90089-2.

Marchesini, G., Webber, B. R., Abbiendi, G., Knowles, I. G., Seymour, M.H., and Stanco, L., 1992. HERWIG 5.1-a Monte Carlo event generator for simulating hadron emission reactions with interfering gluons. Comput. Phys. Commun. 67, 465 (1992). DOI: 10.1016/0010-4655(92)90055-4.

______, 1996. HERWIG version 5.9. arXiv: hep-ph/9607393.

MARK-J Collaboration, 1979. Discovery of Three Jet Events and a Test of Quantum Chromodynamics at PETRA Energies. Phys. Rev. Lett. 43 (1979) 830. DOI: 10.1103/PhysRevLett.43.830.

Martin, A. D., Stirling, W. J., Thorne, R. S., and Watt, G., 2009. Parton distributions for the LHC. Eur. Phys. J. C 63 (2009) 189-285. DOI: 10.1140/epjc/s10052-009-1072-5.

McCauley, T., and CMS Collaboration, 2017. Collision events recorded by CMS in 2016. CMS Collection. CMS-PHO-EVENTS-2017-001. Available: https://cds.cern.ch/record/2241144. (Accessed: 19 June 2020).

Mobs, E., 2018. The CERN accelerator complex - August 2018. OPEN-PHO-ACCEL-2018-005. Available: https://cds.cern.ch/record/2636343. (Accessed: 15 November 2019).

Moraes, A., Buttar, C., and Dawson, I., 2007. Prediction for minimum bias and the underlying event at LHC energies. Eur. Phys. J. C 50, 435–466 (2007). DOI: 10.1140/epjc/s10052-007-0239-1.

Moretti, S., Lönnblad, L., and Sjöstrand, T., 1998. New and Old Jet Clustering Algorithms for Electron-Positron Events. JHEP 08 (1998) 001. DOI: 10.1088/1126-6708/1998/08/001.

Naumann-Emme, S., et al., 2010. Validation of the Jet Energy Corrections in Simulated Events with Top Quarks. CMS Analysis Note. CMS AN-2010/094. http://cms.cern.ch/iCMS/user/noteinfo?cmsnoteid=CMS%20AN-2010/094.

Neutelings, I., 2017. UZH CMS wiki pages. Universität Zürich, Physik-Institut. Available:https://wiki.physik.uzh.ch/cms/latex:example_spherical_coordinates. (Accessed: 03 May 2020).

Paganini, P., 2014. Quantum Chromodynamic. Lecture Notes for Advanced Particle Physics, PHY 5802. Laboratoire Leprince Ringuet, Ecole Polytechnique. Available: http://polywww.in2p3.fr/~paganini/ch5.pdf. (Accessed: 13 November 2019).

Perloff, A., 2012. Pileup measurement and mitigation techniques in CMS. Journal of Physics: Conference Series 404 (2012) 012045. DOI: 10.1088/1742-6596/404/1/012045.

Perloff, A., and Eusebi, R., 2013. JetMETAnalysis/JetResponseAnalyzer software package: A how-to guide for checking out, compiling, and running the package. CMS Analysis Note. CMS AN-13-131.

Pich, A., 1995. Quantum Chromodynamics. FTUV/95-19. IFIC/95-19. arXiv: hep-ph/9505231v1.

______, 2000. Aspects of Quantum Chromodynamic. IFIC/00-5, FTUV/00-5. arXiv: hep-ph/0001118.

______, 2007. The Standard Model of Electroweak Interactions. IFIC/07-27, FTUV/07-0529. arXiv: 0705.4264 [hep-ph].

Pivarski, J., 2008. Beautiful beam-halo tracks in CMS! WordPress.com Web page. Available: https://cornellmath.wordpress.com/2008/09/10/beautiful-beam-halo-tracks-in-cms/. (Accessed: 06 May 2020).

PLUTO Collaboration, 1979. Evidence for Gluon Bremsstrahlung in $e^+ e^-$ Annihilations at High-Energies. Phys. Lett. B 86 (1979) 418-425. DOI: 10.1016/0370-2693(79)90869-4.

Rabbertz, K., 2017. Jet Physics at the LHC: The Strong Force beyond the TeV Scale. Springer International Publishing, 214 p.

Reimers, A., and Karavdina A., 2016. Update on ReReco L2Residual. CMS Jet Energy Corrections and Resolution Meeting (23 Nov 2016). Available: https://indico.cern.ch/event/590291/contributions/2391551/attachments/1381932/2101228/L2Res_L1RC_Comparison.pdf. (Accessed: 25 February 2020).

Ryan, P., 2005. Forward jet production at HERA. Volume 021- International Europhysics Conference on High Energy Physics (HEP2005)- Hard QCD. DOI: 10.22323/1.021.0053.

Saka, H., 2016. HCAL noise study status. Run Organization Meeting: Calorimeters Data Jamboree (27 May 2016). https://indico.cern.ch/event/534040/.

Sakuma, T., and McCauley, T., 2014. Detector and Event Visualization with SketchUp at the CMS Experiment. 2014 J. Phys.: Conf. Ser. 513 022032. DOI: 10.1088/1742-6596/513/2/022032.

Salam, G. P., 2009. Towards Jetography. Eur. Phys. J. C 67 (2010) 637-686. DOI: 10.1140/epjc/s10052-010-1314-6.

Schwartzman, A., 2015. Jet energy calibration at the LHC. arXiv: 1509.05459v1 [hep-ex].

Sjöstrand, T., and van Zijl, M, 1987. A multiple-interaction model for the event structure in hadron collisions. Phys. Rev. D 36 (1987) 2019–2041. DOI: 10.1103/PhysRevD.36.2019.

Sjöstrand, T., Lönnblad, L., and Mrenna, S., 2001. PYTHIA 6.2 Physics and manual. arXiv: hep-ph/0108264.

Sjöstrand, T., et al., 2006. PYTHIA 6.4 Physics and Manual. JHEP 05 (2006) 026. DOI: 10.1088/1126-6708/2006/05/026.

Sjöstrand, T., 2005. Monte Carlo generators for the LHC. Academic Training Lecture Regular Programme. CERN, Geneva, Switzerland. 4-7 Apr 2005. Available: https://indico.cern.ch/event/418172/. (Accessed: 13 February 2020).

______, 2008. PYTHIA 8 Status Report. arXiv: 0809.0303 [hep-ph].

______, 2014. QCD Processes, PYTHIA 8.1. Available: http://home.thep.lu.se/~torbjorn/pythia81html/QCDProcesses.html. (Accessed: 03 May 2020).

Sonneveld, J., and CMS Collaboration, 2017. Commissioning and first results from the CMS phase 1 upgrade pixel detector. CMS-CR-2017-425. arXiv:1807.08987 [physics.ins-det].

Stöver, M., and CMS Collaboration, 2017. Jet energy calibrations at the CMS experiment with 13 TeV collisions. CMS-CR-2017-307. PoS EPS-HEP2017 (2017) 805. DOI: 10.22323/1.314.0805.

Stenson, K., and Rao, A., 2012. Reconstructing a multitude of particle tracks within CMS. CMS Web Page. Available: http://cms.web.cern.ch/news/reconstructing-multitude-particle-tracks-within-cms. (Accessed: 03 May 2020).

Sterman, G., and Weinberg, S., 1977. Jets from Quantum Chromodynamics. Phys. Rev. Lett. 39 (1977) 1436. DOI: 10.1103/PhysRevLett.39.1436.

TASSO Collaboration, 1979. Evidence for Planar Events in $e^+ e^-$ Annihilation at High-Energies. Phys. Lett. B 86 (1979) 243-249. DOI: 10.1016/0370-2693(79)90830-X.

UA2 Collaboration, 1983. Measurement of Production and Properties of Jets at the CERN anti-*p* *p* Collider. Z. Phys. C 20 (1983) 117-134. DOI: 10.1007/BF01573214.

University of Oulu, 2004. Lecture Notes for Advanced Quantum Mechanics. Theoretical Physics, Department of Physics. Available: https://www.oulu.fi/tf/kvmIII/english/2004/20_klein.pdf. (Accessed: 05 November 2019).

Védrine, P., 2015. Large Superconducting Magnet Systems. arXiv: 1501.07169 [physics.acc-ph].

Webber, B. R., 1984. A QCD Model for Jet Fragmentation Including Soft Gluon Interference. Nucl. Phys. B 238 (1984) 492-528. DOI: 10.1016/0550-3213(84)90333-X.

Webber, B. R., 1994. Hadronization. Cavendish–HEP–94/17, 1994, arXiv: hep-ph/9411384v2.

______, 1999. Fragmentation and Hadronization. CERN-TH/99-387. Cavendish-HEP-99/16. arXiv: hep-ph/9912292v1.

______, 2006. Lecture Notes for Gauge Field Theory. Department of Physics. University of Cambridge. Available: https://www.hep.phy.cam.ac.uk/theory/webber/GFT/gft_handout2_06.pdf. (Accessed: 05 November 2019).

______, 2008. QCD Phenomenology at High Energy. CERN Academic Training Lectures 2008. Available: https://indico.cern.ch/event/24749/ . (Accessed: 13 November 2019).

______, 2011. Parton shower Monte Carlo event generators. Scholarpedia, 6(12):10662.Available:http://www.scholarpedia.org/article/Parton_shower_Monte_Carlo_event_generators. (Accessed: 06 May 2020).

Weinberg, S., 1967. A Model of Leptons. Phys. Rev. Lett. 19, 1264 (1967).

Wobisch, M., and Wengler, T., 1998. Hadronization Corrections to Jet Cross Sections in Deep-Inelastic Scattering. arXiv: hep-ph/9907280.

Woithe, J., et al., 2017. Let's have a coffee with the Standard Model of particle physics! Phys. Educ. 52 (2017) 034001. DOI: 10.1088/1361-6552/aa5b25.

Yao, W. M., et al., 2006. Review of Particle Physics. J. Phys. G, 33 1 (2006). DOI: 10.1088/0954-3899/33/1/001.

ZEUS Collaboration, 2000. The Q^2 dependence of dijet cross-sections in γp interactions at HERA. Phys. Lett. B 479 (2000) 37-52. DOI: 10.1016/S0370-2693(00)00311-7.

______, 2002. Dijet production in neutral current deep inelastic scattering at HERA. Eur. Phys. J. C 23 (2002) 13-27. DOI: 10.1007/s100520100845.

______, 2012. Inclusive-jet photoproduction at HERA and determination of α_s. Nucl. Phys. B 864 (2012) 1. DOI: 10.1016/j.nuclphysb.2012.06.006. arXiv: 1205.6153 [hep-ex].

Zweig, G., 1964. An SU_3 Model for Strong Interaction Symmetry and its Breaking. CERN-TH-412. https://cds.cern.ch/record/570209.

https://home.fnal.gov/~chlebana/CMS/Phase1/figs/HCAL-Depth-Segmentation-Phase1-HE-HBOption1.pdf. (Accessed: 20 May 2020).

CURRICULUM VITAE

She graduated from Cukurova University with a BSc in Physics and a double major in Mathematics in 2010. She held an MSc in the Department of Physics at Cukurova University in 2013 by working in the CMS experiment at the CERN. In her MSc dissertation, she focused on two different types of research. Firstly, she studied the noise rates of Hybrid PhotoDiodes (HPDs) in the Hadron Barrel (HB), Hadron Endcap (HE) sub-calorimeter of the CMS-HCAL. She also studied for the Self-Trigger analysis of newly installed Silicon Photo Multipliers (SiPMs) in Hadron Outer (HO) sub-calorimeter of the HCAL. In spring 2013, she has started her PhD in the Department of Physics at Cukurova University. During her PhD, she involved different physics analyses within the CMS experiment and gained experience in test-stand and commissioning of the detector hardware.

APPENDIX

A. Appendix

A.1 Control Plots – Asymmetry Distributions

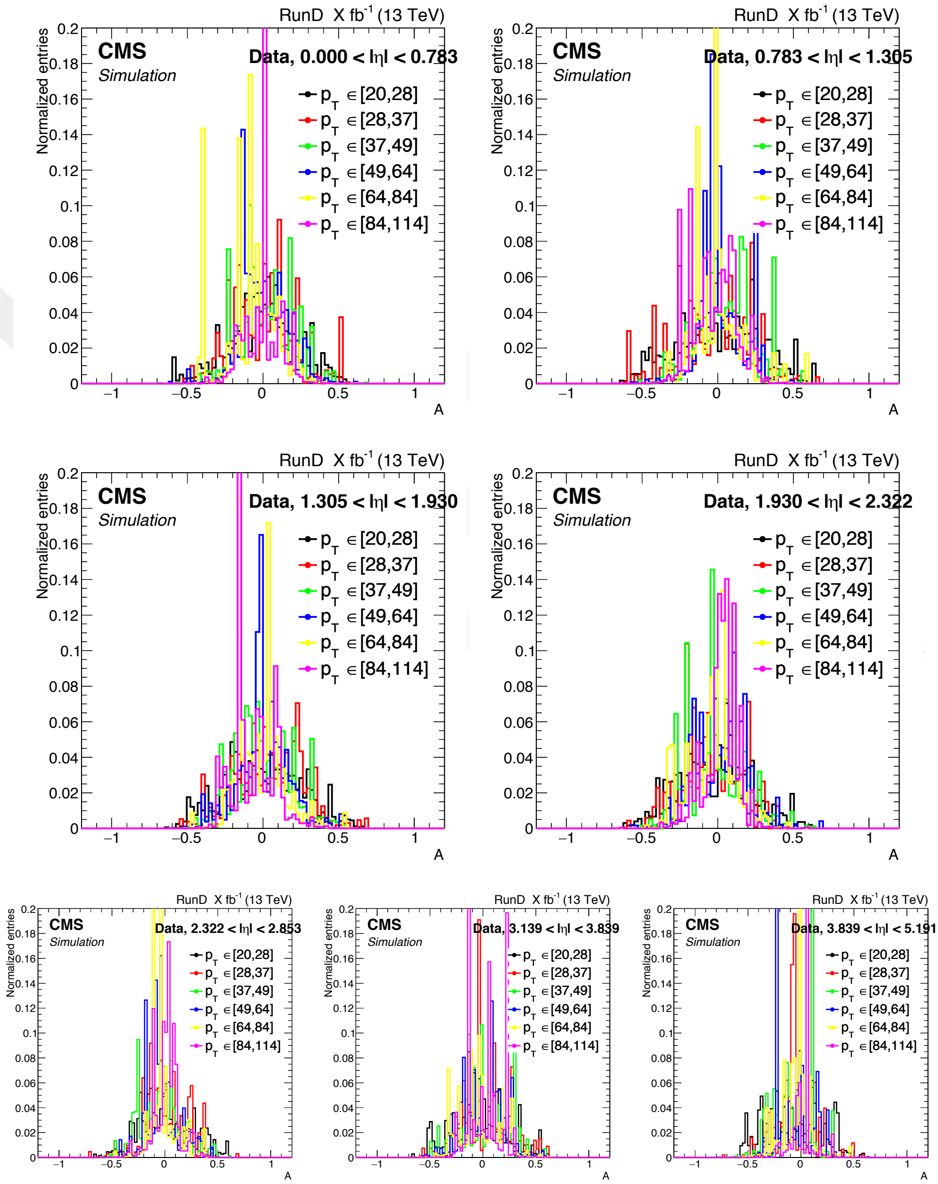

Figure A.1. The asymmetry distributions for all η bins and p_T bins in data.

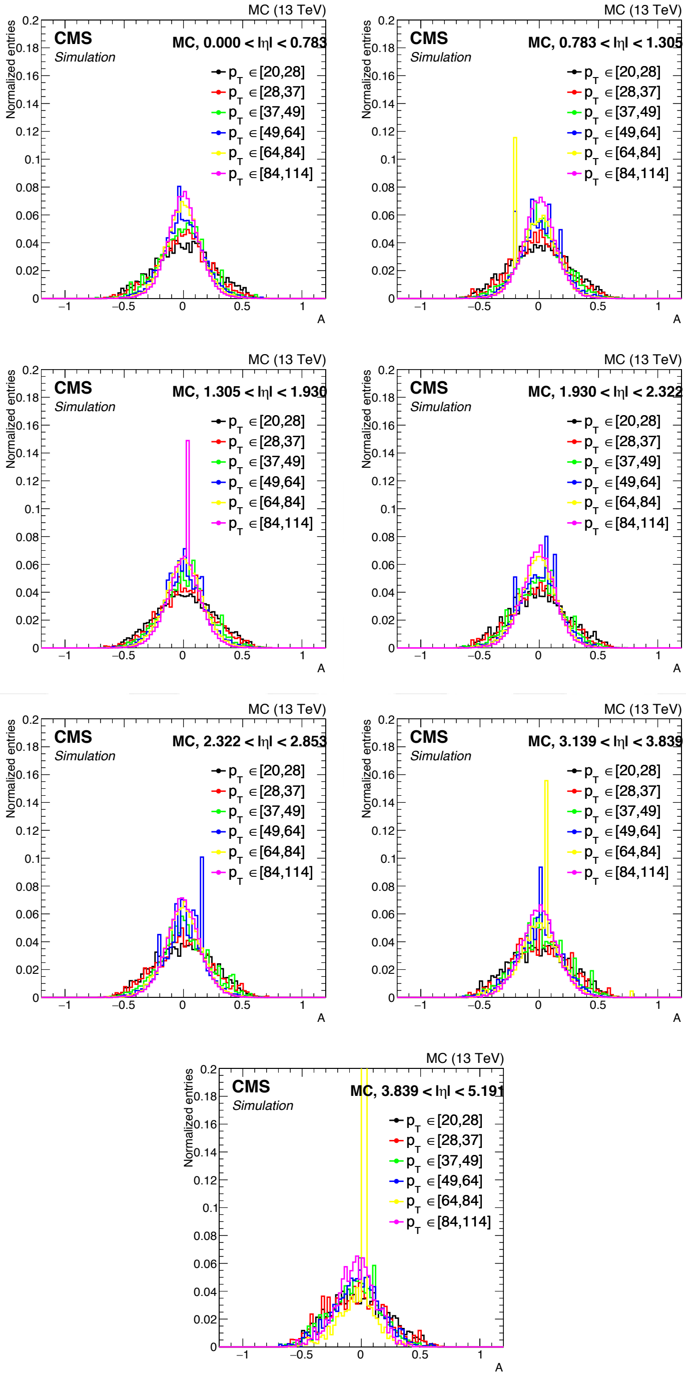

Figure A.2. The asymmetry distributions for all η bins and p_T bins in MC.

A.2 Control Plots – MPF Distributions

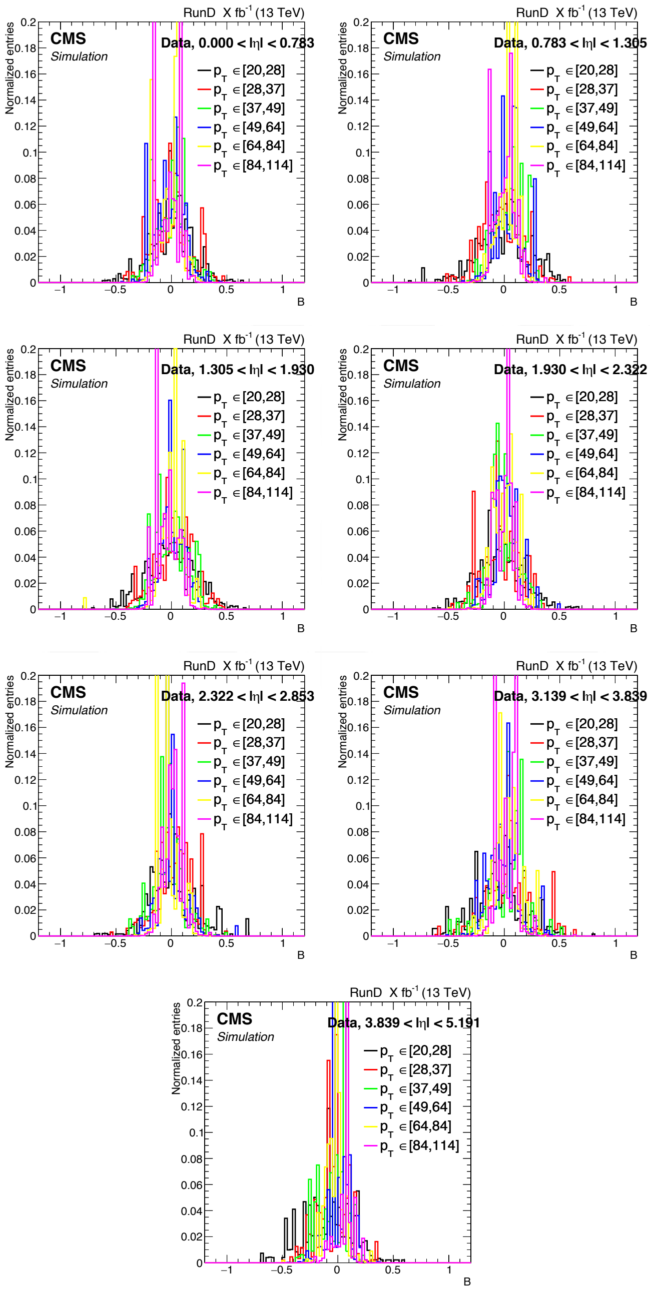

Figure A.3. The MPF distributions for all η bins and p_T bins in data.

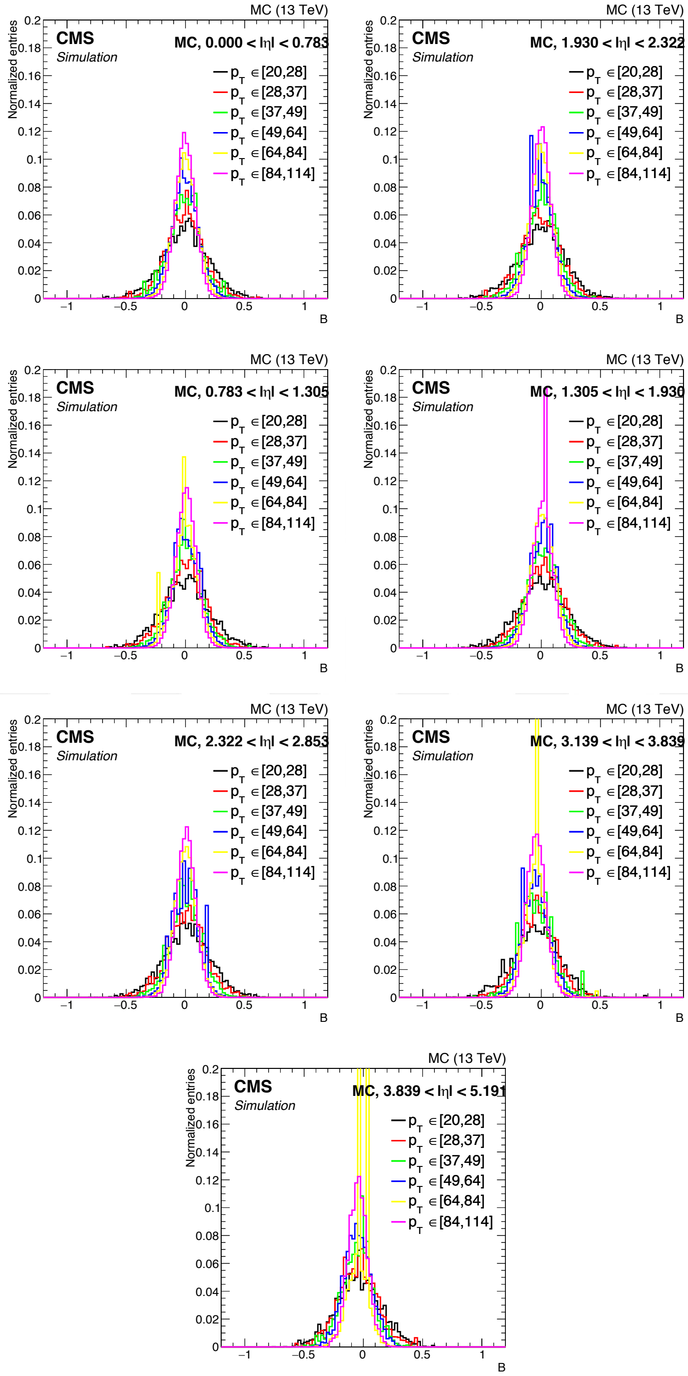

Figure A.4. The MPF distributions for all η bins and p_T bins in MC.

A.3 Control Plots – Asymmetry Distributions for DATA

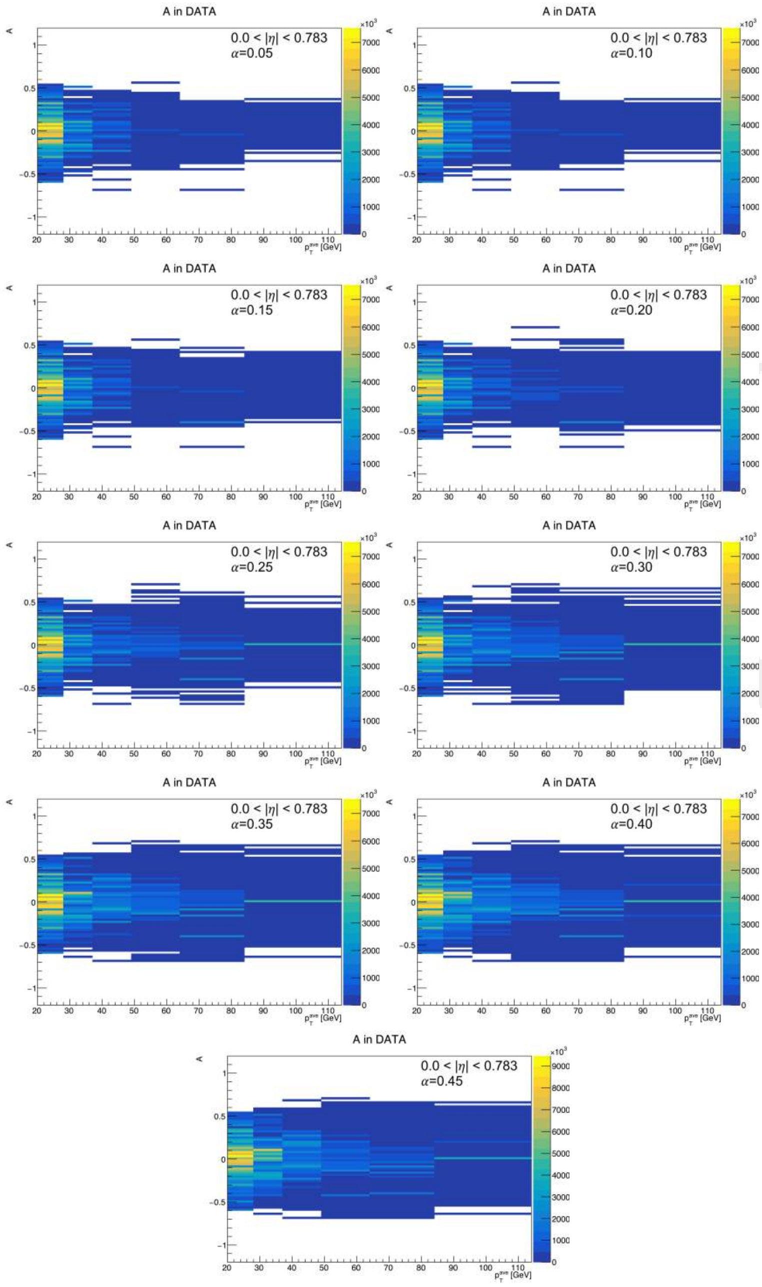

Figure A.5. The distribution of asymmetry quantity in data as a function of p_T^{ave} in bins of $0 < |\eta| < 0.783$ and the nine different α bins from 0.05 to 0.45.

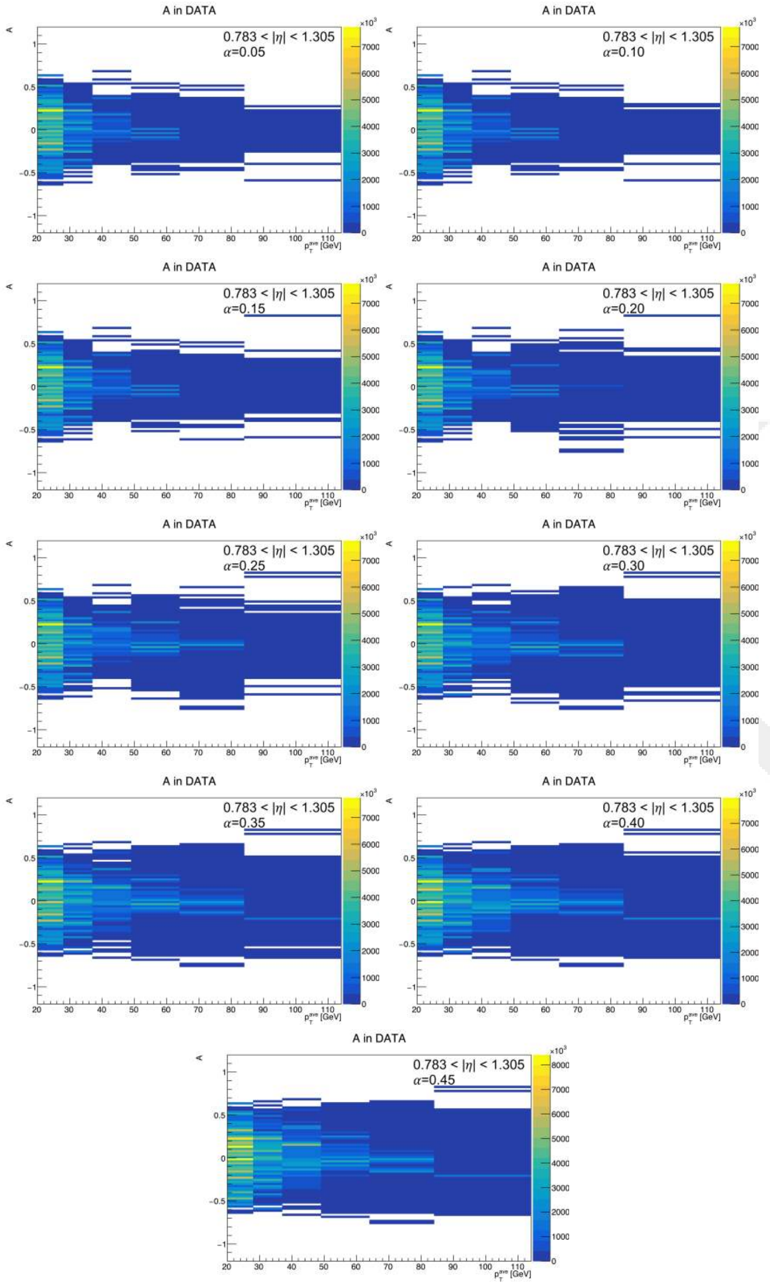

Figure A.6. The distribution of asymmetry quantity in data as a function of p_T^{ave} in bins of $0.783 < |\eta| < 1.305$ and the nine different α bins from 0.05 to 0.45.

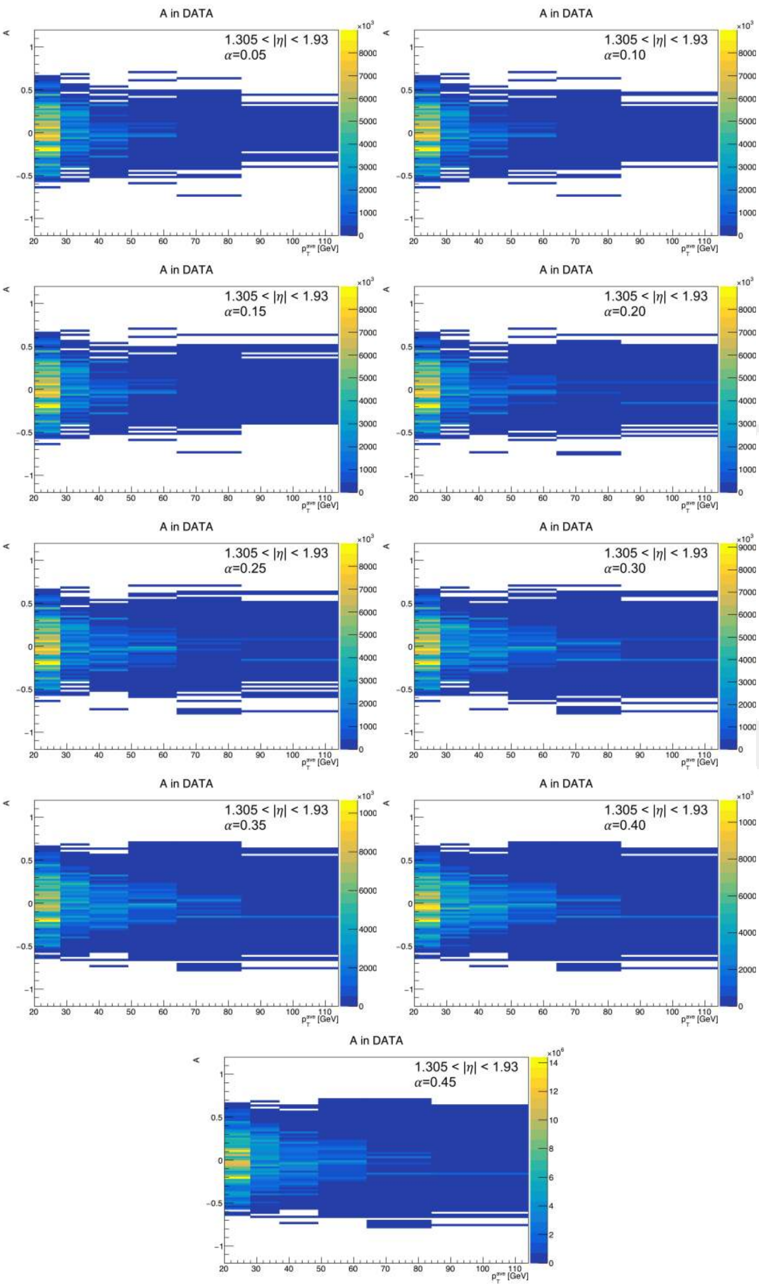

Figure A.7. The distribution of asymmetry quantity in data as a function of p_T^{ave} in bins of $1.305 < |\eta| < 1.93$ and the nine different α bins from 0.05 to 0.45.

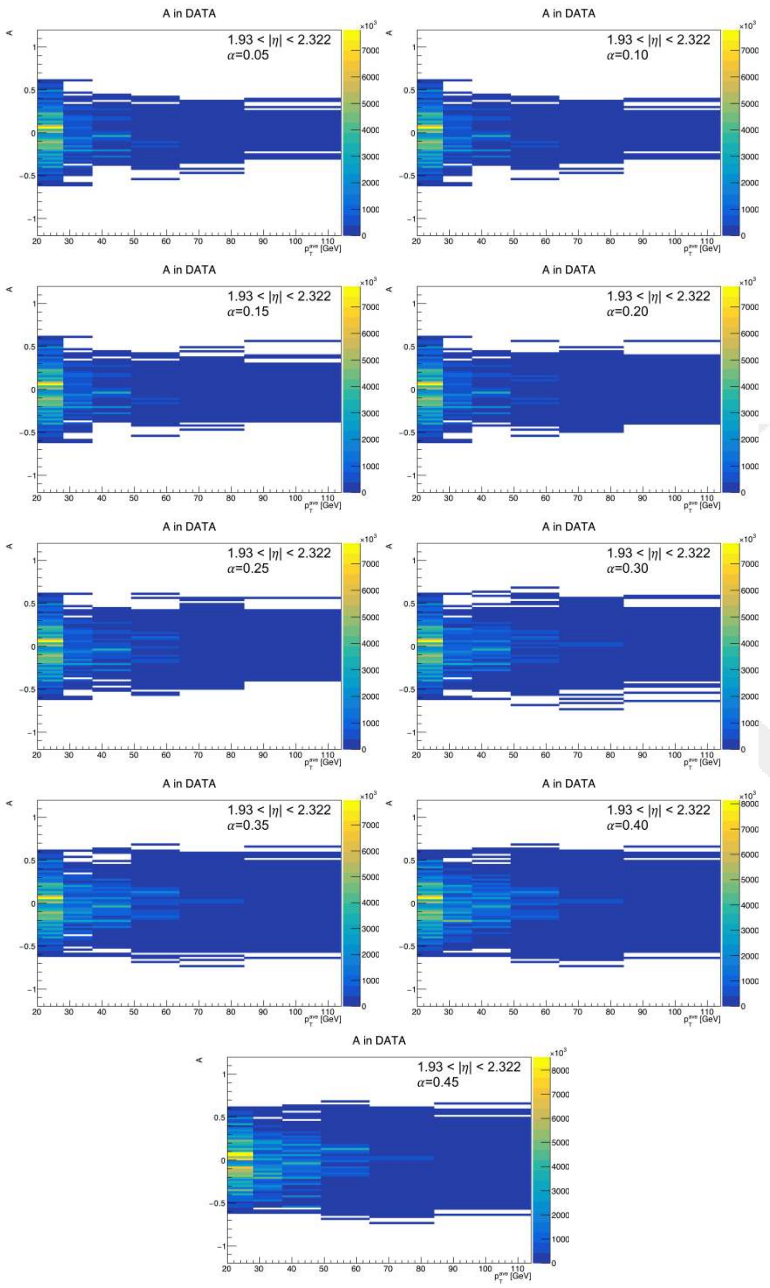

Figure A.8. The distribution of asymmetry quantity in data as a function of p_T^{ave} in bins of $1.93 < |\eta| < 2.322$ and the nine different α bins from 0.05 to 0.45.

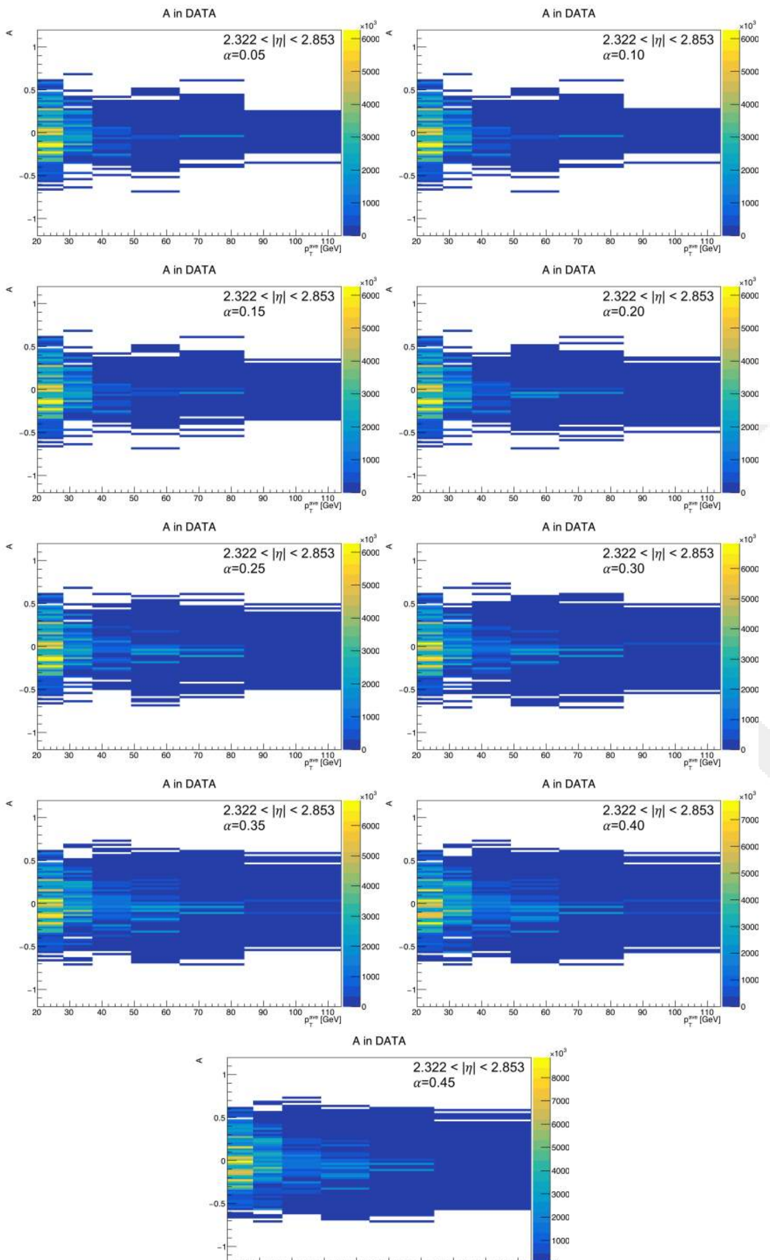

Figure A.9. The distribution of asymmetry quantity in data as a function of p_T^{ave} in bins of $2.322 < |\eta| < 2.853$ and the nine different α bins from 0.05 to 0.45.

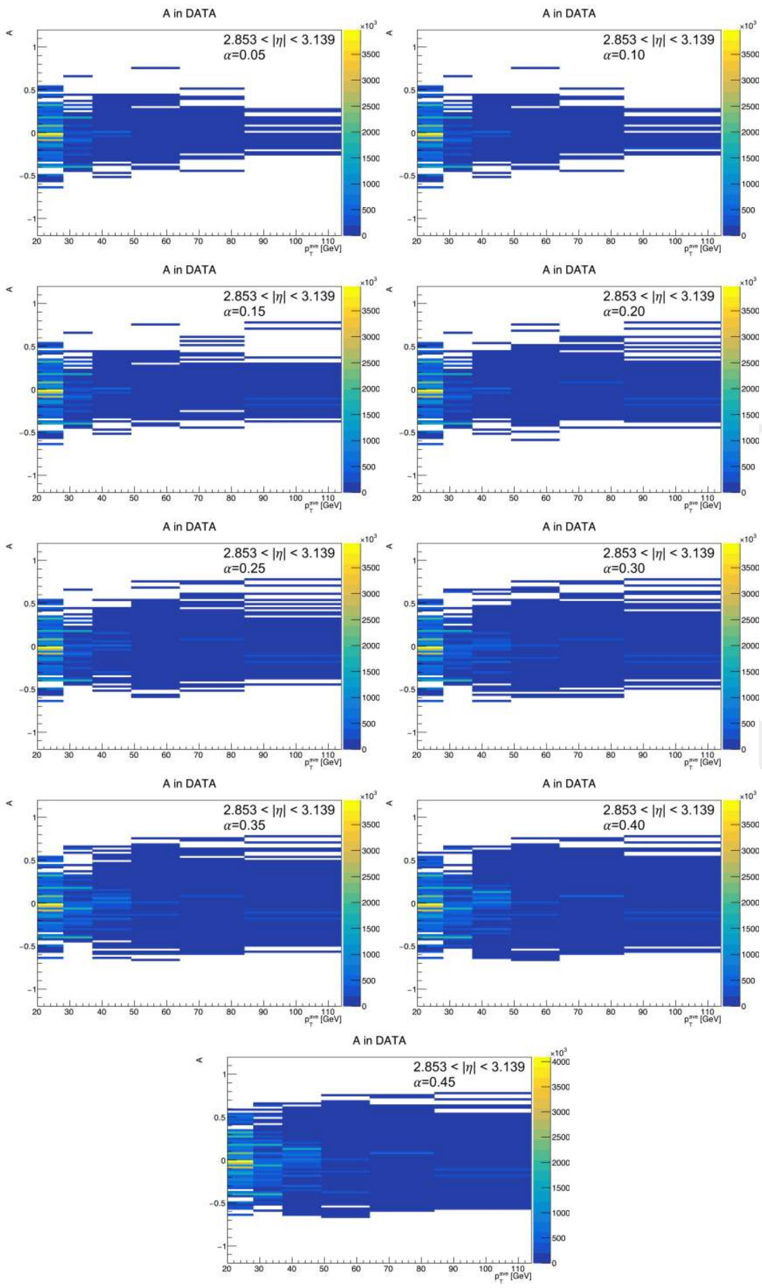

Figure A.10. The distribution of asymmetry quantity in data as a function of p_T^{ave} in bins of $2.853 < |\eta| < 3.139$ and the nine different α bins from 0.05 to 0.45.

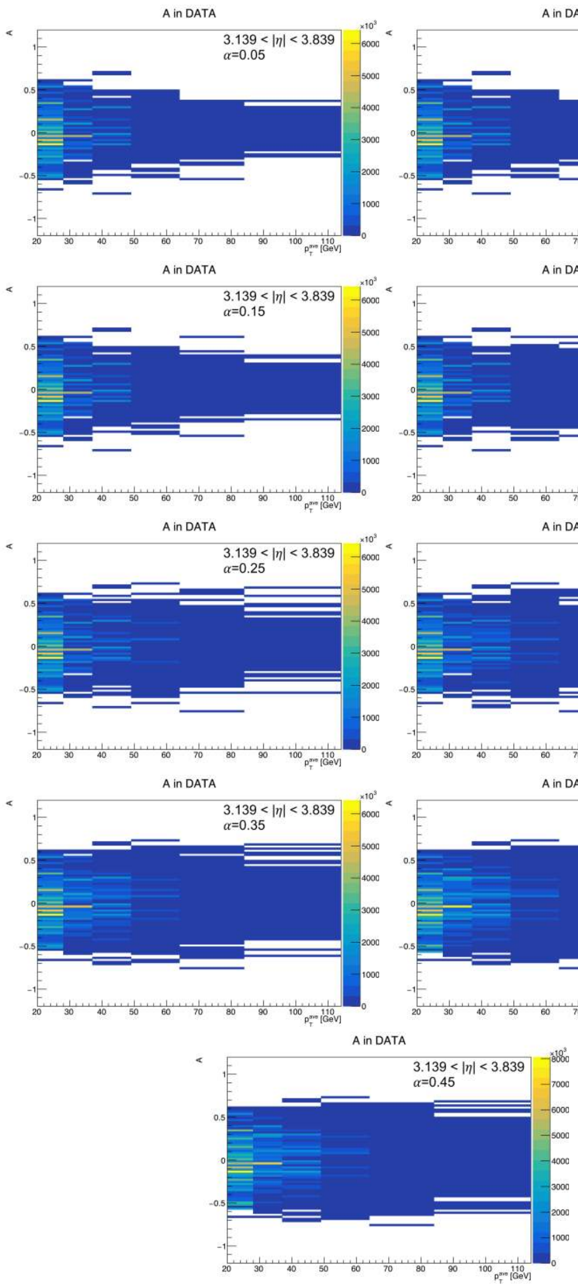

Figure A.11. The distribution of asymmetry quantity in data as a function of p_T^{ave} in bins of $3.139 < |\eta| < 3.839$ and the nine different α bins from 0.05 to 0.45.

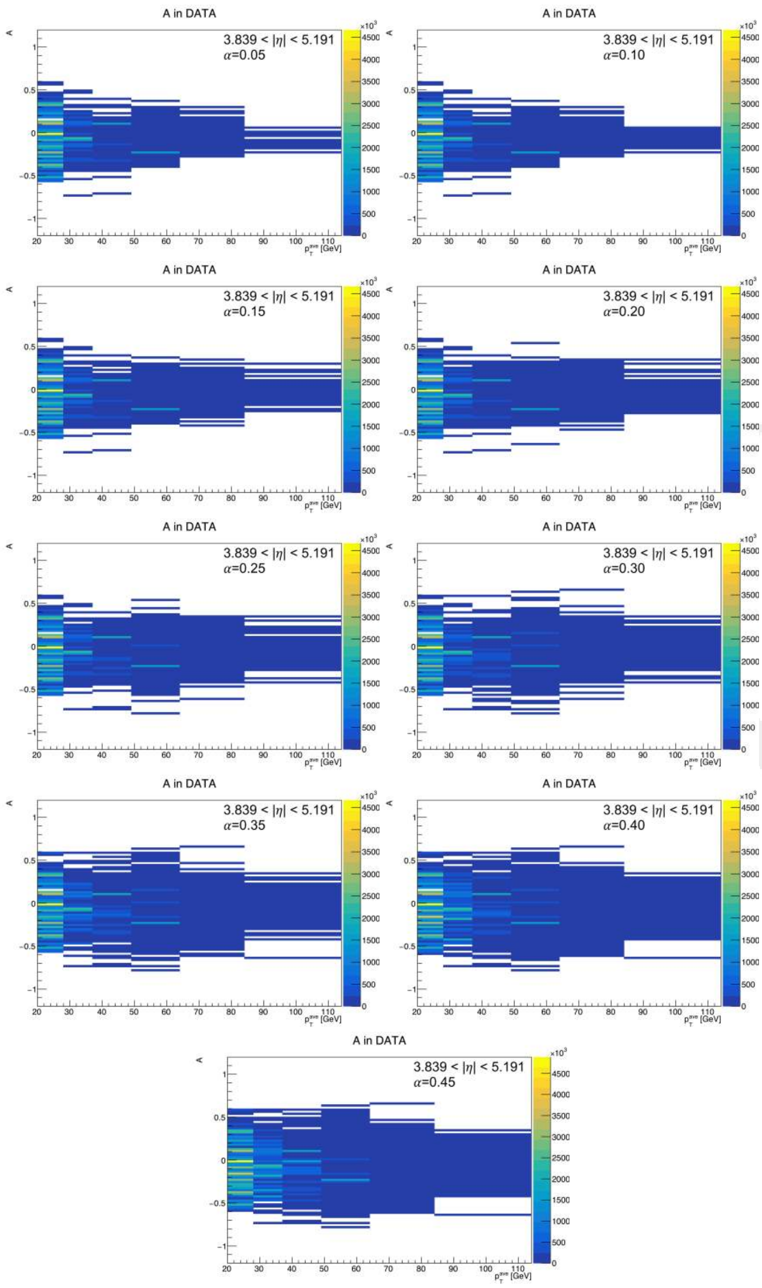

Figure A.12. The distribution of asymmetry quantity in data as a function of p_T^{ave} in bins of $3.839 < |\eta| < 5.191$ and the nine different α bins from 0.05 to 0.45.

A.4. Control Plots – Asymmetry Distributions for MC

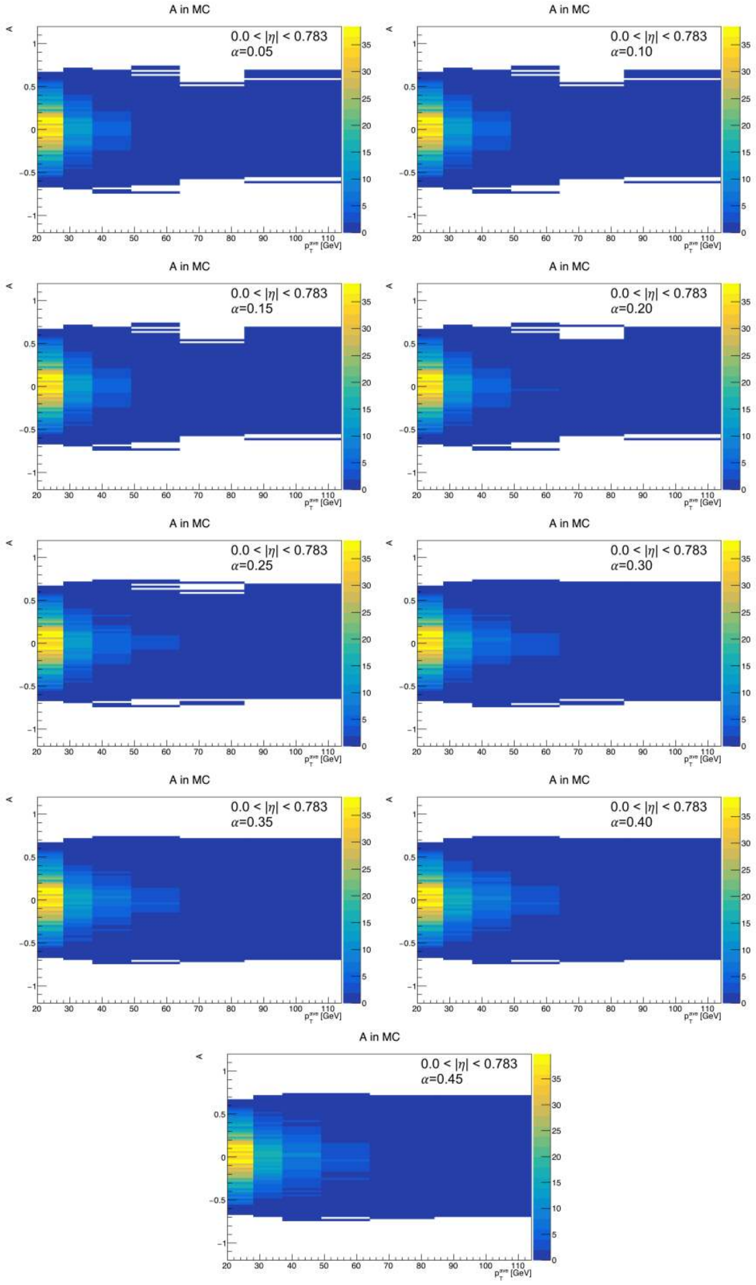

Figure A.13. The distribution of asymmetry quantity in simulation as a function of p_T^{ave} in bins of $0 < |\eta| < 0.783$ and the nine different α bins from 0.05 to 0.45.

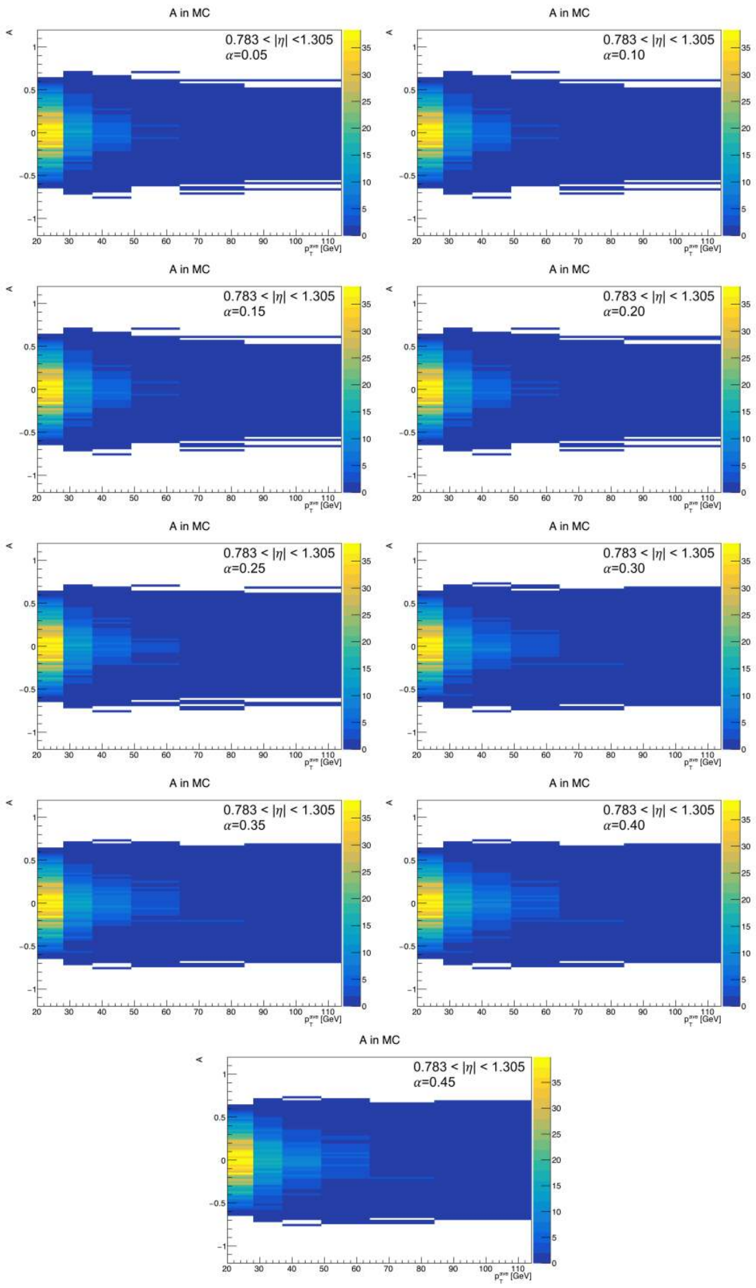

Figure A.14. The distribution of asymmetry quantity in simulation as a function of p_T^{ave} in bins of $0.783 < |\eta| < 1.305$ and the nine different α bins from 0.05 to 0.45.

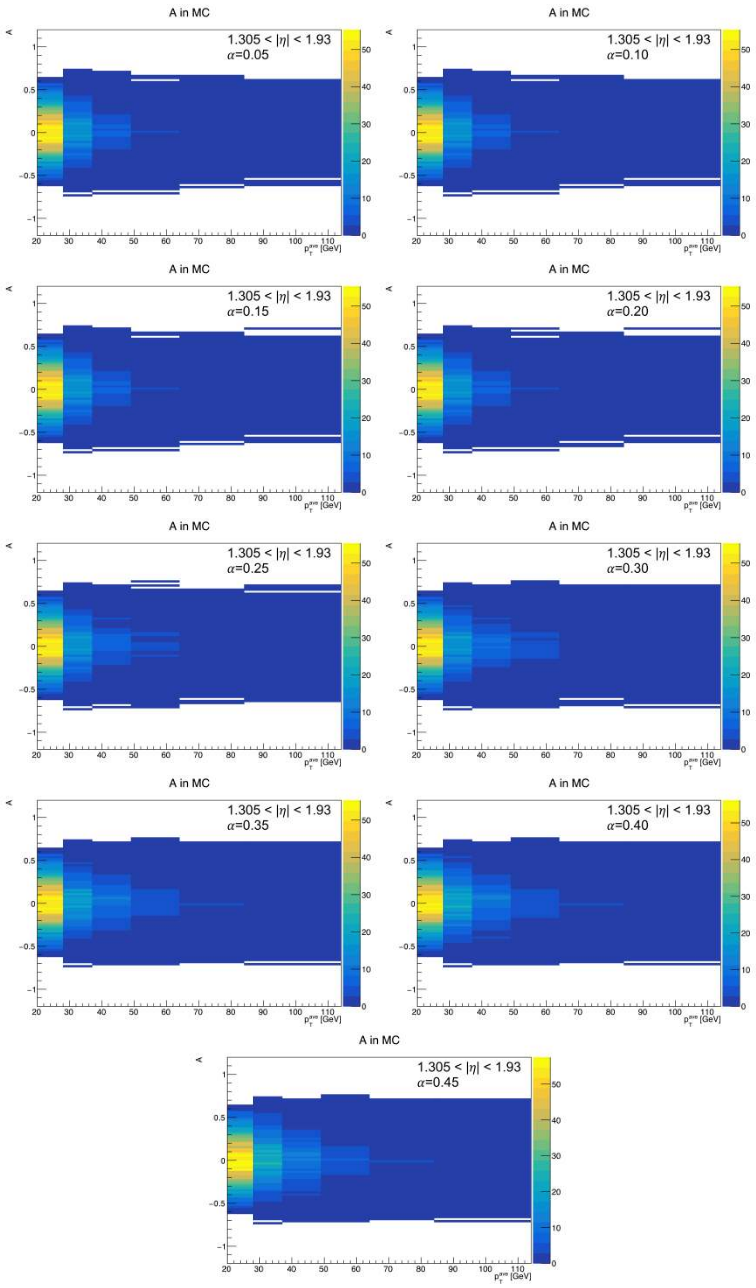

Figure A.15. The distribution of asymmetry quantity in simulation as a function of p_T^{ave} in bins of $1.305 < |\eta| < 1.93$ and the nine different α bins from 0.05 to 0.45.

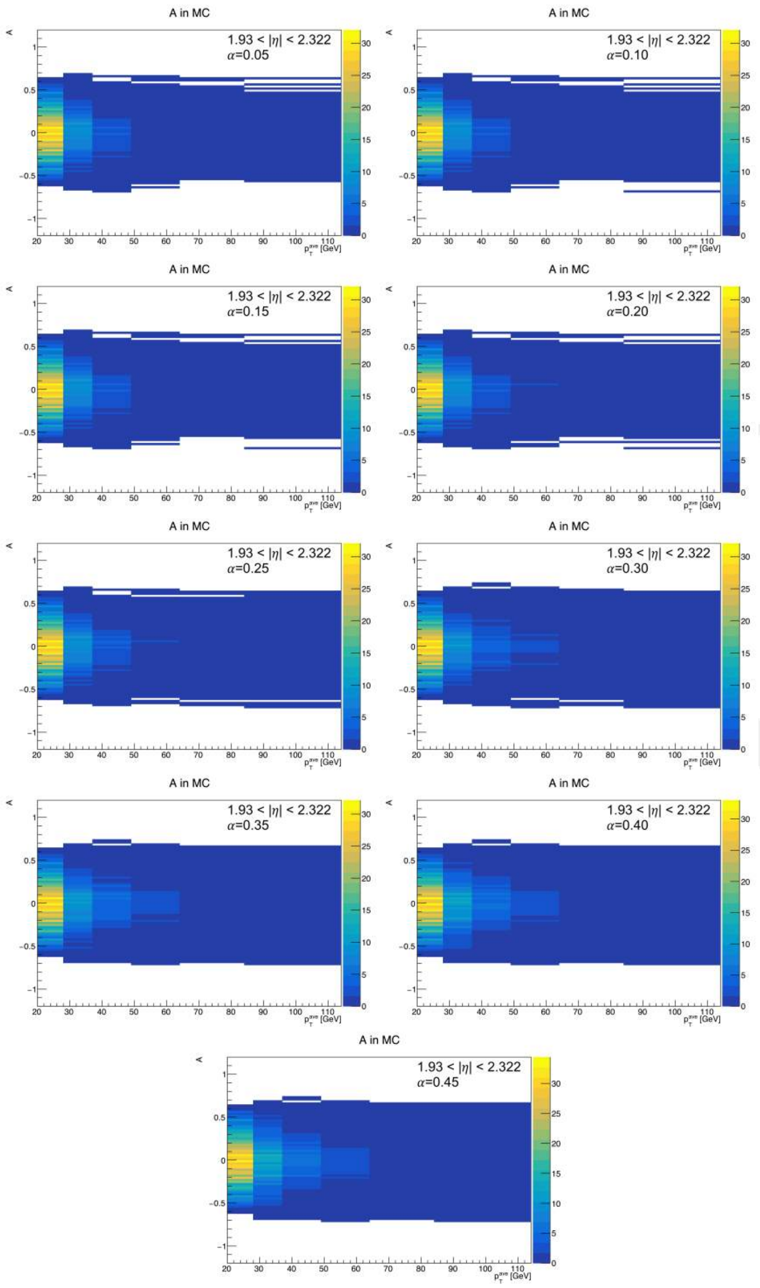

Figure A.16. The distribution of asymmetry quantity in simulation as a function of p_T^{ave} in bins of $1.93 < |\eta| < 2.322$ and the nine different α bins from 0.05 to 0.45.

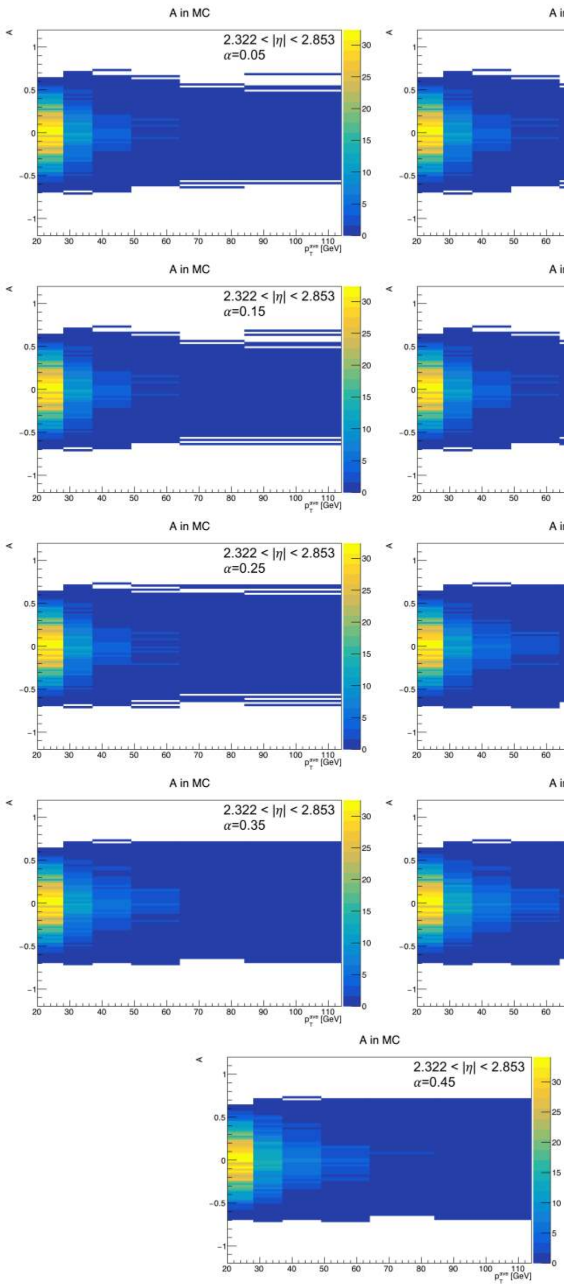

Figure A.17. The distribution of asymmetry quantity in simulation as a function of p_T^{ave} in bins of $2.322 < |\eta| < 2.853$ and the nine different α bins from 0.05 to 0.45.

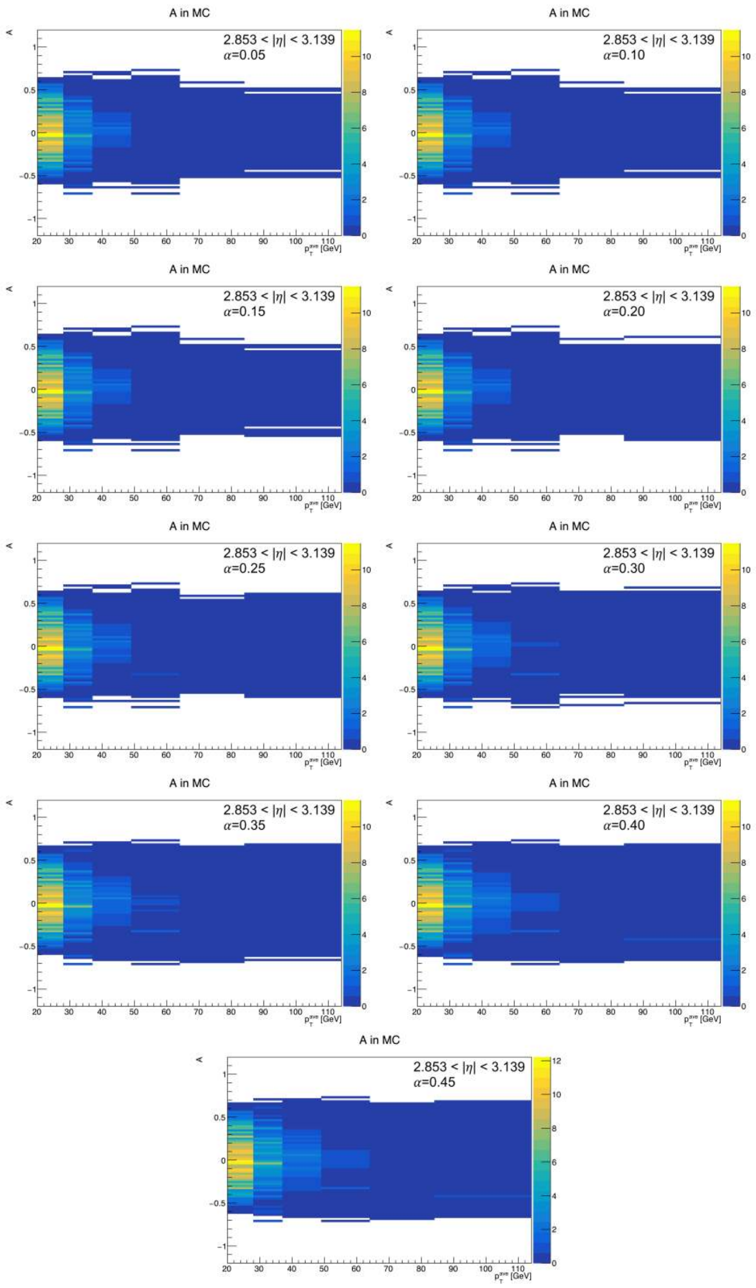

Figure A.18. The distribution of asymmetry quantity in simulation as a function of p_T^{ave} in bins of $2.853 < |\eta| < 3.139$ and the nine different α bins from 0.05 to 0.45.

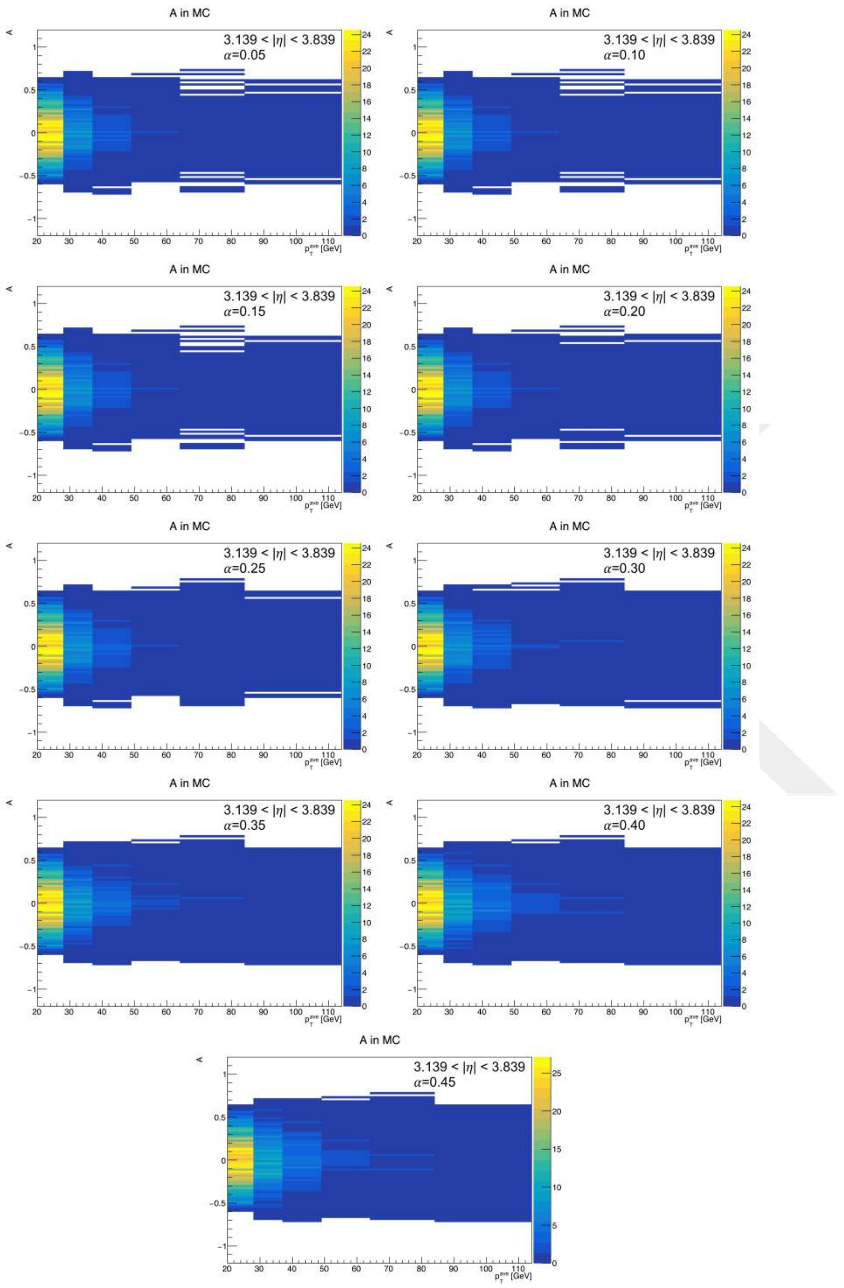

Figure A.19. The distribution of asymmetry quantity in simulation as a function of p_T^{ave} in bins of $3.139 < |\eta| < 3.839$ and the nine different α bins from 0.05 to 0.45.

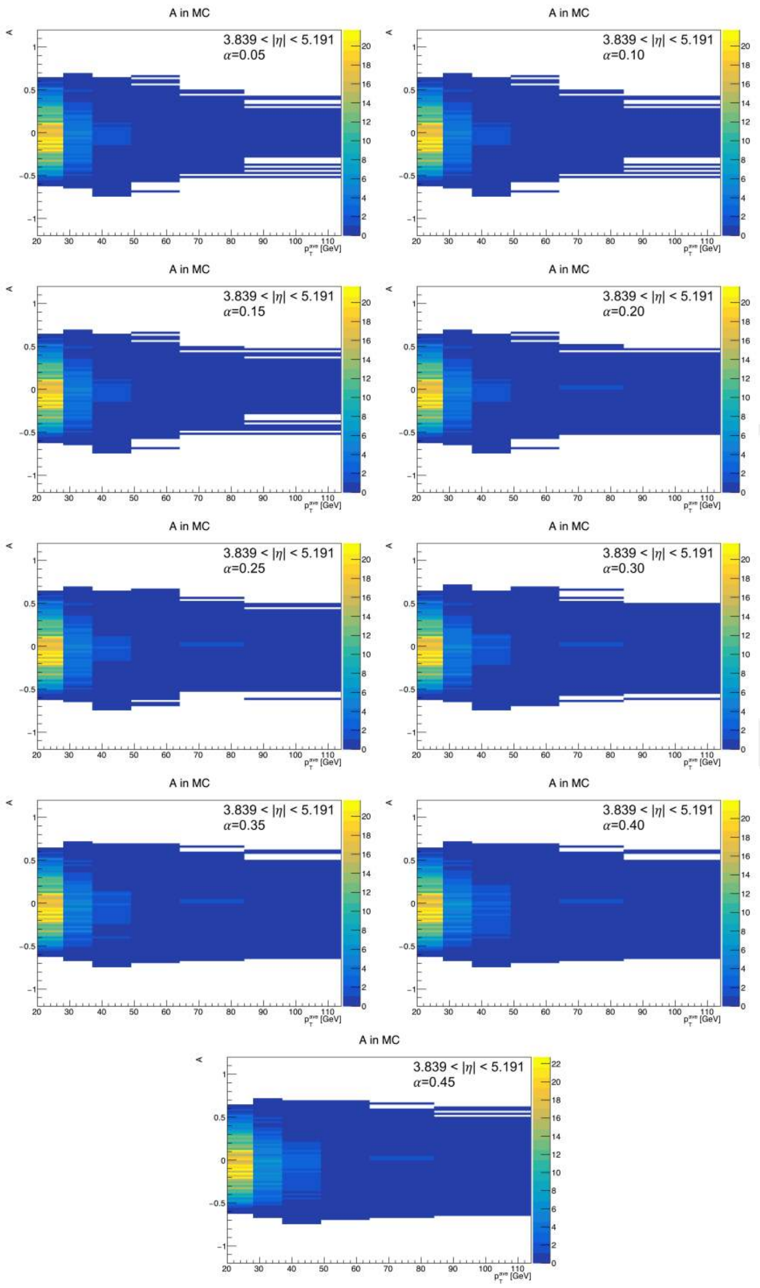

Figure A.20. The distribution of asymmetry quantity in simulation as a function of p_T^{ave} in bins of $3.839 < |\eta| < 5.191$ and the nine different α bins from 0.05 to 0.45.

A.5. Control Plots – The MPF Distributions for DATA

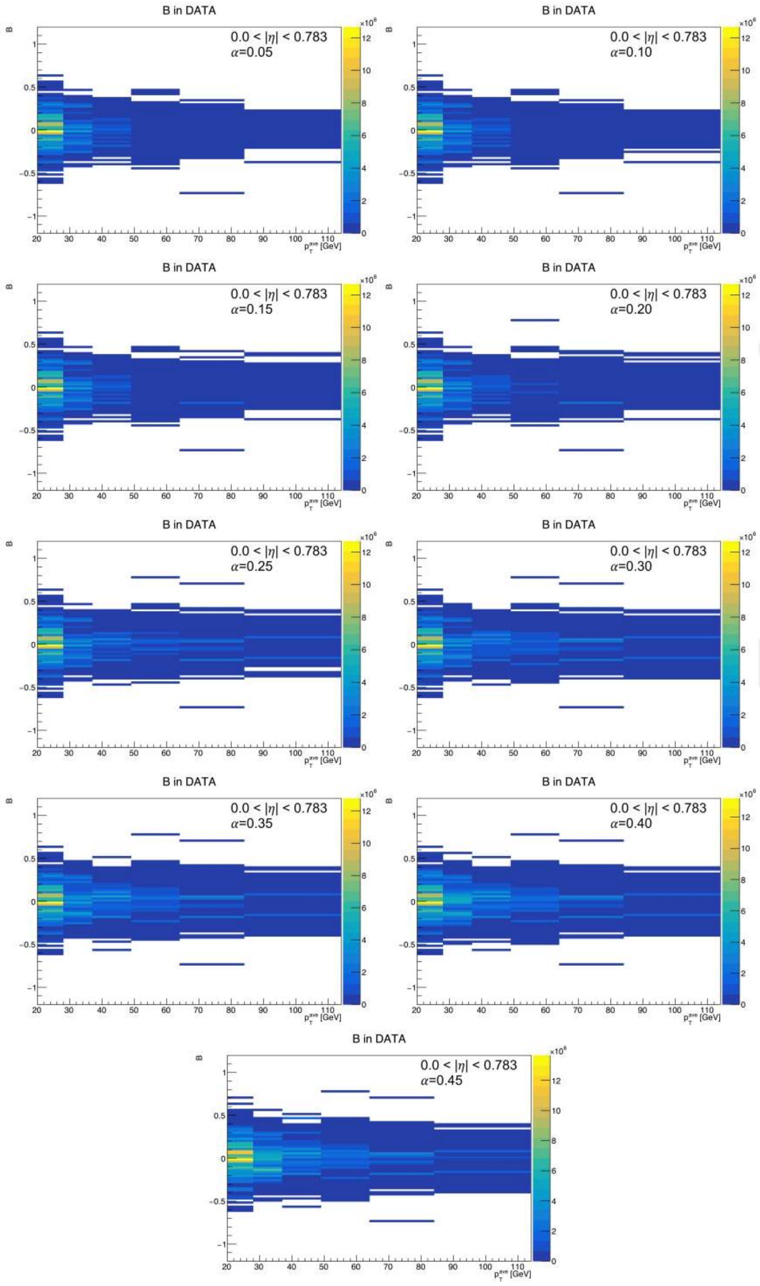

Figure A.21. The distribution of $\mathcal{B}$ quantity in data as a function of p_T^{ave} in bins of $0 < |\eta| < 0.783$ and the nine different α bins from 0.05 to 0.45.

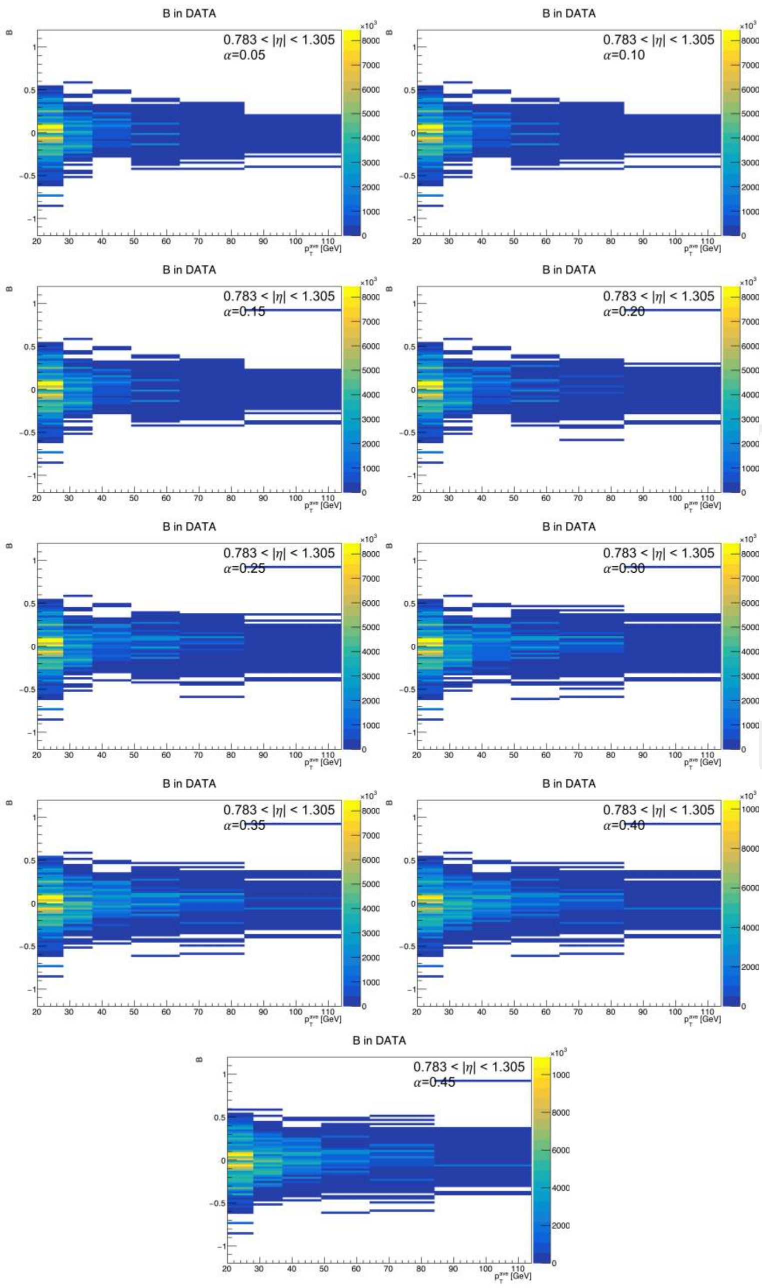

Figure A.22. The distribution of $\mathcal{B}$ quantity in data as a function of p_T^{ave} in bins of $0.783 < |\eta| < 1.305$ and the nine different α bins from 0.05 to 0.45.

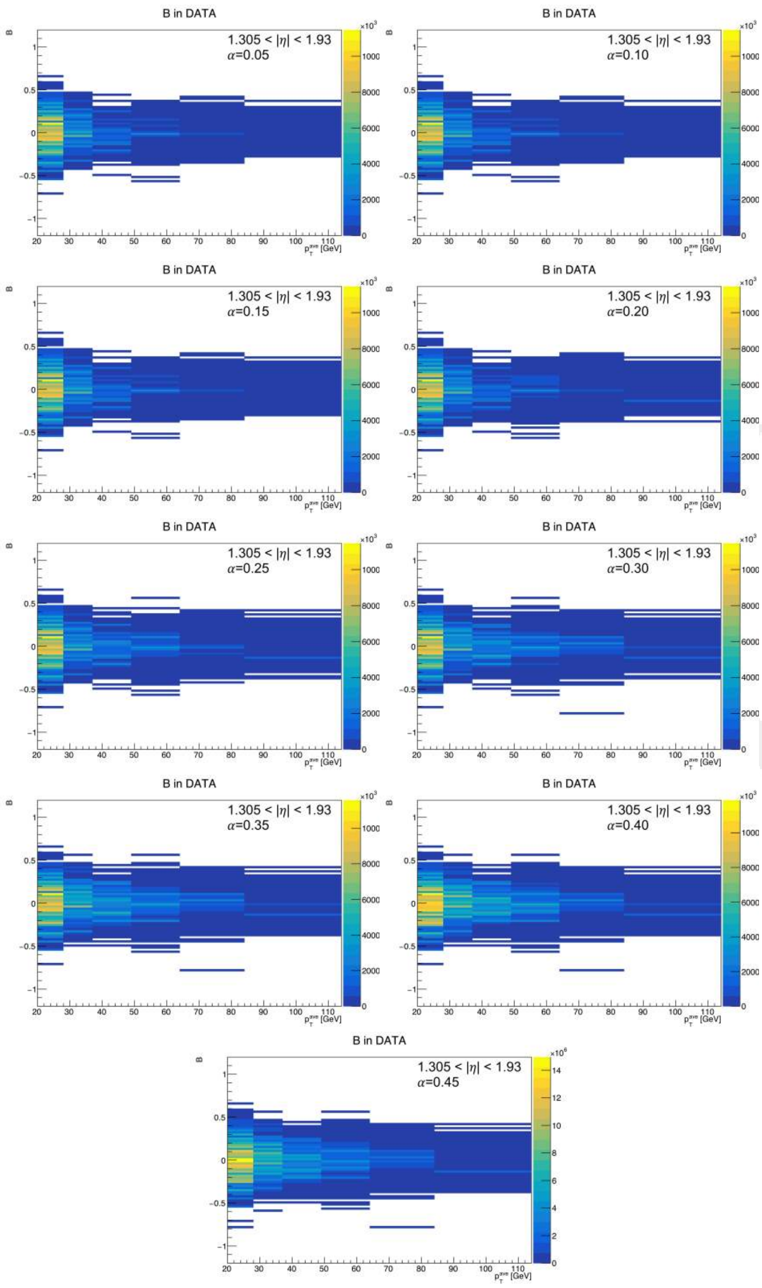

Figure A.23. The distribution of $\mathcal{B}$ quantity in data as a function of p_T^{ave} in bins of $1.305 < |\eta| < 1.93$ and the nine different α bins from 0.05 to 0.45.

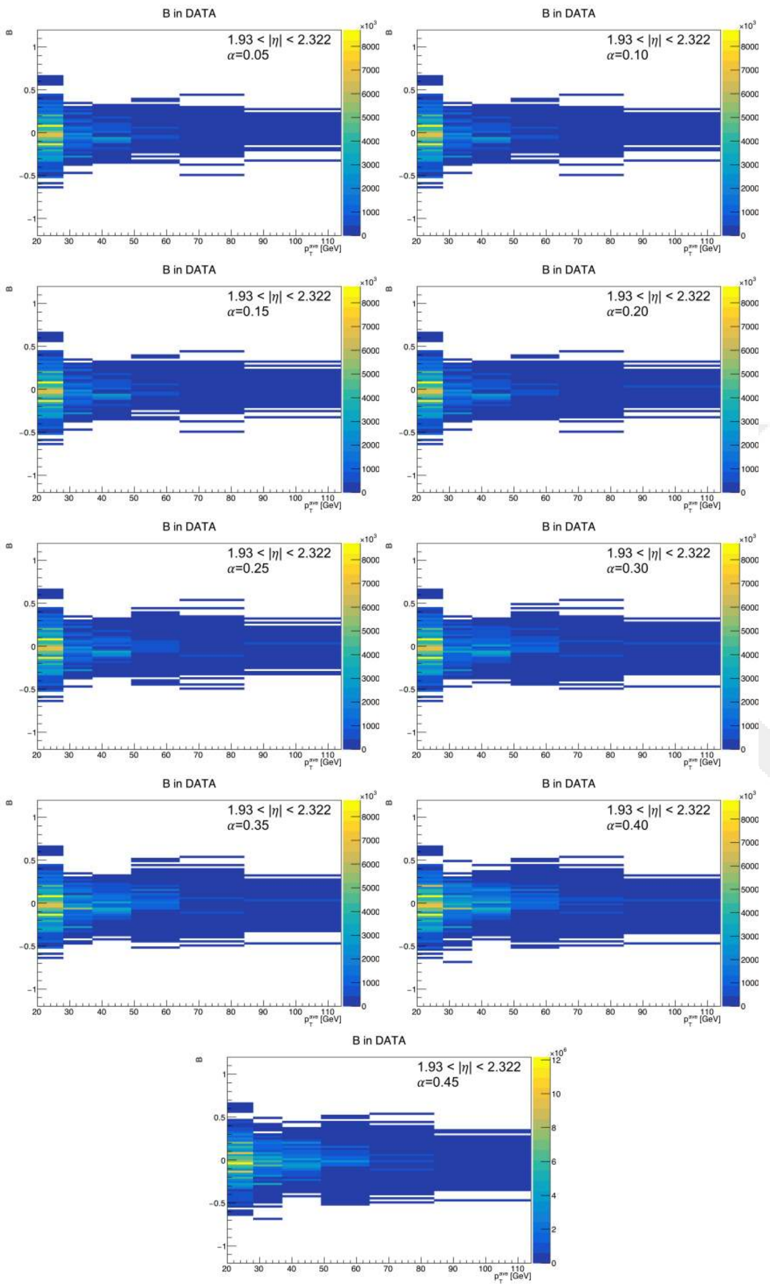

Figure A.24. The distribution of $\mathcal{B}$ quantity in data as a function of p_T^{ave} in bins of $1.93 < |\eta| < 2.322$ and the nine different α bins from 0.05 to 0.45.

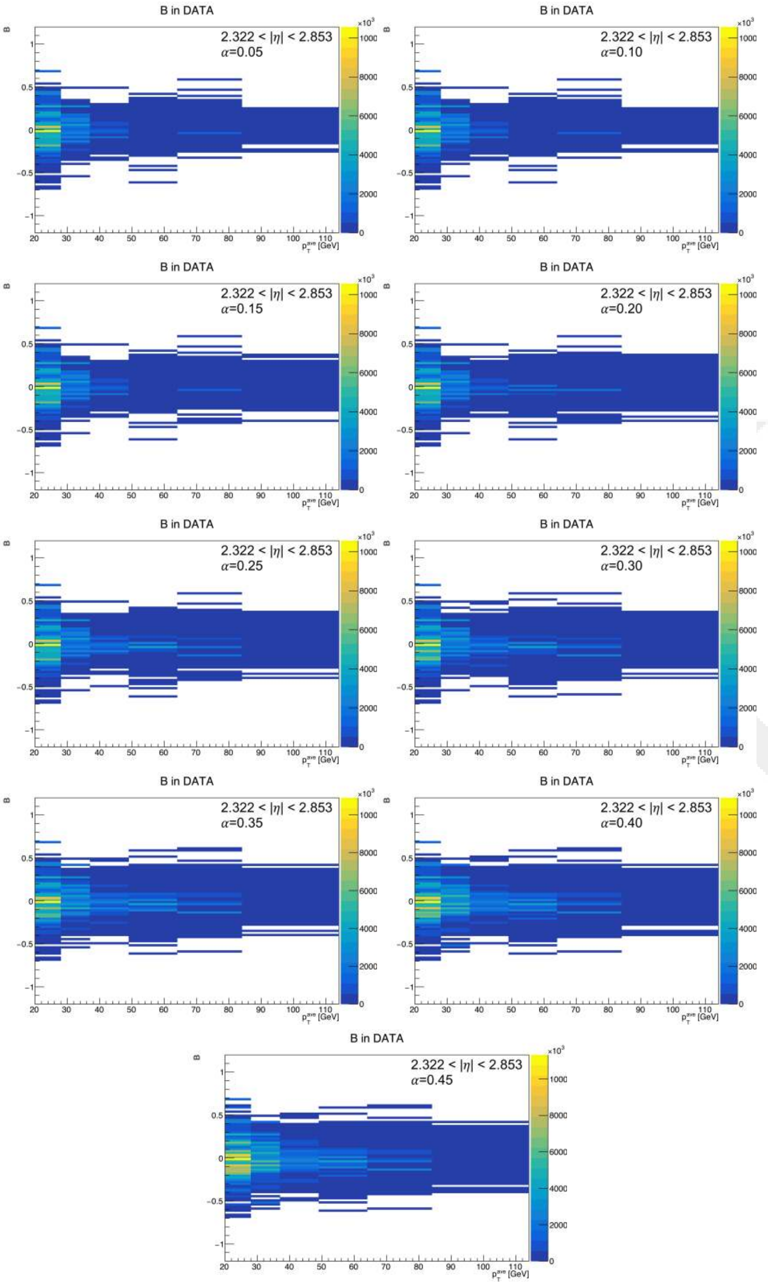

Figure A.25. The distribution of $\mathcal{B}$ quantity in data as a function of p_T^{ave} in bins of $2.322 < |\eta| < 2.853$ and the nine different α bins from 0.05 to 0.45.

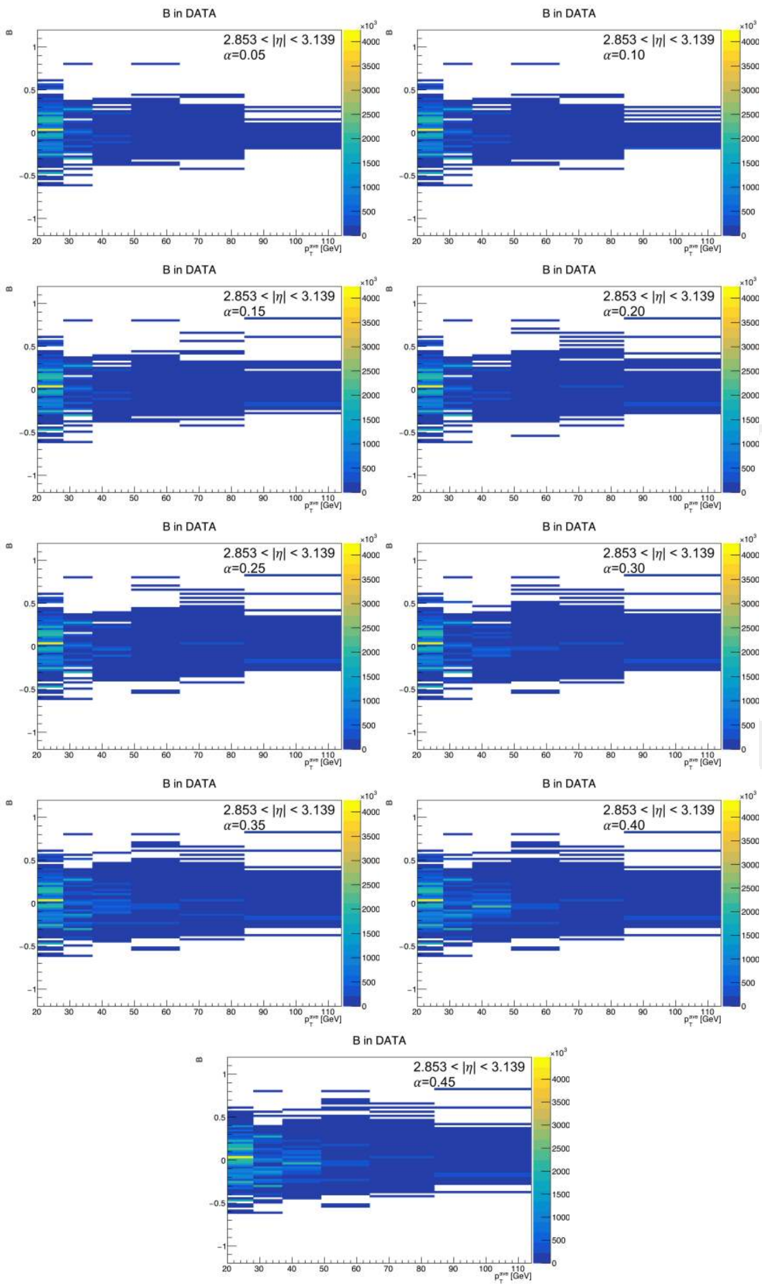

Figure A.26. The distribution of $\mathcal{B}$ quantity in data as a function of p_T^{ave} in bins of $2.853 < |\eta| < 3.139$ and the nine different α bins from 0.05 to 0.45.

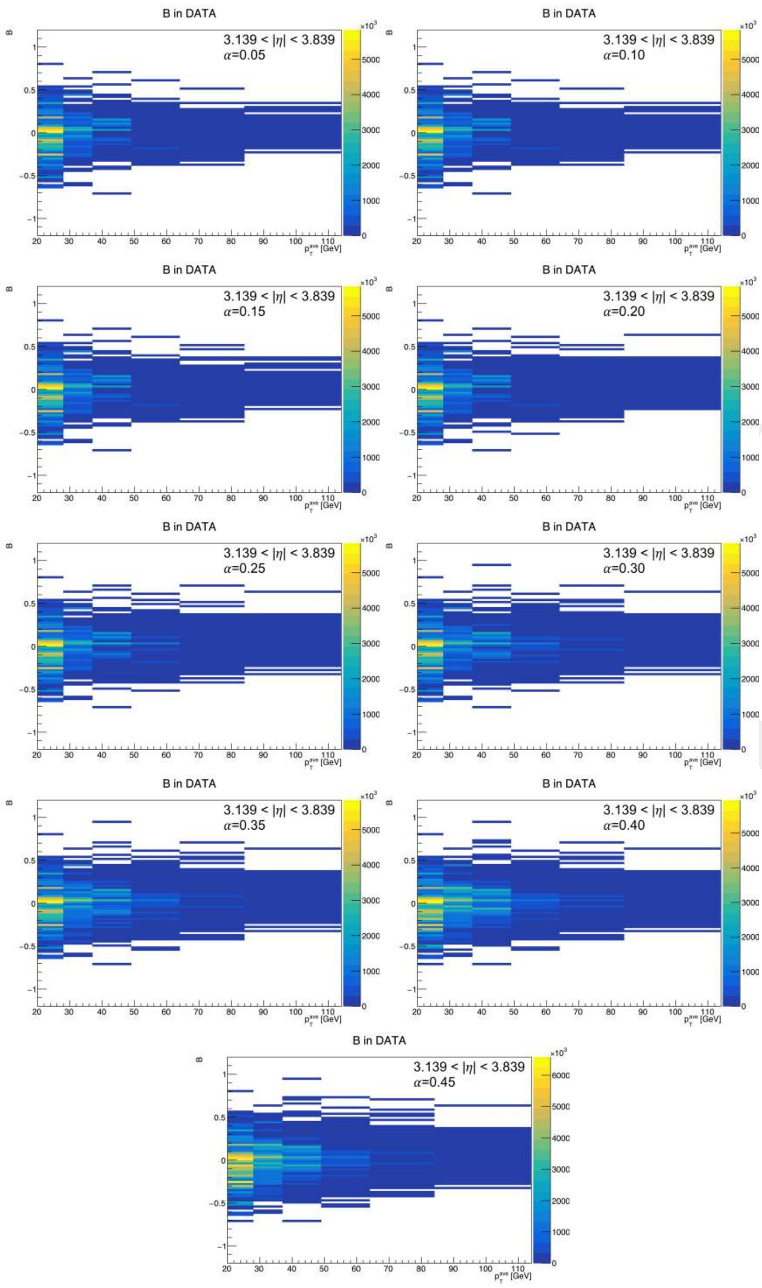

Figure A.27. The distribution of $\mathcal{B}$ quantity in data as a function of p_T^{ave} in bins of $3.139 < |\eta| < 3.839$ and the nine different α bins from 0.05 to 0.45.

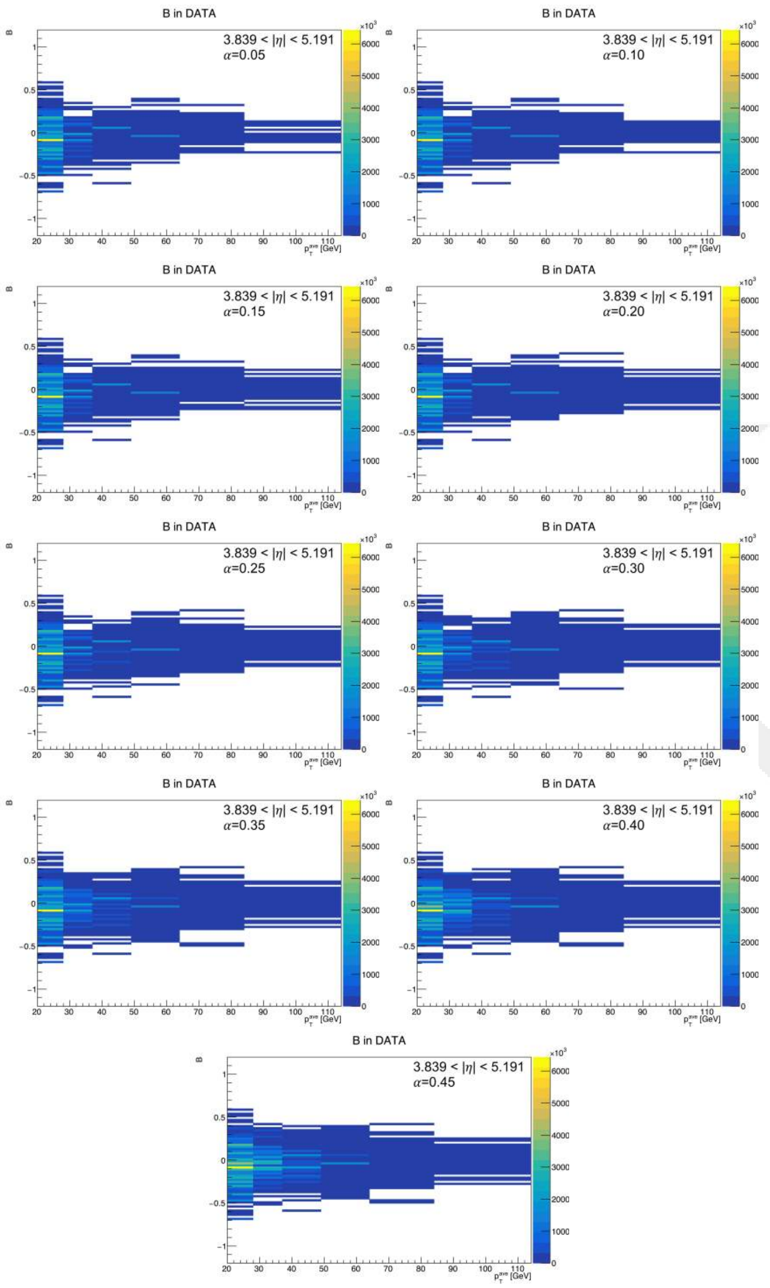

Figure A.28. The distribution of $\mathcal{B}$ quantity in data as a function of p_T^{ave} in bins of $3.839 < |\eta| < 5.191$ and the nine different α bins from 0.05 to 0.45.

A.5. Control Plots – The MPF Distributions for MC

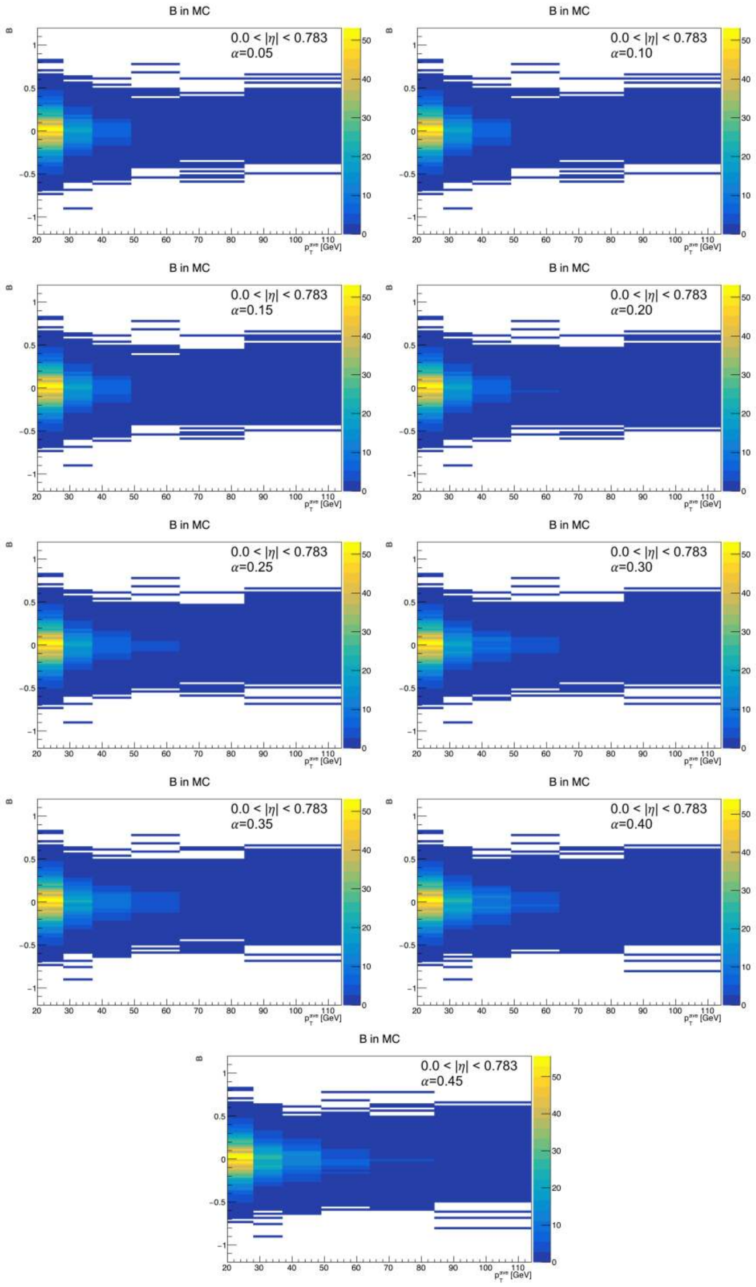

Figure A.29. The distribution of $\mathcal{B}$ quantity in simulation as a function of p_T^{ave} in bins of $0 < |\eta| < 0.783$ and the nine different α bins from 0.05 to 0.45.

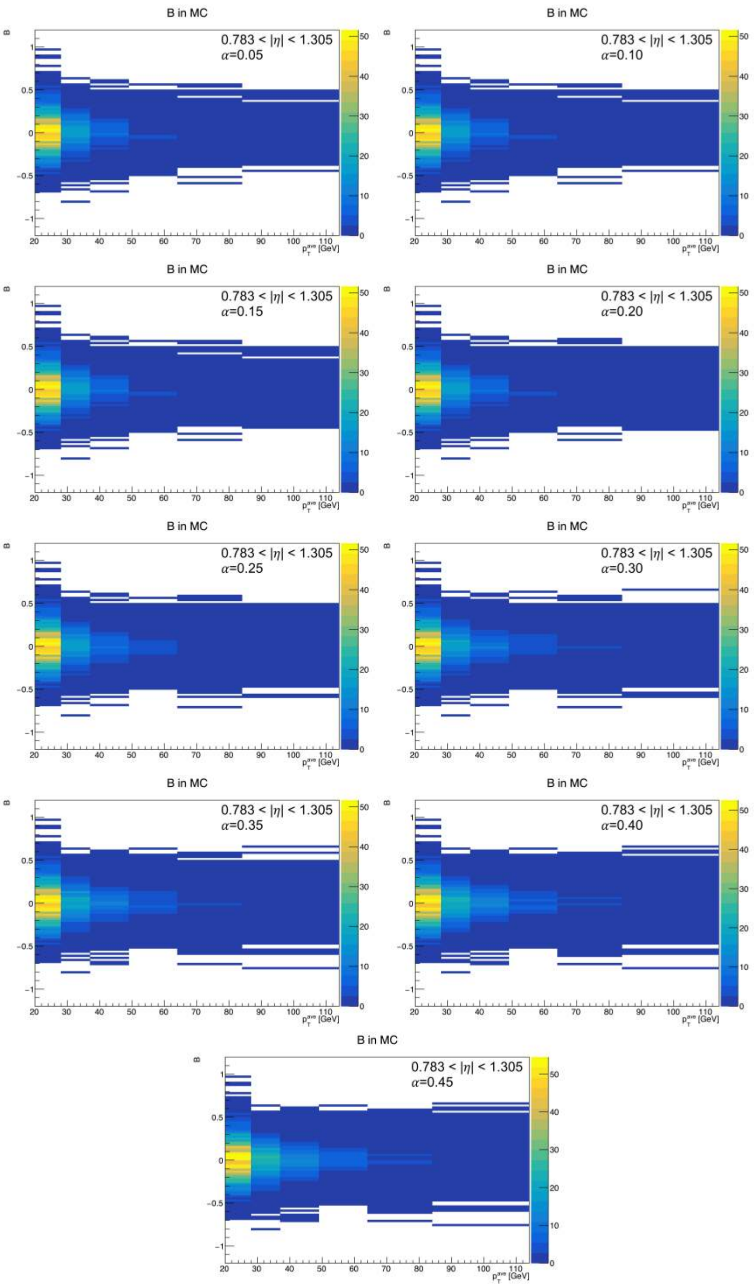

Figure A.30. The distribution of $\mathcal{B}$ quantity in simulation as a function of p_T^{ave} in bins of $0.783 < |\eta| < 1.305$ and the nine different α bins from 0.05 to 0.45.

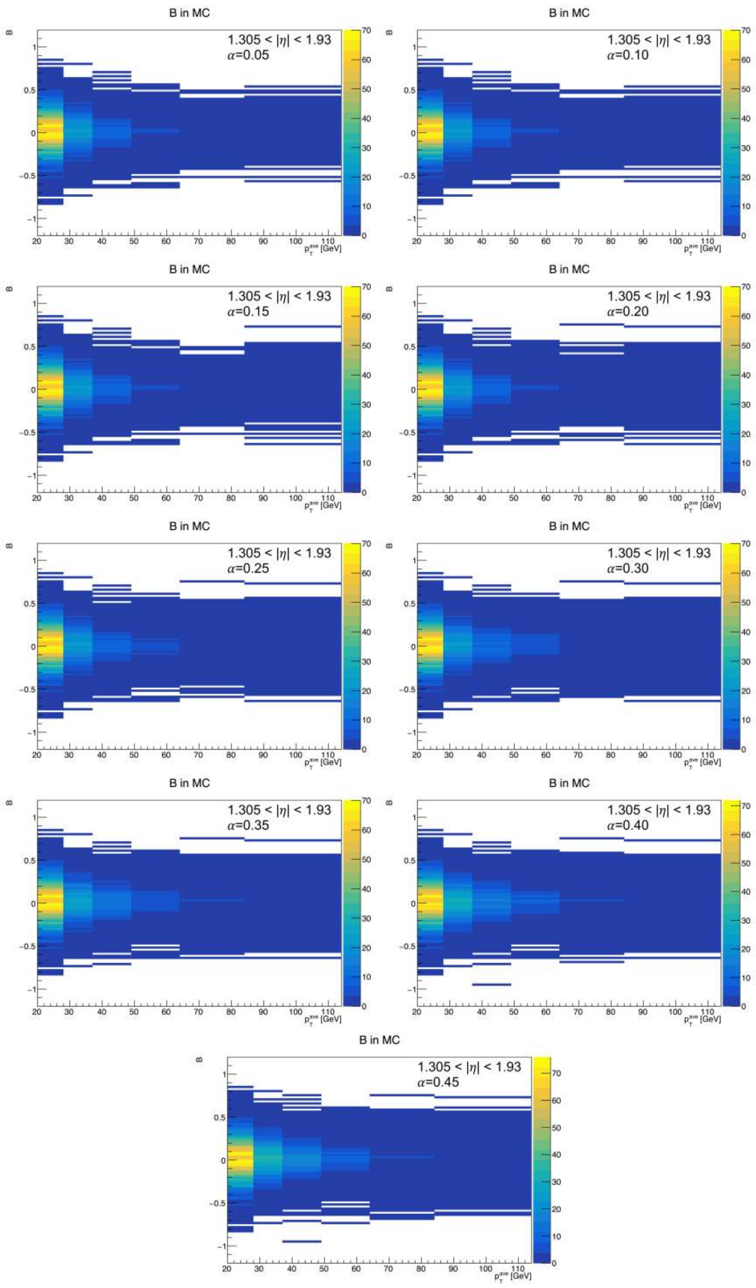

Figure A.31. The distribution of $\mathcal{B}$ quantity in simulation as a function of p_T^{ave} in bins of $1.305 < |\eta| < 1.93$ and the nine different α bins from 0.05 to 0.45.

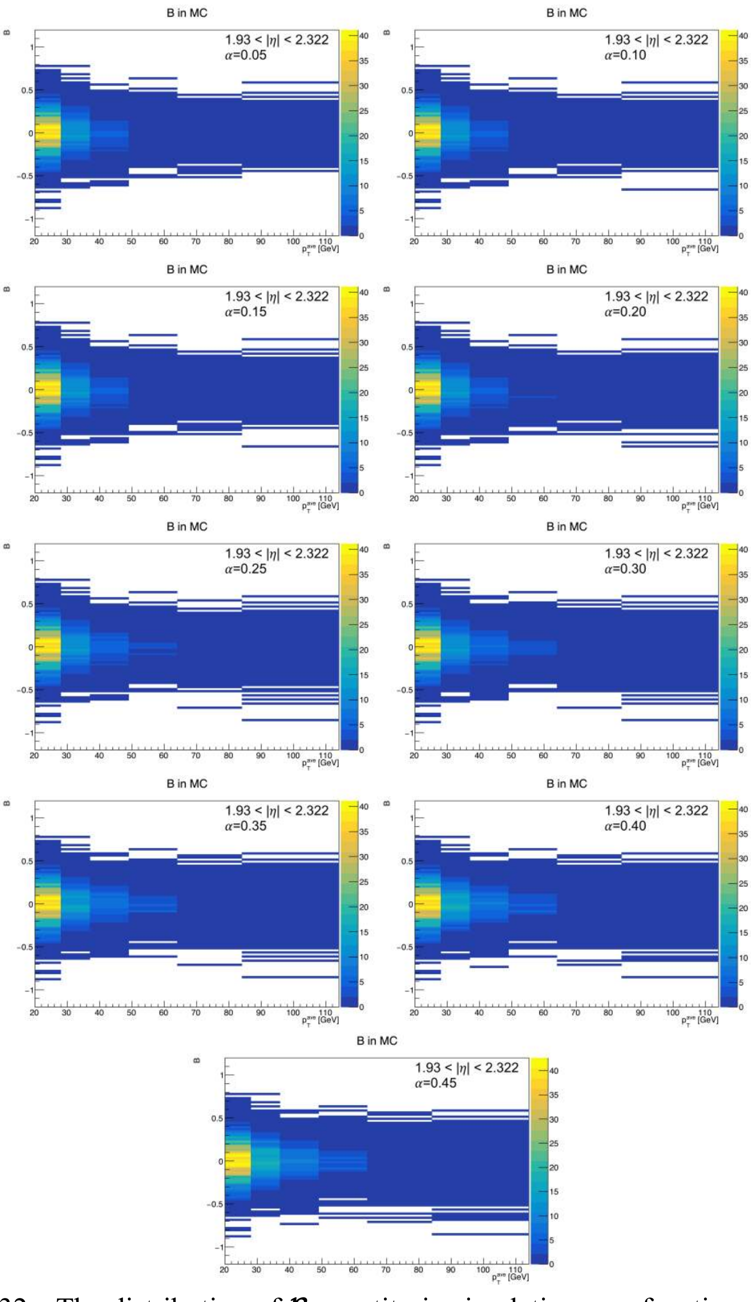

Figure A.32. The distribution of $\mathcal{B}$ quantity in simulation as a function of p_T^{ave} in bins of $1.93 < |\eta| < 2.322$ and the nine different α bins from 0.05 to 0.45.

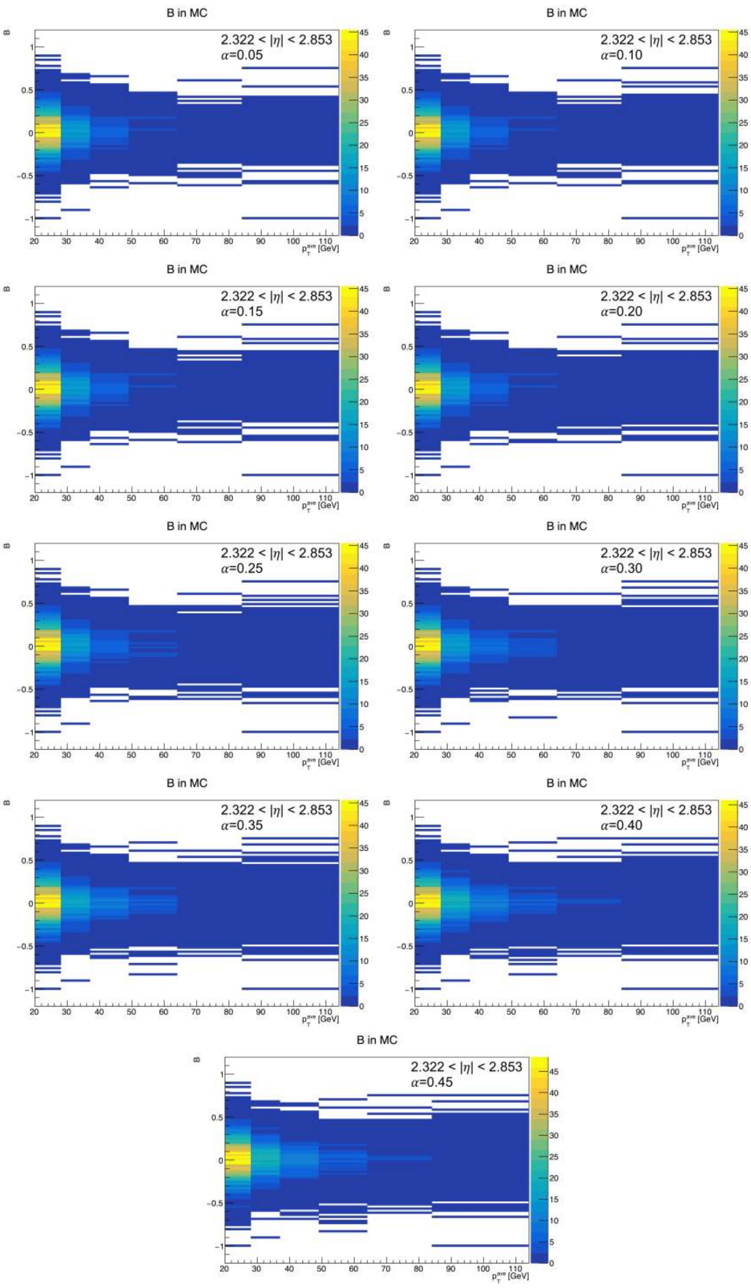

Figure A.33. The distribution of $\mathcal{B}$ quantity in simulation as a function of p_T^{ave} in bins of $2.322 < |\eta| < 2.853$ and the nine different α bins from 0.05 to 0.45.

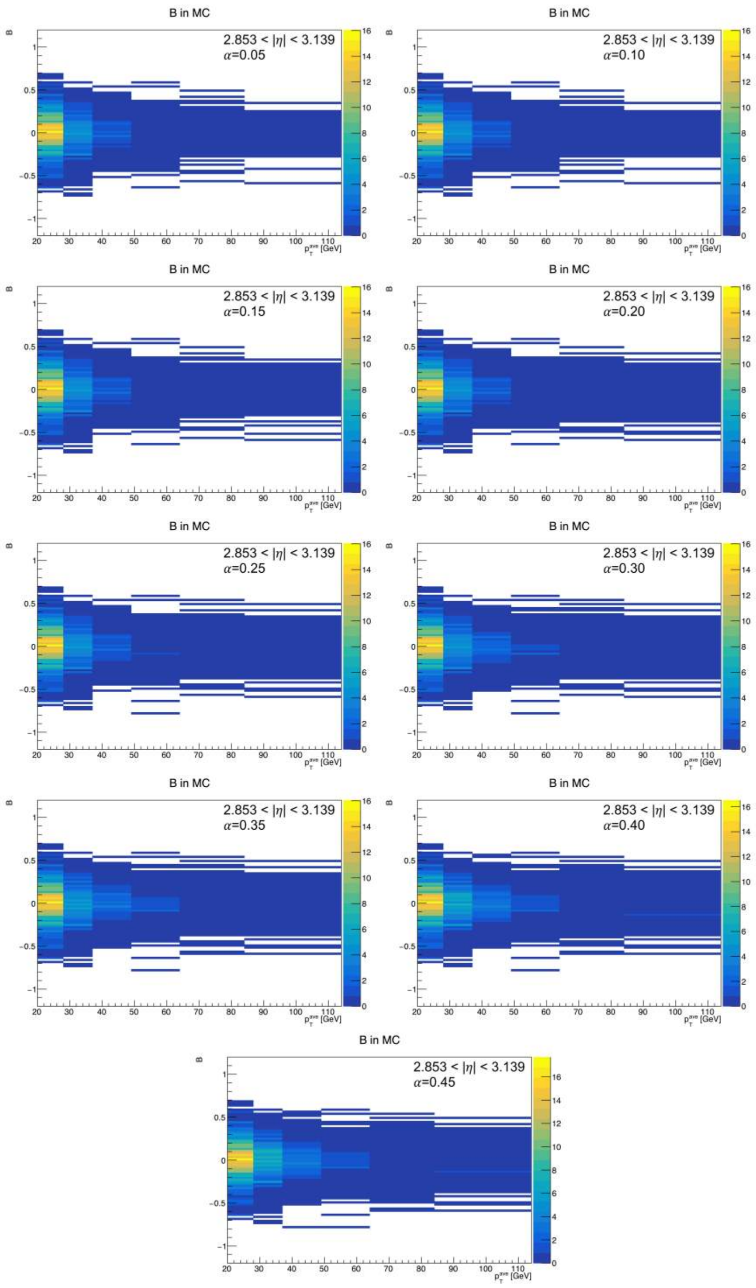

Figure A.34. The distribution of $\mathcal{B}$ quantity in simulation as a function of p_T^{ave} in bins of $2.853 < |\eta| < 3.139$ and the nine different α bins from 0.05 to 0.45.

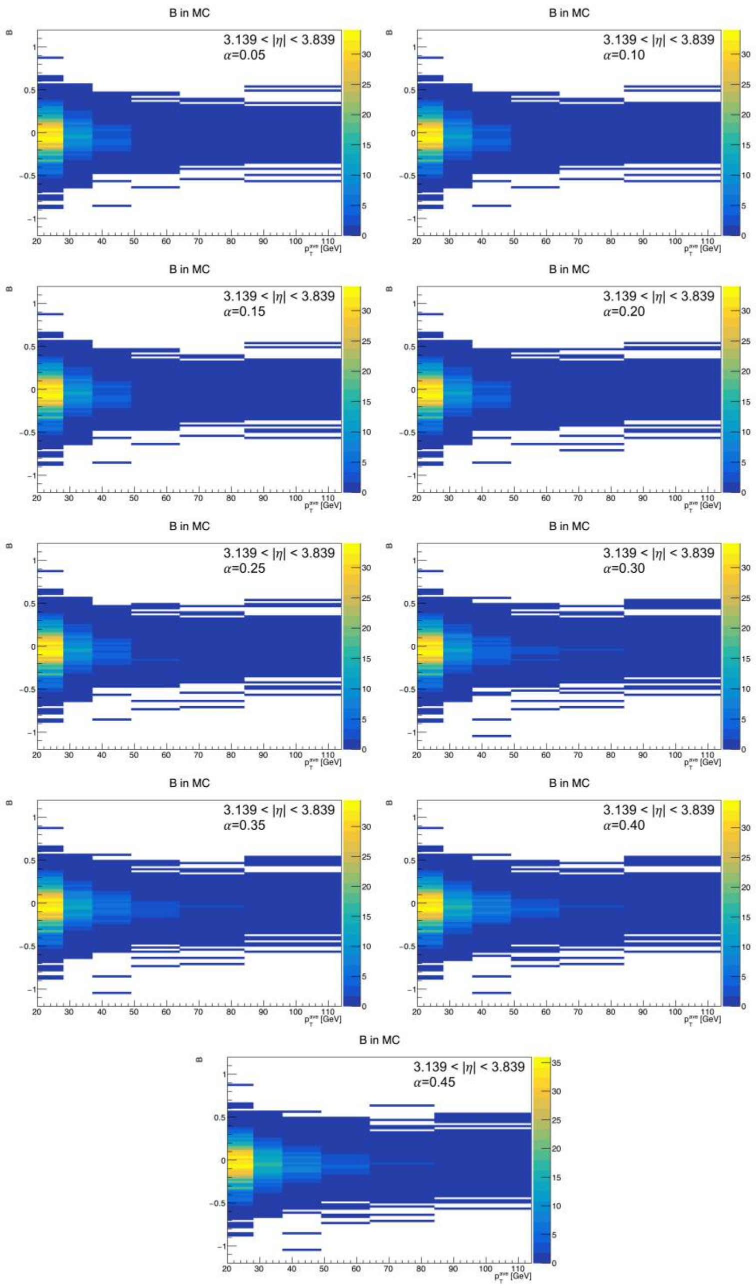

Figure A.35. The distribution of $\mathcal{B}$ quantity in simulation as a function of p_T^{ave} in bins of $3.139 < |\eta| < 3.839$ and the nine different α bins from 0.05 to 0.45.

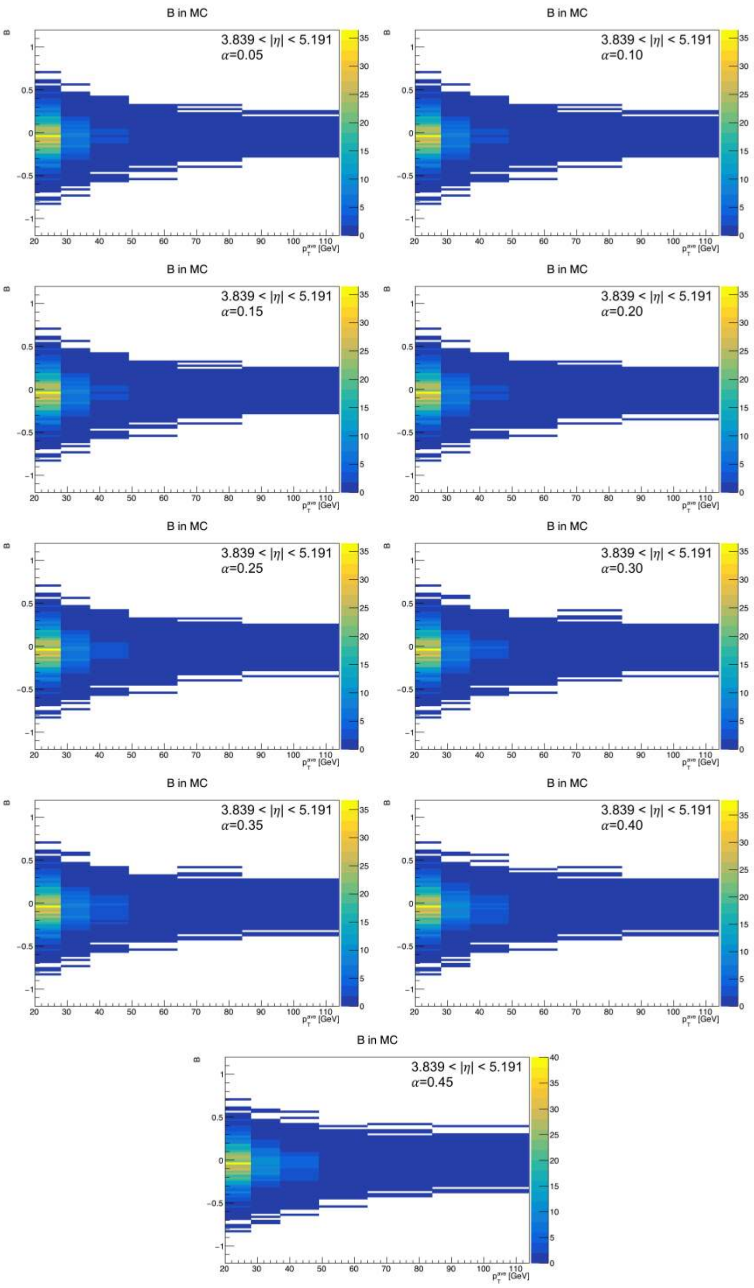

Figure A.36. The distribution of $\mathcal{B}$ quantity in simulation as a function of p_T^{ave} in bins of $3.839 < |\eta| < 5.191$ and the nine different α bins from 0.05 to 0.45.